Estimates of the turbulent kinetic energy (TKE) balance in shelf seas

KYLE F.E. BETTERIDGE, ALEJANDRO J. SOUZA

Proudman Oceanographic Laboratory, 6 Brownlow Street, Liverpool L3 5DA UK
email: kfeb@pol.ac.uk, ajso@pol.ac.uk

Keywords: turbulence, acoustic instrumentation

ABSTRACT

Turbulence is a difficult quantity to measure and to model in the coastal environment, however it is one of the most important as it controls the vertical flux of materials, such as nutrients, sediment and plankton. Developments in measurement techniques, particularly in acoustic instrumentation, have improved the measurements of production and dissipation of turbulent kinetic energy (TKE). Estimates of turbulence production using Acoustic Doppler Current Profilers, ADCPs, have become common and almost routine, and more recently the structure function technique (Wiles et al., 2006) has allowed us to produce estimates of turbulence dissipation. In addition Acoustic Doppler Velocimeters, ADVs, have become the standard instruments to measure turbulence, using direct estimates of the Reynolds stresses and spectral methods for the turbulence dissipation.

The aim of this work will be to look at validating the structure function method against ADV data and then to combine ADVs, ADCPs and Pulse Coherent Acoustic Doppler Profilers, PC-ADPs, to look at the TKE balance throughout the water column. The data involved in this study, which was from Liverpool Bay, showed some differences between the turbulent production measured by an ADCP and the turbulent dissipation measured by an ADV. This paper discusses possible reasons for these differences, and the approaches used to try to correct for them.

Introduction

In recent years there have been important developments in turbulence measurement techniques, particularly in acoustics. Commercial ADCPs can be used to measure turbulence production (e.g., Rippeth et al., 2002) and the availability of ADVs allow point measurements of the TKE to be made from the variance, (for evaluation of the ADV, see for example Voulgaris and Trowbridge, 1999). Measurements of turbulence dissipation, ε, can be made using the spectral method (Huntley, 1988), and when several ADVs are deployed together, or an ADV is deployed in combination with a commercial coherent Doppler profiler to estimate the shear, then turbulence production can also be estimated. An attempt can then be made to close the TKE equation. If accurate measurements are made, it is then possible to robustly test models, e.g., for the effect of buoyancy in the balance between production and dissipation. This work will show results of estimates of the TKE balance applied to data from Liverpool Bay, using an ADV and ADCP, and current attempts to explain differences measured by the two instruments on different tides.

Methods

A 1.2 MHz ADCP, with 0.5 m bin size, and a 5 MHz Sontek ADV, sampling at 25 Hz, were deployed in Liverpool Bay on a frame located in the open coast; a region of freshwater longshore and cross shore influences. The ADV was located on an arm about 0.85 m away from the frame, to reduce any effects from the frame, as seen in Figure 1. The ADV measuring volume and the centre of bin 2 of the ADCP were located about 1.5 m above the seabed. The data were recorded for 10 minutes every hour. The ADCP variance method to estimate the rate of production of turbulent kinetic energy (P) [e.g., Lu and Lueck, 1999], has been used for some time but with few measurements to validate it. One comparison of Reynolds stresses obtained from using this method and that from an ADV is discussed in Souza and Howarth (2005).

The inertial dissipation method, (see e.g., Huntley, 1988), was used to obtain the dissipation from the ADV data. The inertial sub-range is the range of wavenumbers between turbulent energy production and turbulent energy dissipation by viscosity. The energy flux from low to high wavenumbers is equal to the dissipation rate, ε, since there are no local energy sources or sinks. The inertial subrange spectrum is given by

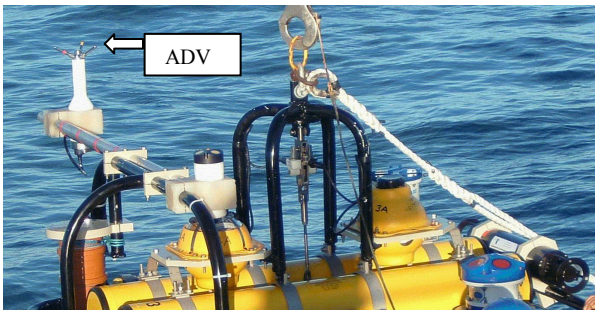

Figure 1. This is a photograph showing the frame with the deployment of an ADCP and ADV in Liverpool Bay. The ADV is pointing upward on an arm about 0.85 m away from the main frame.

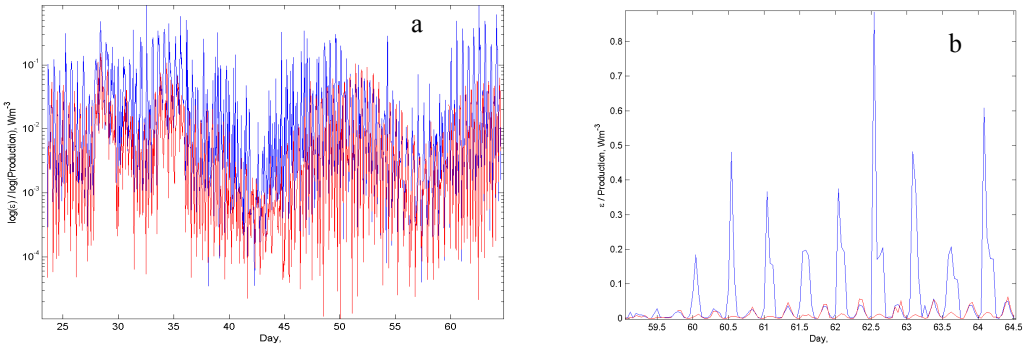

Figure 2. The plots in these figures show the turbulent production and dissipation, in W m^{-3}, from the ADCP and ADV measurements respectively showing (a) over the full 40-day deployment time, and (b) over 5 days towards the end of the deployment.

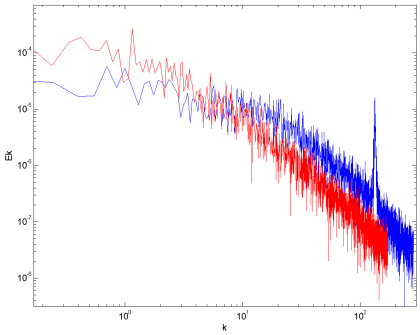

Figure 3. This figure shows the turbulent energy spectra versus wavenumber for a flood tide (shown in red) and an ebb tide (shown in blue) at days 60.54 and 60.83.

$E(k) = \alpha \varepsilon^{2/3} k^{5/3}$, where α is the experimentally determined Kolmogorov constant. A function written by G. Voulgaris for the estimation of the 1-D turbulence spectra $E(k)$ of a velocity time series was used which was based on a method used by Green (1992). Applying Taylor's hypothesis then generates an estimate of the dissipation, ε.

Results and discussion

The production and dissipation estimated from the ADCP and ADV respectively are plotted in Figure 2a for the full duration of the deployment, and for days 60–65 in Figure 2b. The red plot shows the production, and the dissipation is shown in blue.

The results show that there is good agreement on the flood tides, and $P \approx \varepsilon$, but on an ebb tide the turbulent dissipation measured by the ADV is considerably higher than the production values obtained from the

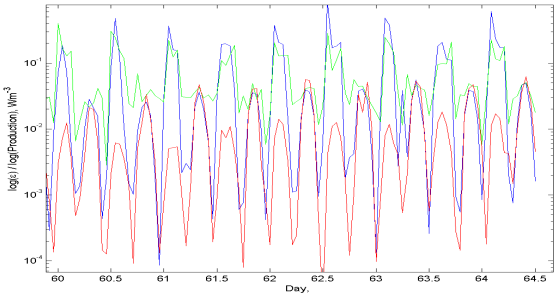

Figure 4. This plot shows the pitch standard deviation measured by the ADV in green as well as the turbulent production and dissipation, in W m^{-3}, from the ADCP (red) and ADV (blue), for the five days towards the end of the deployment.

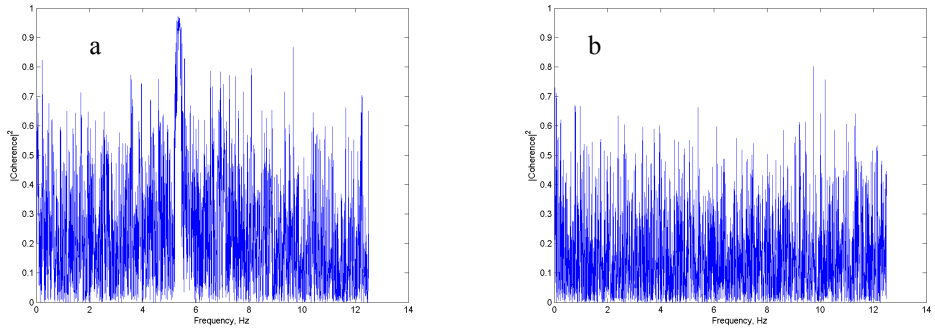

Figure 5. The magnitude-squared coherence is plotted with frequency for record 2 in Figure 5a, and for record 8 in Figure 5b. The records displaying this coherence are the same as those which also show a peak in the energy spectra i.e. record 2 does, but not record 8.

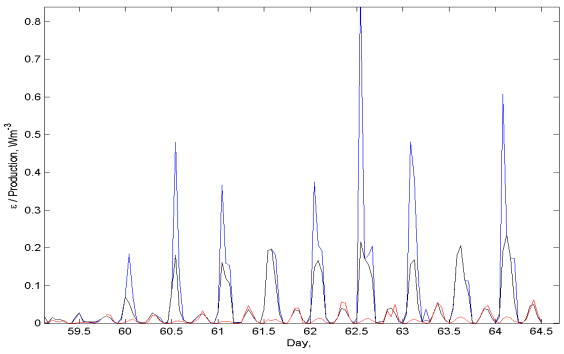

Figure 6. This plot shows the dissipation recalculated from the corrected spectra (shown in black) in addition to the original turbulent dissipation from the ADV in blue, and production obtained from the ADCP (red).

ADCP. If the turbulent spectra for these examples are considered then peaks in the energy/wavenumber spectra are seen at the higher values of k, as shown in Figure 3.

To try to understand what was happening, the pitch standard deviation measured by the ADV was plotted with the production and dissipation, and this is shown in Figure 4. The peaks in the pitch measurements correlate exactly with the higher values of production, and it suggests that the ADV is vibrating on the pipe under these conditions.

Is the vibration in the ADV on the ebb tide due to eddy shedding? Several attempts to eliminate this effect from the data have been made. Initially a simple cut-off of the spectra above $k \approx 90$ was made, however although this reduced the differences seen on the ebb tides, it was too crude a method and was abandoned as data was unnecessarily being removed.

A second attempt to account for the difference by filtering out the peaks in the spectra was made. This method used the coherence between the velocities measured by the ADV. On flood tides there is no coherence between the measured horizontal and vertical velocities *u* and *w*, however on ebb tides a coherence greater than 0.9 is found between u and w and these records are where the turbulent spectra display a peak. Examples are shown in Figure 5.

These coherence peaks were identified for each record and then used to remove the peak in the frequency spectra. 'Corrected' velocities were then generated using an inverse FFT and the spectral method reapplied to calculate the new dissipation rates. The corrected results are shown in Figure 6, where the red and blue plots are P and ε as before and the black data are the corrected dissipation values. The results show that there is a reduction in dissipation for the region of ebb tides, however the results are still not comparable to the production rates measured by the ADCP.

As these differences have not yet been resolved, other approaches will be attempted and results reported to try to explain the remaining difference. In addition the structure function technique will be applied to the ADCP data, to look at the turbulent dissipation and see if this method can be validated against the ADV data.

References

Green, M.O. (1992), Spectral estimates of bed shear stress at subcritical Reynolds numbers in a tidal boundary layer, *Journal of Physical Oceanography*, 22, 903–917, doi:10.1175/1520-0485(1992)022<0903:SEOBSS>2.0.CO;2.

Huntley, D.A. (1988), A modified inertial dissipation method for estimating seabed stresses at low Reynolds numbers, with application to wave/current boundary layer measurements, *Journal of Physical Oceanography*, 18,(2), 339–346, doi:10.1175/1520-0485(1988)018<0339:AMIDMF>2.0.CO;2.

Lu, Y., Lueck, R.G. (1999), Using a broadband ADCP in a tidal channel; part II, Turbulence, *Journal of Atmospheric and Oceanic Technology*, 16, 1568–1579, doi:10.1175/1520-0426(1999)016<1568:UABAIA>2.0.CO;2.

Rippeth, T.P., Williams, E., Simpson, J.H. (2002), Reynolds stress and turbulent energy production in a tidal channel, *Journal of Physical Oceanography*, 32(4), 1242–1251, doi:10.1175/1520-0485(2002)032<1242:RSATEP>2.0.CO;2.

Souza, A.J., Howarth, M.J. (2005), Estimates of Reynolds stress in a highly energetic shelf sea, *Ocean Dynamics*, 55, 490–498, doi:10.1007/s10236-005-0012-7.

Voulgaris, G., Trowbridge, J.H., (1999), Evaluation of the acoustic Doppler velocimeter (ADV) for turbulence measurements, *Journal of Atmospheric and Oceanic Technology*, 15(1), 272–289, doi:10.1175/1520-0426(1998)015<0272:EOTADV>2.0.CO;2.

Wiles, P.J, Rippeth, T.P., Simpson, J.H., Hendicks, P.J. (2006), A novel technique for measuring the rate of turbulence dissipation in the marine environment, *Geophysical Research Letters*, 33, L21608, doi:10.1029/2006GL027050.

Mixing mechanisms in the Liverpool Bay ROFI

MATTHEW PALMER

Proudman Oceanographic Laboratory, 6 Brownlow Street, Liverpool L3 5DA UK
email: rolm@pol.ac.uk

Keywords: strain induced periodic stratification; Liverpool Bay

ABSTRACT

The Liverpool Bay Coastal Observatory has to date collected near-continuous measurements of the vertical structure of temperature, salinity and current velocity from one site for over five years extending measurements to a second site over the past three years. Analysis of this data reveals that a myriad of processes are likely responsible for local controls on vertical structure and transport processes and thus on the fate of freshwater inputs and the distribution of terrestrial sources of nutrients, minerals and pollution.

Here we present a new series of complimentary measurements made within Liverpool Bay in May 2004. Measurements of temperature, salinity and current velocity show Strain Induced Periodic Stratification (SIPS) at the site during the ebb flow and there is some evidence of strain induced convective instability towards the end of the flood phase of the flow consistent with the findings of Rippeth et al. (2001) and Simpson et al. (2002). In contrast to these findings however, we observe enhanced levels of mid-water turbulence during stratification in both turbulent kinetic energy (TKE) dissipation rates derived from velocity microstructure (FLY) and ADCP derived TKE production. This mixing appears to be due to shear driven instability during periodic stratification: due to the shallow nature of the site and strong tidal flows, stratification leads to considerable modification of the current profile resulting in an increase in northerly flow, perpendicular to the otherwise rectilinear E-W flow. Subsequently, the thermocline gradient Richardson number is observed to be near critical during stratification as a result of the increase in vertical shear in the horizontal velocity.

This study suggests therefore that during stratified periods turbulence and subsequently vertical mixing are not directly driven by boundary processes but are the result of a mid-water breakdown of stability, something that current turbulence closure schemes have difficulty in reproducing. These findings also have important consequences on the fate of freshwater entering regions of SIPS and present further contributions to the investigation of controlling processes in regions of freshwater influence (ROFIs).

References

Rippeth, T.P., Fisher, N.R., Simpson, J.H. (2001), The cycle of turbulent dissipation in the presence of tidal straining, *Journal of Physical Oceanography*, 31, 2458–2471.

Simpson J.H., Burchard, H., Fisher, N.R., Rippeth, T.P. (2002), The semi-diurnal cycle of dissipation in a ROFI: model-measurement comparisons, *Continental Shelf Research*, 22, 1615–1628.

Three-dimensional numerical modeling study of the role of bathymetry in the circulation of the Persian Gulf

MASOUD SADRINASAB

Department of Physical Oceanography,
Khorramshahr University of Marine sciences and Technology, Khorramshahr, Iran
email: masoud.sadri@gmail.com

Keywords: bathymetry, numerical modeling, circulation; Persian Gulf

ABSTRACT

The Persian Gulf is an important military, economic and political region owing to its oil and gas resources it is one of the busiest waterways in the world. Due to this importance circulation of the water in the Persian Gulf has been studied since 1918. These studies show an overall anticlockwise circulation of water in the Persian Gulf. However these studies provide mix answers about the role of bathymetry in the circulation. In this study a three-dimensional hydrodynamic model (COHERENS) is employed in a fully prognostic mode to derive circulation of the Persian Gulf. Two different models have been run to simulate circulation of the Persian Gulf. One is with real bathymetry and the other with averaged 35-meters bathymetry. The results showing that bathymetry has a major role on the circulation in the southern part of the Gulf.

A comparison of partitioning when applied to HF radar and wave model spectra

JENNIFER WATERS[1], LUCY WYATT[1], JUDITH WOLF[2], ADRIAN HINES[3], MARTIN HOLT[3]

1. Department of Applied Mathematics, University of Sheffield, Sheffield S3 7RH UK
email: jennifer.waters@sheffield.ac.uk, l.wyatt@sheffield.ac.uk

2. Proudman Oceanographic Laboratory, 6 Brownlow Street, Liverpool L3 5DA UK
email: jaw@pol.ac.uk

3. Met Office, FitzRoy Road, Exeter EX1 3PB UK
email: adrian.hines@metoffice.gov.uk, martin.holt@metoffice.gov.uk

Keywords: directional wave spectrum, partitioning, HF radar, wave model

ABSTRACT

It is useful to partition ocean wave spectra for the classification of wind sea and swell and for detecting weaknesses in models or measuring systems. In this study various partitioning scheme have been investigated and their effectiveness, robustness and feasibility for use in automated systems taken into consideration. The partitioning scheme used by Hasselmann et al. (1996) appears to be the most useful for fully automated processes and therefore the performance of the partitioning method has been analyzed by comparisons of spectra from the Wavewatch III model, the Swan model and from HF radar. This comparison suggests that specific processes are needed to manage the effect of noise and sensitivity on the partitioning method when looking at the different spectra. The research has focused on the Celtic sea region for the 2003 to 2005 period when the Pisces radar system was operational. In addition a Directional Waverider buoy was deployed in the area and the buoy's reconstructed spectra have also been considered.

Partitioning methods

Partitioning of the ocean wave spectrum into different components is a useful tool. It allows for a spectrum to be represented with a reduced set of statistics without having to average over the entire spectrum. After partitioning the wind sea and swell components can be identified, which gives a more detailed picture of the physical situation and can lead to the identification of weaknesses in the models or measurements.

The partitioning methods used by Gerling (1992) and Hasselmann et al. (1994) are both based on the geometric properties of the spectrum. Gerling's method partitions the spectra by increasing a threshold and finding which parts of the spectrum become disconnected as the threshold rises. Hasselmann's method is based on a steepest ascent algorithm; the scheme essentially calculates the basins of attraction of each peak. One of the main disadvantages of Gerling's method is that the partitions are not necessarily distinct. For many cases a partition may be identified, but as the threshold increases this may be split into further disconnected regions. A choice then needs to be made about whether to consider the larger partition or the various smaller partitions. Gerling stated that this process needs to be done manually which restricts the application of this partitioning method for large sets of data or for automated processes such as data assimilation. An advantage of the Gerling method is the natural way in which a noise floor can be removed by thresholding above a certain level; it is certainly beneficial to apply such a process when partitioning noisy radar spectra. Guillaume (Guillaume, 1990; Lefevre et al., 2005) proposed a method of partitioning which first located the peaks within a spectrum. The maximum peak is then considered and all the bins within a certain frequency and direction range are assigned to that peak, and the process is repeated for the next highest peak. The major problem with this method is that it does not take the spread of a wave train into consideration.

Many other schemes which simply partition the spectra by identifying a wind sea have also been proposed. However, all these methods rely on knowledge of the wind speed and since reliable wind speeds are not currently available from HF radar, these methods are unsuitable for this application. They also tend to only

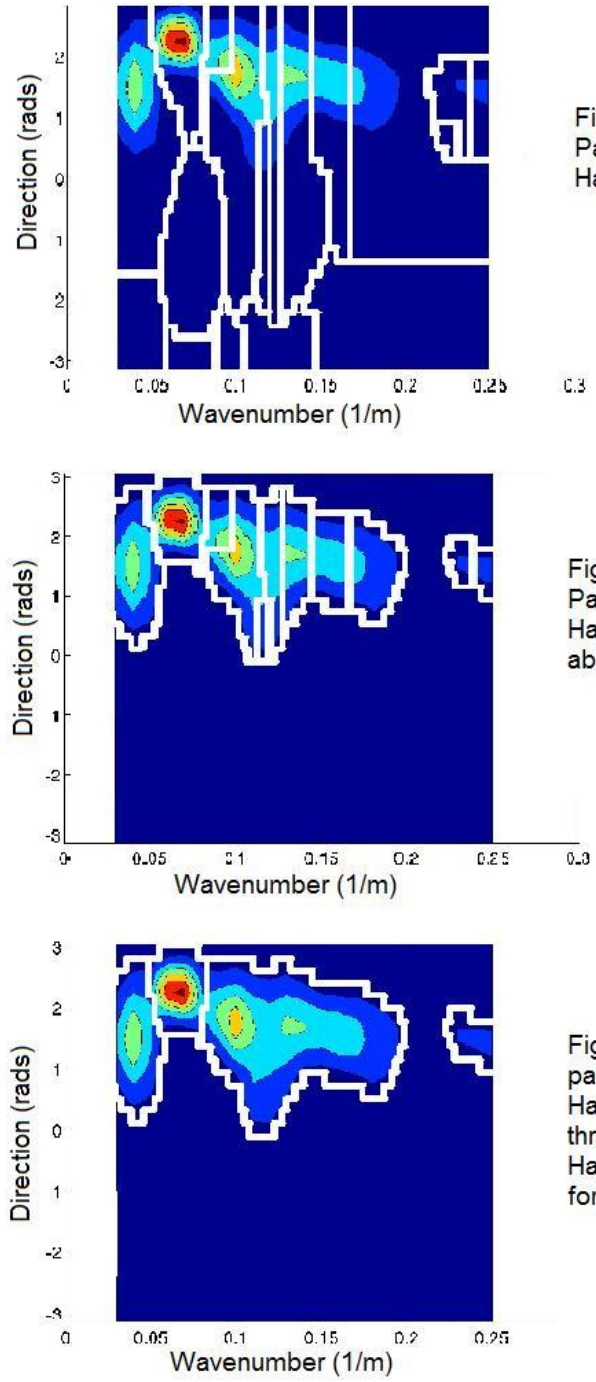

Figure 1. A partitioned radar wavenumber spectrum. 0 radians is north, 1.57 is east, etc.

consider one swell partition and so much of the detail in the spectra may still be lost. Overall the Hasselmann et al. (1994) method for partitioning appears to be the most robust for use in fully automated processes.

Managing the effects of noise and sensitivity on the partitioning scheme

Partitioning will often be over-sensitive and will identify partitions related to noisy peaks. It is therefore necessary to introduce conditions for which partitions should be merged or removed. Hasselmann et al (1996) proposed the following specifications for combining partitions:

1. The peaks are too close.
2. The trough separating the peak is not low enough.
3. The spread is larger than the square distance between the peaks.

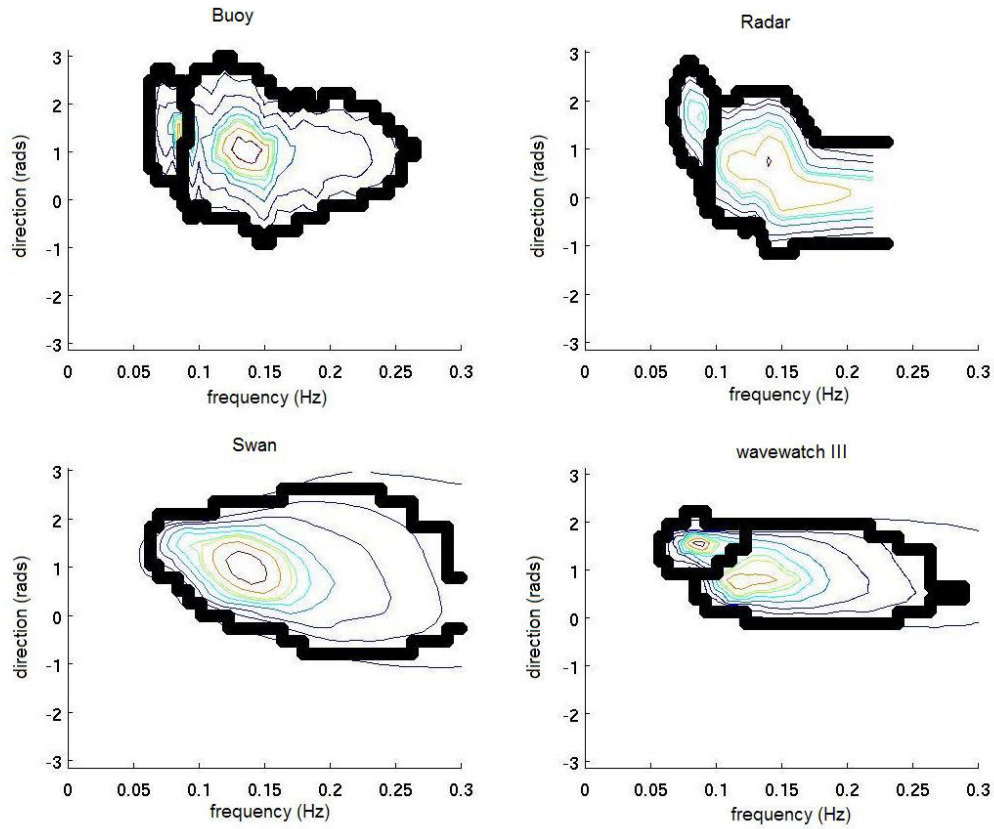

Figure 2. Partitioned spectra from the HF radar, buoy, Swan model and Wavewatch III model for the buoys location in the Celtic Sea at 06:00 12/01/2005.

Hanson et al. (2000) also suggested that partitions with a total energy below a certain level should be discarded and as discussed previously it also seems sensible to apply the partitioning only above a certain threshold. Figure 1 shows the affect of applying these noise controls to a radar measured spectrum, the improvement caused by applying the noise removal methods appears to be significant.

This partitioning scheme has also been applied to spectra outputted from the Swan and Wavewatch III spectral wind-wave models and to spectra estimated from a directional Waverider buoy. Analysis was performed to tune the partitioning scheme for each of the models and observations. It was found that different thresholds and modifications of the Hasselmann et al. (1996) conditions are required for the spectra from the radar, buoy and models in order to optimize the performance. The partitioning scheme and the above mentioned noise control methods were applied to directional frequency spectra from the buoy, radar and models for the location of the buoy in the Celtic sea at 06:00 12/01/2005 and the results can be seen in Figure 2.

Conclusions

The Hasselmann et al. (1994) partitioning scheme, along with the specifications for combining and discarding partitions of Hasselmann et al. (1996) and Hanson (2000) have shown good results. In many cases such as Figure 2, the spectra are partitioned as we would expect. There are obviously some cases where the partitioning scheme is not so successful, but the conditions for combining partitions and removing noise have been chosen to be as robust as possible. From the results in Figure 2 it is possible to identify the key characteristics of the ocean surface at that time. In these spectra a higher frequency partition with large spread has been identified and this is likely to be the wind sea, and in all but the Swan spectra a lower frequency partition which probably corresponds to swell is also seen. Figure 2 also illustrates an example where a possible deficiency in the Swan model has been identified, that is an underestimation by the model of energy in the lower frequencies. This study will now be extended to comparing the mean parameters of cross assigned partitions and to further investigations of the success of the chosen tuning parameters.

References

Gerling, T. (1992), Partitioning sequences and arrays of directional ocean wave spectra into component wave systems*, Journal of Atmospheric and Oceanic Technology*, 9, 444–458.

Guillaume, A. (1990), Statistical tests for the comparison of surface gravity wave spectra with application to model validation, *Journal of Atmospheric and Oceanic Technology*, 7, 552–567.

Guillaume, A. (1994), *Analyzing directional evolution ocean waves for operational research applications*. In: Proceedings of International conference on sea-air interactions and on meteorology and oceanography of the coastal zone, American Meteorological Society.

Hanson, J.L., Phillips, O.M. (2000), Automated analysis of ocean surface directional wave spectra. *Journal of Atmospheric and Oceanic Technology*, 18, 277–293.

Hasselmann S., Hasselmann, K., Bruning, C. (1994), *Extraction of wave spectra from SAR image spectra*. In: Dynamics and modelling of ocean waves, Komen, G., Cavaleri, L., Donelan, M., Hasselmann, K., Hasselmann, S., Janssen, P. (Eds.). pp391–401.

Hasselman, S., Bruning, C., Hasselmann, K., Heimbach, P. (1996), An improved algorithm for the retrieval of ocean wave spectra from synthetic aperture radar image spectra, *Journal of Geophysical Research,* 101, 16615–16629.

Lefevre, J., Quentin, C., Hauser, D., Bidlot, J. (2005), *Partitioning of wave spectra*. In: Measuring and analyzing the directional spectrum of ocean waves. Hauser, D., Kahma, K., Krogstad, H., Wyatt, L.R. (Eds.), COST Office. pp441–454.

Comparing acoustic turbulence profiling techniques

ANTHONY WHIPPLE, RICK LUETTICH

Institute of Marine Sciences, University of North Carolina, 3431 Arendell Street, Morehead City NC 28557-3209, USA
email: whipple@email.unc.edu, rick_luettich@unc.edu

Keywords: turbulence, profiling, AWAC, ADCP, waves

ABSTRACT

This study compares methods of measuring turbulence parameters using two different acoustic current profilers and a single point instrument in the presence of surface gravity waves. A Nortek AWAC, a 1200 kHz Teledyne/RDI ADCP, and a Nortek Vector velocimeter were simultaneously deployed along with an autonomous vertical hydrographic profiler. The AWAC uses a vertical beam which normally measures distance to the surface by monitoring return echoes for the surface reflection. This beam was reprogrammed to return velocity profiles in the same manner as the slanted beams. Use of vertical beam velocities eliminates those measurement uncertainties which are due to the anisotropy of the turbulent field. The ADCP uses slant-beam data, but has the advantage of available low-noise high resolution modes. The vector is a single point device but has much lower noise values and much higher ping rates available than either profiler. The hydrographic profiler measures salinity and temperature of the water in the vertical as well as the local wind velocity. The instrumentation was located near the mouth of the lagoonal Neuse River Estuary in eastern North Carolina, USA.

The variance technique (Stacey et al., 1999) for measuring Reynolds Stress is applied to the ADCP data. The vertical beam on the AWAC gives a direct measurement of the fluctuating vertical velocities allowing nearly direct calculation of turbulent kinetic energy. TKE, (Gargett, 1994). The structure function method of Wiles et al. (2006) can also be applied to both the slant beam and vertical beam data to measure dissipation. All of these methods suffer from contamination due to surface gravity wave motion. Methods developed by Whipple et al. (2006) to reduce wave contamination in Reynolds Stress measurements using the variance technique are adapted to compute TKE with the along beam data and the structure function technique. Results are compared to turbulent quantities calculated using the inertial dissipation technique on data from the single point velocimeter.

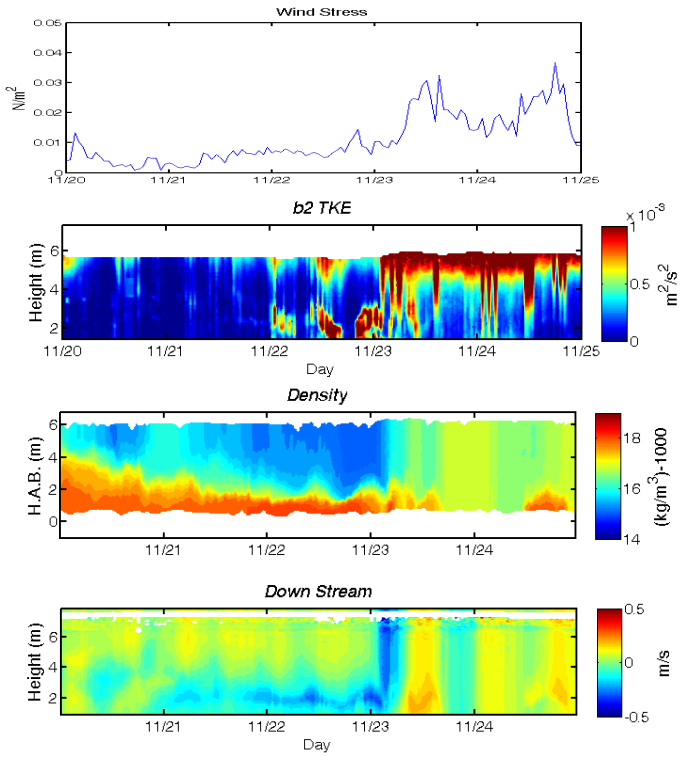

Figure 1. Time series of wind stress, and vertical profiles of turbulent kinetic energy, water density and downstream velocity for 20–24 November.

Results and discussion

Figure 1 presents an example of TKE (with waves removed) computed in the along beam direction from the RDI ADCP. The top panel shows the wind stress during the deployment with the increase on 23 November being associated with a cold front passage. The second panel shows the along beam TKE. The third panel shows the density collected from our autonomous vertical hydrographic profiler, and finally the fourth panel shows the down stream rotated mean

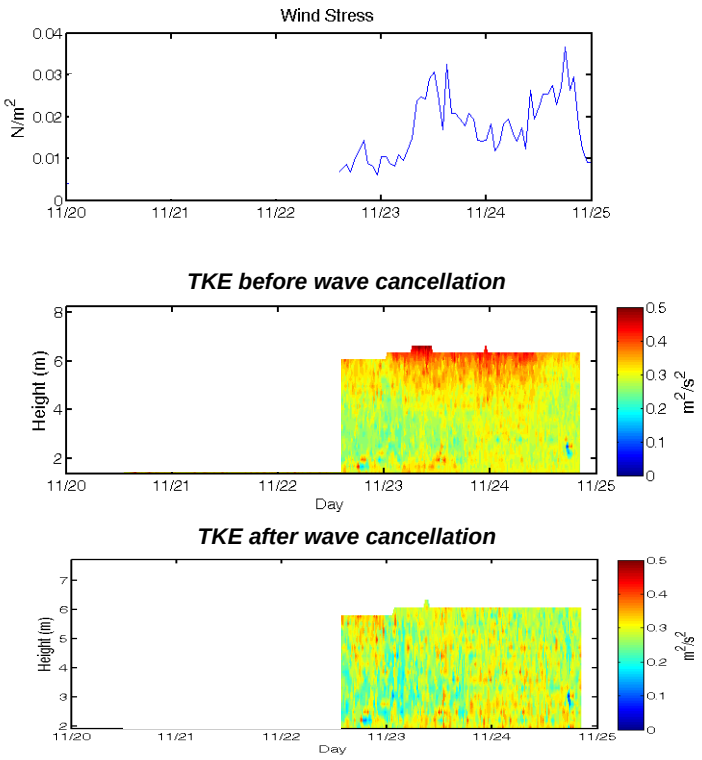

Figure 2. Time series of wind stress, and profiles of turbulent kinetic energy calculations with and without wave cancellation.

velocity profile. Prior to the cold front passage the data show stratified conditions and two layer flow with the less dense surface waters flowing downstream and the more dense bottom water flowing upstream. After the cold front passage the water column mixes vertically and moves barotropically. Panel two shows bursts of TKE in the upstream flowing bottom waters prior to the cold front passage and surface generated TKE after the cold front passage associated with the stronger winds.

To apply our wave cancellation method to the AWAC vertical velocity data, we fit linear wave theory plus a constant offset value to the along beam variance. This constant offset accounts for other sources of variability including turbulence and the instrument noise threshold. The values we obtained for this offset from these fits matched very closely with the values for instrument noise predicted by Nortek's AWAC AST software based on the parameters of our deployment.

Figure 2 shows the TKE calculation before and after wave cancellation. After wave cancellation (bottom pane) the remainder of the data shows that we are essentially at the instrument noise floor predicted to be 0.29 m^2 s^2 for this particular deployment. The first part of the AWAC record was discarded due to the presence of bad data.

Conclusions

The wave cancellation procedure has been shown that it can be generalized for uses beyond Reynolds Stress calculations. It was applied successfully here for both vertical and slant beam TKE computations. The slant beam data show TKE at times and locations in the water column that are associated with physical events where turbulence would be expected to form. The addition of a constant offset parameter was required to obtain good fits to data collected in the vertical. Fits performed using this modified wave cancellation procedure report offset values that match the instrument noise values predicted by the manufacturer extremely well.

References

Gargett, A.E. (1994), Observing turbulence with a modified acoustic Doppler current profiler, *Journal of Atmospheric and Oceanic Technology*, 11, 1592–1610.

Stacey, M.T., Monismith, S.G., Burau, J.R. (1999), Measurements of Reynolds stress profiles in unstratified tidal flow, *Journal of Geophysical Research*, 104(C5), 10933–10949.

Whipple, A.C., Luettich, R.A., Seim, H.E. (2006), Measurements of Reynolds stress in a wind-driven lagoonal estuary, *Ocean Dynamics*, 56(3–4), 169–185, doi:10.1007/s10236-005-0038-x.

Wiles, P.J., Rippeth, T.P., Simpson, J.H., Hendricks, P.J. (2006), A novel technique for measuring the rate of turbulent dissipation in the marine environment, *Geophysical Research Letters*, 33, L21608, doi:10.1029/2006GL027050.

Development of estuary morphological models

JOHN M. HUTHNANCE[1], HARSHINIE KARUNARATHNA[2], ANDREW LANE[1],
ANDREW J. MANNING[3, 6], PAUL A. NORTON[4], DOMINIC E. REEVE[5],
RICHARD L. SOULSBY[6], JEREMY SPEARMAN[6], IAN H. TOWNEND[6], ADRIAN P. WRIGHT[4]

1. Proudman Oceanographic Laboratory, 6 Brownlow Street, Liverpool L3 5DA UK
email: jmh@pol.ac.uk, ale@pol.ac.uk

2. Department of Civil Engineering, University of Glasgow, Glasgow G12 8LT UK
email: karunarathna@civil.gla.ac.uk

3. School of Earth, Ocean and Environmental Sciences, University of Plymouth,
Drake Circus, Plymouth PL4 8AA UK
email: andymanning@yahoo.com

4. ABP Marine Environmental Research Ltd., Waterside House, Town Quay,
Southampton SO14 2AQ UK
email: pnorton@abpmer.co.uk, awright@abpmer.co.uk

5. School of Engineering, University of Plymouth,
Drake Circus, Plymouth PL4 8AA UK
email: dominic.reeve@plymouth.ac.uk

6. HR Wallingford Ltd., Howbery Park, Wallingford OX10 8BA UK
email: r.soulsby@hrwallingford.co.uk, j.spearman@hrwallingford.co.uk,
i.townend@hrwallingford.co.uk

Keywords: estuary, morphology, model, decades

ABSTRACT

Estuaries typically have dense local populations and economic activities, yet face increasing rates of change: freshwater runoff, mean sea-level (MSL) rise and likely increases in flooding events. Outcomes depend on hydrodynamics and sediments, but the sediment regime is challenging to predict. 'Bottom-Up' (B-U) process-based models, using fluid-dynamical and related equations, represent our basic understanding. However, whilst B-U models can accurately reproduce water levels and currents, simulating sediment transports is more problematic; moreover, evolving morphology often depends on relatively small biases. 'Top-Down' (T-D) approaches are generally derived from either (i) analyzing observed morphological evolution or (ii) some form of whole-estuary equilibrium concept (volume, energetics, entropy etc.). Such approaches may be stable for long-term predictions; some are limited to their basis in data and the extent of valid extrapolation may be uncertain; and they may lack a time-scale for evolution. 'Hybrid' approaches combine T-D and B-U elements. Typically, an equilibrium state (T-D concept) constrains the form of evolution and is approached with rates and distributions given by B-U models. The aim is to develop models capable of indicating likely estuarine morphologies 50 years hence. From these should come estimates of associated changes in flood risks under various management and climate-change scenarios. The following describes B-U and Hybrid model developments and applications. We seek to improve confidence through predictions for eight varied UK estuaries, comparing model approaches and the estuaries.

The models

An *Analytical Emulator* has been developed, largely based on 1-D equations for conservation of water and along-estuary momentum (Prandle, 2006). It assumes that tidal amplitudes are broadly uniform along estuaries; then estuarine length and depth are derived in terms of time-averaged river flow and estuary side-slope. Thus the Emulator partly explains how estuarine bathymetries have developed in response to tidal and

riverine inputs (Prandle et al., 2006). Then estuary length and side slope are assumed constant; morphology responds only to changes of river flow among the scenario changes. The uniform side slope renders the Emulator liable to represent channel volume and mean depths poorly. However, it is easy to apply, needing only gross estuary dimensions, MSL, tidal range and river flow. MSL rise gives new values for estuary volume and area. A minimum infill time was estimated from flushing time and mean suspended sediment concentration $\langle C \rangle$ (Prandle, 2004); $\langle C \rangle$ increases with tidal range but is assumed unchanged by raised MSL.

A *Shell Hybrid Regime* model (Wright and Townend, 2006) allows application of a 'regime' relationship with a 1-D process-based (B-U) hydrodynamic model. Regime theory characterizes links between hydrodynamics and estuary form by formulae (here fits to an initial model run) describing an estuary (quasi-) equilibrium, typically in terms of discharge Q:

cross-sectional area $A \propto Q_{max}^{p}$, top width $B \propto Q_{max}^{q}$, mean hydraulic depth $H \propto Q_{max}^{r}$.

Then some condition is altered, e.g., water levels, engineering works. The hydrodynamic model runs the altered simulation and regime relationships are reapplied to update the cross-section, subject to
– no adjustment above the maximum water level
– linear stretching (vertically and horizontally) to required width and area
– constraints (e.g., Holocene surface, solid geology, structures).
The new cross-sections form the basis of the next hydrodynamic model run. This process is iterative until the cross-sections converge. Inter-tidal and plan areas, volumes and hydraulic information are calculated. With many individual cross-sections, the Shell Hybrid Regime model can represent LW and HW areas and volumes accurately. It is widely applicable; it needs MSL, tidal range, river flow and data on estuary form: cross-section areas, breadths and depths at the desired resolution. Structures can limit HW area (a useful attribute); such sections then tend to deepen and inter-tidal area is lost; 'coastal squeeze'. The model predicts depth increases in most estuaries as MSL rises, but substantial infill for the Mersey. To accommodate greater river flow, the model again predicts a (usually) small decrease in inter-tidal area. The approach is most appropriate if there is confidence that a regime condition holds and should persist; if the estuary is subject to rapid change or instability then regime modeling is unsuitable. Interpretation needs care, e.g., forms of morphological change are predicted, but not rates.

Morpho-SandTrack builds on the HR Wallingford SandTrack model for Lagrangian particle-tracking of sand-grains including bedload, suspended load, incipient motion and burial. SandTrack tracks 'tagged' representative grains of sand as they move driven by the flow (predicted by a numerical model; e.g., TELEMAC). The development is to associate a volume of sediment with each tagged grain, and deposit it on the bed as a sediment 'lens' with defined and calibrated maximum thickness and extents. The lenses give the morphodynamic development. By iterating at intervals (e.g., 1 year; re-calculating the hydrodynamics) this has become a morphodynamic model (Soulsby et al., 2007). Thereby Morpho-SandTrack predicts the source (and potentially other characteristics) of deposited sediment as well as its thickness. Applied to the Thames, Morpho-SandTrack predicted morphology over 50 years with annual bed and flow updates. It appears to represent the main outer-estuary features, but fine resolution is needed up-estuary. The model should be applicable as widely as 2-D B-U models [requiring MSL, tidal range, river flow; fine enough bathymetry over the whole area, explicit sediment sources]. Continually repeated flow model runs are needed for evolving morphology, and combine with fine resolution to increase computing demand. The approach is appropriate for detail and if there is a lack of historical guidance.

A *Realignment model* has been developed to predict local morphology and habitats at managed realignment sites (Spearman, 2007) where tides, waves, sediment, vegetation and biology act. Model elements are:

a) Set up initial bathymetry;
b) Calculate time-averaged wave heights and periods;
c) Use model (e.g., TELEMAC-2D) for flow conditions;
d) Derive fields of time-average diffusion coefficient and equilibrium concentration C_E (q.v.)
e) Run sediment transport model: time-averaged, diffusive-only (calculated coefficients, zero mean currents); net erosion $E = w(C_E - C)$ where $E < 0$ is deposition, w is settling velocity, C is actual concentration;
f) Update bathymetry, extrapolate bathymetry change over a longer time;
g) Use new bathymetry (f) as basis to iterate again from (b).

The equilibrium concentration C_E is given by equating deposition during slack water with erosion at other times; C_E depends on currents, waves, friction; erosion, deposition and settling rates. Modeling of a managed realignment at Tollesbury Creek compared well with observed evolution, given the uncertain sediment supply. The model seems a promising basis for management decisions regarding realignment. Simple vegetation effects have been incorporated. The model is applicable where there are data for waves and sea level (mean + tide) at the breach, and bathymetry over the whole (2-D) set-back area, fine enough to resolve channels and banks of interest and desired output features. The approach is most appropriate over a small area requiring detail and lacking historical guidance.

ASMITA (Stive et al., 1998) describes morphological interaction between a tidal basin and its adjacent coastal environment. It schematizes a tidal inlet as aggregated elements: delta (excess sediment volume above a hypothetical non-inlet shoreface); channels (water volume below mean low water); intertidal flats (sediment volume above mean low water). Under constant hydrodynamic forcing (in particular constant MSL), each element is assumed to tend towards a morphological equilibrium, a function of hydrodynamic forcing and basin properties (van Goor et al., 2003). Empirical relations define elements' equilibrium volumes. MSL rise creates accommodation space; the estuary becomes a sink for available sediment. ASMITA has been coded in Matlab, documented, provided with (graphical) control and applied to the Thames Estuary with aggregated flats and channels in each of three sections (Rossington and Spearman, 2007). It was calibrated to historical morphology. Under a 2 mm yr^{-1} MSL rise, ASMITA was able to reproduce Thames Estuary evolution reasonably successfully. Its analytical formulation enables a priori evaluation of its predictive uncertainties. ASMITA has been applied elsewhere; it needs MSL, tidal range, river flow and dimensions (volumes, areas) of the aggregated elements. It is only appropriate for volumes and areas that are fairly represented by a few aggregated elements; calibration on the past probably implies that scenarios should not diverge far from past experience. There is implicit reliance on continued sediment supply.

An *Inverse Model* for evolving morphology has been developed and applied to the Humber (Karunarathna et al., 2008). It uses a diffusion-type evolution equation: $\partial h/\partial t = K(\partial^2 h/\partial x^2 + \partial^2 h/\partial y^2) + source$ as suggested by combining conservation of sediment with sediment transport having a down-slope bias. 'Source' represents non-diffusive phenomena that lead to long-term evolution of morphology. For the Humber, bathymetry data comprised 20 sets since 1851 (15 since 1936). Successive sets allowed 'inversion' for the interim time-average source. To predict future morphology, in principle the evolution equation can be used; the future source function has to be estimated. Extrapolation from past behavior was assessed by Empirical Orthogonal Function (EOF) analysis of the sequence of source functions. In the Humber, 92% of the mean-square data was in the first spatial-structure EOF having near-constant time-series. Hence this first EOF was used as the source function for prediction. One- and three-year predictions compared with the most recent measured bathymetries (2002, 2004) support using the diffusion equation to predict morphology in the Humber. The Inverse model is (only) applicable in this way if past bathymetric data are frequent enough to resolve past changes without aliasing, fine enough to resolve features of interest. In practice, bathymetry seems to be needed about every ten years; perhaps more often for a rapidly-changing (e.g., small) estuary. The model depends on past behavior; it is only appropriate for prediction if (i) future changes are within the range of experience; (ii) the EOFs used have a long-enough integral time and comprise most of the source function.

Estuary scenarios and results

Table 1 entries 'Y' indicate where each model was run. '2.5-D' refers to a finite-difference B-U hydrodynamic model (mass and momentum equations) with 120-m resolution; vertical structure is derived from the sea- surface slope and assumed friction (so controlled by the 2-D solution; Lane, 2004). TE2100 refers to Historical Trend Analysis to 2030 from the TE2100 project. Model predictions were generally inter-compared for 2050. Scenarios to represent possible effects of climate change 50 years hence were: *Mean sea level*: present as baseline; rises of 0.3 m (realistic), 1 m (extreme); *Tidal range*: present as baseline; an increase of 2%; *River flow*: baseline as at present; an increase of 20%.

For *raised mean sea level*, low-water (LW) volumes and areas invariably increase; so usually do high-water (HW) volumes and areas, but less so. Factors in the different response are: hard structures often constrain HW area; effects are relatively larger in shallow water, i.e., at LW and in shallow estuaries generally. Thus inter-tidal area generally decreases – 'coastal squeeze'. However, ASMITA predicts a small increase of Thames inter-tidal area for the present rate of MSL rise. Depth in most estuaries is predicted (by the Hybrid Regime model) to increase; comparably with MSL rise for high waters in the Thames, Blackwater and

Table 1. Estuary-model scenarios

Model	Thames	Blackwater	Humber	Mersey	Dee	Ribble	S'ton Water	Tamar
Emulator	Y	Y	Y	Y	Y	Y	Y	Y
Hybrid Regime	Y	Y	Y	Y			Y	
'2.5-D'				Y	Y	Y		
ASMITA-type	Y							
Morpho-SandTrack	Y							
TE2100	Y							
Realignment		Tollesbury						
Inverse			Y					

Humber. However, infill reduces the depth increase in the Mersey; in Southampton Water, shallow-water area increases as MSL rises, reducing the average depth increase.

Effects of *tidal range* and *river flow* are proportionally greater in shallow water, i.e., at LW compared with HW. Otherwise, realistic changes in tidal range (e.g., +2%) have likely effects O(2%). Southampton Water gains inter-tidal area, apparently related to the position of relatively shallow bed slopes. For a 20% increase in river flow, the Hybrid Regime model gives O(2%) changes in LW and HW areas and volumes, but the Mersey and Blackwater lose inter-tidal area. [The Emulator predicts much larger area and volume increases.]

Flushing times estimated by the Emulator are just a few weeks, and do not correlate with estuary size, as they depend also on tidal range and river flow. [The Emulator estimates flushing time as the time to replace by freshwater, half of the salinity content over the saline intrusion length]. Related *infill times* are some centuries (also from '2.5-D' model predictions), lengthening slightly for rising MSL and shortening slightly for increased river flow. Most infill times indicate enough sediment input to enable the morphology to keep up with sea-level rise. In the Mersey, models indeed suggest infill keeping pace with sea-level rise. For the Thames, a volume increase is predicted before infill keeps pace with faster MSL rise. The Humber Estuary has been surveyed frequently for past trends to give a good guide to development, suggesting that the estuary both responds to the nodal cycle and keeps pace with sea level rise.

Data

The Future-Coast database (Burgess et al., 2002) for 96 English and Welsh estuaries includes: surface area, inter-tidal area, salt-marsh area, shoreline perimeter length, channel length, Spring tidal range, mean river flow, mouth width, HW and LW volumes. It has been augmented (Manning, 2007): more detailed freshwater flows (seasonal statistics), saline intrusion lengths, neap tide equivalent tidal ranges, tidal amplitudes, mean estuary depths and breadths, average side-slopes, LW and HW values of depth, breadth and surface area.

Conclusions

Results show that estuaries have varied individual responses to climate-change scenarios. This puts an onus on modeling any particular estuary studied. Any one model is likely to have uncertainties and not satisfy all requirements. An ensemble can provide scope and validity. Validation against historic change is good practice if attempting to predict long-term changes. If historic change data do not serve, alternative models' predictions should be compared, to help establish the validity of predicted morphologies. The models here give predictions founded on diverse concepts. All can be valuable: to develop an ensemble of possible future scenarios; to broaden the range of quantities predicted.

References

Burgess, K.A., Balson, P., Dyer, K.R., Orford, J., Townend, I.H. (2002), *Future-Coast – the integration of knowledge to assess future coastal evolution at a national scale*, In: 28th International Conference on Coastal Engineering, Vol. 3, 3221–3233. ASCE, New York.

Karunarathna, H., Reeve, D., Spivack, M. (2008), Long-term morphodynamic evolution of estuaries: an inverse problem, *Estuarine, Coastal and Shelf Science*, 77, 385–395.

Lane, A. (2004), Bathymetric evolution of the Mersey Estuary, UK, 1906–1997: causes and effects, *Estuarine, Coastal and Shelf Science*, 59, 249–263.

Manning, A.J. (2007), Enhanced UK Estuaries database: explanatory notes and metadata, *HR Wallingford Tech. Report* TR167, 23pp.

Prandle, D. (2004), How tides and rivers determine estuarine bathymetries, *Progress in Oceanography*, 61, 1–26.

Prandle, D. (2006), Dynamical controls on estuarine bathymetry: Assessment against UK database, *Estuarine, Coastal and Shelf Science*, 68, 282–288.

Prandle, D., Lane, A., Manning, A.J. (2006), New typologies for estuarine morphology, *Geomorphology*, 81, 309–315.

Rossington, K., Spearman, J.R. (2007), *Development of estuary morphological models – application of ASMITA to the Thames Estuary*, HR Wallingford Tech. Report 162.

Soulsby, R.L., Mead, C.T., Wood, M.J. (2007), *Development of a Langrangian morphodynamic model for sandy estuaries and coasts*, HR Wallingford Tech. Report 159.

Spearman, J.R. (2007), *Hybrid modelling of managed realignment*, HR Wallingford Tech. Report 157.

Stive, M.J.F., Capobianco, M., Wang, Z.B., Ruol, P., Buijsman, M.C. (1998), *Morphodynamics of a tidal lagoon and adjacent coast*, In: 8th International Biennial Conference on Physics of Estuaries and Coastal Seas, 1996, 397–407. Balkema, Rotterdam.

Van Goor, M.A., Zitman, T.J., Wang, Z.B., Stive, M.J.F. (2003), Impact of sea-level rise on the morphological equilibrium state of tidal inlets, *Marine Geology*, 202, 211–227.

Wright, A.P., Townend, I.H. (2006), *Predicting intertidal change in estuaries*, In: Proceedings of the 41st Defra Flood and Coastal Management Conference. Paper 04-3.

Past and future evolution in the Thames Estuary

KATE ROSSINGTON, JEREMY SPEARMAN

HR Wallingford Ltd., Howbery Park, Wallingford OX10 8BA UK
email: k.rossington@hrwallingford.co.uk, j.spearman@hrwallingford.co.uk

Keywords: morphological model, sediment budget, sea level rise; Thames estuary, UK

ABSTRACT

The Thames Estuary is a focus for investigation at present because of the TE2100 Project to assess the flood protection requirements necessary to protect London and the neighboring Kent and Essex coastlines throughout the 21st century. In addition the UK Biodiversity Action Programme is acting as a driver for identifying and mitigating the continuing loss of mudflat and saltmarsh from the estuary.

As part of the studies undertaken to inform the management of the estuary, the evolution in morphology and the sediment budget over the last century have been studied in detail. Within the UK Department for Environment, Food and Rural Affairs (DEFRA) project FD2107 this information been used to develop and calibrate a morphological model (based on the ASMITA approach, Stive et al, 1998) capable of identifying the consequences of accelerated sea-level rise on morphological evolution in the Thames Estuary.

Development of a historical sediment budget

The Thames Estuary is affected by sediment from fluvial sources, exchange with the sea, dredging and (historically) by sewage. The contributions of each of these sources have been derived from a combination of sources including work on:

- Thames sediment budget by WPRL (1964), which formed the basis for the seminal work by Inglis and Allen (1957) on the Thames Estuary
- Port of London Authority dredging records
- bathymetric analysis of PLA charts (HR Wallingford, 2006a)
- historical reviews of dredging and disposal of dredged sediment (HR Wallingford, 2006c)
- review of flow and suspended sediments measured in the Lower Thames River (HR Wallingford, 1988, 2006c)
- synoptic surveys of flow/salinity and the Thames Estuary (HR Wallingford, 1971a, b, c and 2004).

An example output of this re-analysis shows how the sediment budget in the muddy part of the estuary (upstream of Lower Hope Point) changed over the course of the 20th century (Table 1).

Table 1. Estimated average net input and export of sediment for the Thames Estuary upstream of Lower Hope Point over the period 1920 to 1990s (dry tones per year).

Sediment source/sink	1920–1970	1970–1990
Fluvial input (Thames + tributaries)	145,000	170,000
Sewage effluent	79,000	42,000
Storm sewage	13,000	13,000
Sewage sludge	28,000*	0
Industrial discharges	21,000	3,000
Morphological change (erosion is +ve)	192,000	-120,000
Total inputs	478,000	108,000
Maintenance Dredging (net placed outside system)	436,000**	95,000
Decomposition of sewage	69,000	24,000
Total outputs	505,000	119,000
Net difference (attributed to marine sources)	**−27,000**	**−11,000**

* The placement of sewage sludge occurred mainly during WWII at a much higher rate. This is an average over the period 1920–1970.

** The placement of maintenance dredging presented is adjusted to account for periods of disposal at Mucking Flats.

Modeling methodology

ASMITA was first presented as a behavior-based model "describing morphological interaction between a tidal lagoon or basin and its adjacent coastal environment" (Stive et al., 1998). The model consists of a schematization of a tidal inlet system with the major morphological elements being viewed at an aggregated scale (Figure1). The major assumption of ASMITA is that, under constant hydrodynamic forcing, each element tends towards a morphological equilibrium which can be defined as a function of hydrodynamic forcing and basin properties (van Goor et al., 2003). The version of the ASMITA model used in this study assumes that the change in volume in any element only occurs through the depth of the element. A version of the model which reproduces change in both area and depth is currently under development.

To apply ASMITA to the Thames estuary a six-element model was used (Figure 1). This schematization was used to capture the variation between the different areas of the estuary. Teddington to Broadness receives the majority of the river input and has historically had the most dredging. This section (referred to henceforth as the inner estuary) is relatively narrow with limited intertidal areas at the margins. The bed of this section consists mainly of gravel, stones, clay and chalk, with the exception of Gravesend Reach and the Mud Reaches. The next section, between Broad Ness and Lower Hope Point (middle estuary) is wider, with some large intertidal areas. Mucking Flats, which have shown rapid accretion in the past, are located in this section. The section between Lower Hope Point and Southend (Sea Reach) is wider and sandier than the landward sections and has large areas of intertidal sand flats as well as some muddier creek systems along the northern shore where saltmarsh grows. In the lower section of the estuary almost all the intertidal areas of the main estuary are backed by sea defenses and the intertidal areas are at levels of MWL or lower.

The sediment exchanges discussed above were introduced into the ASMITA model as sink/source terms. Each of the terms was allowed to vary over the course of the period modeled. Sediment exchanges for future periods were assumed to be the same as the existing values.

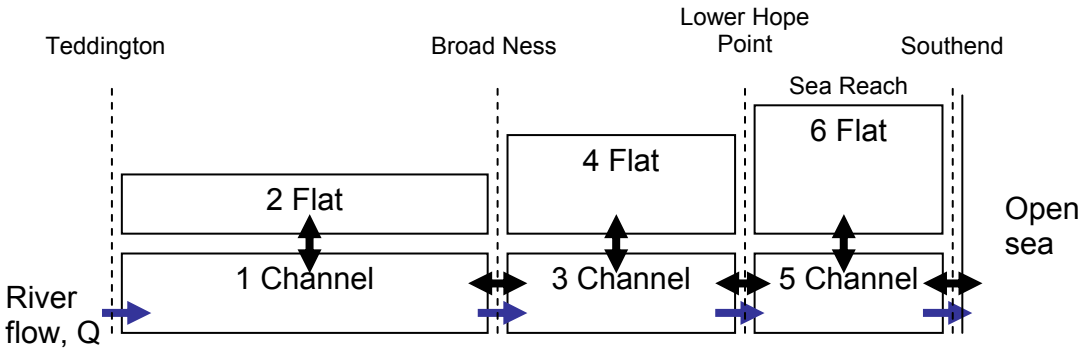

Figure 1. Schematization used for the six-element ASMITA in the Thames.

Results

Morphological evolution assuming historic rates of sea level rise

Assuming a constant rate of sea level rise of 2 mm yr^{-1} sea-level rise, ASMITA was able to reproduce the evolution of the estuary successfully (an example is shown in Figure 2). Brier Skill Scores indicated that ASMITA predictions were better than assuming the volumes continued at their initial values in the five of the six elements. The ASMITA model predicted that in the inner estuary the channel volume increases between 1910 and 1980 when the volume of sediment removed by dredging exceeds the fluvial sediment supply. After 1980, the channel volume decreases slightly, showing a tendency to infill. The volume of tidal flats is relatively constant over time, suggesting that it is close to equilibrium over the time scale of interest.

Morphological evolution assuming DEFRA of sea level rise

The DEFRA (2006) sea level rise scenario was used as sea-level rise forcing in ASMITA to predict the response of the Thames Estuary to accelerated sea-level rise. The DEFRA scenario is for sea level rise to increase from rates of 2 mm yr^{-1} prior to 1990 to 4 mm yr^{-1} currently, rising to 15 mm yr^{-1} by 2085. For convenience the rate of sea level rise after 2115 was taken as a constant value of 15 mm yr^{-1}.

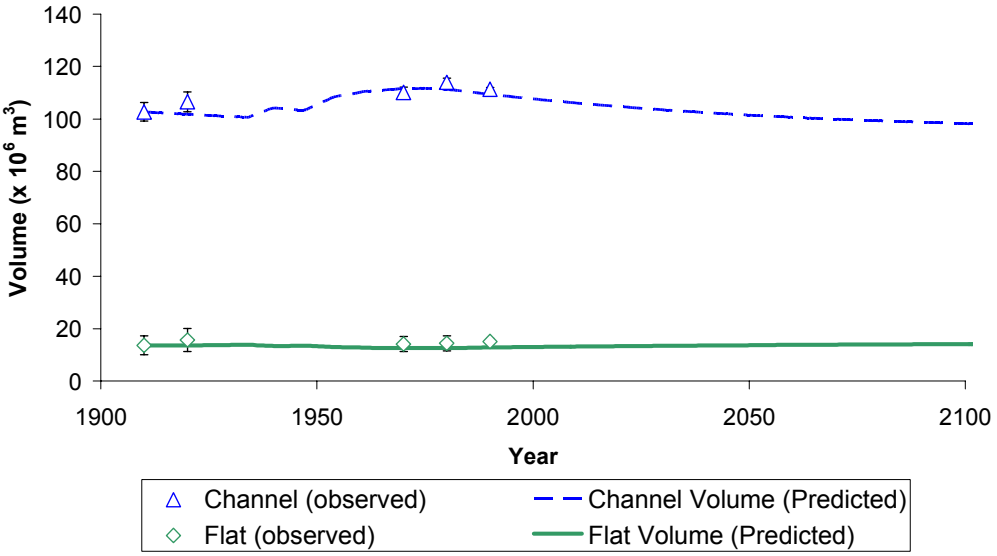

Figure 2. Observed and predicted evolution of the Thames Estuary landward of Broadness assuming a rate of relative sea level rise of 2 mm yr^{-1}.

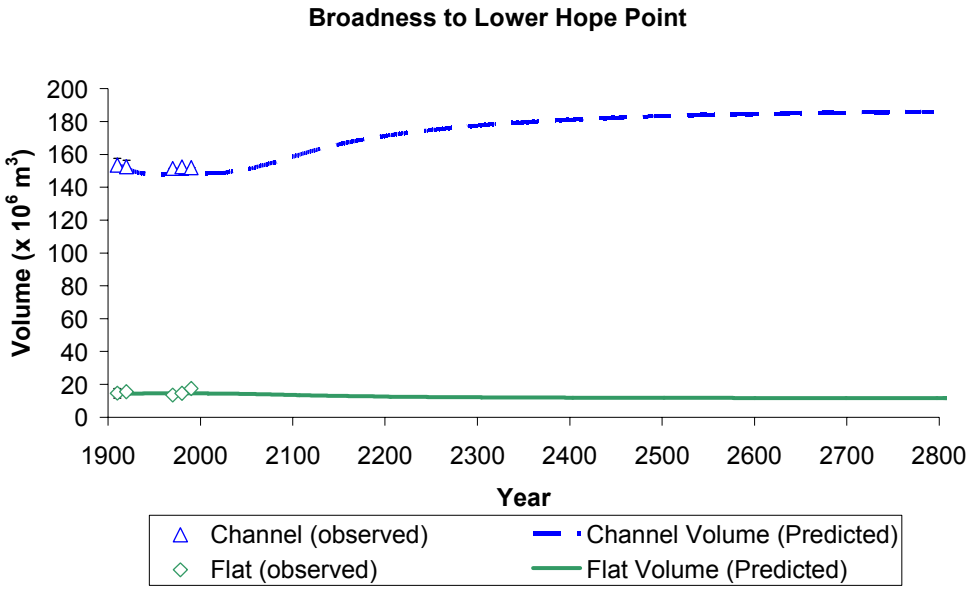

Figure 3. Predicted evolution of the Thames estuary using the DEFRA (2006) sea level rise scenario and assuming a constant rate of 15 mm yr^{-1} after 2115.

The results of the accelerated sea level rise simulation were that channel volumes were predicted to increase and flat volumes were predicted to decrease (see for example Figure 3 which shows the predicted evolution between Lower Hope Point and Broadness). By 2025 (sea-level rise rates of 4 mm yr^{-1}) channel volumes were predicted to be between 4.2% and 5.4% larger than their equilibrium volumes (based on historical morphology). Flat volumes were predicted to decrease by between 4.7% and 6%. In 2115, with predicted sea-level rise rates accelerating to 15 mm yr^{-1}, channel volumes were predicted to be between 11.5% and 12.5% larger than equilibrium. Flat volumes were predicted to decrease by between 10.8% and 18.6%, representing a significant loss in intertidal volume. After 2115 (when sea level rise was assumed to be constant) the estuary was predicted to evolve towards a new steady state where deposition in the estuary could keep pace with sea-level rise.

Conclusions

A combination of comprehensive historical review and morphological modeling using ASMITA successfully reproduced the evolution of the Thames estuary between 1910 and 1990, including the current trend for accretion on intertidal areas. Under conditions of accelerated sea-level rise, ASMITA predicts that channel volumes will increase and flat volumes will decrease. The volume lost depends on the rate of sea-level rise.

It is predicted that under the DEFRA (2006) sea-level rise predictions, 12.5×10^6 m^3 of intertidal sediment will have been lost by 2115, representing a significant intertidal loss. Most of this (10.0×10^6 m^3) will be from the Sea Reach section of the estuary, with the remainder divided between the inner and mid estuary. These values should be seen as an initial assessment and will be refined by future studies associated with ongoing Thames studies and further development of the ASMITA model.

References

DEFRA (2006), *Flood and Coastal Defence Appraisal Guidance, FCDPAG3 Economic Appraisal. Supplementary Note to Operating Authorities – Climate Change Impacts*.

FutureCoast (2002), *FutureCoast Estuary Assessment*. FutureCoast, Halcrow, Swindon.

van Goor, M.A., Zitman, T.J., Wang, Z.B., Stive, M.J.F. (2003), Impact of sea-level rise on the morphological equilibrium state of tidal inlets, *Marine Geology*, 202, 211–227.

HR Wallingford (1971a), *Thames flood prevention investigation, Field Survey Data, Section 10, Gravesend Reach,* HR Wallingford Report EX 552.

HR Wallingford (1971b), *Thames flood prevention investigation, Field Survey Data, Section 11, Coryton*, HR Wallingford Report EX 553.

HR Wallingford (1971c), *Thames flood prevention investigation, Field Survey Data, Section 12, Southend*, HR Wallingford Report EX 554.

HR Wallingford (1988), *Maidenhead, Windsor and Eton Flood Study: morphological model studies*, HR Wallingford Report EX 1695.

HR Wallingford (2004), *TE2100 – DC7, 2005. River Characteristics Survey (2004). Twelve individual transect reports and one summary report*. HR Wallingford Report EX5285.

HR Wallingford (2006a), *Thames Estuary 2100: Morphological changes in the Thames Estuary*. Technical note EP6.8, The Development of a historical sediment budget.

HR Wallingford (2006c), *Thames Estuary 2100: Morphological changes in the Thames Estuary*. Technical note EP 6.4, Historical Trend Analysis.

Inglis, C.C., Allen, F.H. (1957), The Regimen of the Thames estuary as affected by currents, salinities and river flow, *Proceedings of the Institute of Civil Engineers*, 7, 827–878.

Stive, M.J.F., Wang, Z.B., Capobianco, M., Ruol, P., Buijsman, M.C. (1998), *Morphodynamics of a tidal lagoon and the adjacent coast*. In: Physics of Estuaries and Coastal Seas, Dronkers, J., Scheffers, M.B.A.M. (Eds.), A.A. Balkema Publishers, Rotterdam, pp397–407.

Water Pollution Research Laboratory (1964), *Effects of polluting discharges on the Thames Estuary*. The Reports of the Thames Survey Committee and of the Water Pollution Research Laboratory, Water Pollution Research Technical Paper Number 11, Water Pollution Research Laboratory, HMSO.

Water temperature variability in an estuarine tidal channel (Ria de Aveiro, Portugal)

MAGDA C. SOUSA[1], NUNO VAZ[1, 2], JOÃO M. DIAS[1]

1. Departamento de Física, Universidade de Aveiro, Campus de Santiago, 3810-193 Aveiro, Portugal
email: mcsousa@ua.pt, nuno.vaz@ua.pt, joao.dias@ua.pt

2. Instituto Superior Técnico, Universidade Técnica de Lisboa, Av. Rovisco Pais, 1049-001 Lisboa, Portugal
email: nuno.vaz@ist.utl.pt

Keywords: water temperature, optical fiber; Espinheiro channel, Ria de Aveiro

ABSTRACT

Although monitoring and forecasting estuarine conditions are now almost considered routine activities, our knowledge about physical processes in these environments may be further improved through the development of innovative pre-operational systems. At an estuarine tidal channel located inside Ria de Aveiro lagoon (NW coast of Portugal), water temperature is being monitored using a new technology composed by an optical sensing cable integrating fiber Bragg grating sensors. This cable is fixed along the channel bed, from the lagoon inlet to the river mouth, and is connected to a data logger and to a GSM system. Results of a 1-year monitoring of water temperature were analyzed in terms of two major forcing: tides and meteorological conditions. The data under analysis consist in 18 annual time series of water temperature from sampling locations 500 m distant, allowing the study of its spatial and temporal variability. The temporal evolution of the longitudinal water temperature gradients was studied and mathematical techniques such as spectral analysis and Empirical Orthogonal Functions (EOFs) were applied to the data. The analysis of the results gave way to the improvement of the knowledge about the physical characteristics and behavior of this channel.

This technology produces sound results, revealing its ability as a pre-operational system to monitor water temperature in estuarine systems.

Introduction

Temperature plays many roles in the estuary: as water temperature increases, the capacity of water to hold dissolved oxygen becomes lower. Water temperature also influences the rate of plant photosynthesis (Wang et al., 2007), the metabolic rates of aquatic organisms (Atkinson et al., 1987), and the sensitivity of organisms to toxic wastes, parasites, and diseases.

The Espinheiro Channel (Figure 1) is one of the four main branches of Ria de Aveiro, a mesotidal and shallow coastal lagoon located in the northwest coast of Portugal. This channel connects the major source of freshwater of the lagoon, Vouga River, to the Atlantic Ocean, and by this reason is ideal to perform studies such as the one proposed here. This lagoon is a very important system in the region where it is located due to the intense human activity related with the economic and social exploitation of its waters. The Espinheiro channel is approximately 11 km long, has an average width of 200 m and a mean depth, along its longitudinal axis, of about 10 m. The tides are semidiurnal, being M_2 and S_2 the most important constituents, as they represent more than 90% of the tidal energy (Dias et al., 1999).

The characteristics of Ria de Aveiro, as well as other estuarine systems, make permanent monitoring particularly important for its managed support. The use of conventional sampling technologies of physical parameters revealed to be very expensive and hard to use in high spatial and temporal scales. Water temperature is closely connected to many biological and chemical processes in the estuary. For this reason, and because it is easily measured, temperature is commonly monitored. To monitor the water temperature there are various instruments, the largest part of them based on the use of thermistors (type of resistor with resistance varying according to its temperature), but most are only used for short time periods (Vaz and Dias, 2008). With the purpose of long term monitoring water temperature and without the need of regular human

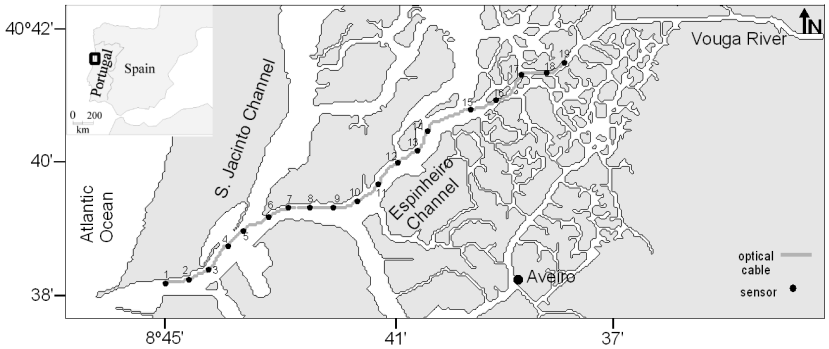

Figure 1. Study area with the location of the optical cable.

intervention, a new technology composed by an optical longitudinal cable integrating fiber Bragg grating sensors was developed and installed in the Espinheiro channel.

The objectives of this work are the study of the water temperature variability in the Espinheiro channel, evaluating the importance of the main forcing mechanisms: tides and meteorological conditions. The water temperature is monitored using the new technology described above. The data under analysis consist of 18 annual time series of water temperature, allowing the study of its spatial and temporal variability. The temporal evolution of the longitudinal water temperature gradients is studied and mathematical techniques such as spectral analysis and Empirical Orthogonal Functions (EOFs) are applied to the data.

Methodology

The water temperature is obtained through an optical sensing cable integrating fiber Bragg grating sensors. This cable is fixed along the channel bed, from the lagoon inlet to the river mouth, and is connected to a data logger and to a GSM system. It has 18 sensors (separated by 500 m) allowing the long term and real time monitoring of this channel with an excellent spatial resolution. The data used in this study results of 1-year measurements of water temperature (from September 2004 to October 2005, when Portugal was under a severe drought). It must be noted that in Figure 1, 19 sensors are represented, but sensor 16 is inactive. Sensor 1 is located near the mouth of the lagoon and the last one (sensor 19) is located near the channel's head, close to the mouth of the Vouga River. These sensors were used as a reference to the Atlantic Ocean and to the Vouga River. Data were analyzed in order to study the spatial and temporal water temperature variability in the Espinheiro channel.

A simple water temperature data statistical analysis was performed to study the spatial variability along the Espinheiro channel, as well as its temporal variability. The water temperature dependence on available meteorological and tidal data was also investigated. Spectral analysis was used to clearly identify the frequency of the processes controlling the dynamics of the Espinheiro channel. The study of the energy spectrum provides an alternative way of estimating the attenuation of the tidal and subtidal signals in different frequencies while progressing landwards.

The Empirical Orthogonal Functions (EOF) method is useful to analyze the variability of a single field, in this case, water temperature. Among the several available methods of analysis, EOF analysis is a particularly useful tool in studying large quantities of multi-variate data. EOF analysis is used to decompose a time series into its orthogonal component modes, the first few of which can be used to describe the dominant patterns of variance in the time series. Generally, the lowest modes have the largest spatial scales and represent the most dominant modes of variability. This method is fully described in Emery and Thompson (1997). Finally, correlations between the water temperature measured in the sensors and the forcing variables were calculated.

Results and discussion

Figure 2 shows the average water temperature distribution along the Espinheiro channel for some of the months under analysis. These figures are obtained monthly-averaging the water temperature data from each sensor. In general, during the winter months, water temperature is nearly constant along the channel; decreasing slightly towards the channel's head. In summer, the water temperature is not homogeneous. It can be observed that near the channel's head (which is the fluvial region), the water temperature ranges from

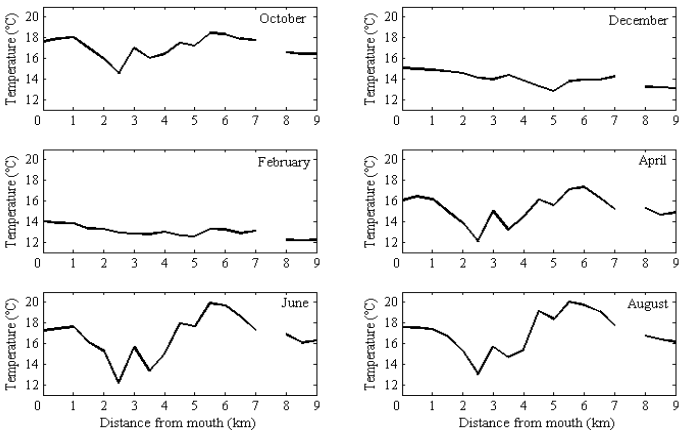

Figure 2. Mean water temperature along the Espinheiro channel.

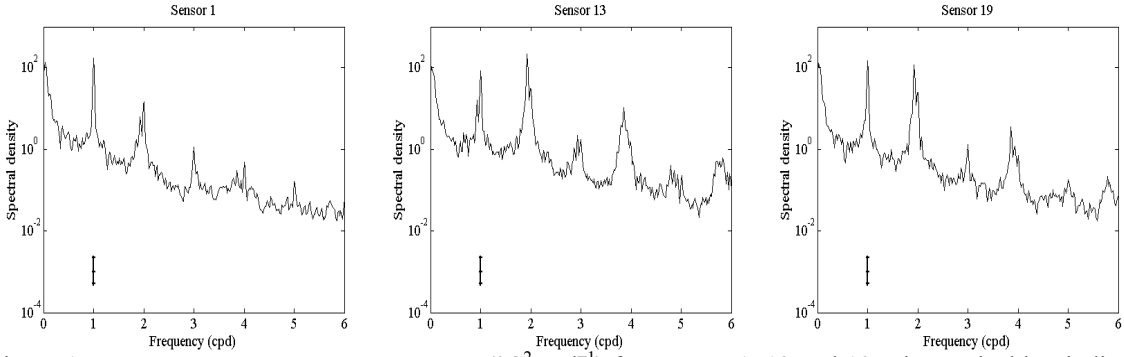

Figure 1. Water temperature energy spectrum ($°C^2\ cpd^{-1}$) for sensors 1, 13 and 19. The vertical bar indicates the 95% confidence level.

13°C during winter to 16/17°C during summer. At the mouth of the channel, the water temperature ranges from 14°C during winter to 17/18°C during summer. It can also be observed that the water temperature values decay throughout the season (autumn–winter) and that an inversion of the temperature values between the beginning of autumn and the end of winter occurs. In fact, in October, the ocean temperature values are higher than the river values. The longitudinal water temperature variability is lower, due to the minor water temperature difference between the mouth and the channel's head. Independently of the month, the water temperature between positions 2.5 and 3.5 km is the lowest. Between positions 5.5 and 6.5 km the water temperature is the highest during spring and summer (about 20°C). This can be due to the channel's shallowness, and the key role of the meteorological variables like air temperature and solar radiation in the heating/cooling cycle of the water. The water temperature distribution is less dependent on the river discharge and it is closely related to the inter-annual air temperature variation.

Spectral density plots were used to determine the power spectrum and to find any periodic short time scale phenomena. Before performing the spectral analysis, the time series trend was removed. Energy spectral density plots of the water temperature measured in sensors 1, 13 and 19 are depicted in Figure 3. The most energetic peaks are found at the diurnal and semidiurnal frequencies, but contributions at tridiurnal and quarterdiurnal tidal frequencies also affect the dynamics of the area. Results also indicate that subtidal processes are usually less energetic than the tidal oscillations, except in situations of extreme events, when the subtidal frequencies are amplified along the channel.

Two main peaks are observed for sensor 1: one diurnal and one semidiurnal. The diurnal peak is the most energetic (almost 10 times higher). In sensor 19, three main peaks are observed, one diurnal, one semidiurnal and one quarterdiurnal. The diurnal peak is the most energetic one, but with a slight difference to the semidiurnal peak that is associated to the tidal main periodicity. The peak, corresponding to 4 cycles per day frequency, probably originates from the non-linear interaction between the propagation of the main tidal constituents and the bottom friction. Concerning sensor 13, the same effect can be observed, but the semidiurnal peak is more energetic than the diurnal one. The diurnal peak in the spectrum can be explained as follows: the Ria de Aveiro is a shallow water estuarine system with mean depth of about 1 m, and the water temperature is conducted not only by the tide, but also by heating from solar radiation incidence, that has a diurnal periodicity.

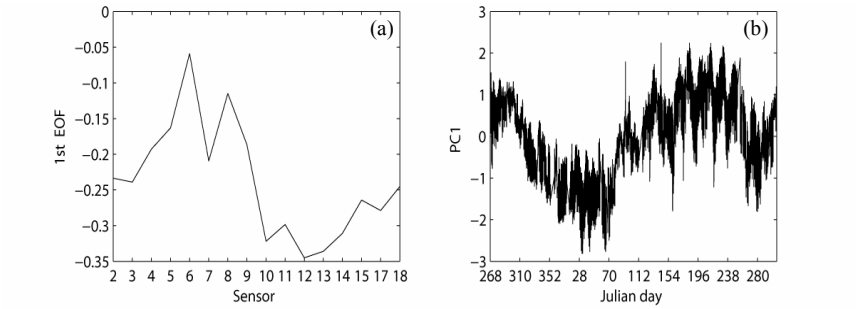

Figure 2. Spatial (a) and temporal (b) distribution of the water temperature first EOF.

EOFs are used to ascertain the most significant coherent mode of variation in the channel. The highest coherent component (PC1, the first EOF) (Figure 4a and 4b) explains 85% of the total variance of the water temperature inside the channel. PC1 is closely related to the inter-annual variation of the air temperature. This first EOF represents a non-homogeneous behavior along the channel; this may be a consequence of the river inflow importance on the establishment of the water temperature in the channel. In fact, the temporal variation of the first EOF (PC1, Figure 4b) is strongly correlated to the seawater temperature (0.9498) and freshwater temperature (0.9560), and is moderately correlated to the air temperature (0.6790). Strong correlations were found between PC1 and all water temperature and air temperature data, with the exception of water temperature recorded in sensors 6 and 8. That is, the annual water temperature pattern follows the annual variation of the air temperature.

Conclusions

The results showed the importance of the major forcing factors influencing water temperature behavior in the Espinheiro channel. Water temperature spectral analysis reveals high energy peaks in both semidiurnal and diurnal frequencies, demonstrating the importance of meteorological variables in the modulation of water temperature in shallow areas like the study area. EOF analysis indicates that much of the variability in the water temperature time series can be accounted for by the first component. Using correlation techniques, it was determined that the first EOF is attributed to the annual variation of the air temperature. The water temperature distribution is closely related to meteorological conditions, like air temperature, incoming solar radiation, especially because of the shallowness of the Espinheiro channel.

The results reveal that this technology produces reliable results and can therefore be used as a pre-operational system to monitor water properties like temperature in estuarine systems.

Acknowledgements

This research was financed by the FCT and FEDER (Portugal) through the AMDRAPHYD Project (POCI/AMB/57928/2004). Nuno Vaz is supported by the Portuguese FCT through a post-doc grant (SFRH/BPD/37325/2007).

References

Atkinson, M.J., Allanson, B.R., Imberger, J. (1987), Fine-scale oxygen variability in a stratified estuary: patchiness in aquatic environments, *Marine Ecology*, 36, 1–10.

Dias, J.M., Lopes, J.F., Dekeyser, I. (1999), Hydrological characterization of Ria de Aveiro, Portugal, in early summer, *Oceanologica Acta*, 22(5), 473–485.

Emery, W.J., Thompson, R.E. (1997), *Data Analysis Methods in Physical Oceanography*. Pergamon Press. 634pp.

Vaz, N., Dias, J.M. (2008), Hydrographic characterization of an estuarine tidal channel, *Journal of Marine Systems*, 70, 168–181.

Wang, D., Chen, Z., Wang, J., Xu, S., Yang, H., Chen, H., Yang, L., Hu, L. (2007), Summer-time denitrification and nitrous oxide exchange in the intertidal zone of the Yangtze Estuary, *Estuarine, Coastal and Shelf Science*, 73, 43–53.

Extending ASMITA to distinguish saltmarsh from tidal flats

MICHIEL KNAAPEN, IAN H. TOWNEND, CAROLINE FLETCHER,
KATE ROSSINGTON, JEREMY SPEARMAN

HR Wallingford Ltd., Howbery Park, Wallingford OX10 8BA UK
email: i.townend@hrwallingford.co.uk, k.rossington@hrwallingford.co.uk,
j.spearman@hrwallingford.co.uk

Keywords: behavior-based model, salt marsh, tidal flats

ABSTRACT

ASMITA is a behavior-based model describing a tidal inlet system with the major morphological elements being viewed at an aggregated scale (Stive et al., 1998). The model predicts the evolution of a system through the sediment exchange between these (Figure 1) which depends on the hydrodynamic forcing, basin properties and sediment availability.

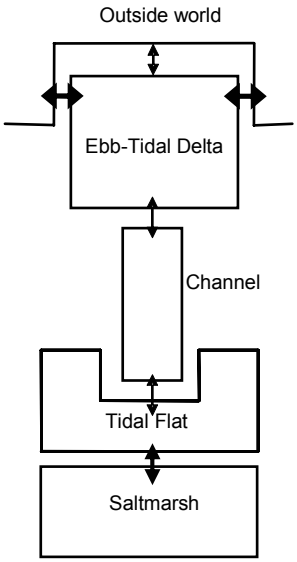

We propose an extension of ASMITA by dividing the inter-tidal element into a marsh and a tidal-flat element. The presence of vegetation increases sedimentation and reduces erosion on the marsh giving a different sediment exchange as the sediment exchange on tidal flats. The introduction of a new element requires a sediment exchange between the marsh element and the tidal-flats element. Recently published work on salt marsh dynamics is adapted to describe the sediment exchange as a function of the vegetation type and density and the vegetation density as a function of water depth. The resulting model is compared to observations of marsh development in time for different estuaries.

Figure 1. ASMITA schematization and element definitions.

References

Stive, M.J.F., Wang, Z.B., Capobianco, M., Ruol, P., Buijsman, M.C. (1998). *Morphodynamics of a tidal lagoon and the adjacent coast*. In: Physics of Estuaries and Coastal Seas, Rotterdam, Balkema.

Predicting sand bank occurrence in the North Sea

H. HENRIËT VAN DER VEEN, SUZANNE J.M.H. HULSCHER

Water Engineering and Management, University of Twente,
P.O. Box 217, 7500 AE Enschede, Netherlands
email: h.h.vanderveen@utwente.nl, s.j.m.h.hulscher@utwente.nl

Keywords: sand banks, bed patterns, tides; North Sea

ABSTRACT

Sandy shallow seas, like the North Sea are very dynamic. Several morphological features are present on the seabed, from small ripples to sand waves and large tidal sand banks. Sand banks have a wavelength between 1 and 10 km and can have a height of several tens of meters. They can induce significant depth variations and have an impact on human activities that take place in the North Sea. Therefore, it is important to know where sand banks occur and what their natural behavior is. Here we use an idealized model to predict the occurrence of sand banks in the North Sea. Also, we carry out a sensitivity analysis of two model parameters, namely the viscosity variation parameter (ε) and the level of zero intercept (z_0), to investigate their influence on the model results. The results show that the model is able to predict the occurrence of sand banks in the North Sea in 64.8% of the area and that the value of the level of zero intercept has a large influence on the results.

Introduction

Shelf seas like the North Sea are areas that are biologically highly active and provide most of the world's main fisheries. Often, the seabed contains high concentrations of oil and gas supplies and most shelf seas are very busy shipping areas. In most shelf seas, sediment is widely abundant and due to the fact that in these areas the largest part of the tidal and wave energy is dissipated, the bed is shaped in a range of bed forms by the tidal flow over the erodible bed (Brown et al., 1999). The smallest of these forms are ripples, with a height in the order of centimeters and somewhat larger are megaripples, here we focus on the largest offshore bed forms: sand banks. An overview of sand bank occurrence in the North Sea is given in Figure 1.

Sand banks can either be formed by the tide or are relict features (e.g. left overs from old coastal dunes). Banks that are formed by the tide can be either actively maintained or moribund. Actively maintained sand banks are formed by the modern (late Holocene) tidal regime. Moribund sand banks were formed during periods of lower sea levels, they occur in deeper water where the present tidal current is too weak to form sand banks (no sediment transport occurs under the present tidal current) (Collins et al., 1995).

The North Sea is a shallow shelf sea. Tides in the southern part are semi-diurnal and tidal amplitudes range from 2.4 m in the Strait of Dover to 0.6 m further to the north (Davies et al., 1997). At spring tide, surface velocities vary from 1.4 m s^{-1} in the west and south, to 0.7 m s^{-1} along the Dutch coast and to the north (Hydrographical_Survey, 2000). The seabed consists mainly of fine to medium sands (125–500 µm), but at some places in the Strait of Dover and off the East Anglia coast, patches of gravel have been observed (Jarke, 1956).

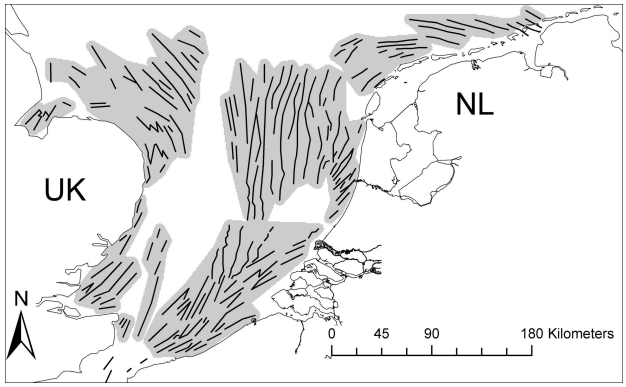

Figure 1. Overview of the Southern North Sea. Black lines denote sand bank occurrence (after Dyer and Huntley, 1999). The gray areas denote the digitized areas used for comparison with model results.

Bed forms interact with human activities, as the North Sea is intensively used for different purposes. User functions that are affected by the large-scale morphology are navigation, telecommunication cables, oil and gas transportation (pipelines), oil and gas mining, sand extraction, artificial islands and offshore wind farms. For safety reasons, it is important to know where the bed forms occur or might be generated and which parameters are crucial herein. Here we investigate to what extent the model of Hulscher (1996) is able to predict the occurrence of sand banks in the North Sea.

Model

The three-dimensional model of Hulscher (1996) explains how tidal currents form rhythmic bed patterns in sandy beds. The model is based on the three-dimensional shallow-water equations, applied to a tidal flow. An empirical bed load transport, which includes slope effects, models the sediment transport and the bed level changes are calculated using a sediment balance. In Hulscher (1996), tide and seabed are regarded as a coupled system. The bed patterns are assumed to be free instabilities of this system. A linear stability analysis is performed to study pattern dynamics, which means that only small amplitude perturbations are considered. The model calculates growth rates for every wavelength and orientation which characterize the spatial structure of the pattern. If all growth rates are negative, all bed patterns are damped and so the flat bed is stable. In this research we define a flat bed as a bed where no large-scale bed forms occur. However, if at least one bed pattern has a positive growth rate, the flat bed is unstable and a wavy bed pattern develops. For a more elaborate description of the model, see van der Veen et al. (2006).

Here, we used the model to predict the occurrence of tidal sand banks in the North Sea. In the case of a moderate resistance (small $\hat{S}$ and large E_v), the Stokes boundary layer is much thicker than the water depth and the vertical shear in the horizontal velocities is small. Then the flow resembles the depth-averaged (2DH) flow in the sand bank model of Hulscher et al. (1993).

Values of the resistance parameter ($\hat{S}$) and Stokes number (E_v) are estimated by fitting the partial slip model used in Hulscher (1996) to a more realistic turbulence model, including the no-slip condition at the bed and a parabolic eddy viscosity distribution (Hulscher and Roelvink, 1997), leading to the following expressions:

$$E_v = \frac{3\pi u}{4H\sigma}\frac{\kappa^2 B}{A} \tag{1}$$

$$\hat{S} = \frac{3\pi u}{4H\sigma}\frac{\kappa^2 B}{A(AB-\frac{1}{3})} \tag{2}$$

$$A = \left[\ln\left(\frac{H}{z_0}\right) - \frac{1}{\varepsilon} + \frac{1-\varepsilon}{\varepsilon}\ln\left(\frac{1-\varepsilon}{1-\varepsilon z_0/H}\right) + \frac{\varepsilon-1}{\varepsilon^2}\ln(1-\varepsilon)\right] \tag{3}$$

$$B = \frac{3-2\varepsilon}{6} \tag{4}$$

in which, κ (0.41) is the von Kármán constant, u is the depth-averaged flow velocity, H is the local mean depth, σ is the tidal frequency and ε is the viscosity variation parameter (which denotes the influence of waves), which may vary between 0 and 1, where $\varepsilon = 1$ represents a parabolic distribution over the water column and a rigid lid approach and $\varepsilon = 0$ represents a linear increase of the eddy viscosity (Soulsby, 1990). The parameter z_0 denotes the level of zero-intercept (the level above the seabed, where the flow velocity is zero). The value of z_0 varies with grain size and can also be influenced by the occurrence of bed forms like ripples and megaripples. To predict the occurrence of sand banks in the North Sea, we used values of z_0 based on the characteristics of megaripples in the North Sea (Tobias, 1989). This is analogous to Hulscher and Van den Brink (2001) and references herein and is defined by:

$$z_0 = 2\Delta_r\left(\frac{\Delta_r}{\lambda_r}\right)^{1.4} \qquad \text{(Soulsby,1983)} \tag{5}$$

in which $\Delta_r = \alpha_{\mathrm{mr}} H$ and $\lambda_r = \beta_{\mathrm{mr}} H$ (van Rijn, 1993) where α_{mr} (0.03) and β_{mr} (0.5) are dimensionless coefficients for the megaripple regime in the North sea (Tobias, 1989).

A grain size dependency is included in the model. The grain size of the sediment influences the initiation of motion of the grains. Sediment transport takes place if the bed shear stress (τ_b) exceeds the critical shear stress (τ_{cr}). The bed shear stress τ_b and the critical bed shear stress τ_{cr} are calculated using the site-specific parameters (grain size, water depth and flow velocity) as input parameters, for a complete overview of the data used, see van der Veen (2008). In the model we assume that sediment transport takes place if the bed

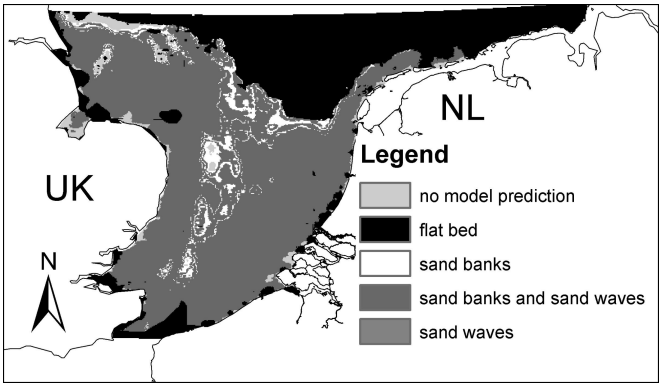

Figure 2. Model prediction of large-scale bed forms in the North Sea.

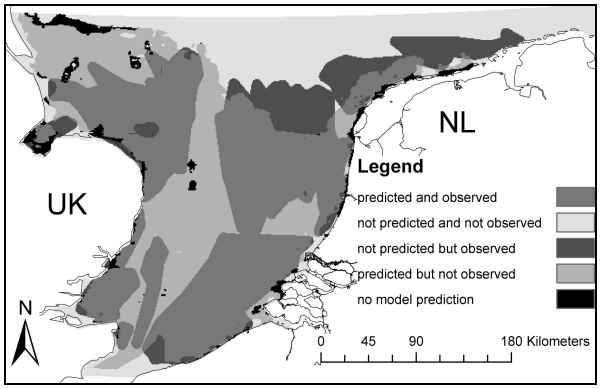

Figure 3. Comparison of model predictions with observations of sand banks.

shear stress exceeds the critical bed shear stress:

$$\tau_b \le \tau_{cr} \rightarrow \vec{S}_b = 0$$
$$\tau_b > \tau_{cr} \rightarrow \vec{S}_b = \alpha |\vec{\tau}_b|^b \left\{ \frac{\vec{\tau}_b}{|\vec{\tau}_b|} - \lambda \vec{\nabla} h \right\}. \quad (6)$$

We use a general sediment transport equation and only take into account bed load, which is assumed to be dominant in offshore tidal regimes (Hulscher, 1996). Parameter b (~3) denotes the non-linearity of transport in relation with the bed shear stress, λ (usually 2) is a bed-slope correction term, h denotes the height of the bed form and α is a bed load transport proportionality parameter.

Results

Figure 2 shows the prediction (with default values $\varepsilon = 0.5$), of sand bank occurrence in the North Sea. As can be seen in Figure 2, the occurrence of sand banks is predicted in a large part of the southern North Sea. In a small area in the middle of the southern North Sea, between the British coast and the Dutch coast, sand banks are predicted exclusively. In the northern part of the North Sea a flat bed is predicted. Note that also sand waves are predicted by the model, but here we only focus on the prediction of sand banks and do not discuss the prediction of sand waves.

Figure 3 shows the comparison between the model results and observations of sand banks. The categories 'predicted and observed' and 'not predicted and not observed' represent the cases for which the model gives a correct prediction. As can be seen, there is an over-prediction in the occurrence of sand banks (predicted but not observed). Also, the sand bank area in the northern part of the North Sea, off the coast of the Dutch Wadden isles is not predicted correctly by the model. Quantitatively, the model gives a correct prediction in 64.5% of the area and an incorrect prediction in 32.5% of the area (in 3% of the area, the model does not give a prediction).

Also, we performed a sensitivity analysis of two input parameters namely the viscosity variation parameter (ε) and the level of zero intercept (z_0), which have a large range of possible values, to determine which values of these parameters lead to an optimal prediction of sand banks in the North Sea. The results show that the

influence of ε is rather limited. With the values of z_0 that are used to predict the occurrence of sand banks in the North Sea (which vary between 0.023 and 0.064 m), we obtain a correct prediction for the occurrence of sand banks in 64.5% of the area. The maximum is reached when we use values of z_0 that are slightly smaller (80%). In this case a correct prediction is given for 64.8% of the area, but the difference is very small.

Conclusions

Without any tuning or calibration, the occurrence of sand banks in the North Sea is predicted correctly in 64.5% of the area. However, the area in which sand banks are predicted is too large. Apparently, there is room for further improvement, other physical processes predicting the occurrence of sand banks in the North Sea might be added in the model or, alternatively, the occurrence of sand banks with small amplitudes is still underestimated. The sensitivity analysis shows that the influence of the level of zero intercept (z_0) in the turbulence model is important for the quality of the predictions. The optimal prediction is made when we use a variable value of z_0 based on dimensionless coefficients for the megaripple regime (Equation 5) with values of z_0 that are very close to the original values that are used in the model, (0.023 and 0.064 m). When we take 80% of the variable values of z_0 this gives the most optimal results (a correct prediction in 64.8% of the area).

Acknowledgements

This research is part of the project PhD@Sea, which is substantially funded under the BSIK-programme of the Dutch Government and supported by the consortium WE@Sea, and the Lowland and coastal water management for Northern Netherlands project of the Cartesius Institute.

References

Brown, E., Colling, A., Park, D., Phillips, J., Rothery, D., Wright, J. (1999), *Waves, tides and shallow-water processes*. Oxford, The Open University.

Collins, M.B., Shimwell, S.J., Gao, S., Powell, H., Hewitson, C., Taylor, J.A. (1995), Water and sediment movement in the vicinity of linear sandbanks: the Norfolk Banks, southern North Sea, *Marine Geology*, 123, 125–142.

Davies, A.M., Kwong, S.C.M., Flather, R.A. (1997), Formulation of a variable-function three-dimensional model, with application to the M_2 and M_4 tide on the North-West European Continental Shelf, *Continental Shelf Research*, 17, 165–204.

Dyer, K.R., Huntley, D.A. (1999), The origin, classification and modeling of sand banks and ridges, *Continental Shelf Research*, 19, 1285–1330.

Hulscher, S.J.M.H. (1996), Tidal-induced large-scale regular bed form patterns in a three-dimensional shallow water model, *Journal of Geophysical Research*, 101(C9), 20727–20744.

Hulscher, S.J.M.H., de Swart, H.E., de Vriend, H.J. (1993), The generation of offshore tidal sand banks and sand waves, *Continental Shelf Research*, 101(C9), 1183–1204.

Hulscher, S.J.M.H., Roelvink, J.A. (1997), *Comparison between predicted and observed large-scale sea bed features in the southern North Sea*. University of Twente, Netherlands.

Hulscher, S.J.M.H., van den Brink, G.M. (2001), Comparison between predicted and observed sand waves and sand banks in the North Sea, *Journal of Geophysical Research*, 106(C5), 9327–9338.

Hydrographical_Survey (2000), *Tidal heights and streams, Coastal waters of the Netherlands and adjacent areas*. Royal Dutch Navy, Hydrographical Survey, HP33, pp308.

Jarke, J. (1956), Der Boden der Südlichen Nordsee, *Deutsche Hydrografische Zeitschrift*, 9, 1–9.

van Rijn, L.C. (1993), *Principles of sediment transport in rivers, estuaries and coastal seas*. Aqua Publications, Amsterdam.

Soulsby, R.L. (1983), *The bottom boundary layer of shelf seas*. In: Physical Oceanography of Coastal and Shelf seas, Johns, B. (Ed.), Elsevier, Amsterdam. pp189–266.

Soulsby, R.L. (1990), *Tidal-current boundary layers*. In: The Sea, le Mehaute B., Hanes, D.M. (Eds.), Ocean Engineering Science, John Wiley and Sons, New York. Vol. G, Part A. pp523–566.

Tobias, C.J. (1989), *Morphology of sand waves in relation to current, sediment and wave data along the Eurogeul, North Sea*. Rep. Geopro 1989.01, Dept. Physical Geography, University of Utrecht, Netherlands.

van der Veen, H.H. (2008), Natural and human induced seabed evolution, Ph.D. Thesis., University of Twente, Enschede, Netherlands.

van der Veen, H.H., Hulscher, S.J.M.H., Knaapen, M.A.F. (2006), Grain size dependency in the occurrence of sand waves, *Ocean Dynamics*, 56, 228–234. doi: 10.1007/s10236-005-0049-7.

Patch behavior and predictability properties of modeled sand ridges on the inner shelf

HUIB E. DE SWART[1], NICOLETTE C. VIS-STAR[1], DANIEL CALVETE[2]

1. Institute for Marine and Atmospheric Research Utrecht, University of Utrecht, P.O. Box 80000, 3508 TA Utrecht, Netherlands
email: h.e.deswart@phys.uu.nl, n.c.vis-star@phys.uu.nl

2. Department of Applied Physics, Universitat Politècnica de Catalunya, Off. B4, Campus Nord, 08034 Barcelona, Spain
email: calvete@fa.upc.es

Keywords: shoreface-connected ridges, nonlinear spectral model, subharmonic modes

ABSTRACT

Patches of shoreface-connected sand ridges (hereafter abbreviated as sfcr) are found on storm-dominated inner shelves, with a characteristic spacing between successive crests of several kilometers (Swift et al., 1978; Antia, 1996, Harrison et al., 2003). Typically, a patch consists of 4–8 ridges. The sfcr migrate in the direction of the storm-driven current, with a velocity of several meters per year. The estimated lifetime of the sfcr is several thousands of years. The crests can reach up to one-third of the water depth in the shallowest areas, and troughs are excavated by the same amount below the mean seabed level. The sfcr have asymmetrical bottom profiles, with gentle slopes on the landward (upstream) side and steep slopes on the seaward (downstream) side. As the sfcr seem to affect the stability of the beach (van de Meene and van Rijn, 2000), gaining more fundamental understanding about their dynamics is relevant for coastal zone management purposes.

Several studies focused on gaining fundamental understanding about the dynamics of sfcr. Trowbridge (1995) demonstrated that sfcr can grow due to feedbacks between the waves (which stir sediment from the bottom), the storm-driven current (which transports the sediment) and the sandy bottom. In subsequent studies (cf., Vis-Star et al., 2007) it was demonstrated that improved formulations for waves and sediment were necessary to obtain good agreement between model predictions and field observations. A drawback of these models, which employ linear stability analysis, is that they only apply to bedforms having small heights compared to the water depth, whereas observed sfcr have heights of several meters.

The finite-amplitude behavior of sfcr was investigated by Calvete and de Swart (2003). They find that, after the initial growth stage, the sand ridges become asymmetrical and their height tends to a constant value. However, their results do not explain the patch behavior of sfcr, which might be a consequence of the fact that in their model waves are described by severe parameterizations. Therefore, in the present study an extended nonlinear model of sfcr is investigated in which wave properties are calculated using physical principles. The objectives are to study the sensitivity of modeled ridges to offshore wave properties and to investigate the possible occurrence of patch behavior.

Model and method

The model simulates the evolution of storm-driven currents, waves and the sandy bottom on the inner shelf. Only the situation during storms is considered; it is assumed that during fair weather the water motion is too weak to erode sediment from the bottom. The domain that is considered extends seawards from the toe of the shoreface (Figure 1). Wave properties (frequency, wavenumber, angle of propagation and height) are calculated with a shoaling-refraction model. The currents are governed by the depth-averaged shallow water equation and changes in the bed level result from mass conservation of sand. Transport of sand is due to the joint action of waves (which stir sand from the bottom), currents and bed slopes.

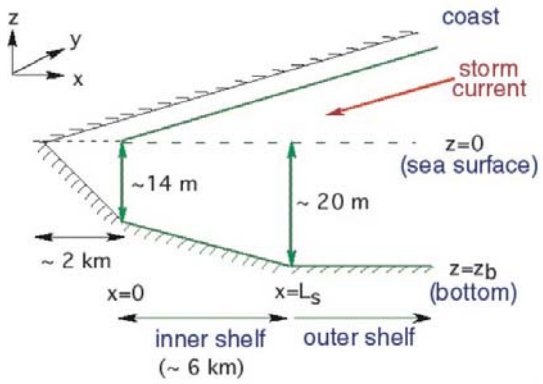

Figure 1. Model geometry and basic state situation. Parameter values are representative for Long Island inner shelf.

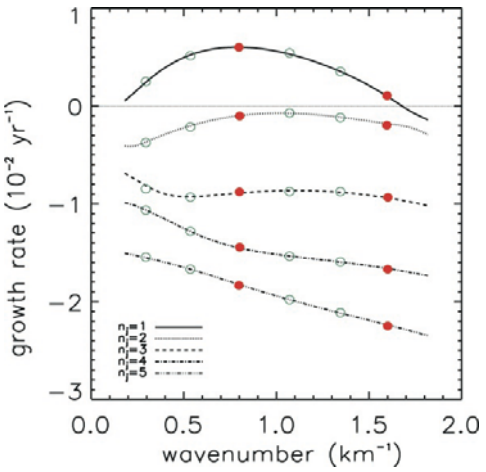

Figure 2. Growth rate of linear eigenmodes versus longshore wavenumber k. Different curves represent different cross-shore eigenmodes. Red dots indicate the most preferred mode and its superharmonics. Green dots with $k < k_p$ represent subharmonic modes. Here $N = 3$.

This model allows for a morphodynamic equilibrium state which is uniform in the longshore direction (no sand ridges present). It describes a storm-driven flow over a transversely sloping bottom. Next, the dynamics of perturbations evolving on this basic state is considered. A spectral model is derived by expanding these perturbations in known linear eigenmodes of the system, substituting these expansions in the equations of motion and finally performing a Galerkin projection. This results in a set of nonlinear differential equations that govern the temporal evolution of the amplitudes of the bottom modes. The amplitudes of the flow and sediment concentration depend nonlinearly on the bottom amplitudes and are described by algebraic equations.

Figure 2 illustrates that the resolved modes include the initially most preferred mode, which has longshore wavenumber k_p, its superharmonics (with longshore wavenumbers $k > k_p$), as well as $(N - 1)$ subharmonic modes (with longshore wavenumbers $k < k_p$; the smallest wavenumber is k_p/N). Specific emphasis is put on the role of subharmonics in generating patches of sfcr. This is because adding subharmonics implies that modes become more closely spaced in the spectral domain, thereby potentially allowing for the occurrence of group (or modulation) behavior.

Results

Runs were performed with parameter values representative for storm conditions at the micro-tidal inner shelf of Long Island (USA). At this location (40° latitude) the inner shelf bottom slope $\beta = 1.1 \times 10^{-3}$. The wind stress is 0.4 N m^{-2} in the southward direction. The offshore wave height is $H = 1.5$ m, the wave period is $T = 11$ s and the offshore angle of wave incidence is $\Theta = -20°$.

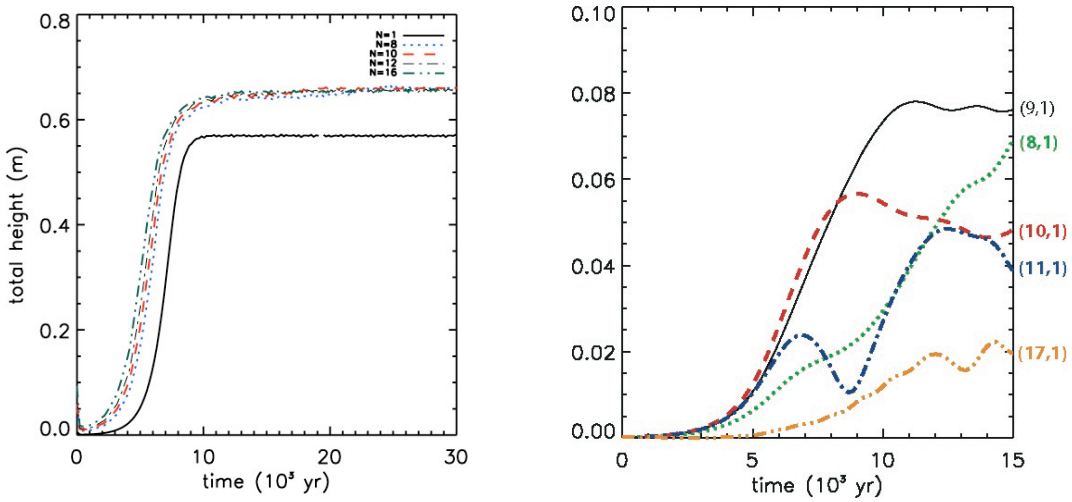

Figure 3. Left: height of sand ridges versus time for different number of subharmonic modes. Right: Time evolution of different bottom modes for $N = 10$. The initially most preferred mode is the (10,1) mode.

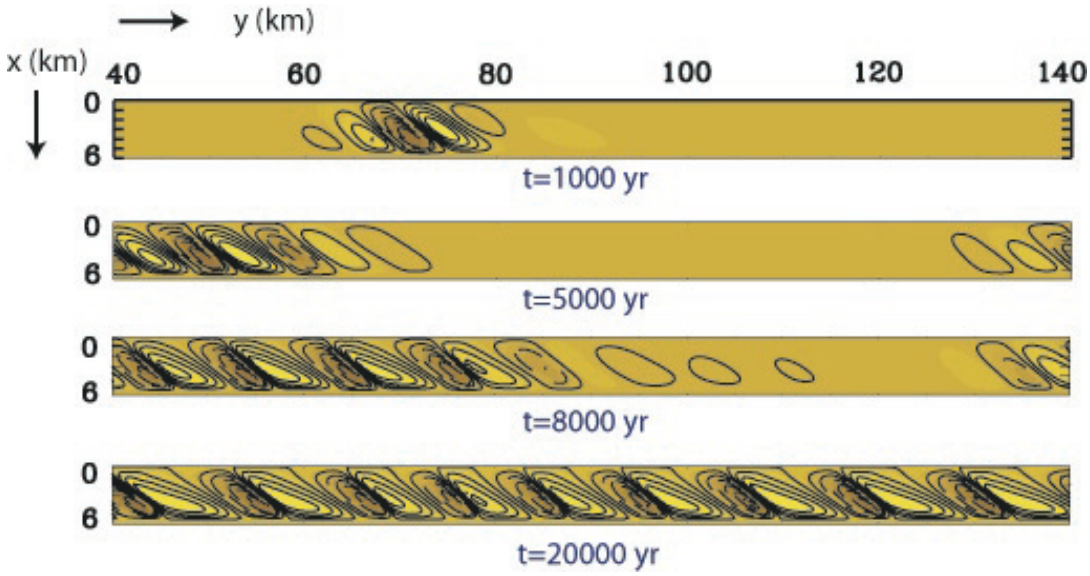

Figure 4. Modeled nonlinear evolution of shore-connected sand ridges on the shelf. In each panel the landward boundary is at $x = 0$.

The time evolution of the height of the bedforms is shown in the left panel of Figure 3 for different N. The slope β is 20% of its real value. Initially the ridges grow exponentially in time; after ~8000 years their height is constant. Results are robust for changes in N. The right panel of Figure 3 shows time series of the five largest bottom modes at $t = 15000$ yr ($N = 10$). The (10,1) mode initially has the largest amplitude, but in the course of time the (9,1) mode starts to dominate. The saturated pattern is dominated by the (8,1) mode, which implies that the alongshelf spacings between successive ridges has increased by ~20%.

Figure 4 shows bottom patterns at different times (case $N = 10$). Note that the ridges occur in patches. They ridges migrate several meters per year in the direction of the storm-driven current (negative y-direction).

Individual time series of modal amplitudes and bottom patterns turn out to be strongly dependent on the choice for N. As the latter parameter is not well known the model results suggest that the detailed evolution of ridges can not be predicted over long time intervals.

Conclusions

The present study demonstrates that sand ridges initially form as free morphodynamic instabilities, during which their height grows exponentially in time. On the long term the maximum height of the ridges becomes constant and their spatial pattern becomes highly asymmetrical.

If subharmonic modes are included the nonlinear model shows that in the course of time the spacing between ridges increases by ~20% and that the ridges occur in patches.

Given the fact that the age of sfcr is quite smaller than the saturation timescales predicted by the model suggests that observed ridges have not reached their final stage of development yet. In the transient stage the sfcr occur in patches and the number of ridges per patch is in the observed range of 4–8. Model results further indicate that the detailed evolution of the sfcr is only predictable over a finite time interval, whereas the overall characteristics (e.g., migration speed, finite bedform height and alongshore spacing) are also predictable for long time scales.

References

Antia, E.E. (1996), Shoreface-connected ridges in German and US Mid-Atlantic bights: similarities and contrasts, *Journal of Coastal Research*, 12, 141–146.

Calvete, D., de Swart, H.E. (2003), A nonlinear model study on the long-term behavior of shoreface-connected sand ridges, *Journal of Geophysical Research*, 108(C5), doi:10.1029/2001JC001,091.

Harrison, S.E., Locker, S.D., Hine, A.C., Edwards, J.H., Naar, D.F., Twichell, D.C. (2003), Sediment-starved sand ridges on a mixed carbonate/siliciclastic inner shelf off west-central Florida, *Marine Geology*, 200, 171–194.

Swift, D.J.P., Parker, G., Lanfredi, N.W., Perillo, G., Figge, K. (1978), Shoreface-connected sand ridges on American and European shelves: a comparison, *Estuarine and Coastal Marine Science*, 7, 257–273.

Trowbridge, J.H. (1995), A mechanism for the formation and maintenance of the shore oblique sand ridges on storm-dominated shelves, *Journal of Geophysical Research*, 100(C8), 16071–16086.

Vis-Star, N.C., de Swart, H.E., Calvete, D. (2007), *Finite amplitude dynamics of shoreface-connected ridges: Role of waves.* In: River, Coastal and Estuarine Morphodynamics, RCEM 2007, Dohmen-Janssen, C.M., Hulscher, S.J.M.H. (Eds.), Taylor and Francis, pp691–698.

Effects of wind and wave forcing on modeling waves and tides in the Irish Sea

YONGPING CHEN[1], SHUNQI PAN[1], JUDITH WOLF[2], YANLIANG DU[1]

1. School of Engineering, University of Plymouth, Drake Circus, Plymouth PL4 8AA UK
email: yongping.chen@plymouth.ac.uk, shunqi.pan@plymouth.ac.uk, yanliang.du@plymouth.ac.uk

2. Proudman Oceanographic Laboratory, 6 Brownlow Street, Liverpool L3 5DA UK
email: jaw@pol.ac.uk

Keywords: wind forcing, wave forcing, POLCOMS, WAM; Irish Sea

ABSTRACT

Waves, tides and tidal surge will have significant contributions to the water levels in the nearshore areas and along coastline, which in turn are the main causes for coastal flooding and erosion, particularly under the storm conditions. Therefore, predicting accurately the wave heights and the sea levels affected by waves, tides and storm surge becomes essential for the assessment and quantification of the risk from coastal flood and erosion. However, this will require an advanced and integrated modeling system to include major and important meteorological, oceanic, coastal and nearshore processes at different scales, as well as their interactions. As part of recently NERC-funded project EPIRUS, POLCOMS – a mesoscale tide and surge model and COAST2D – a coastal zone process model are combined to provide down-scaled and detailed regional parameters of tides, waves and surge from the meteorological inputs. This paper presents the preliminary results from POLCOMS coupled with the ProWAM model set for the Irish Sea, with a special focus on assessing the effects of wave and wind forcing between the nested domains.

Introduction

The current UK coastal defenses have been designed to withstand the storm events with a return period of 50–100 years. However, the threats from the increased severity and frequency of extreme storm events have become even more evident in recent years. The recent UK Department for Environment, Food and Rural Affairs (DEFRA) report (DEFRA/EA, 2003) has clearly indicated significant UK assets at risk from flooding by the sea at £132.2 billion and from coastal erosion at £7.8 billion. With the accepted predictions of the sea level rise, these values are expected to grow in the future. Complete protection of coastal communities has become more difficult or impossible in some cases. Therefore, accurately predicting and assessing the risk from coastal flood and erosion becomes one of the most effective approaches to minimize the loss due to the extreme events.

The NERC funded project – EPIRUS (Ensemble Prediction of Inundation Risk and Uncertainty arising from Scour) under the FREE (Flood Risk from Extreme Events) research program between the Universities of Plymouth and Bristol, aims to utilize and integrate the existing start-of-the-art meteorological, oceanic and coastal models with a 'from clouds to coasts' approach to predict the coastal erosion and flood (Zou et al., 2008). Part of the project on tide, surge and wave modeling is to combine a 3-D tide and surge model – POLCOMS, developed at Proudman Oceanographic Laboratory (POL) which is coupled with the third-generation wave model ProWAM, and a coastal zone model – COAST2D to bridge the global atmospheric models and surf-zone models. The tide, surge and wave modeling system takes meteorological data from the weather models at a spatial scale of ~1000s of kilometers and predicts the wave and tidal surge parameters in the coastal area of ~10s/100s of kilometers for more detailed studies of sediment transport and wave overtopping with surf-zone models at a scale of ~100s of meters. However, this paper presents the preliminary results of the integrated ocean/coastal modeling system with a particular focus on the sensitivity tests of the nested POLCOMS/ProWAM models set for the Irish Sea.

Methodology

Tide, surge and wave modeling transforms quantitatively the meteorological parameters to oceanic and coastal wave and tidal conditions using a set of well-established models with different temporal and spatial scales. These conditions will be consequently used to study the wave overtopping and erosion in the surf zone. The integrated tide, surge and wave modeling system used in the study consists the following components, a schematic diagram of which is shown in Figure 1:

1) Atlantic WAM model (ocean base scale) to provide wave forcing for regional models (~1000s of km);
2) POLCOMS (regional scale), taking the regional meteorological information (wind and atmospheric pressure) to provide waves, swell and surges for local models (~100s of km);
3) COAST2D (coastal zone scale) to provide further detailed hydrodynamics in the coastal zones, to provide conditions for coastal flooding and erosion studies (~10s of km).

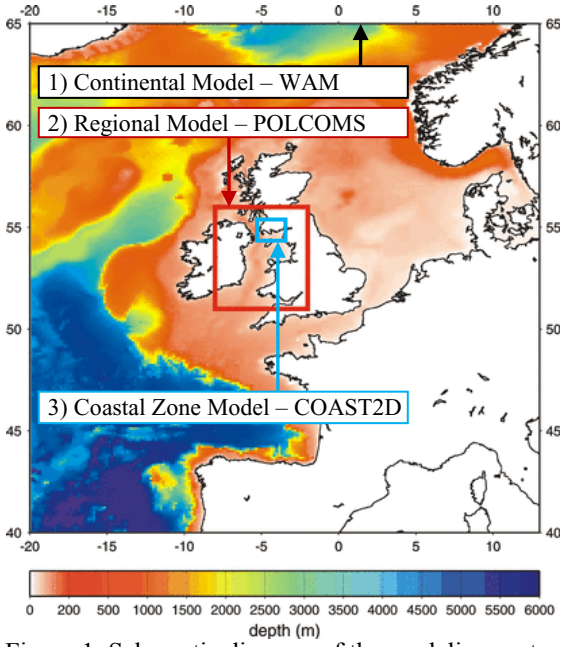

Figure 1. Schematic diagram of the modeling system.

The POLCOMS model has been developed at Proudman Oceanographic Laboratory (POL) for many years and is a baroclinic three-dimensional current model with coverage of both the deep ocean and the continental shelf. Further details of the model can be found elsewhere (Holt and James, 2001). The model recently incorporates the third-generation wave model, ProWAM, with an option of two-way coupling to quantitatively predict waves and currents (Wolf et al., 2002). The operation of the POLCOMS model requires both wave and tidal conditions at open boundaries. The former is provided by running the ProWAM model in a larger area with the wind information, normally produced by a meteorological model, and the latter is provided from the tidal constituents from harmonic analysis or other tidal surge model, further details can be found in the work of Osuna et al. (2004). The output of the POLCOMS model will provide the boundary conditions to drive the coastal zone model COAST2D in a specific site with a much finer resolution.

The COAST2D model includes the main coastal processes, such as wave refraction/diffraction, breaking, reflection, tides, wave-current interaction, taking offshore wave, tide and storm surge conditions from the regional model (POLCOMS). The phase-resolving wave module has recently incorporated to take account of reflection due to the defense structures such as breakwaters and sea walls. Further description can be found in Pan et al. (2007). The COAST2D model will be used in conjunction with POLCOMS to predict the detailed nearshore wave and current climates at specific sites, and to provide the hydrodynamic conditions to the surf zone models for studying coastal flooding and erosion.

Due to the nature of the EPIRUS project with the proposed ensemble predictions of storm events from clouds to coasts, it becomes important to understand how the perturbations propagate through the down-scaling processes. To this end, tests have been designed for different forcing scenarios, including wave forcing only (the wave boundary conditions for the nested domain from coarser grid), wind forcing only (surface wind forcing over the fine grid) and combined wave and wind forcing to study the sensitivity of the model. The results from these tests are compared and analyzed, and the effects of these forcings on overall wave predictions are investigated.

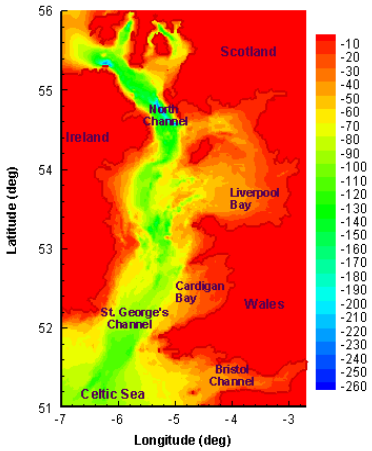

Figure 2. Bathymetry (m) used in POLCOMS for the Irish Sea.

Model setup and boundary conditions

The modeling system was setup in the Irish Sea for these tests. The regional model covers an area from 51°N to 56°N latitude and from 7°N to 2.7°W longitude, with a spatial resolution of 1/60° by 1/40° in latitude and longitude directions respectively, as shown in Figure 2.

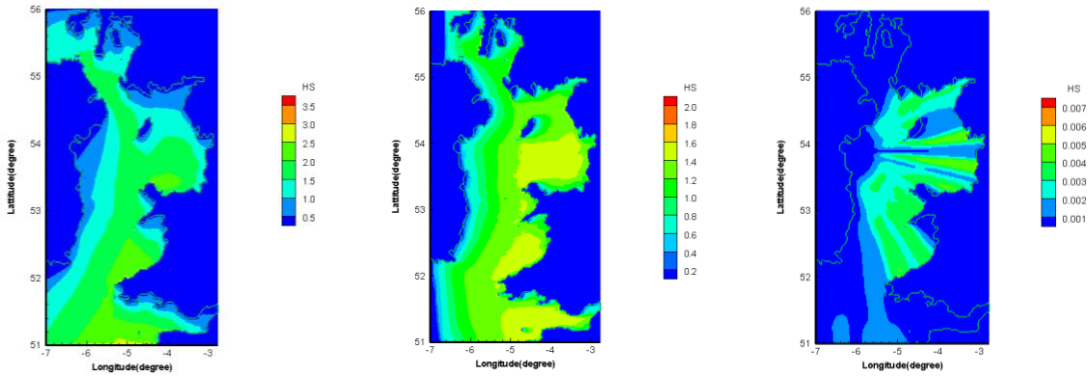

(a) wave and surface forcings (b) westerly wind forcing only (c) pressure forcing only

Figure 3. Computed significant wave height (in m).

The wave boundary conditions for the POLCOMS model are generated by implementing a stand-alone WAM model, covering part of Northeast Atlantic Ocean (NEA) from 40°N to 65°N latitude and 25°W to 15°E longitude, with a coarse grid of 1° by 1° in both directions. The WAM model outputs the directional wave spectra at the open boundary points for the nested Irish Sea model shown in Figure 2 in hourly intervals. The tidal boundary conditions for the nested Irish Sea model are provided from the combination of nine tidal constituents, i.e., M_2, M_4, S_2, N_2, L_2, MU_2, K_1, O_1 and Q_1 with a reference to a date in 1988. The tidal elevations and currents for specific dates were then calculated from these constituents at each time step. The surface forcing for the POLCOMS model were provided by surface winds and atmospheric pressure in the Irish Sea region with a 1° × 1° resolution at six-hourly intervals from 01/01/2003 to 01/02/2003 (ERA40). The same dataset was also extrapolated for the surface forcing required by the WAM model in the coarse grid.

Results

Initial tests were carried out with POLCOMS to investigate the model's response to the surface wind forcing and pressure forcing, including (a) full wind and pressure forcing with wave forcing specified at the boundaries; (b) with an hypothetical westerly wind forcing of 10 m s^{-1} uniform speed only; (c) with the pressure forcing only. Since the latter two cases are both hypothetical, no wave forcing from the boundaries was imposed. The model results of the significant wave height (H_s) after 120 hours model run for these three test conditions are shown in Figure 3. It can be clearly seen that the model responded well to these forcings. As shown in Figure 3(b) qualitatively, a reasonable wave field has been generated by the model inside the computational domain, with wave heights around 1.8 m in the eastern Irish Sea for a 10 m s^{-1} uniform wind field. Figure 3 (b) also clearly shows areas of lower wave height along the west boundary where the wave field was developed, as no wave forcing was imposed along this boundary in this case. The effect of the wave forcing from the boundary will be investigated further in late sections. As shown in Figure 3 (c), the pressure forcing has little effect on generating wave field within the domain. Although not shown here, the effect of surface forcing on the tidal level predictions is found to be negligible throughout the domain.

As noticed from the initial tests, the wave forcing from the boundaries has a significant effect on the wave field prediction in the area near the boundaries. In order to quantify the wave forcing effects, further tests were carried out with the following scenarios: (a) with the wave forcing provided from the nested coarser WAM model, but without surface forcing; (b) with the surface forcing only; and (c) with both wave forcing from the boundaries and surface forcing. Figure 4 shows the computed wave heights under these conditions. Figure 4 (a) shows the wave height distribution from the model run with scenario (a). The figure indicates the affected area from the wave forcing from the boundaries near the south-west and north-west corners. Significant influence can be seen up to 1/2 degree inside the domain, but such an influence is quickly reduced further afield. Similarly, in Figure 4 (b) which shows the computed wave height for scenario (b), an area where wave field was developed near the southern boundary can be clearly seen. It appears to take about 1 degree spatial distance for waves to be fully developed under the given conditions. The computed wave heights with the coupled wave and wind forcings are shown in Figure 4 (c) as a reference case for overall comparison. The results highlight that the effect of wave forcing can be significant, particularly in the areas near the boundaries, but it can propagate further afield up to 100s of km inside of the domain, see Figure 4 (a) and (c). Therefore, due consideration should be given to such an effect depending on the location of interest.

The computed wave heights are further examined in time series at selected locations in the Irish Sea. Shown in Figure 5 are four locations selected with different distances to the southern boundary, namely, Point 1# near the southern boundary; Point 17# near the centre of the domain; Point 14# for Cardigan Bay and Point 13# for

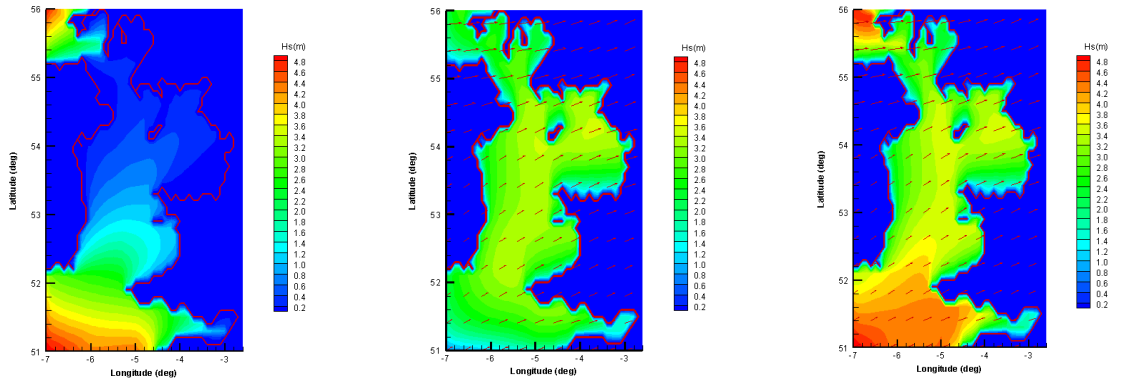

(a) wave forcing only (b) wind forcing only (c) coupled wind and wave forcings

Figure 4. Computed significant wave height.

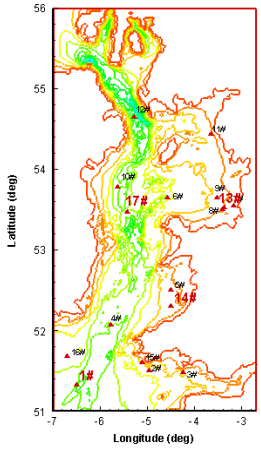

Figure 5. Selected locations.

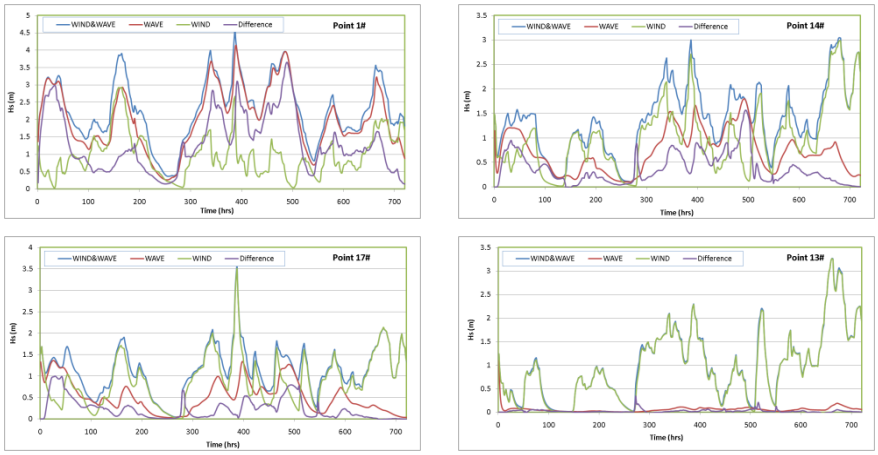

Figure 6. Time series of the computed significant wave height at selected locations ['Difference' = $H_s|_{\mathrm{WIND\&WAVE}} - H_s|_{\mathrm{WIND}}$].

Liverpool Bay. As shown in Figure 6, at Point 1# which is the closest locations to the southern boundary, the computed wave height with fully coupled wave and wind forcings is similar to that with wave forcing only, but exhibits a significant difference from that with wind forcing only, as expected. In contrast, at Point 13# for Liverpool Bay which is the furthest point from the southern boundary, the effect of the wave forcing from the boundaries is negligibly small, and the computed wave height at this location with fully coupled wave and wind forcings largely reproduces with that with wind forcing only case. Similarly, the impact of wave forcing from the boundaries is considerably more significant at Point 14# than that at Point 17# for Cardigan Bay.

Conclusions

A down-scaling modeling system, aiming to transform the global meteorological information to the local coastal zone, has been setup and tested in the Irish Sea. The initial sensitivity tests on the wind and wave forcings show that the computed wave field is sensitive to both forcings. The results indicate that correct boundary conditions are crucial to yield reliable tide, surge and wave modeling using POLCOMS.

References

DEFRA/EA (2003), *Beach Lowering in Front of Coastal Structures*, Report FD1916/TR1.

Holt, J.T., James, D.J. (2001), An s-coordinate density evolving model of the northwest European continental shelf: 1, Model description and density structure, *Journal of Geophysical Research*, 106, 14015–14034.

Osuna, P., Wolf, J., Ashworth, M. (2004), *Implementation of a wave-current interaction module for the POLCOMS system*, Internal Document No. 168, Proudman Oceanographic Laboratory, Liverpool, UK.

Pan, S., Wolf, J., Chen, Y., Bell, P., Du, Y., Fernando, P., Li, M. (2007), *Modelling nearshore waves with presence of shore-parallel breakwaters*. In: Coastal Structures 2007, Venice, Italy, 2nd-4th July 2007.

Wolf, J., Wakelin, S.L., Holt, J.T. (2002), *A coupled model of waves and currents in the Irish Sea*. In: Proceedings of the 12th International Offshore and Polar Engineering Conference, Kitakyushu, Japan, Vol. 3, pp108–114.

Zou, Q.-P. et al., (2008), Ensemble prediction of inundation risk and uncertainty arising from scour (EPIRUS), Extended Abstracts, ICCE 2008.

Great water temperature changes of 1.5°C per decade in Tokyo Bay, Japan – its causes and consequences

TETSUO YANAGI

1. Research Institute for Applied Mechanics, Kyushu University,
Kasuga 816 8580, Japan
email: tyanagi@riam.kyushu-u.ac.jp

Keywords: sea surface temperature changes; Tokyo Bay

ABSTRACT

Decreasing rates of sea surface temperatures (SST) in summer and their increasing rates in winter in Tokyo Bay, Japan from 1976 to 1997 attain 1.5°C per decade – 30 times greater than the global SST increasing rate of 0.5°C per century. Such large SST changes resulted from intensified estuarine circulation in Tokyo Bay due to increased fresh water discharge due to increased water use on land and decreased tidal amplitude attributable to large scale reclamation. Direct anthropogenic effects are much greater than the global warming effect on SST change in coastal seas.

The effect of turbulence levels on particle size and the optical properties of coastal waters

KATH M. BRAITHWAITE[1], DAVID G. BOWERS[1], W. ALEX M. NIMMO SMITH[2], JOHN H. SIMPSON[1], COLIN F. JAGO[1]

1. School of Ocean Sciences, College of Natural Science, Bangor University, Menai Bridge, Anglesey LL59 5AB UK
email: k.m.braithwaite@bangor.ac.uk, d.g.bowers@bangor.ac.uk, j.h.simpson@bangor.ac.uk, c.f.jago@bangor.ac.uk

2. School of Earth, Ocean and Environmental Sciences, University of Plymouth, Drake Circus, Plymouth PL4 8AA UK
email: alex.nimmo.smith@plymouth.ac.uk

Keywords: particle size, turbulence, optical properties

ABSTRACT

Observational data are presented from a study of particle size, turbulence and optical properties carried out in Plymouth Sound and the Menai Strait, UK. The aim of these programs is to develop a method for measuring near-surface suspended particle size from space and to test theoretical relationships between flocculated particle size and ambient turbulence in the ocean. The first challenge is to relate particle size to an inherent optical property that can be measured from space, in this case the scattering coefficient per unit concentration (b^*). Simultaneous measurements of particle size from LISST instruments and a new submersible digital holographic particle imager (SDHPI) are presented. The specific scattering coefficient has been measured by radiometers and transmissometers and gravimetric analysis. Turbulent kinetic energy dissipation has been measured with an ADCP and ADV. Observations have been carried out over a number of tidal cycles in Plymouth Sound, and over a whole year in the Menai Strait, to investigate the effect of cycles of turbulence and the response of particles to flocculation and dis-aggregation processes to be investigated. The results of these unique experiments will be presented and the application to measuring particle size from space explained.

Tidal dynamics and sediment transport processes in the Khour Musa estuary, Iran

MAJID JANDAGHI ALAEE[1], CHARITHA B. PATTIARATCHI[2], MORTEZA KOLAHDOUZAN[1]

1. Pouya Tarh Pars Consulting Engineers, 50 Moghadam Street, 1596965611 Tehran, Iran
email: m.j.alaee@ptpco.com, m.koladozan@ptpco.com

2. School of Environmental Systems Engineering, University of Western Australia, MO15, 35 Stirling Highway, Crawley 6009, Western Australia, Australia
email: chari.pattiaratchi@uwa.edu.au

Keywords: flow and sediment characteristics; Khour Musa estuary, Iran

ABSTRACT

Khour Musa estuary, located in the northwest of the Persian Gulf, is more than 90 km long and has a maximum tidal range of 5 m. The Musa estuary divides to three branches (Figure 1): (1) Mahshahr estuary; (2) Merimus estuary; and, (3) Douragh estuary. The current study was concentrated on the Mahshahr estuary. Extensive field observations were undertaken to examine the dominant flow patterns as well as sediment characteristics and behavior in the study region using ADCPs and suspended sediment sampling. Although some vertical density stratification was observed, the field data indicated that the strong tidal currents (up to 1 m s^{-1}) dominated the flow field. The residual flow pattern indicated a two-layer system with the flow in surface 10 m flowing upstream (north-east). In contrast, the residual flow in the bottom 6 m was directed downstream. Flow curvature induced strong secondary flow in the water column and the flood/ebb assymetry strongly influenced the residual currents in the vertical and the net sediment transport pathways. A three-dimensional numerical model was used to investigate the hydrodynamics and sediment transport to complement the field measurements. Complex topography of the Khour Musa estuary, the irregular shape of branches of the estuary and influences of very flat wet/dry areas were important factors in the selection of numerical domains and various open boundaries. Numerical simulations reproduced the field observations.

Figure 1. Left: Location of Imam Port in Persian Gulf; Right: the main study region.

Flocculation settling characteristics of mud:sand mixtures

ANDREW J. MANNING[1, 2], JEREMY SPEARMAN[1], RICHARD S.J. WHITEHOUSE[1]

1. HR Wallingford Ltd., Howbery Park, Wallingford OX10 8BA UK
email: a.manning@hrwallingford.co.uk, j.spearman@hrwallingford.co.uk, r.whitehouse@hrwallingford.co.uk

2. School of Earth, Ocean and Environmental Sciences, University of Plymouth, Drake Circus, Plymouth PL4 8AA UK
email: andymanning@yahoo.com

Keywords: mixed sediment, flocculation, settling velocity, laboratory simulation

ABSTRACT

Sediments present in many European estuaries tend to be regarded as being predominantly muddy. These muds are a combination of both clay minerals and biological matter, which tend to exist as flocs when entrained into suspension (Kranck and Milligan, 1992). Due to their porous structure, mud flocs demonstrate a lower effective density than their constituent particles, but exhibit a significantly quicker settling velocity; a result of a Stoke's Law relationship between floc size and settling velocity. Furthermore, in an estuarial system, flocculation is a dynamically active process which readily reacts to changes in turbulent hydrodynamic conditions (Manning, 2004).

In many estuarine systems muds become mixed with sands (van Ledden, 2003), and the proportion of muds and sands in the subtidal and intertidal sediments can vary in space and in time (Uncles et al, 1998). When natural muds become mixed with sandy sediments, for example in estuaries, this has a direct effect on the flocculation process, and resultant sediment transport regime. Much research has been completed on the erosion and consolidation of mud:sand mixtures (as reviewed by Whitehouse et al, 2000), but very little is known quantitatively about how mixed sediments interact whilst in suspension, particularly in terms of floc fall rates.

This paper presents findings from a laboratory study funded by the R&D program of HR Wallingford which examined the flocculation settling dynamics for three different mud:sand mixtures, at different imposed turbulent shear stresses and suspended concentration levels, within a mini-annular flume.

Methodology

This study utilized an annular flume at the University of Plymouth to create a consistent and repetitively turbulent environment. This mini-flume is a research proven tool which can be used to shear sediment whilst in suspension under controlled conditions. The annular flume has an outer diameter of 1.2 m, a channel width of 0.1 m and a maximum depth of 0.15 m, along with a detachable roof 10 mm thick. It has been used in numerous cohesive sediment experiments, e.g., Manning and Dyer (1999). The flume roof is driven by an electronic AC motor that is controlled by a digital motor control unit. The hydrodynamics were measured by a mini-ADV (Acoustic Doppler Velocimeter) probe, from which the turbulent kinetic energy (TKE) could be calculated at the floc extraction depth.

The low intrusive video-based LabSFLOC – Laboratory Spectral Flocculation Characteristics - instrument (Manning, 2006) was used to measure floc/aggregate properties, for each population, which included: floc size (D), settling velocity (Ws), porosity, suspended mass and mass settling flux. Floc population sampling comprised careful extraction of a suspension sample at a distance of 22 mm above the flume channel base. The floc sample was then quickly transferred to a Perspex settling column, whereby each floc was observed using a high resolution (10 µm lower limit) miniature underwater video camera (Manning and Dyer, 2002a) as they were settling. The video camera floc images are silhouettes enabling the floc/particle structure to be more visible. Using specially derived algorithms, it was possible to produce spectral distributions of floc size, settling velocity, porosity, suspended mass of sediment and mass settling flux of sediment.

The mini-annular flume channel was filled with 45 liters of saline water (a salinity of 20 ±0.2), to a level that reached the top of the annular ring (0.13 m depth). Pre-mixed mud:sand slurries of predetermined ratios (75% mud and 25% sand; 50% mud and 50% sand; and 25% mud and 75% sand) were introduced into the mini-annular flume water column. Three total suspended concentrations were used at each ratio: 200 mg l^{-1} (±3%), 1000 mg l^{-1} (±4.3%) and 5000 mg l^{-1} (±4.7%). For each run four increments of rotational motor speed were used to shear the sediment slurries at shear stresses ranging from 0.06–0.9 Pa (at the floc sampling point). The sediment was sheared for 30 minutes at each stress increment, to achieve equilibrium aggregational conditions. Each run was initiated at the fastest rotational velocity and decreased towards the slowest speeds as the run progressed. Further details of the protocols are outlined by Manning et al. (2007).

The sand used in these experiments was the 'Redhill 110' type, which is a well rounded and closely graded silica sand used by HR Wallingford for model testing with mobile sediment beds. Redhill 110 has a d_{50} of about 110 µm, a d_{10} of 70 µm and a d_{90} of approximately 170 µm. The experimental mud sample was obtained from the surface down to a depth of about 50 mm from the Calstock region of the upper Tamar Estuary (UK). This particular mud was used as its floc properties are widely reported from earlier studies (e.g., Mory et al., 2002; Bass et al., 2006). In addition baseline suspensions of pure mud and pure sand were utilized to provide benchmark conditions for comparison purposes.

Results

Data were assessed in terms of macrofloc (D >160 µm) and microfloc (D <160 µm) settling parameters: Ws_{macro} and Ws_{micro}, respectively. For pure muds, the macroflocs are regarded as the most dominant contributors to the total mass settling flux (Manning and Dyer, 2002b). Figure 1 shows the macrofloc and microfloc averaged settling velocity plots which cover both the experimental concentration and shear stress range for suspensions comprising 75% mud and 25% sand. The solid lines correspond to the 25% sand mixed suspensions; the dotted curve lines are the contrasting 100% mud suspension outputs, and the straight dotted lines represent the d_{50} and d_{10} settling rates of pure sand grains determined by 'SandCalc' software (HR Wallingford, 1998).

The dotted curve lines (top) are representative of 100% mud macrofloc settling velocities, whilst the single blue curved dotted line (bottom) represents the settling behavior of pure mud microflocs. Lines indicating SandCalc estimated settling velocities of unhindered d_{10} and d_{50} pure sand grains are also plotted. The initial

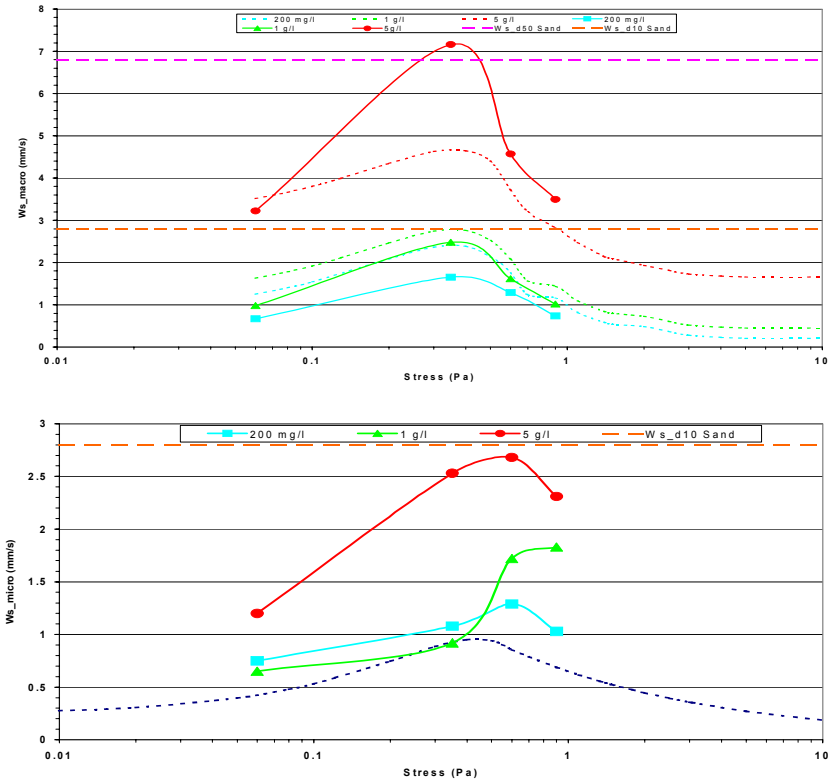

Figure 1. Ws_{macro} (top) and Ws_{micro} (bottom) values for 75% mud and 25% sand (75M:25S) suspension concentrations, plotted against shear stress. Solid lines + symbols indicate mixed sediment floc data points.

findings indicated that by adding just 25% sand to a pure mud suspension, produced a distinct effect on the Wsmacro (Figure 1, upper panel). At 0.2 g l^{-1} concentration and lowest shear stress, Wsmacro = 0.65 mm s^{-1}: half the Wsmacro of pure mud. As the turbulent shear stress increased, flocculation increased and Wsmacro rose to a maximum of 1.7 mm s^{-1}, but this was still slower than pure mud suspensions.

The smaller mixed sediment microfloc fractions observed in the 75M:25S suspension, all settled faster than the pure mud equivalent (see blue curved dotted line on Figure 1, lower panel). Manning and Dyer (2007) showed that for varying levels of suspended concentration, generically pure mud microfloc settling in turbulent flows can be represented by a single curve. In contrast, mixed sediment microfloc fall velocities are dependent upon both concentration and shear stress variations, and therefore require unique representation for each combination (i.e., as with macroflocs). Where the macrofloc mixed fraction showed settling peaks at 0.35 Pa, similar to natural muds (Manning, 2004), the mixed Ws_{micro} tended to produce a maximum at the higher turbulent shear stress of 0.6 Pa. For example, at the lowest concentration Ws_{micro} reduced to 0.75 mm s^{-1} at the lowest stress, increased to 1.3 mm s^{-1} at 0.6 Pa and then reduced again to ~1 mm s^{-1} at the maximum stress. Interestingly at the middle SPM level, the microfloc fractions were seen to be settling 14% slower than those formed during the 200 mg l^{-1} run, throughout the lower half of the stress range data points. With a step up in the shear stress to 0.6 Pa, the 1 g l^{-1} Ws_{micro} jumped from 0.9 mm s^{-1} to 1.7 mm s^{-1}.

Raising the 75M:25S suspension concentration to 5 g l^{-1} significantly enhanced the settling dynamics of both macrofloc and microfloc fractions at their respective optimum shearing stresses. This also created a change in the macrofloc structure; these macroflocs were nearly three times more dense than the lower concentration increments and about 8% less porous. These characteristics meant that the macrofloc settling velocity peaked at 7.2 mm s^{-1}, which was about 85% faster than the 100% mud equivalent, and 0.4 mm s^{-1} (6%) quicker than a d_{50} sand grain. At a velocity of 2.7 mm s^{-1} the value for Ws_{micro} was virtually the same as that of a d_{10} sand grain and 1.7 mm s^{-1}quicker than pure mud.

Higher sand content mixtures produced values of Ws_{micro} that were quicker than pure mud, at the detriment of the corresponding macroflocs (Figure 2, lower panel). All 75S:25M Ws_{micro} values exceeded pure mud settling values by more than a factor of two. Similarly the majority of the microfloc samples also exceeded the settling rate exhibited by a d_{10} sand grain. The microfloc settling rates were further enhanced at the high concentration; at an SPM of 5 g l^{-1} the Ws_{micro} peaked at 4.7 mm s^{-1}. This was about five times faster than the value for 100% mud, and not quite double the equivalent 75% mud microfloc settling rate.

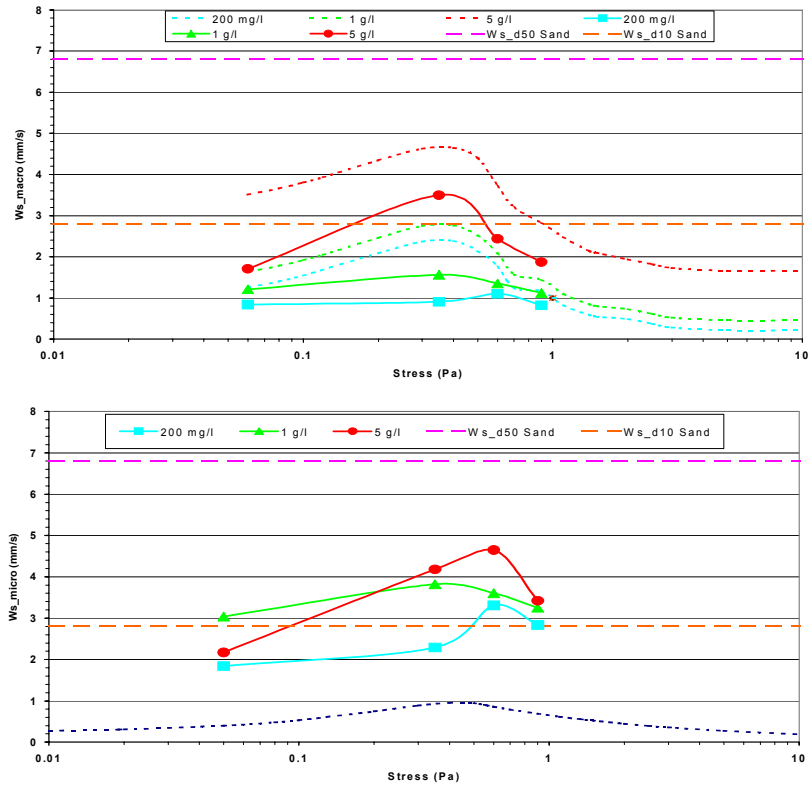

Figure 2. Ws_{macro} (top) and Ws_{micro} (bottom) values for 25% mud and 75% sand (75S:25M) suspension concentrations, plotted against shear stress. Solid lines + symbols indicate floc data points; dotted lines are 100% mud equivalents. Lines indicating SandCalc-estimated settling velocities of unhindered d_{10} and d_{50} pure sand grains are also plotted.

In contrast to the 75M:25S results, all macrofloc fractions (Figure 2, upper panel) settled significantly slower within the less cohesive 75S:25M suspensions than for their mud only equivalent values. At maximum ambient concentration, the fastest settling macrofloc fraction still only fell at 3.5 mm s^{-1}; this was the sole macrofloc fraction to exceed the settling velocity of d_{10} sand. This macrofloc settling rate was 1.2 mm s^{-1} slower than the quickest Ws_{micro} from the same test.

Conclusions

Results of the settling of mixtures of muds and sands have been evaluated. Most importantly this study has demonstrated that flocculation is an extremely important factor with regards to the depositional behavior of mud:sand mixtures, and these factors must be considered when modelling mixed sediment transport in the estuarine or marine environment. Some observations from the study demonstrated the following settling velocity patterns:

- With more sand content present in a mixture of mud and sand, the settling velocity of microflocs is increased and the settling velocity of macroflocs is decreased.
- For a suspension with 75% mud, the macrofloc settling characteristics were very similar (±10%) to pure mud at low (200 mg l^{-1}) and intermediate (1 g l^{-1}) concentrations at all shear stress increments.
- For a suspension with 75% sand the values of Ws_{macro} were generally smaller than $Ws_{micro.}$
- In contrast suspensions with 25% sand produced Ws_{macro} values faster than the Ws_{micro} rates.
- The quickest Ws_{micro} appears to consistently occur at a higher level of turbulent shear stress ($\tau \sim 0.6$ Pa), than both the macrofloc and microfloc fractions from suspensions of natural (100%) muds.

References

Bass, S.J., Manning, A.J. Dyer, K.R. (2006), *Preliminary findings from a study of the upper reaches of the Tamar Estuary, UK, throughout a complete tidal cycle: Part I. Linking sediment and hydrodynamic cycles*. In: Maa, J.P.-Y., Sanford, L.P., Schoellhamer, D.H. (Eds.), Coastal and Estuarine Fine Sediment Processes – Proc. in Marine Science 8, Amsterdam: Elsevier, pp1–14, ISBN: 0-444-52238-7.

HR Wallingford, (1998). *SandCalc: Marine Sands Calculator Interface*. Version 2.0 for Windows. Software by Tessela & HR Wallingford.

Kranck, K. Milligan, T.G. (1992). Characteristics of suspended particles at an 11-hour anchor station in San Francisco Bay, California, *Journal of Geophysical Research*, 97, 11373–11382.

van Ledden, M. (2003), *Sand-mud segregation in estuaries and tidal basins*. Ph.D. Thesis, Delft University of Technology, The Netherlands, Report No. 03-2, ISSN 0169-6548, 217pp.

Manning, A.J. (2004), *The observed effects of turbulence on estuarine flocculation*. In: Ciavola, P., Collins, M.B. (Eds.), Sediment Transport in European Estuaries, Journal of Coastal Research, SI 41, 90-104.

Manning, A.J. (2006), *LabSFLOC – A laboratory system to determine the spectral characteristics of flocculating cohesive sediments*. HR Wallingford Technical Report, TR 156.

Manning, A.J., Dyer, K.R. (1999), A laboratory examination of floc characteristics with regard to turbulent shearing. *Marine Geology*, 160, 147–170.

Manning, A.J., Dyer, K.R. (2002a), The use of optics for the in-situ determination of flocculated mud characteristics, *Journal of Optics A: Pure and Applied Optics*, Institute of Physics Publishing, 4, S71–S81.

Manning, A.J., Dyer, K.R. (2002b), *A comparison of floc properties observed during neap and spring tidal conditions*. In: Winterwerp, J.C., Kranenburg, C. (Eds.), Fine Sediment Dynamics in the Marine Environment – Proc. in Marine Science 5, Amsterdam: Elsevier, pp. 233-250, ISBN: 0-444-51136-9.

Manning, A.J., Dyer, K.R. (2007), Mass settling flux of fine sediments in Northern European estuaries: measurements and predictions, *Marine Geology*, 245, 107-122, doi:10.1016/j.margeo.2007.07.005.

Mory, M., Gratiot, N., Manning, A.J., Michallet, H. (2002), *CBS layers in a diffusive turbulence grid oscillation experiment*. In: Winterwerp, J.C., Kranenburg, C. (Eds.), Fine Sediment Dynamics in the Marine Environment – Proc. in Mar. Science 5, Amsterdam: Elsevier, pp.139-154, ISBN: 0-444-51136-9.

Manning, A.J., Spearman, J., Whitehouse, R.J.S. (2007), *Mud:Sand Transport – Flocculation & Settling Dynamics within Turbulent Flows, Part 1: Analysis of laboratory data*. HR Wallingford Internal Report, IT 534, 32pp.

Uncles, R.J., Stephens, J.A., Harris, C. (1998), *Seasonal variability of subtidal and intertidal sediment distributions in a muddy, macrotidal estuary: the Humber-Ouse, UK*. In: Sedimentary Processes in the Intertidal Zone, Black, K.S., Paterson, D.M., Cramp, A. (Eds.), Geological Society, London, Special Publications, 139, pp211–219.

Whitehouse, R.J.S., Soulsby, R., Roberts, W., Mitchener, H.J. (2000), *Dynamics of Estuarine Muds*. Thomas Telford, London, 232pp.

Ferry-based observations of the transport of total suspended matter through the Texel inlet

JANINE J. NAUW[1], LUCAS M. MERCKELBACH[2], HERMAN RIDDERINKHOF[1]

1. Royal Netherlands Institute for Sea Research, Landsdiep 4,
1797 SZ 't Horntje (Texel), Netherlands
email: jnauw@nioz.nl, rid@nioz.nl

2. National Oceanography Centre, Southampton,
European Way, Southampton SO14 3ZH UK
email: l.merckelbach@noc.soton.ac.uk

Keywords: sediment transport, acoustic Doppler current profiler, long-term observations

ABSTRACT

The Texel inlet is one of the main connections between the North Sea and the Wadden Sea, the biggest National Park within the Netherlands. Model studies have shown that the extension of the harbor near Rotterdam in 2008 increases the horizontal extend of the coastal river, composed of diluted outflow water from the Rhine. The total suspended matter (TSM) concentration therefore decreases within the coastal zone, which may even affect the TSM flux through the Texel inlet.

A unique set of observations with an acoustic Doppler current profiler (ADCP) mounted beneath the ferry crossing the Texel inlet is used to determine the current residual TSM flux. Besides vertical velocity profiles, ADCPs also register profiles of the acoustic backscatter intensity. The latter, corrected for geometric spreading and attenuation, is linear related to the TSM concentration, if depth-averaged flow velocities are small. For large flow velocities, the relation becomes quadratic in the vertical derivate of the TSM concentration. Dedicated calibration cruises in the Texel inlet were performed to determine the device dependent constants.

A least squares harmonic analysis applied to the time-series between 2003 and 2005 revealed that the sediment import from the North Sea into the Wadden Sea is about 7.0 million tones per year although the residual water transport varies sign. This suggests that the sediment transport is tidally driven and processes such as settling and scour lag are involved, while the residual water transport is less dependent on tides and possibly related to mechanisms such as differential set-up and wind-driven transport.

Introduction

This study forms part of a project that involves the extension of the harbor near Rotterdam, called Maasvlakte-2 and possible changes in the TSM transport as a result of that. The bulk of the suspended Matter along the Dutch coast has its origin in the river Rhine. Due to the density difference between the saline water from the North Sea and the fresh water from the river Rhine, the latter turns north due to the Coriolis force. Mixing between both water masses is relatively low and cross-shore density gradients remain visible all the way to the Texel inlet. Most of the suspended matter remains trapped within this so-called coastal river and is also transported to the north.

This year, the harbor near Rotterdam will be extended further into the North Sea. Model studies have shown that this extension causes a broadening of the coastal river. As the suspended matter content of the river Rhine remains unchanged, the TSM concentration within the coastal zone decreases – by as much as 50 mg l^{-1}close to the harbor. Although the effects on the Wadden Sea based on these model results seem negligible, it is not unthinkable that a decrease in the TSM concentration in the coastal river has an effect on transport of TSM, nutrients and larvae to the Wadden Sea. As the Wadden Sea is a National Park, thereby protected under European regulations, any changes must be monitored.

Method

Since 1998, the Royal Netherlands Institute for Sea Research (NIOZ) has a unique cooperation with the company TESO (Tessels Eigen Stoomboot Onderneming), that manages ferry transport between the Dutch mainland and the island of Texel. An ADCP is mounted, about 4.3 m below sea level under the hull of the ferry 'Schulpengat'. It sends acoustic pings in three directions to measure vertical profiles of the velocity in earth coordinates using Doppler shift. It also records vertical profiles of the backscatter intensity for each of the three beams. It pings several times per second while the ferry is underway. There are about 32 crossings per day, 7 days per week and about 300 days per year. The backscatter intensity can be used as a measure for the TSM concentration. NIOZ has been assigned to ascertain the present TSM flux in the Texel inlet so that it can be compared with future TSM fluxes after the harbor extension is complete. To remove erroneous profiles and reduce the amount of data, some processing is done. Data are gridded onto 50 evenly distributed points over the inlet, aligned along tidal flow streamlines, similar to Buijsman and Ridderinkhof (2007).

The suspended sediment concentration can be derived from the backscatter intensity, $K(N - N_t)/10$ (in dB), after it has been corrected for geometric spreading, r^2, and attenuation, $e^{4r\alpha}$. Multiplying by a device dependent constant, k_t, leads to the acoustic scattering cross-section, σ:

$$\sigma = k_t 10^{(K(N-N_t)/10)} r^2 e^{4r\alpha} . \tag{1}$$

The device dependent constant needs to be derived from field measurements. In the classical theory, the acoustic scattering cross-section is linear related to the concentration:

$$\sigma \sim c \qquad k \geq \frac{k_\eta}{2\gamma} . \tag{2}$$

This classical theory assumes that the TSM particles are randomly distributed in the water column and that the reflected wavefronts have no coherent structure. Usually this is a good assumption, but in the Texel inlet horizontal velocities can become so large that the Kolmogorov wavelength can be of the same size or even bigger than the wavelength of the sound wave. In that case, the turbulent eddies on the Kolmogorov scale cause redistributions of the TSM particles in such a way that particles are no longer randomly distributed, but related to the background vertical concentration gradient. This causes wavefronts to join together and results in enormous peaks in the backscatter intensity. Merckelbach (2006) showed that the acoustic scattering cross-section, σ, is related to the vertical gradient of the concentration squared in this so-called turbulent regime

$$\sigma \sim \left(\frac{dc}{dz}\right)^2 \qquad k < \frac{k_\eta}{2\gamma} . \tag{3}$$

The measure for the Kolmogorov wavenumber, k_η, is based on the kinematic viscosity, ν, and the dissipation rate of turbulent kinetic energy, ε. Moreover, a common parameterization is used for the dissipation rate depending on depth, z, and the friction velocity, u_*; κ is the von Kármán constant:

$$k_\eta = 2\pi\left(\frac{\varepsilon}{\nu^3}\right)^{\frac{1}{4}}; \qquad \varepsilon \approx \frac{u_*^3}{h\kappa}\frac{h-z}{z} \qquad u_* = \frac{\overline{U}}{20} \tag{4}$$

leading to a depth-averaged critical velocity $|U| \sim 0.85$ m s^{-1}, above which classical theory no longer holds.

Calibration cruises are performed every three months in the Marsdiep inlet with the research vessel 'Navicula' to determine the device dependent constant, k_t, of the ADCP beneath the ferry. During one tidal cycle we remain on anchor close to the transects of the ferry and take vertical TSM profiles every 20 minutes with an Optical Backscatter Sensor (OBS) mounted on a CTD and by filtration. Moreover, a similar ADCP mounted beneath the Navicula samples vertical profiles of the velocity and acoustic backscatter at a frequency of 1 Hz during the entire survey. Figure 2 (left) shows the concentration as determined from the acoustic backscatter measured with the ADCP beneath the Navicula using only Equation (1) against the TSM concentration from OBS profiles. Clearly, a linear relation exists for profiles for which the depth-averaged velocity is less than 0.5 m s^{-1} (black dots) and classical theory obviously holds. The associated device dependent constant is $k_{t,nav} = 1.16 \times 10^{-11}$. The right-hand figure shows the linear relation between the corrected backscatter intensities of the ADCP beneath the ferry and the Navicula at the time of the passage of the ferry, giving a device dependent constant for the ADCP beneath the ferry of $k_{t,fer} = 8.18 \times 10^{-11}$.

Applying the theory from Merckelbach (2006) improves the results considerably. Black (red) in the left-hand panel of Figure 3 shows all of the data points for which the classical theory (turbulent regime) holds. In some cases, however, the concentration is extremely underestimated. Based on the Kolmogorov length scale, these points are assumed to be in the turbulent regime, but in practice they are still in the classical regime. Therefore, an iterative method is constructed based on the probability of finding data in the turbulent regime

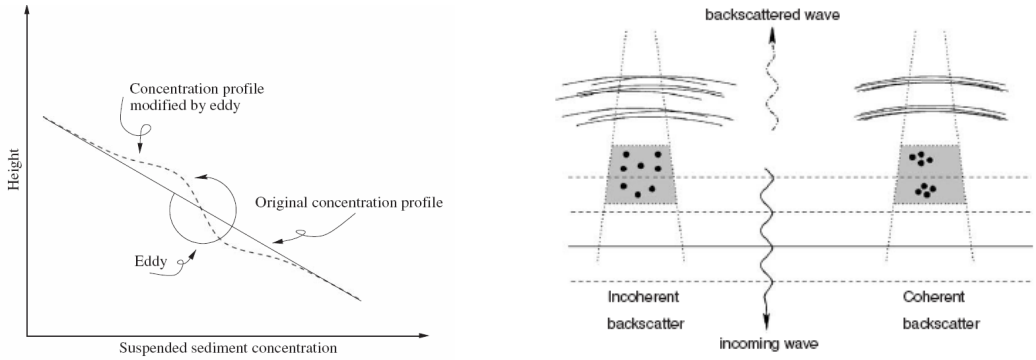

Figure 1. Left: Modification of a background concentration profile by an eddy on the Kolmogorov length scale. Right: Effect of the redistribution of TSM particles on the reflected sound wave from the ADCP.

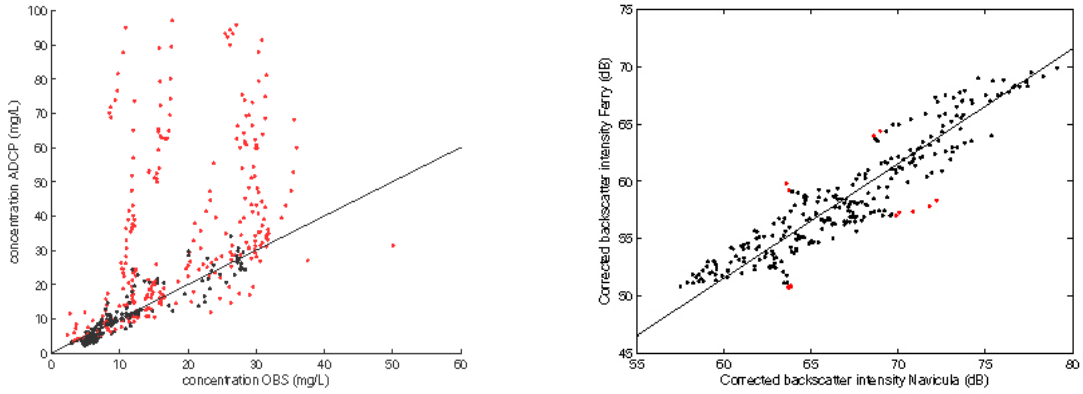

Figure 2. Left: TSM concentration as determined by Equations (1) and (2) versus measured concentration (mg l^{-1}), i.e., in the classical regime. Black (red) indicates measurement for which the depth-averaged velocity is less (more) than 0.5 m s^{-1}. Right: Corrected backscatter intensity of the ADCP under the ferry versus that of the ADCP on the Navicula (in dB) at the time of the passage of the ferry.

(for details see Nauw et al., 2008). The iterative method performs better one way as extreme outliers are removed (Figure 3, right). However, the spread along the one-to-one line is much larger than with the 'direct' method from Merckelbach (2006).

If the entire water column is in the turbulent regime, a boundary condition is needed to solve Equation (3). This boundary condition follows from the turbulent spectrum, which should be continuous at $k = k_\eta$, where the turbulent and the classical regime meet. It is applied to the third bin and giving the following condition:

$$c_3 \sim \left(\frac{u_*}{u_{*,c}} \right)^{-3.75} \sigma_3 . \qquad (4)$$

Results and conclusions

The channel-mean velocity, TSM concentration and TSM flux is determined for each crossing of the ferry between 2003 and 2006 as both the calibration as well as the ferry data are the most reliable in this interval. A blow-up of these data for September 2003 is shown in Figure 4. Left shows that the semi-diurnal M_2 and spring-neap tidal (related to S_2) cycles are the dominant contributions in determining the channel mean velocity. The concentration and therefore the TSM flux are influenced by the spring-neap tidal cycle irrespective of the method used, direct or iterative.

The time-series of 15 September 2003 (right-hand panel) show a maximum flood velocity of 1.23 m s^{-1} and a (negative) maximum ebb velocity of 1.10 m s^{-1}. The flood phase lasted nearly six hours and shows signs of a double high tide; the ebb phase lasts longer, e.g., 6 hours and 23 minutes. These values are comparable to the mean values of the entire 3-year long time-series. The maximum TSM concentration is about 45 (35) mg l^{-1} in the flood (ebb) phase and occurs about one hour after the maximum flood (ebb) velocity is attained. This is probably related to local resuspension of silt particles after slack tide.

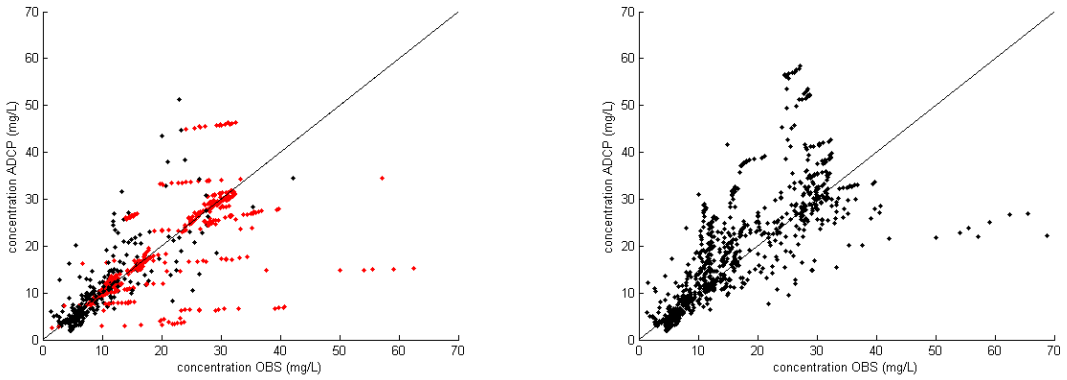

Figure 3. Left: TSM concentration from acoustic backscatter as determined by Equations (1), (2) and (3) versus the measured concentration (mg l^{-1}). Black (red) dots indicate measurements in the classical (turbulent) regime. Right: TSM concentration from acoustic backscatter using an iterative method based on Equations (1–3).

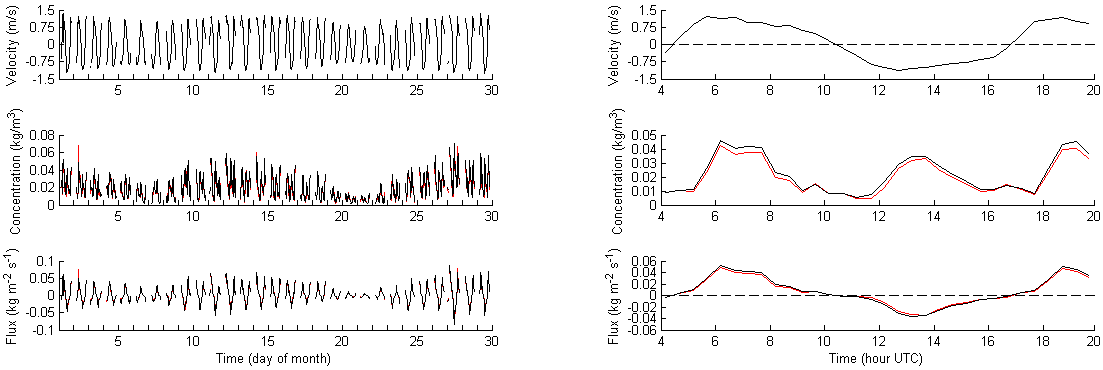

Figure 4. Left: Channel-mean velocity (m s^{-1}), concentration (kg m^{-3}) and TSM flux (kg m^{-2} s^{-1}) during the September 2003. Right: enlargement of 15 September. Black (red) shows the direct (iterative) method by Merckelbach (2006) (see Nauw et al., 2008).

Table 1. Least squares harmonic analysis coefficients applied to the transport (10^3 m^3 s^{-1}) for each year and for the whole 2003–2006 time series.

Trans	Period	All	2003	2004	2005
a_0		0.85	−0.98	1.66	2.17
M_2	12h 25′	67.5	66.8	70.4	68.6
S_2	12h 00′	18.2	16.9	17	18.7

Table 2. Same as in Table 1, but applied to the flux (10^{-3} kg m^{-2} s^{-1}).

Trans	Period	All	2003	2004	2005
a_0		3.4	3.1	2.1	4.4
M_2	12h 25′	22.5	25.4	15	23.7
S_2	12h 00′	8.6	8.9	8.4	8.6

A least squares harmonic analysis (Buijsman, 2007) is applied to the transport and TSM flux time series. The residual value is determined by the coefficient a_0. In 2003, transport is directed from the Wadden Sea to the North Sea (negative); in other years there is import into the Wadden Sea. Moreover, residual transport is only a fraction of the tidal prism as seen in the much larger coefficients associated with the M_2 and S_2 constituents. TSM flux, on the other hand, doesn't change sign. In all years there is net residual import into the Wadden Sea with a mean of 3.4×10^{-3} kg $m^{-2}s^{-1}$, i.e., about 7.0 million tonnes per year. This means the residual water transport may be dominated by processes other than tidal flow, such as differential set-up and wind-driven transport. However, the flux is linked to the tide, combined with processes such as scour lag and settling lag (Postma, 1954).

References

Buijsman, M.C., Ridderinkhof, H. (2007), Long-term ferry-ADCP observations of tidal currents in the Marsdiep inlet, *Journal of. Sea Research,*. 57, 237–256.

Merckelbach, L.M. (2006), A model for high-frequency acoustic Doppler current profiler backscatter from suspended sediment in strong currents, *Continental Shelf Research*, 26, 1316–1335.

Nauw, J.J., Merckelbach, L.M., Ridderinkhof, H. (2008), *Observations of the total suspended matter flux through the Marsdiep inlet*. (In preparation.)

Postma, H. (1954), Hydrography of the Dutch Wadden Sea. Thesis Groningen. *Arch. Neerland. Zoologie*, X, 4e Livraison, 106.

Suspended particulate matter: tidal and seasonal variation in two mesotidal estuaries – Douro and Minho (NW Portugal)

ANA ISABEL O. SANTOS, MARIA JOÃO BALSINHA, ANABELA T.C. OLIVEIRA

Marinha-Instituto Hidrográfico, Rua das Trinas 49, 1249-093 Lisboa, Portugal
email: ana.santos@hidrografico.pt, maria.balsinha@hidrografico.pt, anabela.oliveira@hidrografico.pt

Keywords: suspended particulate matter, sediment export, rivers, continental shelf

ABSTRACT

This work aims to present a group of results obtained during two observational surveys of the ECOIS project (Estuarine contributions for inner shelf dynamics), during September 2005 and February 2006, in the Minho and Douro estuaries (northern Portugal). Results obtained during summer in extreme draught conditions and after raining season, aim to contribute to the understanding of the sediment dynamics of these particular estuaries, which behave like partially mixed systems, with significant differences between spring and neap tide regimes (Santos et al., 2006). Variations in suspended particulate matter signature (mineralogical) during neap and spring tidal cycles and high and low river runoff allow the deduction of sedimentary sources for the lower estuarine, and the understanding of potential sediment export onto the inner continental shelf.

Introduction

Up to the 20th century, fluvial discharge has been the main mechanism of sediment input into the northwestern Portuguese littoral zone. However, the most important fluvial systems have been subject to human intervention. The construction of dams imposed fixed barriers to the free circulation of sediments. The case of the Douro River's effect on the northern Portuguese coast is exemplary of this kind of intervention (Andrade, 1997). Actually, the upstream limit of the Douro estuary was artificially set by the Crestuma-Lever dam (Vieira et al, 2000). Little is known about the Minho River's dynamics and most authors recognize the Douro as the main source of sediments onto the NW Iberian continental shelf (Dias et al., 2002; Araújo et al., 2002).

Most of the estuarine sediments derive directly from the weathering of high mountains (>1000 m) of the Minho and Douro basins mainly dominated by granites and schist-greywacke formations. The Douro River has a deeply incised meandering valley with a funnel shape estuary. By contrary, Minho River presents a wider valley with alluvial deposits. In the lower estuary higher sedimentation rates and slow currents, give rise to the development of extensive sand banks like 'Boega' and 'Amores' islands. Both estuaries are sea-shore partially blocked by a south spit resulting from littoral drift. Project ECOIS (Estuarine Contributions to Inner Shelf Dynamics) intend to evaluate in which way the variability of the Douro and Minho runoff induces changes in estuarine and inner shelf dynamics.

This paper aims to disclose some results of this project in what concerns estuarine sediment dynamics during neap and spring tidal cycles, during a low and high river runoff surveys (September 2005 and February 2006). In order to characterize the mineralogical signature of both rivers and recognize mineral tracers only selected tidal cycles (Minho 2005 – neap tide, and Douro 2006 – neap and spring tide) are presented here.

Methods

Two surveys were carried out in the Douro (Figure 1A) and Minho estuaries (Figure 1B). The first survey took place in summer conditions, under extremely low river runoff conditions (8 September to 10 October 2005), and the second one in winter conditions, with higher river discharge (20 February to 19 March 2006). For this work the data obtained in two fixed hydro-sedimentological stations were used – one in each estuary, during a period of 30 hours for the first survey and of 15 hours in the second one. In both cases both spring and neap tides periods were observed using current meter and hydrological profiles with surface and bottom water sampling for characterization of suspended particulate matter (SPM). In the fixed hydrological/current

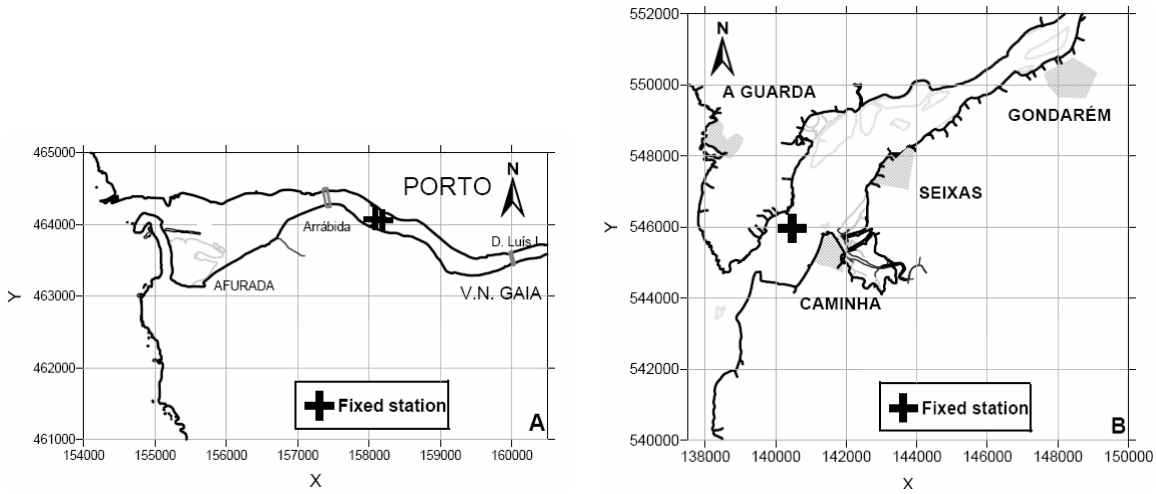

Figure 1. Fixed station position in the Douro (A) and Minho (B).

meter stations, current profiles were obtained using an Aanderaa RCM9, equipped with additional sensors of temperature, conductivity, pressure and turbidity (interval of observation between 0–20 NTU, nephelometric turbidity units), configured with 1-minute sampling intervals. The profiles were executed with 1-hour interval. Water samples were collected using a direct pumping and filtration system (resolution of 1 ml). An Aanderaa RCM7 currentometer was also coupled to the hose to guarantee the water sampling depth.

Mineralogical analysis was performed directly on the filters. XRD measurements were performed on a PANalytical diffractometer, using CuKα radiation. Scans were run between 2° and 35° 2θ. Peak areas of the basal reflections of the main minerals were determined using the X'Pert HighScore program (Version 1.0f) and weighted by empirically estimated factors. For semi-quantitative determination, criteria recommended by Schultz (1964), Thorez (1976) and retaken by Rocha (1993) have been followed.

Results and discussion

In September 2005, the Douro and Minho mean river discharges were 62 $m^3 s^{-1}$ and 82 $m^3 s^{-1}$ respectively and in February 2006 the mean river discharge increased to 767 $m^3 s^{-1}$ in the Douro and 690 $m^3 s^{-1}$ in the Minho.

In summer 2005, the Minho estuary revealed a highly stratified structure during neap tide (Figure 2A). A clear asymmetry was observed between flood and ebb in both neap and spring conditions. In neap tides the turbidity maxima occur near the bottom (>2 NTU) during the flood maximum (Figure 2B). As far as mineralogical composition is concerned (Figure 2D), the more common minerals are illite (mean 65%), kaolinite (mean 15%) and chlorite (mean 6%), followed by quartz (mean 3%) feldspars (6%) and calcite (2%). Using the minerals as tracers, at surface for neap tide (Figure 2D), calcite shows an intermittent behavior, being more important during flood than during ebb, reflecting the stronger signature of oceanic waters as opposed to estuarine water masses, richer in feldspars and mica. Near bottom, calcite is more persistent, showing the relatively higher importance of oceanic water masses in the lower estuary's water column, with the introduction of feldspars and quartz with direct relation to flood maximum (>30 cm s^{-1}), that promotes local resuspension of bottom sediments. This mineralogy is in agreement with mean composition of fine estuarine bottom sediments, also collected in September 2005. The bottom sediments are predominantly sandy with low content of silt and clay (<3%). The fine fraction composition is very rich in mica/illite (mean 40%), feldspars (30%) and quartz (mean 13%). Calcite was not detected, denoting the transport in suspension of biogenic remains by oceanic waters.

For the Douro River, in winter 2006, during spring tide (Figure 3A), the water columns is only homogeneous in ebb maximum, during the rest of the cycle the water columns is strongly stratified with higher temperature and salinity oceanic waters at bottom and low temperature and salinity estuarine waters at surface. Turbidity bottom maxima are associated with maximum flood currents (Figure 3B). Most likely these maxima result from resuspension of bottom material due to bottom friction generated by flood fluxes. During neap tides the water column is permanently homogeneous (Figure 3E), occupied by estuarine water mass, with higher turbidity than in summer (mean value changes from 1.83 mg l^{-1} to 8.5 mg l^{-1}, at surface waters). The maximum velocity was measured at surface (Figure 3F) related to the Crestuma Dam discharge (ECOIS team, 2007). SPM mineralogical composition in the Douro estuary shows, as in Minho estuary, has a

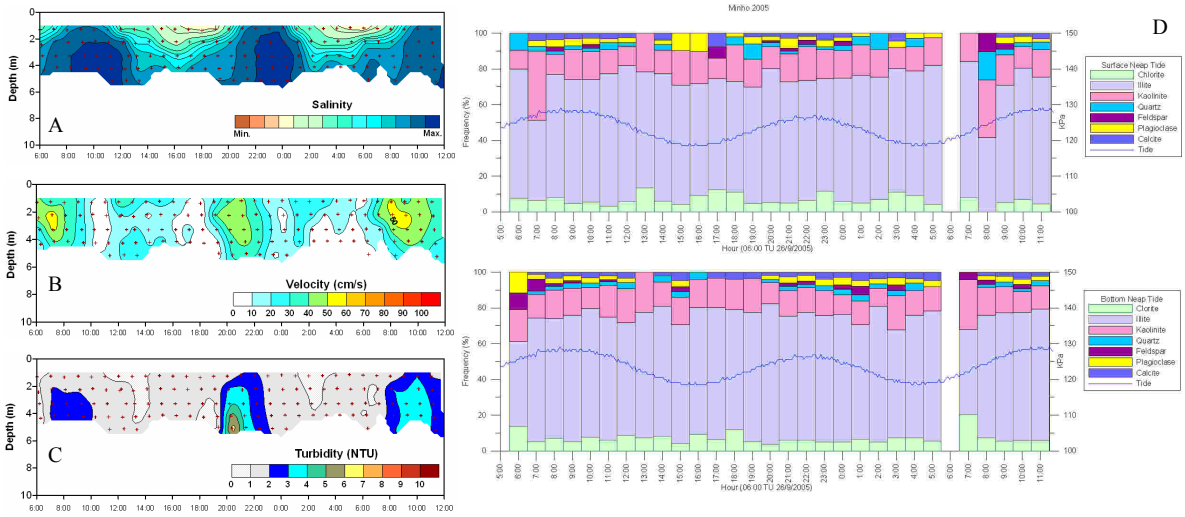

Figure 2. Neap tide variation of velocity and salinity (A), turbidity (NTU) (B) and SPM mineralogical composition (C), with tide representation (blue line), observed in Minho fixed station (September 2005).

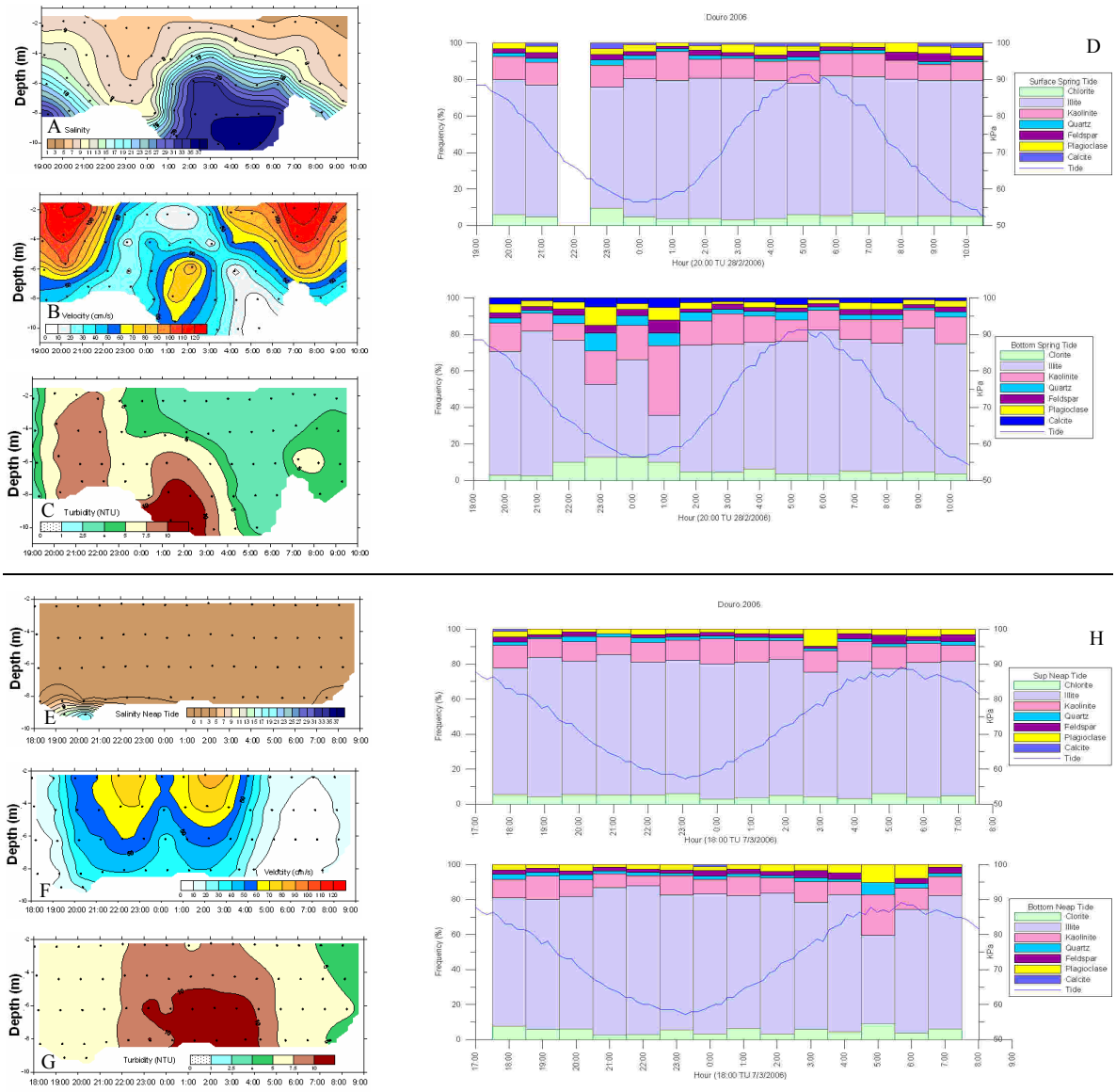

Figure 3. Variation of salinity (A, E), velocity (B, F), turbidity (NTU) (C, G) and SPM mineralogical composition (D, H) with tides (blue line) observed during spring and neap tides at the Douro fixed station (February 2006).

predominance of clay minerals: illite (mean 70%), kaolinite (mean 12%) and chlorite (mean 5%), followed by quartz (mean 2%) feldspars (6%) and calcite (1%). Likewise in the Minho estuary, minerals can be considered good tracers of water masses (Figure 3D). In spring tides (February 2006) the constant presence of calcite, near bottom highlight the predominance of oceanic water. The increase of feldspar, quartz and chlorite percentage is related with the change of tidal velocity, near bottom caused by the entrance of the flood wave (>50 cm s^{-1}). The resuspension of the bottom sediments by flood currents, induce the decreasing of mica/illite (planar habit). Near the surface, the presence of calcite is much more intermittent, higher during flood and almost negligible during ebb, when fresh water prevails.

During neap tide (Figure 3H), when fresh water prevails and the water column is homogeneous, an increase of feldspars (plagioclase and K feldspar) and quartz was observed associated with the absence of calcite (Douro River mineralogical signature). The bottom sediments are also predominantly sandy with high content of mica (mean 52%); feldspars (mean 33%), quartz (mean 19%) and calcite (mean 1%).

Conclusions

Below-average river runoff in both the Douro and Minho present a partially mixed water column, typical of mesotidal estuaries (Santos et al, 2006). Both estuaries have the same mineralogical composition, mica/illite being the more abundant mineral, followed by kaolinite and chlorite. However, different percentages of calcite, feldspar and quartz can be related with origins of water masses and correlated with tidal wave near-bed friction. This process can cause local resuspension of fine bottom sediments deposited in a previous tidal cycle. In the Minho River, downstream estuarine transport during ebb, and resuspension of bottom material with upstream transport during flood, are observed. For the Douro, during spring and neap tides in winter 2006: the predominance of fresh water at surface with the Douro River SPM mineralogical signal substantiates the sediment export to the inner shelf, during ebb. SPM mineralogical signature coupled with hydrological and current measures is a good proxy for understanding lower estuaries' sediment dynamics. It is also vital to recognize these estuaries' influence on NW Iberian inner shelf dynamics (Oliveira et al, this issue).

Acknowledgements

This study has been supported by the ECOIS (POCTI/CTA/48461/2002) FCT project. The authors would like to thank all the participants in the ECOIS field campaigns; scientific team, technicians, students and crew of UAM Fisália and UAM Coral.

References

Andrade, C.F. (1997), *Dinâmica, Erosão e Conservação das Zonas de Praia*. Monografia. Edição do Comissariado da Exposição Mundial de Lisboa de 1998, 88pp., Lisboa.

Araújo, M.F., Jouanneau J.-M., Valério, P., Barbosa, T., Gouveia, A., Weber, O., Oliveira, A., Rodrigues, A., Dias, J.M.A. (2002), Geochemical tracers of northern Portuguese estuarine sediments on the shelf, *Progress in Oceanography*, 52, 277–297.

Dias, J.M.A., Gonzalez, R., Garcia, C., Diaz-del-Rio, V. (2002), Sediment distribution patterns on the Galicia-Minho continental shelf, *Progress in Oceanography*, 52, 215–23.

ECOIS team (2007), *Relatório de Progresso relativo ao segundo ano de execução*. Projecto Nº POCTI/CTA/48461/2002. Programa Operacional de Ciência Tecnologia e Inovação – Ministério da Ciência e Ensino Superior, Portugal.

Oliveira, A., Santos, A.I., Morgado, A., Silva, A.J. (2008), Suspended sediment mineralogical signature – an approach to understand shelf water hydrodynamics. (This issue.)

Rocha, F. (1993), *Argilas Aplicadas a Estudos Litoestratigraficos e Paleoambientais na Bacia Sedimentar de Aveiro*. PhD Thesis, Aveiro University, 399pp.

Santos, A. I., Balsinha, M.J., Oliveira, A., Silva, A.J. (2006), *Tide induced variability in the hydrography and dynamics of the Minho and Douro estuaries during low runoff*. In: Proceedings of the 5th Symposium on the Iberian Atlantic Margin.

Schultz, L.G. (1964), *Quantitative interpretation of mineralogical composition from X-ray and Chemical data for the Pierre shale*. United States Geological Survey Professional Paper, 39I-C, 1-3

Thorez, J. (1976), In G. Lelotte (Ed.), *Practical identification of clay minerals*.

Vieira, M.E.C., Bordalo, A. (2000), The Douro Estuary (Portugal): a mesotidal salt wedge, *Oceanológica Acta*, 23(5), 585–594.

A coastal deployment of a commercial multiple frequency acoustic backscatter sediment profiler

ANDREW M. SMERDON[1], PETER D. THORNE[2]

1. Aquatec Group Limited, High Street, Hartley Wintney RG27 8NY UK
email: asmerdon@aquatecgroup.com

2. Proudman Oceanographic Laboratory, 6 Brownlow Street, Liverpool L3 5DA UK
email: pdt@pol.ac.uk

Keywords: multi-frequency acoustic backscatter, suspended sediment profiles

ABSTRACT

Recently, an Aquatec AQUA*scat* 1000 multiple frequency acoustic backscatter suspended sediment profiler was deployed from 10 October 2006 to 29 November 2006 and from 4 December 2006 to 18 January 2007, at Sea Palling in Norfolk, on the North Sea coast, as part of the LEACOAST2 EPSRC shore parallel breakwater study. The objective of the study is to evaluate the effects of shore parallel breakwaters in tidal environments on coastal morphology. The instrument deployments are intended to provide validation and calibration data for new numerical process models. Sediment traps and two other acoustic backscatter instruments were also deployed to obtain site samples and comparative data.

The AQUA*scat* 1000 and two further acoustic backscatter systems built by Proudman Oceanographic Laboratory (POL) were each deployed on the sea bed on multi-instrument tripod frames in the locations shown in Figure 1.

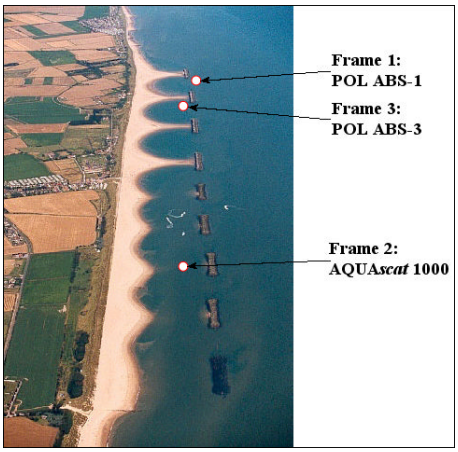

Figure 1. Positions of ABS systems.

Acoustic backscatter principles

Young et al. (1982) and Hay (1983) first described monitoring instruments that measured acoustic backscatter from suspended sediment, and Libicki et al. (1989) developed a detailed theoretical approach for the interpretation of acoustic backscatter data from a single frequency device. The technique involves transmitting a pulse of high frequency, directional, acoustic energy, typically in the range 0.5 to 5 MHz into the suspension, and analyzing the received signal to obtain a time series of scattered signal strength. Knowledge of the sound speed in the water allows the data to be converted into a profile of signal intensity versus range from the transmitting element. Scattered signal strength is related to the amount of material in suspension, and there has been considerable research effort to describe this relationship and thus to derive suspended load from backscatter strength.

In a series of theoretical studies of backscatter characteristics from suspended glass spheres, Thorne et al. (1993) developed a general form function for a suspension of regular shaped scatterers, which was tested against laboratory experiments. The form function describes the backscattering characteristics of the scatterers as a function of incident frequency and mean particle radius. Later work by Thorne et al. (1995) on irregularly shaped scatterers showed the general principles applied to regularly shaped scatterers with moderate size distribution is similar to a first order approximation to that of irregularly shaped scatterers, such as would be found in marine sediment. Thorne and Hanes (2002) summarized the relationship between a measured backscatter signal P and mass concentration M as follows:

$$M = \left(\frac{Pr\psi}{K_s K_t} \right)^2 \cdot e^{4r\alpha} \qquad (1)$$

where r is range from the transducer, ψ corrects for the acoustic transducer beam characteristics in the near field, α describes signal attenuation due to the suspended sediment and water absorption, K_t is a system constant, derived during calibration, and K_s is given by:

$$K_s = \left(\frac{F_m}{\sqrt{a_s \rho_s}} \right) \tag{2}$$

where F_m is the sediment form function, a_s is the mean sediment radius and ρ_s is the sediment density. Hay and Sheng (1992) described and tested a method of particle size determination using multi-frequency acoustic backscatter. The principle is to use the dependence of the backscatter form function for suspended particles with $k\,a_s$, where k is the wave number equal to $2\pi f/c$, and c is speed of sound. Using frequencies of 1 MHz, 2.25 MHz and 5 MHz, Hay and Sheng were able to estimate particle sizes in the range 50 µm to 170 µm to between 10% and 20%. They also noted that once the relative sensitivities of the three frequencies had been established, the calibration of the system was site independent.

AQUA*scat* 1000 acoustic backscatter instrument

In 1992, Aquatec manufactured a data acquisition system for a three frequency acoustic backscatter probe, similar to that described in Pearson and Thomas (1991). Over the coming decade they continued to manufacture various research instruments based on these principles for institutions studying bottom boundary layer processes around the world. In 2001, when the original technology became obsolete, Aquatec designed a new instrument using the latest available techniques, and the first AQUA*scat* was produced. The AQUA*scat* 1000, launched in 2006 is the latest evolution of the technology. The instrument is controlled by a digital signal processor (DSP), which also carries out signal processing and analysis. A programmable logic array is used for high frequency signal generation and filtering. Up to four transducers are driven through a multiplexer from amplified, digitally generated signals. The same transducers are used to receive the backscattered response, which is amplified using a linear amplifier with programmable gain and high speed, broadband data acquisition. The digitized signal is then mixed digitally down to I and Q components in the bandwidth of interest – for example 75 kHz for approximately 1 cm spatial sampling with a nominal 1500 m s^{-1} speed of sound. This approach to signal acquisition and processing results in both a stable, measurable gain and low noise, both of which aid in calibration. Data are stored on Compact Flash, and may be accessed at the end of a deployment or in real time by high speed USB communications.

A typical instrument is pictured in Figure 2. All the electronics described above, and a battery pack for short deployments, are incorporated within the 1000 m depth rated aluminum housing. The instrument shown includes four narrow-beam acoustic transducers at frequencies between 0.5 MHz and 5 MHz, all arranged close to the instrument axis – unlike Doppler current profilers, which have divergent beams. This means that all transducers observe the same volume of water. The configuration used in the deployment described in this paper allows the transducers to be connected to the main instrument via individual cables, so they may be arranged in any orientation, and for this deployment they were arranged facing vertically down towards the bed.

Calibration

The key to successful use of acoustic backscatter for measurement of suspended sediment is an effective method of calibration. During the developmental stages of this type of instrument, there has been a strong emphasis on building calibration tanks that have a homogeneous suspension over a relatively long depth profile. Such tanks have been described by Thorne and Hanes (2002). Aquatec have designed and built a similar sediment tower shown in Figure 3.

Figure 2. AQUA*scat* 1000S instrument.

The tower is 0.4 m diameter and 2.1 m deep, with a conical bottom to prevent deposition of sediment. The sediment suspension is pumped from the bottom and re-injected at two elevations. A mechanical stirrer is used to ensure mixing at the injection points. Calibrations were carried out with suspensions of glass spheres at a quarter phi size interval. Typically calibrations were carried out at three sizes for each of the instrument's frequencies.

Figure 3. Sediment tower.

The purpose of calibration is to establish the system constant K_t described in Equation (1) for each of the instrument's transducers (Betteridge et al., 2008). This is achieved by taking 10,000 samples of vertical backscatter profile in the sediment tower to minimize the effects of acoustic scattering variability. Pump samples were taken at a 0.6 m to establish actual concentration. The plots in Figure 4 illustrate the stages in the calibration process.

In Figure 4a, measured signals are corrected for the effects of spreading loss and attenuation that are a function of range from the transducer. The apparent increase of signal with range on the 4 MHz trace occurs when the recorded signal drops to the system noise floor. In Figure 4b, K_t is calculated assuming the tank has a constant mass concentration based on the pump samples. The 4 MHz value steps to zero near 1.4 m range as values beyond this range have been discarded because the recorded signal value was too low. In Figure 4c, using the frequency least affected by sediment-related attenuation (in this case the blue 1 MHz trace) the actual concentration profile is calculated. In Figure 4d, K_t is recalculated for each frequency using the actual concentration profile.

Results

The AQUA*scat* 1000 was configured with fixed gain. It records to 16-bit digital resolution and has an operational range of approximately 80 dB. The system worked at 1.0 MHz, 2.0 MHz and 4.0 MHz, with a pulse repetition frequency of 128 Hz, averaged internally over 32 profiles to give 4 Hz stored profiles, with 0.01 m range bins over a range of 1.28 m. Each burst contained 5280 profiles (22 minutes of data) and from these profiles the mean linear voltage averaged over the burst has been calculated.

For the analyses presented in this paper, mean particle size has been determined from sediment traps from earlier deployments and from the convergence of acoustic concentrations at the three frequencies. Because no independent suspended sediment samples were obtained, then for consistency, the same d_{50} of 300 µm was used for the analysis of the ABS data on each of the three instruments. The linearized voltages were used with the previously measured K_t to obtain suspended sediment concentration profiles at each of the three frequencies. A similar process was applied to the POL ABS instruments. Figure 5 overleaf shows on the left a time series of calculated suspended sediment concentration at a single elevation of 0.075 m above the bed for each of the three instruments (blue line) with the standard deviation (green line) derived from the three frequencies used. The use of acoustics allows accurate detection of the bed so that concentration can be measured relative to the bed position.

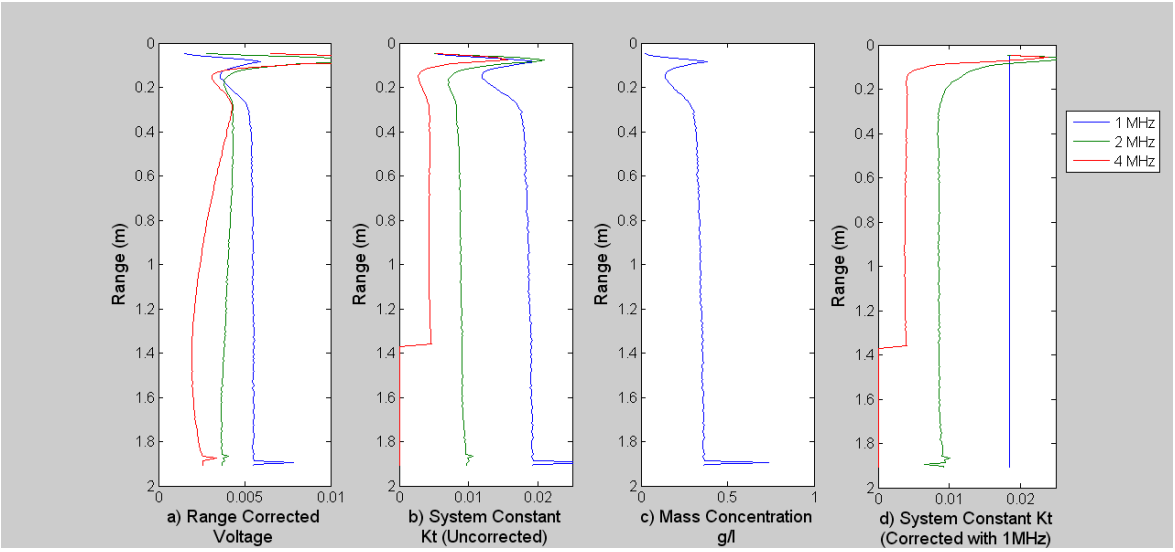

Figure 4. Calibration process.

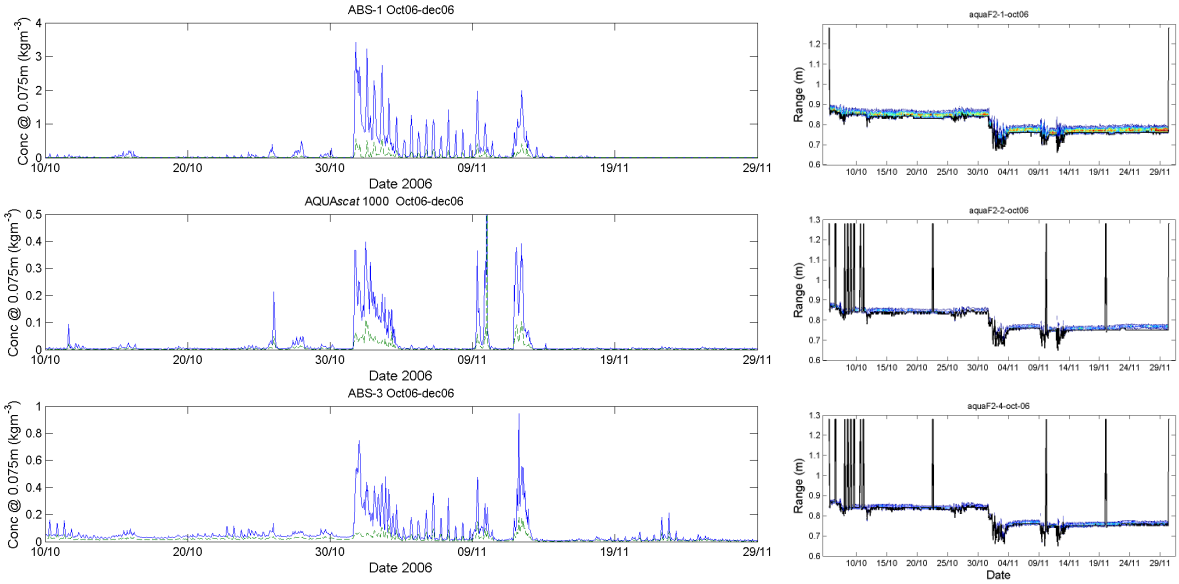

Figure 5. Left: suspended sediment concentration at 0.075 m above the bed for POL ABS-1 on frame 1, the AQUAscat 1000 ABS on frame 2 and POL ABS-3 on frame 3. Right: bed range from each AQUAscat transducer.

Discussion and further work

In the results presented here, we have carried out acoustic backscatter inversions using an assumed mean particle size based on knowledge from previous physical measurements. The AQUA*scat* 1000 was shown to function without problems throughout the deployment, and has recorded data that has similar temporal characteristics to acoustic data recorded elsewhere at the site. Acoustic detection of the moving bed position means that suspension profiles can be related to elevation above the bed. This initial analysis allows us to identify areas of particular interest, which can then be selected for a full multi-frequency inversion, which will provide a more detailed description of particle size distribution.

References

Aquatec Group Limited (2006), *AQUAscat 1000 Acoustic Backscatter System Data Sheet*, URL: www.aquatecgroup.com/download/datasheet/aquascat/AQUAscat1000.pdf.

Betteridge, K.F.E., Thorne, P.D., Cooke, R.D. (2008), Calibrating multi-frequency acoustic backscatter systems for studying near-bed suspended sediment transport processes, *Continental Shelf Research*, 28, 227–235.

Hay, A.E. (1983), On the remote acoustic detection of suspended sediment at long wavelengths, *Journal of Geophysical Research*, 88(C12), 7525–7542.

Hay, A.E., Sheng, J. (1992), Vertical profiles of suspended sand concentration and size from multifrequency acoustic backscatter, *Journal of Geophysical Research*, 97(C10), 15661–15677.

Libicki, C., Bedford, K.W., Lynch, J.F. (1989), The interpretation and evaluation of a 3-MHz acoustic backscatter device for measuring benthic boundary layer sediment dynamics, *Journal of the Acoustical Society of America*, 85(4), 1501–1511.

Moate B.D., Thorne. P.D., Cooke R.D., Betteridge, K.F.E. (2007), POL ABS calibrations 2005–2007. Proudman Oceanographic Laboratory Internal Report No. 183, July 2007. 36pp.

Pearson, N.D., Thomas, M.R. (1991), An instrument to measure seabed boundary-layer processes, *IEEE Journal of Oceanic Engineering*, 16(4), 338–342.

Smerdon, A.M., Caine, S.J. (2007), A commercial multi-frequency acoustic backscatter instrument for profiling of suspended sediment size distribution and load.

Thorne, P.D., Hardcastle, P.J., Soulsby, R.L. (1993), Analysis of acoustic measurements of suspended sediments, *Journal of Geophysical Research*, 98(C1), 899–910.

Thorne, P.D., Hanes, D.M. (2002), A review of acoustic measurement of small-scale sediment processes, *Continental Shelf Research*, 22, 603–632.

Thorne, P.D., Waters, K.R., Brudner, T.J. (1995), Acoustic measurements of scattering by objects of irregular shape, *Journal of the Acoustical Society of America*, 97(1), 242–251.

Young, R.A., Merrill, J.T., Clarke, T.L., Proni, J.R. (1982), Acoustic profiling of suspended sediments in the marine bottom boundary layer, *Geophysical Research Letters*, 9(3), 175–188.

Measurements of sediment diffusivity profiles over rippled beds under waves

PETER D. THORNE[1], ALAN G. DAVIES[2], PAUL S. BELL[1]

1. Proudman Oceanographic Laboratory, 6 Brownlow Street, Liverpool L3 5DA UK
email: pdt@pol.ac.uk, psb@pol.ac.uk

2. School of Ocean Sciences, College of Natural Science, Bangor University, Menai Bridge, Anglesey LL59 5AB UK
email: a.g.davies@bangor.ac.uk

Keywords: acoustics, diffusivity, suspensions, waves, ripples

ABSTRACT

Predictions for the form of suspended sediment concentration profiles differ according to the flow, the seabed sediment and, importantly, the bed forms. Most of the formulations used are underpinned by the classical Fickian concept of gradient diffusion originating from kinetic molecular theory, where random molecular movements induce mixing. In the case of suspended sediments in field situations, it is the turbulent fluctuations in the vertical velocity component that give rise to the upward mixing process. In the simplest case the time averaged vertical turbulent diffusion of sediment, q_v, is considered to be balanced by the settling of the suspended sediment under gravity, such that:

$$q_v = w_s C \qquad \text{where} \qquad q_v = -\varepsilon_s \frac{\partial C}{\partial z} \ . \tag{1}$$

Here C is the time-averaged sediment concentration at height z above the bed, w_s is the sediment settling velocity, and ε_s is the sediment diffusivity. The vertical profile of ε_s is frequently linked to the eddy viscosity, ν_t, used to model the transfer of momentum by turbulent eddies. The eddy viscosity, ν_t, here represents the product of a turbulent velocity scale and a mixing length scale. Both of these factors therefore affect the sediment diffusivity which is commonly expressed as $\varepsilon_s = \beta\nu_t$ where the coefficient β is either assumed to be a constant, or is sometimes considered to have a functional dependence upon the sediment in suspension and the flow parameters. Hitherto, there has been no consensus on a general form for profiles of the sediment diffusivity or eddy viscosity, though constant and linear profiles with height above the bed, have been used in many near-bed sediment studies.

Despite the wide use of gradient diffusion, several studies (Sleath, 1982; Ribberink and Al-Salem, 1994; Osborne and Vincent, 1992; Fredsøe et al., 1999; Thorne et al., 2003) have indicated that this is not always the dominant process generating the suspended sediment concentration profile, particularly for sediment entrainment by waves over rippled beds. These studies have shown that, if the ripples are relatively steep with $\eta_r/\lambda_r \geq 0.12$ where η_r is the ripple height and λ_r is the ripple wavelength, then the mixing close to the bed is dominated by a coherent process involving boundary layer separation, on the lee-side of the ripple crest, during each wave half-cycle near maximum flow velocity. The resulting lee-wake vortex remains attached to the bed entraining sediment into the flow as it grows in size and strength. At flow reversal the sediment-laden vortex is ejected into the water column, carrying sediment to several ripple heights above the bed. This process is coherent and repeatable, with two main periods of sediment entrainment during the cycle at around the times of flow reversal. This sediment mixing process is thus fundamentally different from that associated with gradient diffusion.

The present study represents a contribution towards our understanding of these fundamental mixing processes. There are relatively few measurements of near-bed sediment diffusivity profiles collected at full scale in the marine environment and even less where the form of the diffusivity profile has been related to detailed sediment entrainment processes. Here we present results of acoustic measurements of near-bed diffusivity profiles. The measurements were made in the Deltaflume of Deltares, which allowed sediment processes to be studied at full scale. The experiments were conducted beneath weakly-asymmetrical, regular, surface waves with heights, H, and periods, T, in the respective ranges H = 0.6–1.1 m and T =4–6 s for the medium sand and H = 0.5–1.1 m and T = 4–5 s for the fine sand. The medium sand had d_{50} = 330 μm, while

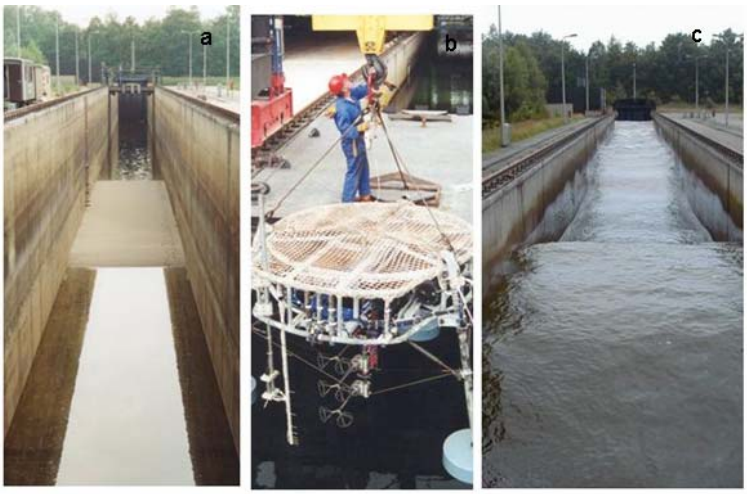

Figure 1. (a) Photograph of the Deltaflume showing the sand bed at approximately midway along the flume and the wave generator at the far end of the flume. (b) The instrumented tripod platform, STABLE, used to make the measurements. (c) A surface wave propagating along the flume.

the fine sand had, d_{50} = 160 μm. The sediments were located in a layer of thickness 0.5 m and length 30 m, approximately halfway along the flume, where the mean water depth was 4.5 m.

The main instrument platform used was STABLE-Sediment Transport And Boundary Layer Equipment (Figure 1b), the systems relevant to the present study were: a multi-frequency acoustic backscatter system, ABS, a pumped sampling system, an acoustic ripple profiler, ARP, and electromagnetic current meters, ECMs. All electronic measurements were synchronized. Typically an experiment consisted of propagating waves over the bed for about an hour, until the bed-forms came to nominal equilibrium, and then collecting data for a 17-min period. High-resolution vertical profiles of the suspended sediments were measured using a triple-frequency ABS The ABS provided 128 backscatter profiles each second, at each of the three frequencies, 1 MHz, 2 MHz and 4 MHz, with a spatial resolution of 0.01 m over a height of 128 range bins (1.28 m). Physical samples of the suspension were obtained by pumping through nozzles located at ten heights above the bed between 0.053–1.55 m. The collected samples of the suspension were sieved to provide the mass size distribution with height above the bed. These were used to calibrate and assess the veracity of the backscatter measurements and provide profiles of w_s. To establish whether ripples were present on the bed, and to monitor their evolution and migration, a specifically designed acoustic ripple profiler, ARP, was used. The ARP operated at 2.0 MHz, and provided sub-centimeter measurements of the bed location over a 3 m transect along the direction of wave propagation. To measure the flow three ECMs were located at 0.3, 0.6 and 0.91 m above the bed. They provided measurements of the along-flume and vertical components of the flow velocity at 8 Hz.

Measurements of the suspended concentration were collected with the ABS over a 17-min period and averaged to give mean concentration profiles. For each experiment three independent concentration profiles were obtained, one for each frequency. Since 13 experiments were carried out above the medium sand and seven were carried out above the fine sand, this resulted in 39 and 21 mean concentration profiles in the respective cases. Using the bed echoes the concentration profiles were referenced to the undisturbed bed, such that in the plots that follow z is the height above the undisturbed bed, with a vertical sampling interval of 0.01 m. Using the mean concentration profiles, the sediment diffusivities ε_s were calculated for each experiment, with w_s determined from a d_{50}s particle size profile fitted to the pumped sample data:

$$\varepsilon_s = \frac{-\frac{w_{sj}+w_{sk}}{2}\frac{C_j+C_k}{2}}{\frac{(C_k-C_j)}{\Delta_{jk}}} \tag{2a}$$

$$z = \frac{z_j + z_k}{2} \tag{2b}$$

where Δ_{jk} was the separation between range bins j and k. For the near-bed layer 0.01–0.21 m above the bed, j and k were taken as adjacent range bins while, between 0.21–0.43 m, j and k were defined as two range bins apart and, above 0.43 m, as four range bins apart. This increase in the separation of j and k with height above the bed smoothed the derivative of the concentration profile and reduced the scatter in ε_s.

The resulting sediment diffusivity profiles were normalized using (3), namely:

$$z / k_s \qquad \varepsilon_s / U_o k_s \ . \tag{3}$$

These normalizations are based on the expressions for sediment diffusivity used by Nielsen (1992) and Van Rijn (1993). The equivalent bed roughness has been taken in (3) as $k_s = 25\eta_r(\eta_r/\lambda_r)$ and U_o is the wave orbital velocity amplitude at the bed. The normalized diffusivity profiles were averaged to give a mean result for all experiments. For the medium sand the result is shown in Figure 2a. The form of ε_s was found to be constant with height up to a level equal to approximately $1.3k_s$; above this ε_s increased linearly with height. For the case of the fine sand the result is shown in Figure 2b. For this case it can be seen that there was no constant ε_s region; here ε_s simply increased linearly with height above the bed. The solid lines in the figures are empirical fits to the data.

To explain the difference in the respective ε_s profiles, advantage has been taken of the high temporal-spatial resolution available with acoustic systems. Using intra-wave ensemble averaging, detailed images have been built up of the variation in concentration with both the phase of the wave and also height above the bed.

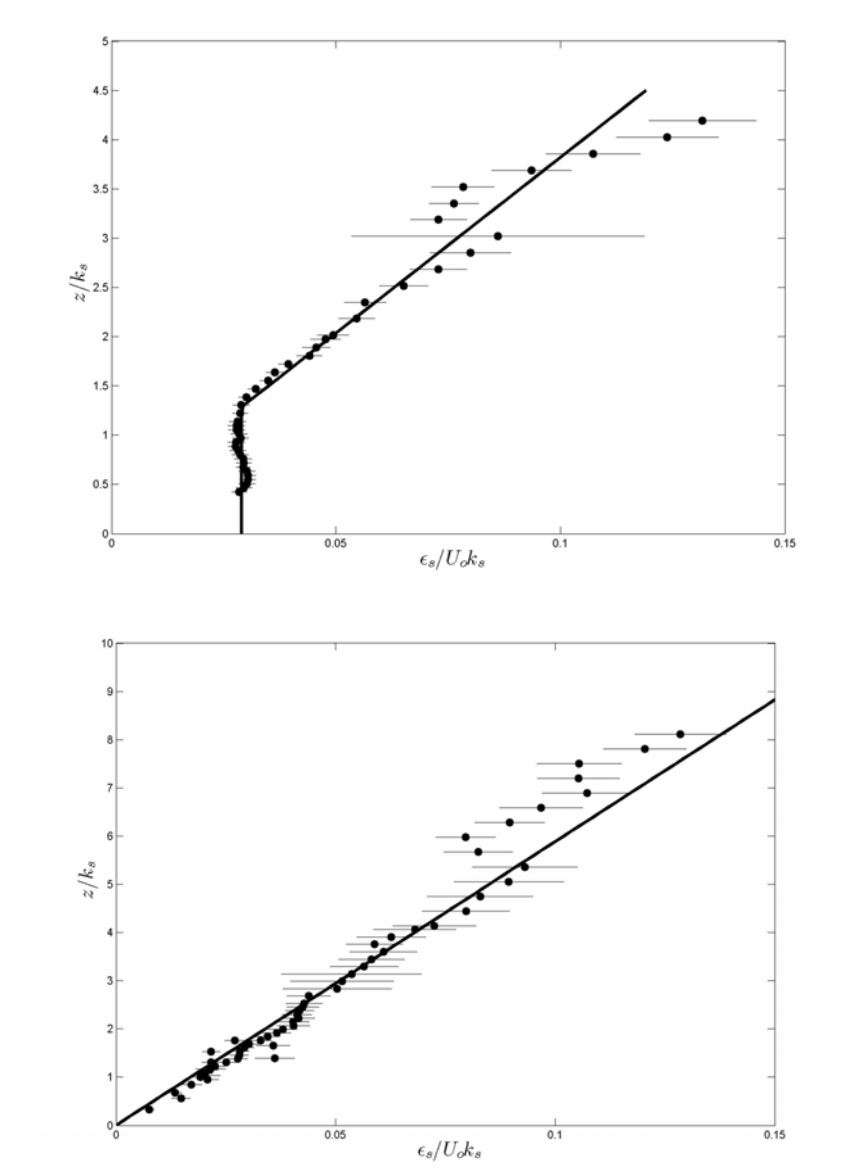

Figure 2. Measured normalised sediment diffusivity (●) over a) medium sand bed and b) fine sand bed.

These intra-wave observations, combined with measurements of the bedforms, have been used to reveal the mechanisms of suspended sediment entrainment in the respective cases (for the medium sand case, see Davies and Thorne, 2005). The poster details the underlying processes that lead to the results shown in Figure 2 and considers the implications of these processes for large scale modeling of sediment transport over rippled beds.

References

Davies A.G., Thorne P.D. (2005), Modelling and measurement of sediment transport by waves in the vortex ripple regime, *Journal of Geophysical Research*, 110, C05017, doi:10.1029/2004JC002468.

Fredsoe, J., Andersen, K.H., Sumer, B.M. (1999), Wave plus current over a ripple-covered bed, *Coastal Engineering*, 38(4), 177–221.

Nielsen, P. (1992), *Coastal Bottom Boundary Layers and Sediment Transport*. Advanced series on ocean engineering, Vol. 4, World Scientific, Singapore, 324pp.

Osborne, P D., Vincent, C.E. (1996), Vertical and horizontal structure in suspended sand concentrations and wave induced fluxes over bedforms, *Marine Geology*, 131, 195–208.

Ribberink, J.S., Al-Salem, A.A. (1994), Sediment transport in oscillatory boundary layers in cases of rippled beds and sheet flow, *Journal of Geophysical Research*, 99(C6), 12707–12727.

van Rijn, L.C. (1993), *Principles of sediment transport in rivers, estuaries and coastal seas*. Aqua publications, Netherlands. 633pp.

Sleath J.F.A. (1982), The suspension of sand by waves, *Journal of Hydraulic Research*, 20(5), 439–452.

Thorne P.D., Davies, A.G., Williams, J.J. (2003), Measurements of near-bed intra-wave sediment entrainment above vortex ripples, *Geophysical Research Letters*, 30(20), 2028, doi:1029/2003GL018427.

Experimental verification of acoustic Doppler velocimeter (ADV®) performance in fine-grained, high sediment concentration fluids

DAVID W. VELASCO, CRAIG A. HUHTA

SonTek/YSI, 9940 Summers Ridge Road, San Diego CA 92121-2997, USA
email: dvelasco@sontek.com, chuhta@sontek.com

Keywords: ADV, fluid mud, experimental verification, acoustic performance

ABSTRACT

Since its introduction in the early 1990s, the acoustic Doppler velocimeter (ADV®) has become a standard tool for accurate single-point velocity measurements in support of a variety of applications, from hydraulics research to benthic boundary layer studies (Voulgaris and Trowbridge, 1998; Lane et al., 1998; Chang and Hanes, 2004; Trevethan et al., 2006). One area it has been used is fine-grained sedimentation and transport studies in the laboratory and in the field (Fugate and Friedrichs, 2002; McCool and Parsons, 2004). Despite its widespread use, two questions still remain unanswered concerning the performance of the acoustic Doppler velocimeter: 1) Do ADVs work in high concentration fluids (e.g., 1–100+ g l^{-1}, i.e., fluid mud)? 2) If so, up to what concentration will they work? So far, the prevailing answers to these questions are: 1) 'sometimes', and 2) 'high'. No specific answers have ever been provided due to the complexities in determining these limitations, such as: the difficulty in keeping such concentrations in suspension in a controlled environment; the fundamental need to use an instrument employing a different technology as a reference; and, the difference in acoustic response generated by the sediment type and flocculation status. This study evaluates ADV performance in a range of fluid mud concentrations through an experimental approach that does not seek to compare the ADV response to known velocities or other instruments, but rather through proxy data quality parameters, two of which automatically collected by the ADV. Natural and synthetic fine-grained sediments are used as scatterers to produce concentrations in the fluid mud range.

Preliminary test

As a proof of concept for this study, a preliminary test was conducted with a 5 MHz SonTek ADVOcean system, which is best suited for high concentration fluids given its relatively low carrier frequency. Using synthetic particles (glass oxide spheres; on the order of 8 µm diameter; uniformly distributed), a suspension of approximately 100 g l^{-1} was created and placed in a 20-liter tank. The particles were kept in suspension by continuously stirring with a paddle. The ADVOcean was placed such that its sampling volume was close to the center of the tank. Five short data bursts were collected at 10 Hz for at least one full minute, and velocity, signal amplitude and correlation values recorded. During the first data run, the solution was continuously diluted to about 50% of original concentration, while data was being collected, in an attempt to capture the incipient change in the ADV's data. For subsequent runs, the solution was diluted between data runs to about 50% of the previous run's concentration.

Prior to each data run a signal amplitude profile, commonly referred to as BeamCheck, was collected for each beam. Sample BeamCheck data is shown on Figure 1 for the initial concentration, plus two subsequent dilutions. All three beams showed great agreement and so were averaged together. Actual concentrations were not determined for the dilutions, but sufficient particles remained in the fluid throughout all dilutions to return optimal acoustic scattering conditions; that is, the fluid was never excessively diluted such that no acoustic scattering could take place. As expected, the initial concentration nearly completely attenuated the acoustic pulse such that a sampling volume peak could not be easily identified in that BeamCheck (solid file in Figure 1). Signal attenuation is also believed to have caused a shift in the sampling volume peak location.

Signal amplitude, correlation and velocity data for the first (~100 g l^{-1}) and fourth (~10 g l^{-1}) runs are shown on Figures 2 and 3. As anticipated, the signal amplitude values for both runs show high values, with the larger concentration fluid acting to absorb the acoustic pulse and thus return relatively lower amplitudes. Signal correlation values for the first run show values well below the recommended 70-80% threshold, but show a small increase as the fluid is diluted. Consequently, velocity values for the first run start unrealistically high but do show a noticeable decrease with dilution. This suggests concentrations of perhaps

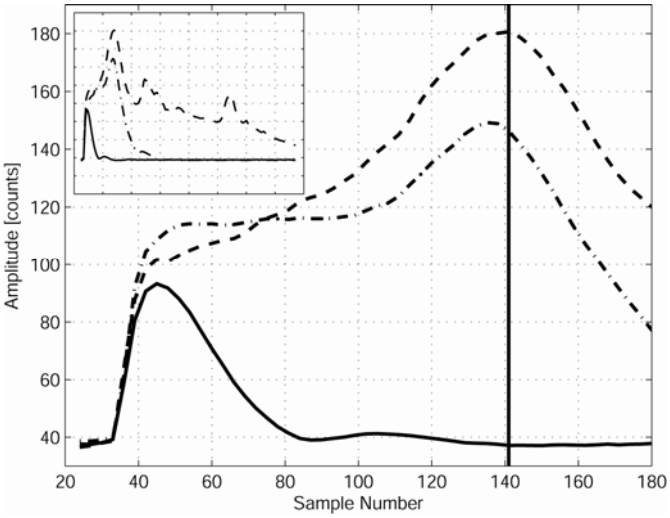

Figure 1. Signal amplitude profiles (BeamCheck) from a 5 MHz SonTek ADVOcean at three concentrations. Solid line is ~100 g l^{-1}, dash-dotted line is ~40–50 g l^{-1}, and dashed line is ~10 g l^{-1}. Inset shows profile to its full extent. Each sample corresponds to approximately 14 mm of distance. Peak locations for each concentration are 141, 135 and 105 samples. Vertical line represents peak location (141 samples) under optimal scattering conditions.

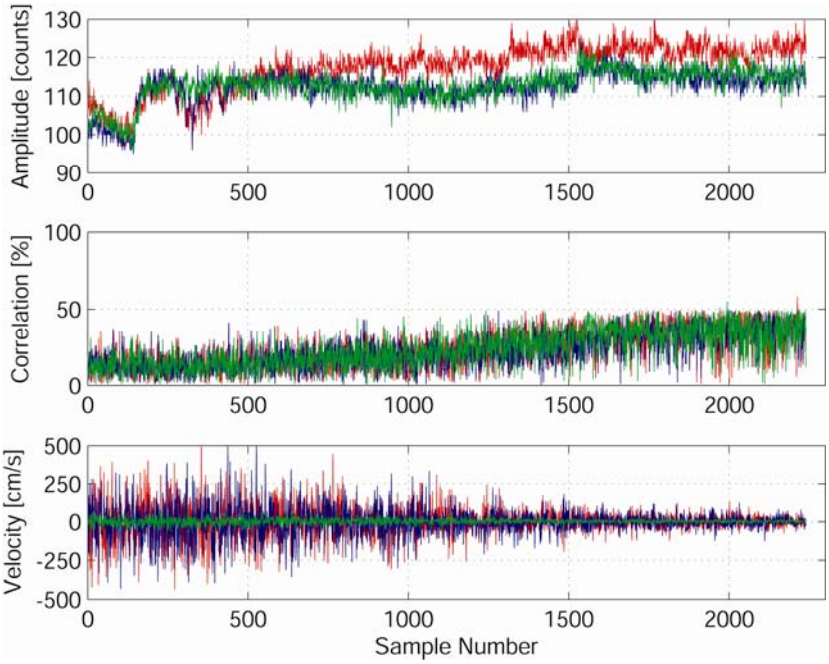

Figure 2. Signal amplitude, correlation and velocity for first test run (~100 g l^{-1}).

>50 g l^{-1} can be successfully measured by the ADVOcean. Data from Figure 3 (fourth run, ~10 g l^{-1}) show near flawless data, with strong and steady signal amplitude values and > 98% correlation values. Velocity data are as expected for the test conditions.

Scope of work

The three data quality parameters mentioned above (BeamCheck, signal amplitude and correlation) are used in this study to evaluate the quality of ADV data across three carrier frequencies: 16, 10 and 5 MHz. Analysis of these data is used to determine relative concentration values (and respective velocity ranges) within which the ADV will reliably measure velocity. An empirical approach is used to model the ADV's response at given concentrations and so define guidelines for evaluating the quality of velocity data from fine-grained, high concentration fluids.

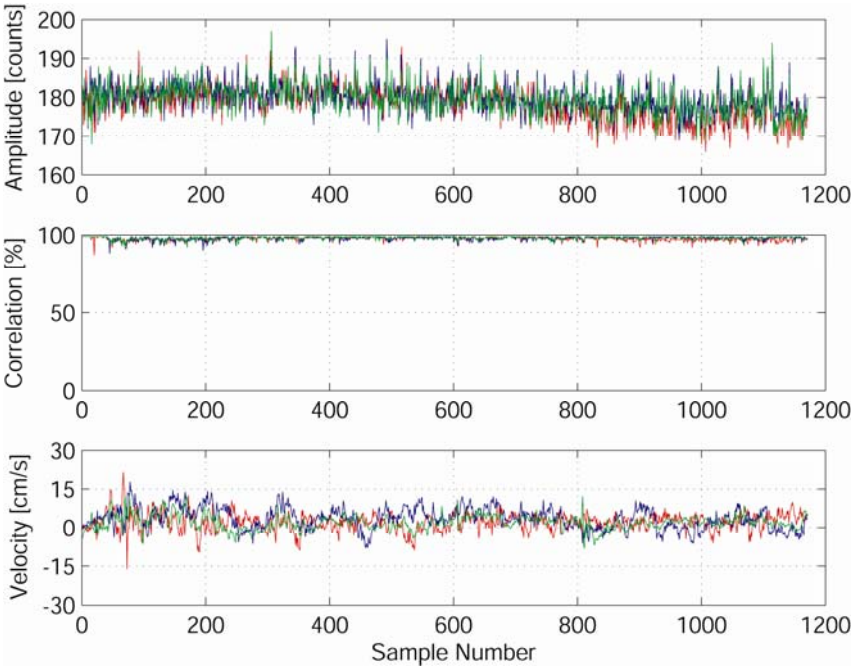

Figure 3. Signal amplitude, correlation and velocity for fourth test run (~10 g l^{-1}).

References

Chang, Y.S., Hanes, D.M. (2004), Suspended sediment and hydrodynamics above mildly sloped long wave ripples, *Journal of Geophysical Research*, 109, C07022, doi: 10.1029/2003JC001900.

Fugate, D.C., Friedrichs, C.T. (2002), Determining concentration and fall velocity of estuarine particle populations using ADV, OBS and LISST, *Continental Shelf Research*, 22, 1867–1886.

Lane, S.N., Biron, P.M., Bradbrook, K.F., Butler, J.B., Chandler, J.H., Crowell, M.D., McLelland, S.J., Richards, K., SandRoy, A.G. (1998), Three-dimensional measurements of river channel topography and flow processes using acoustic Doppler velocimetry, *Earth Surface Processes and Landforms*, 23, 1247–1267.

McCool, W.W., Parsons, J.D. (2004), Sedimentation from buoyant fine-grained suspensions, *Continental Shelf Research*, 24, 1129–1142.

Trevethan, M., Chanson, H., Brown, R. (2006), *Two series of detailed turbulence measurements in small subtropical estuarine system*. Report No. CH 58/06, Division of Civil Engineering, The University of Queensland, ISBN 1864998520.

Voulgaris, G., Trowbridge, J.H. (1998), Evaluation of the acoustic Doppler velocimeter (ADV) for turbulence measurements, *Journal of Atmospheric and Oceanic Technology*, 15, 272–289.

Wave generated lutoclines offshore of Cassino Beach, Brazil

SUSANA B. VINZON, SAULO MEIRELLES, THIAGO LEÃO

Coastal and Oceanographic Engineering Area, Ocean Engineering Program/COPPE,
Federal University of Rio de Janeiro, Brazil
email: susana@peno.coppe.ufrj.br, smrocha@peno.coppe.ufrj.br, zleao@email.com

Keywords: lutocline height, wave attenuation, muddy bottom

ABSTRACT

Offshore Cassino Beach, Southern Brazil, a mud deposits is observed, mainly originated from the sediments flushed from the adjacent Patos Lagoon. Episodically, and associated with storm waves able to transport the mud from offshore to the beach, the usual sandy beach is covered by mud. This is a unique process along the Brazilian coastline.

In order to determine fluid mud properties such as density, and thickness and extension of the mud layer, a short cruise was carried out in April 2008. Waves and density profile, using both cores and Densitune probe, were measured in several stations along an across-shelf transect off Cassino Beach, Southern Brazil. The data is compared with results obtained by applying a lutocline height equation, derived by Vinzon and Mehta, 1998, where the lutocline height is a function of wave and suspended sediment properties. The interplay between waves and lutocline is addressed, showing a strong coupling through the wave damping.

Introduction

The action of water waves over a soft marine mud bottom can elevate the mud-water interface to a level that depends on the balance between both mechanical energy imparted to raise the potential energy of the suspension and the negative buoyancy of the suspension beneath the interface. On the other hand, this lutocline plays an important role in the wave damping, creating a feed back relationship.

A mud deposit is observed offshore Cassino Beach, Southern Brazil (Figure 1). This deposit is mainly originated from the fine sediments flushed from the adjacent Patos Lagoon, driven by meteorological tides (Vinzon et al., in press). The mud, located between the 6 m and 15 m isobaths, migrates episodically from offshore to the beach, associated with storm waves. In these situations, the typical sandy beach is covered with a substantial amount of mud (Figure 2). This is a unique process along the Brazilian coastline (Calliari et al., 2000) meaning a risk for tourism and fauna.

Fluid mud represents a considerable management problem in rivers, lakes, estuaries, and shelves by impeding navigation, reducing water quality and damaging equipment. According to McAnally et al. (2007), large difficulties are found, at the current state-of-art concerning fluid mud processes and management, in understanding, but also detecting, measuring and sampling the fluid mud layers.

The present study aimed to obtain simultaneous measures of the suspended sediment profile and waves, detecting the primary lutocline height induced by waves, and the wave characteristics, in order to contribute to the understanding in the interplay between waves and mud bottom.

Methodology

Along the transect depicted in Figure 1, in front of Cassino Beach, in situ density profiles and waves were measured. It was used a density measuring probe, DENSITUNE (STEMA Survey Services, 2007), based on the response of a vibrating-fork, provided with a pressure sensor. The probe is dropped from the boat at each station, recording the density profile. In addition, cores were collected at each station in order to compare with densimeter's results.

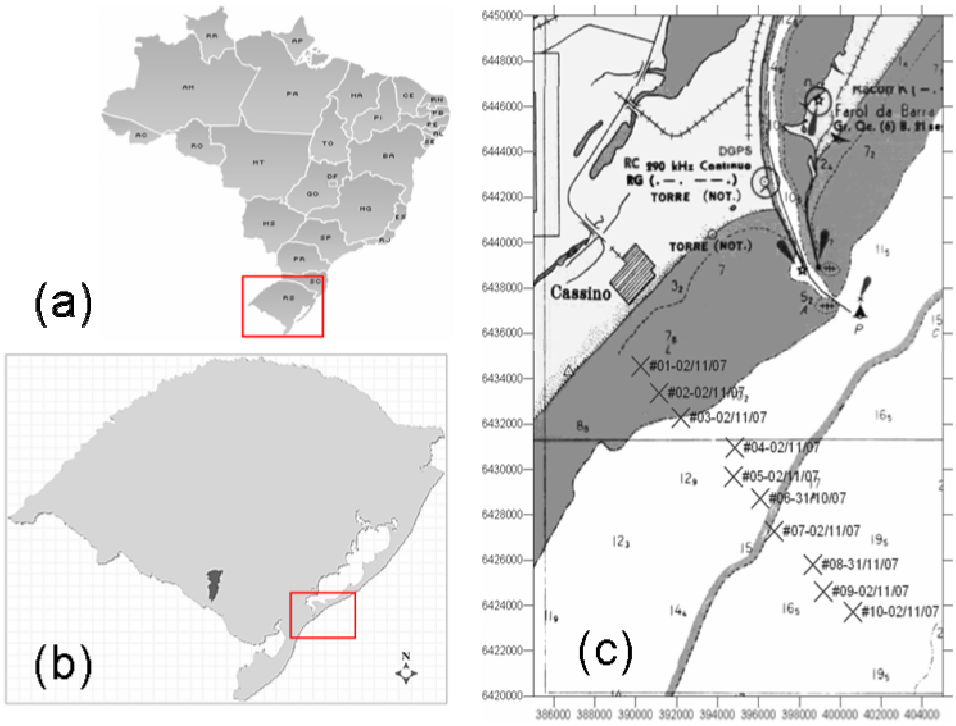

Figure 1. Study area. (a) Brazil map with the location of Rio Grande do Sul State. (b) Location of Cassino Beach in Rio Grande do Sul State (c) Study region showing the stations along the transect (UTM).

Figure 2. Cassino Beach after a storm causing the transport of mud to the shoreface (picture courtesy of Aline Lisniowski).

Table 1. Day of measurement, depth and distance from station #10

Station	Day in April 2008	Depth (m)	Distance from Stn #10 (km)
#005	10	4.5	14.2
#01	9	7.0	13.5
#02	10	8.0	12.0
#03	10	9.0	10.5
#04	10	10.0	9.0
#05	9	11.0	7.5
#06	10	12.5	6.0
#07	9	14.1	4.5
#10	continuous	18.0	0.0

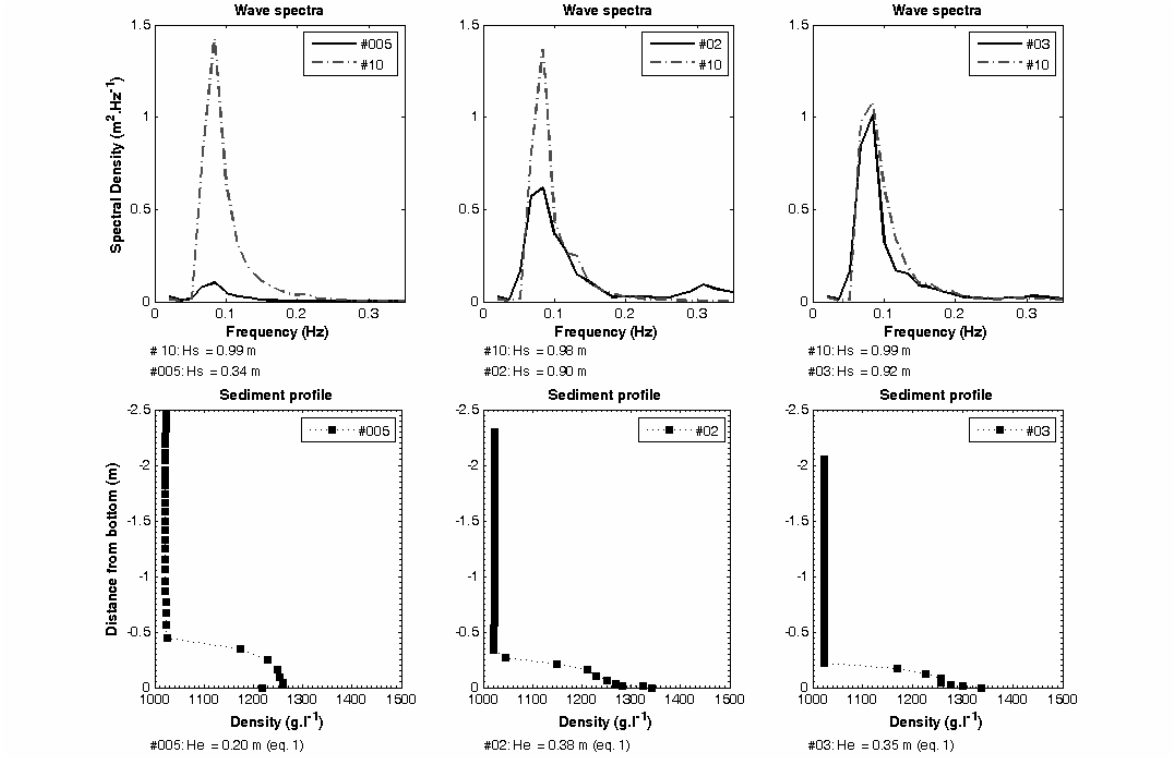

Figure 3. Upper panel: wave spectra for station #10 and stations #005, #02, #03, respectively. Lower panel: Sediment profile for stations #005, #02, #03, respectively. Data collected on April 10, 2008.

Waves were measured continuously during the experiment at the farthermost station (#10), located at a depth of 18m. Moving towards the coast, short record of waves (longer than 17min) at the successive stations were recorded together with the density profiles, and coring in some of the stations. The depth and distance from station #10 of each station are presented in Table 1.

Results

Figure 3 shows the comparison of the wave spectra of the measurements on 11 April 2008, at station #10 (farthermost one) and stations #005, #02 and #03. Shoaling coefficients for the peak period are 1.01, 0.91 and 0.89, respectively, indicating that wave height would increase towards the coast with no dissipation. Thus, wave damping is expressive, reducing almost 40% the wave height from station #02 to #005, distance 2.2 km.

Vinzon and Mehta (1998) proposed the following equation in order to estimate the lutocline height generated by waves for fairly rough boundary layer:

$$H_e = 0.65\left[\frac{(a_b^3 k_r)^{3/2}}{T^3 \dfrac{\rho_s - \rho_w}{\rho_w} g w_s C_v}\right] \tag{1}$$

where a_b is the bottom horizontal wave orbital amplitude, T is the wave period, k_r is the hydraulic roughness, w_s is the settling velocity, C_v is the mean volumetric concentration of solids in suspension, ρ_s is the particle density and ρ_w is the water density. H_e calculated with Equation 1 for the measurements in Figure 3 are also indicated. Figure 4 shows a comparison between the measure lutocline height and the calculated with Equation 1 for all the measurements.

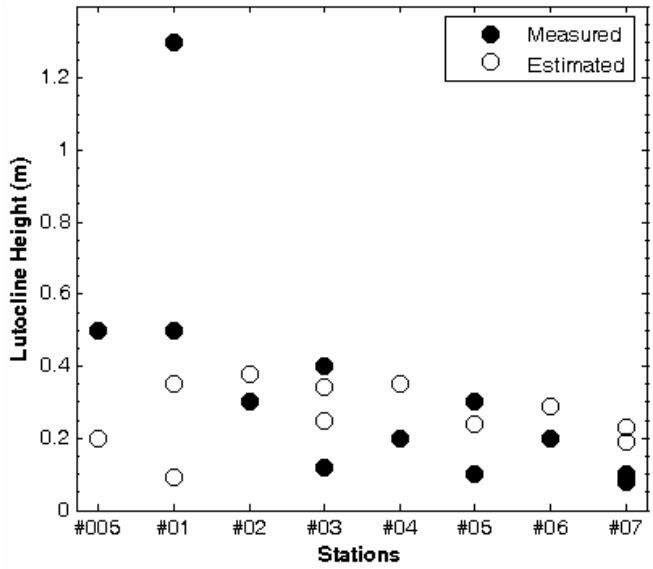

Figure 4. Comparison between measured and estimated (Equation 1) lutocline heights.

Conclusions

It was observed that lutocline height generally increase towards the coast. However, for the only measurement at the shallowest station #005, the lutocline height decreased. There was no measurements on the same day at station #01 to compare. Then is not possible to confirm if this decrease is due to the larger slope at #005, which would prevent the further increase in the lutocline height or if it is due to differences in the mud deposit characteristics.

The estimate of the lutocline heights with equation 1 shows a fairly agreement with the measurements, for the deeper stations, where moderated wave damping is observed. At stations #01 and #005 the lutocline height is underestimated. More investigations are being carried out concerning the basic assumption of Equation 1 regarding the local energy balance and the rough turbulent wave boundary layer.

References

Calliari, L.J., Speranski, N.S., Torronteguy, M, Oliveira, M.B. (2000), The mud banks of Cassino Beach, Southern Brazil: Characteristics, Processes and Effects, *Journal of Coastal Research*, Proceedings of ICS 2000, pp1–9, New Zealand.

McAnally, W.H., Friedrichs, C., Hamilton, D., Hayter, E., Shrestha, P., Rodriguez, H., Sheremet, A., Teeter, A., (2007), Management of fluid mud in estuaries, bays, and lakes, Part 1: Present state of understanding on character and behavior, *Journal of Hydraulic Engineering*, 133, 9–22.

STEMA Survey Services (2007), *DensLog: density acquisition module V4.0, User's Manual*, STEMA Survey Services b.v., Netherlands.

Vinzon, S.B., Mehta, A.J. (1998), A mechanism for the formation of lutoclines by waves, *Journal of Waterway, Port, Coastal, and Ocean Engineering*, ASCE, 124(3), 147–149.

Vinzon, S.B., Winterwerp, J.C., Nogueira, R., de Boer, G. (2008), Mud deposit formation on the open coast of the larger Patos Lagoon – Cassino Beach system, *Continental Shelf Research*. (In press.)

Wave, currents and sediment transport observed during the LEACOAST2 experiment

JUDITH WOLF[1], ALEJANDRO J. SOUZA[1], PAUL S. BELL[1], PETER D. THORNE[1], RICHARD D. COOKE[1], SHUNQI PAN[2]

1. Proudman Oceanographic Laboratory, 6 Brownlow Street, Liverpool L3 5DA UK
email: jaw@pol.ac.uk, ajso@pol.ac.uk, psb@pol.ac.uk, pdt@pol.ac.uk, rdco@pol.ac.uk

2. School of Engineering, University of Plymouth,
Drake Circus, Plymouth PL4 8AA UK
email: shunqi.pan@plymouth.ac.uk

Keywords: waves, currents, sediment transport; southern North Sea

ABSTRACT

The LEACOAST2 project (http://pcwww.liv.ac.uk/civilCRG/leacoast2/) is studying the effect of a shore-parallel breakwater system on the evolution of coastal morphology at Sea Palling on the east coast of England, facing the southern North Sea. Here there are strong tidal currents, and occasional storm wave conditions. The sediments are mixed with their composition ranging from coarse sand to silt supplied from the soft boulder clay cliffs to the north; these sediments are quite mobile under tide and wave stirring. The breakwaters have trapped sand in embayments, with tombolos and salients behind the breakwaters, while some sand bypassing outside the system seems to occur. As part of this project data were collected from three instrumented tripods deployed near the breakwaters, during two field campaigns (March–May 2006 and October 2006–January 2007). The instrumentation includes acoustic and optical instrumentation (ADCP, ADV, LISST and bedform scanners). Observations of waves, currents and bathymetry have also been made using an X-band radar deployed for two years to monitor the whole area over a range of several kilometers. A large dataset has been successfully obtained. Here we present an overview of the observed hydrodynamic conditions, sediment transport and bedforms from this experiment.

Data collection

Figure 1 shows the location of Sea Palling on the Norfolk coast of the southern North Sea with a photograph showing the beach and the reef system, clearly showing the effect of the breakwater system on the coastal morphology in trapping sand in tombolos and salients. The first LEACOAST project focused on the effects of storm events on the beach morphology (Dolphin et al., 2004; Pan et al., 2005). There remain questions about the quantity of sand transported through or bypassing the system and the relative importance of tides and storms in this process. The LEACOAST2 project extends the dataset, supplementing the beach surveys

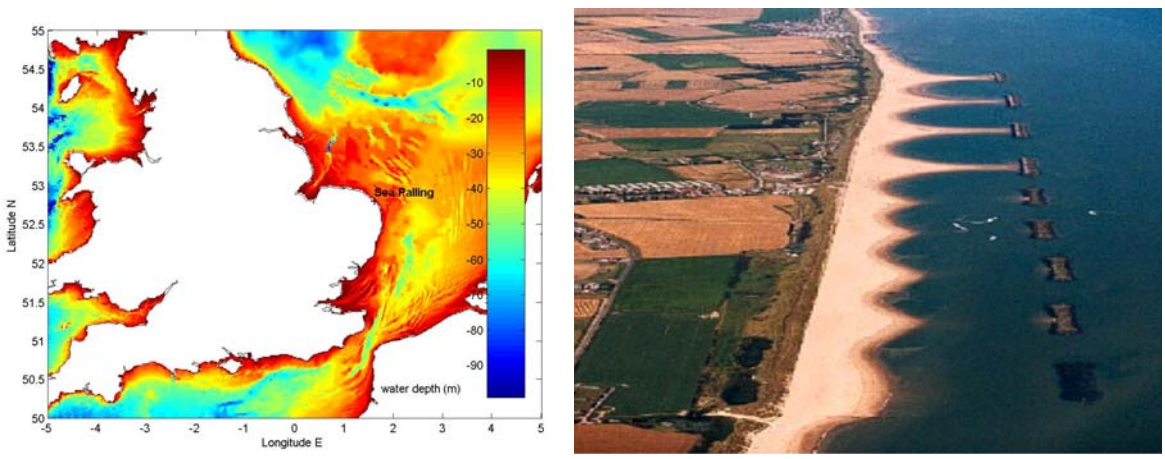

Figure 1. Location of Sea Palling and aerial photo of shore-parallel breakwaters.

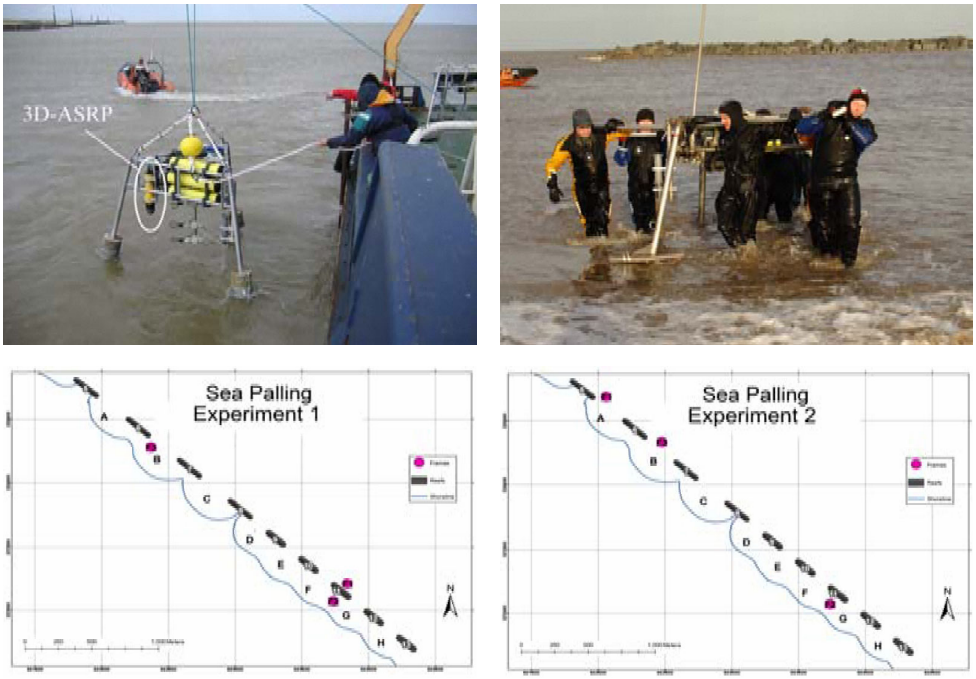

Figure 2. Experiment 1 and Experiment 2 showing locations of in-situ tripods (purple circles).

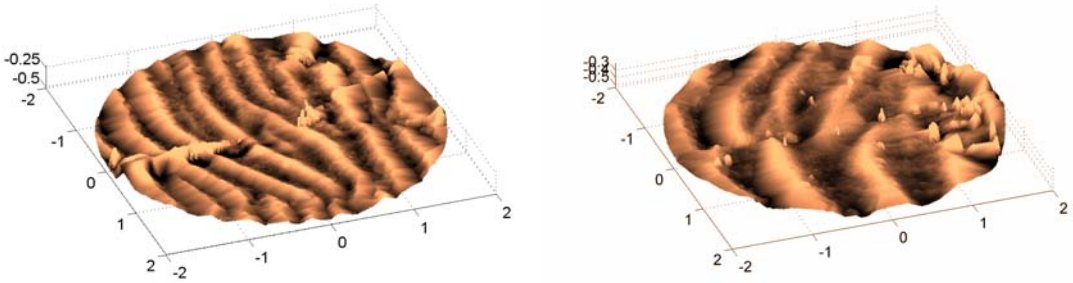

Figure 3. Examples of bed ripples.

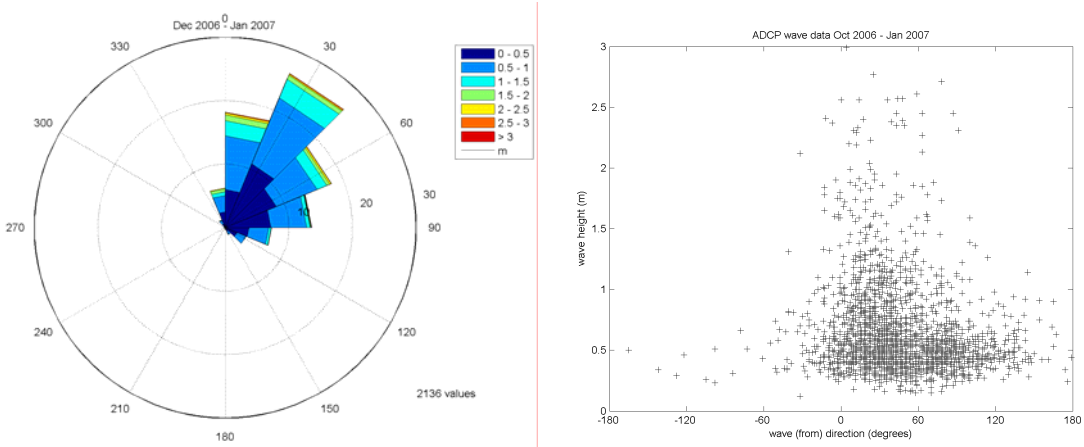

Figure 4. Wave rose and wave height versus direction plot.

with monitoring by X-band radar (as described in Bell et al., 2004) and ARGUS video and extending the modeling (Pan et al., 2007). Here we present a preliminary description of the hydrodynamic conditions, suspended sediments and bedforms collected by a range of acoustic instruments. Data were collected from three instrumented tripods deployed near the breakwaters (F1, F2, F3, see Figure 2), during two experiments: Experiment 1 (March–May 2006), Experiment 2.1 (October–December 2006) and 2.2 (December 2006–January 2007). The instrumentation included acoustic and optical instrumentation (ADCP, ADV, LISST and bedform scanners). One tripod (F2) was deployed in the intertidal zone. The others were deployed in water

depths of 6–8 m (tidal range is about 2 m). A large dataset has been successfully obtained. The mobility of the bed is illustrated by the variety of bedforms observed by the ripple scanners, e.g., see Figure 3. As will be seen in the results presented below it is a challenging problem to interpret the data collected in such dynamic conditions in combined waves and currents and with a mobile bed.

Wave climate at Sea Palling

From observed and model winds for 2006–7 it can be seen that the strongest winds are from W, N and NE. W winds are blowing offshore and in these conditions wave heights are negligible. N and NE storms can generate high waves and storm surges. Figure 4 shows the distribution of recorded waves showing the maximum wave height is from just north of shore-normal, suggesting wave-induced long-shore currents will be to the south.

1st November storm

During Experiment. 2.1 the largest storm occurred with wave heights at F1 reaching 3 m on 1 November as shown by the ADCP record (Figure 6). **A positive surge of 1.87 m occurs on 31 October.** Also, the surge current overwhelms the normal tidal reversal leading to persistent southerly flow for several tidal cycles.

Sediment fluxes

Time series of sediment flux (kg m^{-2} s^{-1}) were calculated as a product of ABS sediment concentration and ADV flow velocity. The range to the bed for the ABS on frame F1 is plotted in Figure6, in which the levels of the ADVs are also indicated by dashed lines. Where these intersect the range to bed (solid line) it may be seen that some of the instruments are contaminated by the bed echo on burial. Sudden changes in level may correspond to scouring/settling/burial of the rig at the onset of storm events. F1 (outside breakwater) seems to gradually settle during the first few days of Experiment 1. In Experiment 2.1 an abrupt change in level occurs on 30 October–1 November at the onset of a storm. F1 also rotated 30° in azimuth at that time. F1 experiences further burial in successive storms, e.g., 14 November, and was recovered on 17 November.

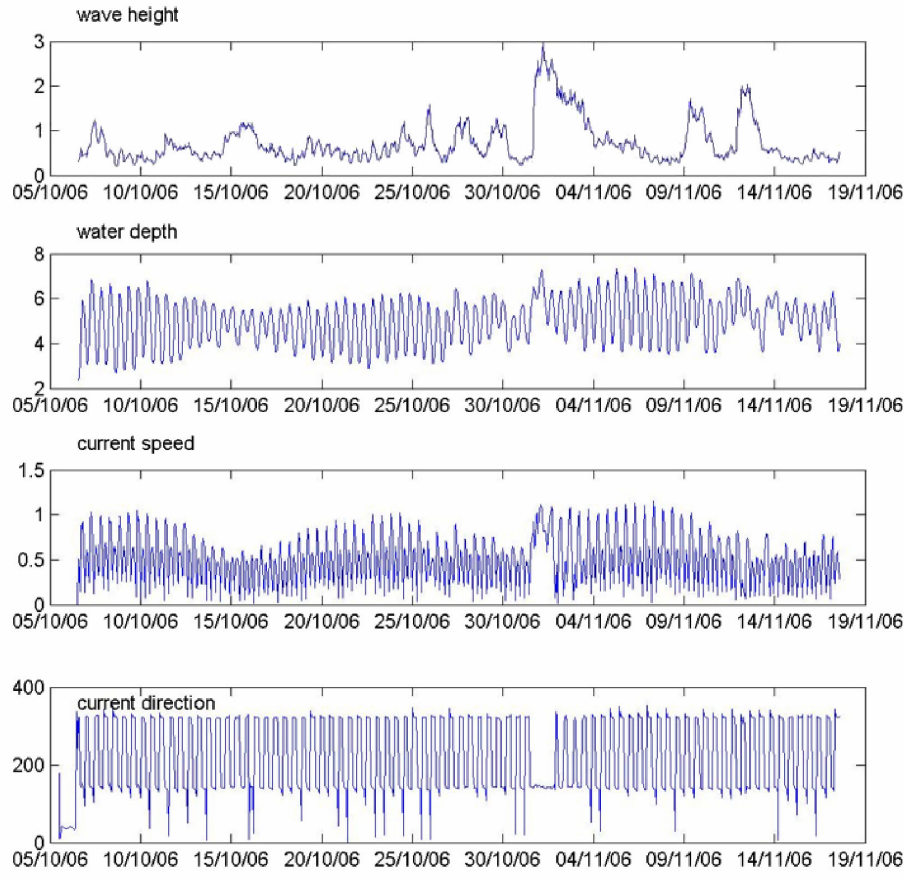

Figure 5. ADCP record from F1 Experiment 2.1.

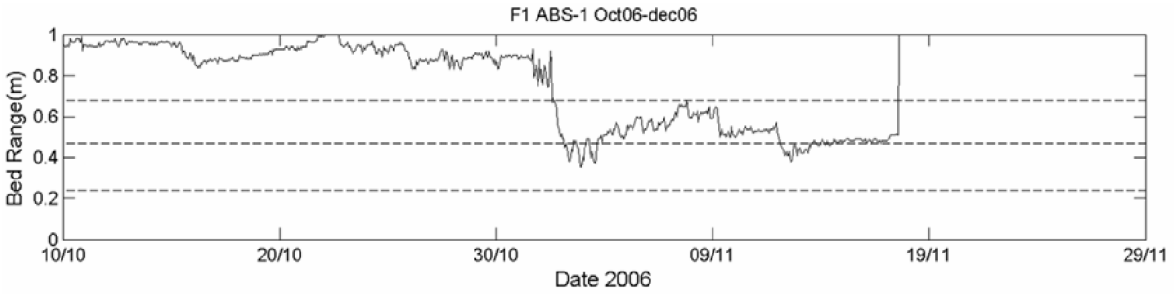

Figure 6. Range to bed of ABS instrument (F1 Experiment 2.1), dotted lines show heights of three ADVs.

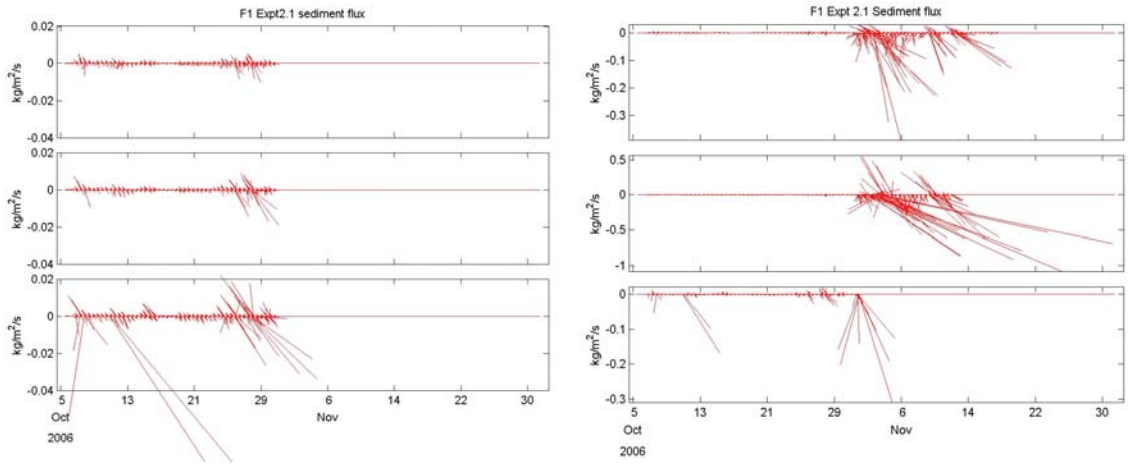

Figure 7. Sediment fluxes at F1. Left, right sides have different scales before/after 1 November 2006 storm.

Stick plots of sediment flux at the three ADVs on F1 are plotted in Figure7. In the early part of the record the sediment flux can be seen to be tidally-dominated. It was necessary to rescale the stick plots after the storm when sediment concentrations increased by several orders of magnitude due to resuspension and the net transport is then to the south. The middle and bottom fluxes after 1 November are affected by burial and contamination with bed echo.

Summary

First results from analysis of the LEACOAST2 in situ data have shown the highly dynamic nature of the sediment transport regime. Tides, waves and storm surges have been observed during the experimental periods in 2006–7. Tidal conditions can be seen to move the sediment but episodic storm events increase the sediment flux by several orders of magnitude. Further work is in progress to interpret these data.

References

Bell, P.S., Williams, J.J., Clarke, S., Morris, B., Vila Concejo, A. (2004), Nested radar systems for remote coastal observations, *Journal of Coastal Research*, SI 39. (Proceedings of the 8th International Coastal Symposium, Itajaí-SC, Brazil.) 438–489. ISSN 0749-0208.

Dolphin, T.J., Taylor, J.A., Vincent, C.E., Bacon, J.C., Pan, S., O'Connor, B. (2004), *Storm-scale effects of shore-parallel breakwaters on beaches in tidal settings (LEACOAST)*, In: Proceedings of the International Conference on Coastal Engineering, Lisbon, Portugal. American Society of Civil Engineers (ASCE). Vol. 3, pp2849–2861.

Pan, S., Fernando, P., Li, M., Zhu, Y., O'Connor, B., Vincent, C., Taylor, J., Dolphin, T. Bacon, J. (2005), *Effect of shore parallel breakwaters on coastal morphology under storm conditions*. In: Coastlines, Structures and Breakwaters, Allsop, W.H. (Ed.), Thomas Telford, London. pp64–73.

Pan, S., Wolf, J., Chen, Y., Bell, P. S., Du, Y., Fernando, P., Li, M. (2007), *Modelling nearshore waves with presence of shore-parallel breakwaters*. In: Coastal Structures 2007, Venice, Italy, 2–4 July 2007.

A new method for acquiring high-resolution transects in an estuary

ALECIA KELLY[1], MICHAEL COATES[1, 2], LAURIE LAURENSON[1], DANIEL IERODIACONOU[1]

1. School of Life and Environmental Sciences, Deakin University, P.O. Box 423, Warrnambool 3280, Victoria, Australia
email: arke@deakin.edu.au, michael.coates@deakin.edu.au, laurie.laurenson@deakin.edu.au, daniel.ierodiaconou@deakin.edu.au

2. GGT UDRH, Flinders University, Warrnambool 3280, Victoria, Australia (*present address*)

Keywords: groundwater, SCAMP, geo-spatial, estuary

ABSTRACT

This article presents a new method to obtain continuous, high-resolution transects along an estuary. A boat-mounted pneumatic-hydraulic vertical traverse allowed a high-speed conductivity-temperature-depth logger to be continuously profiled through the surface layer as the boat moved along the estuary. These data were integrated with data from Differential Geographic Positioning System (DGPS), resulting in transects with a 30-m-horizontal and 10-cm-vertical resolution.

Introduction

Anthropogenic demands on estuaries have led to increased contaminant and nutrient loads (e.g., de Jonge et al., 2002), and this are particularly severe for the estuaries of southern Australia where the Mediterranean climate leads to low summer flows and, coupled with the small tides in these regions, there is insufficient flow to keep the estuary open. Consequently, a sandbar fills their mouths, isolating the estuaries from the ocean for extended periods, and allowing contaminant and nutrient concentrations to build up. The effects of groundwater inflow during this period have not been studied in detail, principally because it is almost impossible to locate the groundwater entry points and measure their flow rates (e.g., Beck et al., 2007). The identification of such flows and their impact on the estuarine ecology require measurements on a fine horizontal scale (1 m to 10 m).

CTD sensors have been used on a number of autonomous platforms including gliders, surface drifters, and Autonomous Underwater Vehicles (AUVs) and are capable of providing continuous fine-scale data. These techniques are predominantly applied in oceanic environments where depth is not a limiting factor. However, few attempts have been made to obtain continuous fine-scale observations within estuaries due to the limited depth and inherent difficulties with their topography. An Undulating Towed Body Sampler has recently been applied in shallow coastal waters (<30 m) by the United States Department of Commerce, National Marine Fisheries Service (Berman and Sherman, 2001). Whilst this technique has provided detailed observations of the water column it is constrained by high set-up and operational costs, including the need to have trained technicians to monitor performance, operation and maintenance both during and between deployments. There is a need, therefore, for an integrated approach to obtaining fine-scale continuous data using affordable off the shelf technology that is readily available in shallow coastal environments.

The development of new geo-spatial and other technologies allows such measurements to be acquired. We present a new method for determining such measurements along an estuary, developed from earlier work of Coates and Folkard (2008, submitted). The method used a Self-Contained Autonomous Microstructure Profiler (SCAMP) in a new way as a sophisticated, high-precision, high-speed logger attached to a custom-built, vertically-profiling traverse mounted on the survey vessel, allowing geo-referenced profiles to be acquired as the vessel traversed the estuary. This combination provided physical data at approximately 30-m-horizontal and 10-cm-vertical resolution throughout the study site.

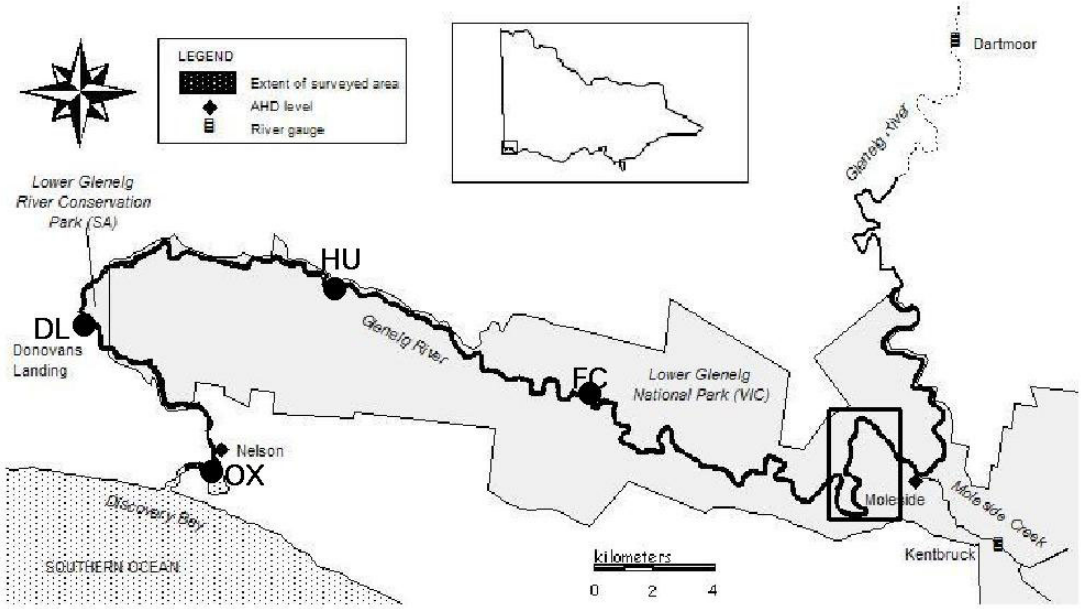

Figure 1. A map of the Glenelg Estuary, located in the extreme SW of the state of Victoria in Australia. The small box marks the location of the survey area shown in Figure 2b. The letters mark other survey stations: Oxbow Lake (OX), Donovans Landing (DL), Hutchessons (HU) and Forest Camp (FC).

Methods

The Glenelg estuary is one of Victoria's longest, at over 70 km long (Figure 1) to the limit of the salt water penetration at Dartmoor, and averages 6m to 8m deep. For much of its length, the estuary cuts through Gambier Limestone (Boutakoff, 1963), resulting in deep gorge sections that have vertical to near-vertical limestone cliffs with heights of 30 m to 50 m. It is located in the South-East Karst Province of South Australia and a variety of cave types have developed in the soft porous Gambier limestone (Grimes, 1994). As a result of this and the permeable nature of the sandy surface soils in the Glenelg region, very little surface run-off occurs, and rain falling on the plains percolates down to an extensive aquifer system that feeds the Glenelg River. Even in summer, groundwater base flows rarely fall below ~30 ML per day (Water Resources, 1989). It was the desire to locate these sources that provided the impetus for our technique.

The data for each transect were acquired with a SCAMP, a self-contained data-acquisition unit designed to measure temperature, temperature gradient, conductivity, fluorescence (if fitted) and pressure at a sample rate of 100 Hz. It is usually operated in a stand-alone, free-descending or free-ascending mode, but, in our study we are using it as a high-precision, high-speed CTD (conductivity-temperature-depth) logger. It is secured in a guard cage attached to a pneumatic-hydraulic traverse mounted on the side of the trailer vessel 'Melosira' (Figure 2a). Such a system avoids having electric motors on an open deck. The drive piston is hydraulic, using distilled water as the hydraulic fluid to prevent environmental contamination. The hydraulic drive avoided compressibility effects of using air alone, and allowed the vertical-profile speed to be accurately controlled by flow-control valves. Hydraulic pressure was provided by an on-deck air compressor.

Transects were built up using continuous profiles as the Melosira cruised along the estuary at a speed of approximately 1 m s^{-1}, during which data were acquired during both descending and ascending phases since the vessel motion ensured that the SCAMP sampled undisturbed water. The vertical speed was 10cms^{-1}, and the vertical data were binned into 10-cm bands. Based on the 30-second profiling time and ~1 m s^{-1} vessel speed, each descending or ascending profile was assumed to represent the average of a 30-metre-long section of the river. The geo-spatial position of the profiler was logged every second using a Trimble Differential Geographic Positioning System (DGPS). Post-processing differential corrections provided a spatial accuracy of ±3 m.

Results

An earlier survey (Coates and Lierich, unpublished data) suggested significant groundwater flow into the estuary upstream of Forest Camp, entering as a warmer (>5°C) intrusion located at a depth of approximately two metres. A survey to identify the source of this water was undertaken in late October, 2007, from the

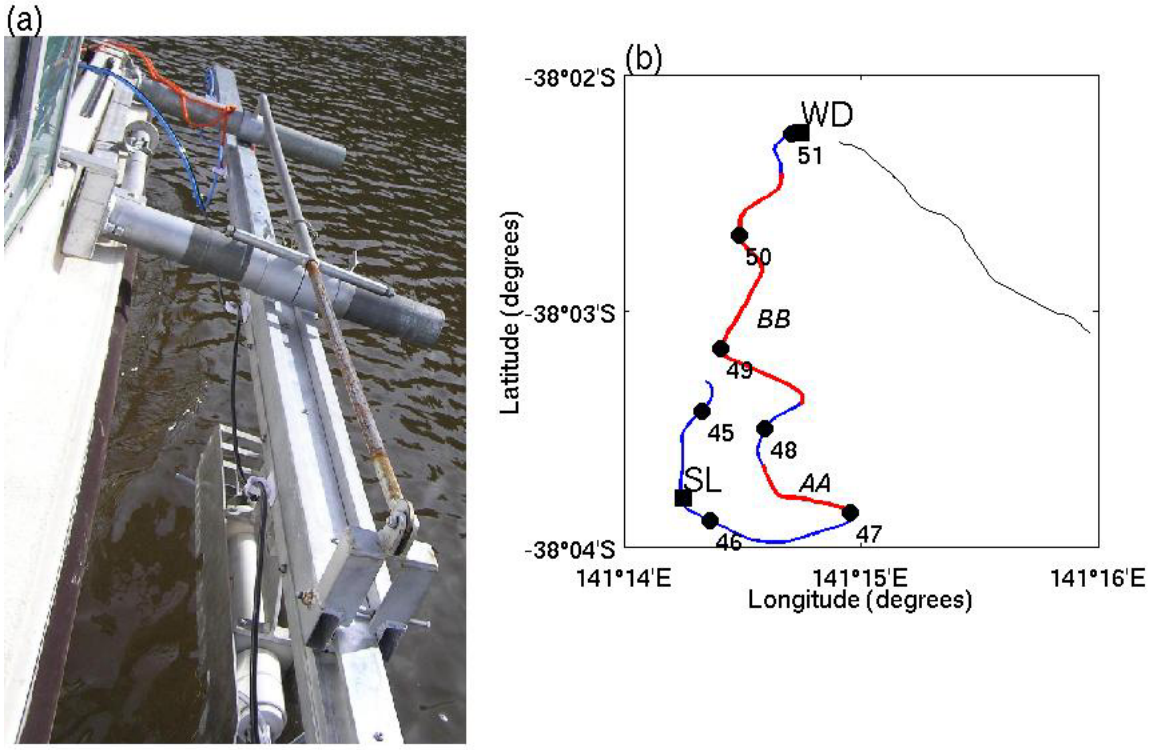

Figure 2. (a) The traverse stowed for transport. The support frame rotates on the forward post and is braced back to the rear post. The traverse frame slides within the support frame allowing it to be fixed at a prescribed depth. The piston is bolted between the ends of the traverse. The SCAMP is visible underneath in its cage mounted on the piston carriage. (b) The survey track beginning just downstream of Saunders Landing (SL) and finishing at Wild Dog Bend (WD). Distances (km) from the river mouth are indicated by the small filled circles. See the text for details of the sections *AA* and *BB* marked with thicker lines.

45 km point along the estuary, just downstream of the Saunders Landing site, to the 51 km point at the Wild Dog Bend site. The survey track generated from the DGPS data acquired during the survey is shown in Figure 2b. The resulting temperature and salinity transects are shown in Figure 3. Immediately apparent is the detailed spatial structure visible. Considerable high-frequency wave motion can be seen on the thermocline, consistent with internal-wave activity.

What is perhaps more striking in Figure 3 are the strong temperature spikes apparent along sections *AA* and *BB*. Variable solar heating due to shading from the surrounding cliffs could be invoked as a cause of this temperature variability but a simple heat-flux calculation shows that we can neglect this cause. Even assuming an unrealistic mean heat-flux difference between the illuminated and shaded regions of 500 W m^{-2} sustained over twelve hours, the resulting temperature increase is just 0.2°C in a 2-m deep layer, much less than the observed variability. As it is known that groundwater is entering the estuary, it seems most likely that this warmer and slightly brackish water is of groundwater origin. The salinity plot suggests a slight thickening of the halocline along the *BB* transect, also suggestive of an influx of brackish groundwater into the estuary. Consequently, the technique allows, for the first time, the identification of groundwater entry points into an estuary. Further surveys are to be undertaken to refine the groundwater entry points following which water currents will be measured with an ADCP to estimate volume fluxes, and SCAMP casts will be undertaken to measure the turbulence.

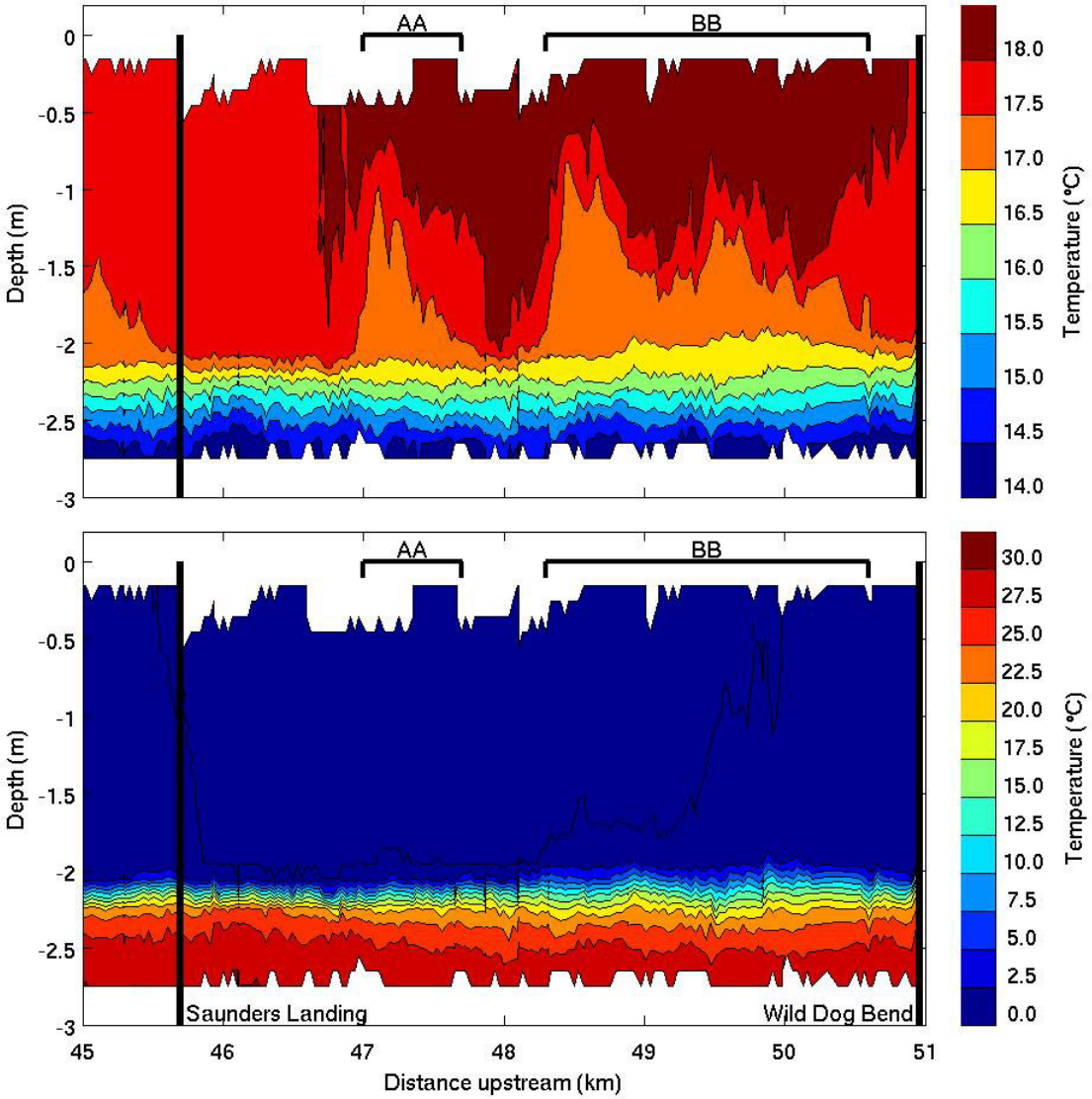

Figure 3. Temperature and salinity sections over the survey track from just downstream of Saunders Landing to Wild Dog Bend. See the text for details of sections *AA* and *BB*, also marked on Figure 2b.

References

Beck, A.J., Rapaglia, J.P., Cochran, J.K.I., Bokuniewicz, H.J., Yang, S. (2007), Submarine groundwater discharge to Great South Bay, NY, estimated using Ra isotopes, *Marine Chemistry*, doi:10.1016/j.marchem.2007.07.011.

Berman, M., Sherman, K. (2001), An undulating towed body sampler for monitoring marine ecosystems. *Sea Technology Magazine*, Narragansett, Rhode Island.

Boutakoff, N.A. (1963), Geology and geomorphology of the Portland area.

Coates, M.J., Folkard, A.M. (2008), The effects of littoral-zone vegetation on turbulent mixing in lakes, *Limnology and Oceanography*. (Submitted.)

Grimes, K. (1994), The South-East Karst Province of South Australia, *Journal of Environmental Geology*, 23(2), 134–148.

de Jonge, V.N., Elliott, M., Orive, E. (2002), Cause, historical development, effects and future challenges of a common environmental problem: eutrophication, *Hydrobioligica*, 475/476, 1–19.

Department of Water Resources (1989), *Water Victoria: a resource handbook.* Victorian Government Printing Office, Melbourne.

Sensitivity analysis of a morphodynamic modeling system applied to a coastal lagoon inlet

SANDRA PLECHA[1], NUNO VAZ[1, 3], XAVIER BERTIN[2], PAULO DA SILVA[1], ANABELA T.C. OLIVEIRA[2], ANDRÉ FORTUNATO[2], JOÃO MIGUEL DIAS[1]

1. Departamento de Física, Universidade de Aveiro, Campus de Santiago, 3810-193 Aveiro, Portugal
email: sandraplecha@ua.pt, nuno.vaz@ua.pt, psilva@ua.pt, joao.dias@ua.pt

2. Laboratório Nacional de Engenharia Civil, Departamento de Hidráulica e Ambiente, Núcleo de Estuários e Zonas Costeiras, 1700-066 Lisboa, Portugal
email: xbertin@lnec.pt, aoliveira@lnec.pt, afortunato@lnec.pt

3. Instituto Superior Técnico, Universidade Técnica de Lisboa, Av. Rovisco Pais, 1049-001 Lisboa, Portugal

Keywords: morphodynamics, sensitivity analysis, lagoon inlet; Aveiro lagoon

ABSTRACT

This work investigates the morphological changes at the inlet of a complex coastal system (Ria de Aveiro lagoon). This study was carried out using bathymetric data analysis and numerical simulations obtained with the 2DH morphodynamic modeling system MORSYS2D. The present simulations considered only tidal forcing and a sensitivity analysis was performed by tuning the formula used to compute the sediment fluxes and the sediment characteristics (d_{50}) The comparison of numerical results with bathymetric data shows that the bottom changes are over-predicted when the formula of Bhattacharya et al. (2007) is considered, and more realistic numerical solutions are obtained with the formula of van Rijn (1984).

Introduction

Numerical models are important tools to understand the morphodynamic changes in inlets, especially in coastal systems with high morphological complexity, such as the Ria de Aveiro lagoon.

In the past, regular maintenance dredging was performed by the Aveiro Harbor Administration (A.P.A.), due to sand accretion to the north of the inlet, as a result of the interruption of the longshore drift by the construction of the jetties. However, this operation was interrupted leading to sand accretion in this area, probably resulting in very important changes in the sediment fluxes, affecting the bathymetry of the Ria de Aveiro inlet and adjacent areas.

Recent bathymetric surveys revealed that erosion occurred at the entrance of the channel close to the north jetty and sand deposition occurred close to the south jetty. These changes in the bathymetry of the inlet might threaten the stability of the north jetty and the navigation in the main channel. In this context, the development of numerical systems that simulate the trends of deposition or erosion in the Ria de Aveiro lagoon inlet can improve our knowledge of the behavior of the system.

The aim of this work is to analyze the sensitivity of the 2DH morphodynamic modeling system MORSYS2D (Fortunato and Oliveira, 2004, Fortunato and Oliveira, 2007, Bertin et al., 2008) to different parameterizations and sediment sizes, applied to the Ria de Aveiro lagoon.

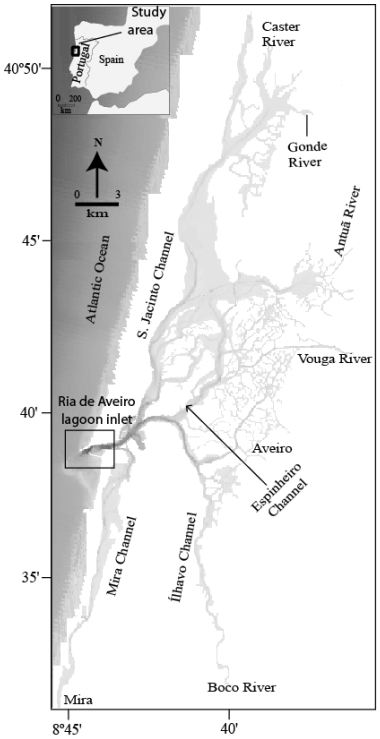

Figure 1. Location and bathymetry of the Ria de Aveiro lagoon.

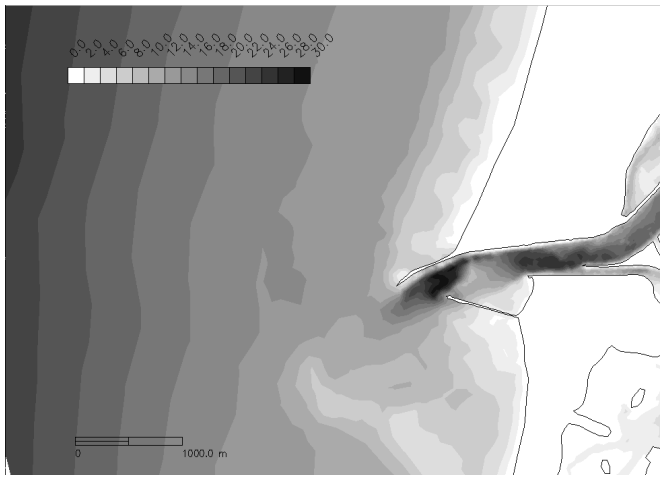

Figure 2. Bathymetry of the Ria de Aveiro lagoon inlet. Bathymetric data are from 2002.

Study area

The Ria de Aveiro is a shallow water coastal system located in the NW of the Iberian Peninsula (40°38′N, 8°45′W) (Figure 1). This lagoon has several channels and intertidal areas, resulting in a very complex system. The Ria de Aveiro is connected with the Atlantic Ocean through an artificial inlet built in the 19th century, composed by one inlet channel (~350 m wide and 2 km long) fixed by two jetties.

The morphodynamic behavior of this channel and coastal surrounding zones is complex due to highly energetic oceanic wave climate conditions and strong tidal currents (~2 m s^{-1}, Vaz, 2007), whose interaction is not well understood/studied. Although, a recent study reveals that during the period 1988–2002, the Ria de Aveiro lagoon inlet presented bathymetric changes of about 14 m (Plecha et al., 2007).

Methods

This study was carried out by bathymetric data analysis and numerical simulations. The bathymetric data were obtained by the Aveiro Harbor Administration (A.P.A.) between 1987/88 and 2002 and the numerical simulations were performed with the 2DH morphodynamic modeling system MORSYS2D. This modeling system integrates a hydrodynamic model (ELCIRC, Zhang et al., 2004), which calculates tidal elevations and currents, a wave model (SWAN, Booij et al., 1996), which computes the wave climate, and a module that computes sand fluxes and updates the bottom topography (SAND2D, Fortunato and Oliveira 2004, 2007, Bertin et al., 2008). The setting-up of the hydrodynamic model is based on the work of Oliveira et al., (2007).

The bathymetric data from 2002 are considered as initial conditions for the numerical model. The bathymetry of the Ria de Aveiro lagoon inlet is illustrated in Figure 2. The simulations performed to analyze the sensitivity of MORSYS2D were made for a time period of 180 days and only the tidal forcing in the ocean open boundary was considered. The analysis is made by computing the difference between the initial and final bathymetries (in meters), using several sediment transport formulae (for example, Bhattacharya et al., 2007 and van Rijn, 1984) and different sediment characteristics (d_{50}).

Results

In this work only the results obtained with the simulations using a grid of variable d_{50} are presented, although simulations to analyze the influence of the grain size in the evolution of the bathymetry had been also performed. The tested values for d_{50} were 0.5 and 1.0 mm.

The analysis of the results obtained, when the Bhattacharya et al. formulation is used, reveal very distinct values for d_{50} = 0.5 mm and 1 mm (not shown in this work). In the area between the jetties is observed an offshore movement of the higher depths, revealing erosion trends in this area. Moreover, a higher depth between the jetties is obtained when is used the value of 1 mm for d_{50}. The patterns of erosion/deposition obtained for these two simulations are similar. The results obtained for the simulations using the van Rijn and Karim-Kennedy formulations are more realistic. Both results reveal erosion trends near the north jetty and

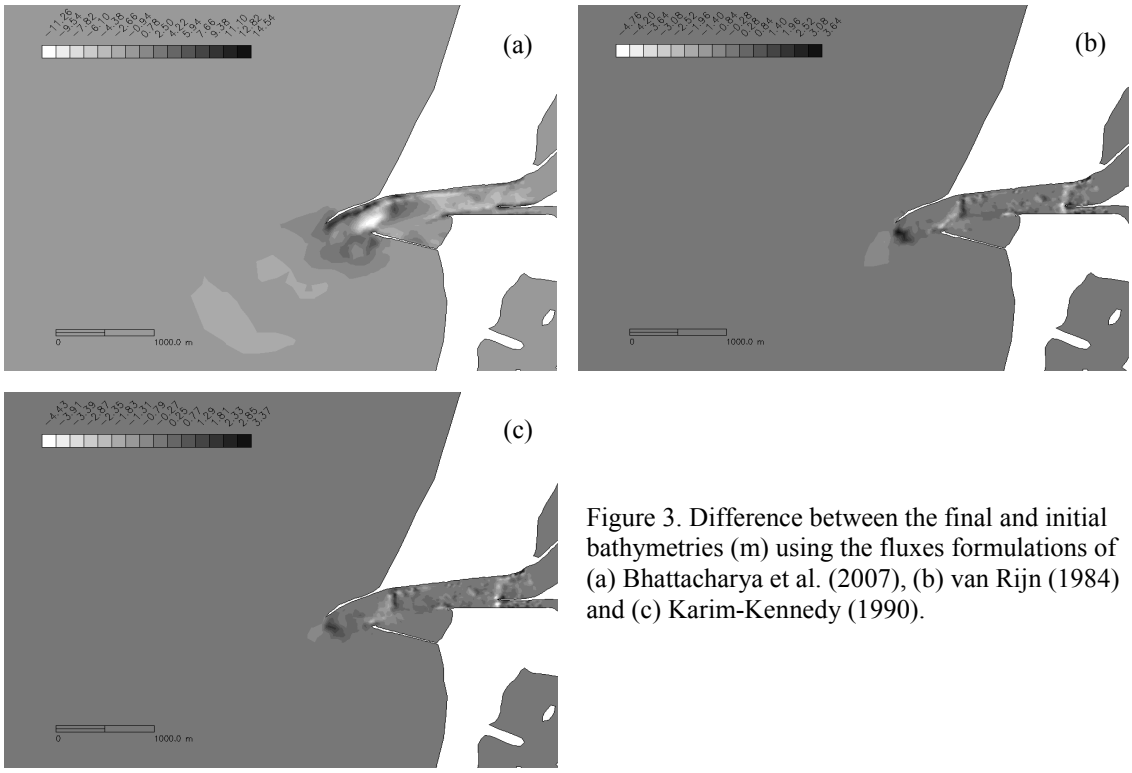

Figure 3. Difference between the final and initial bathymetries (m) using the fluxes formulations of (a) Bhattacharya et al. (2007), (b) van Rijn (1984) and (c) Karim-Kennedy (1990).

deposition between the jetties. For the van Rijn formulation with a d_{50} of 0.5 mm the deposition value is 3 m and with a d_{50} of 1 mm is 1 m. A higher values are obtained for the Karim-Kennedy formulation, 4 m for erosion and 5 m for deposition, for d_{50} = 0.5 mm.

The results obtained for the simulations with a grid of variable d_{50}, are presented in Figure 3. Differences between the final and initial bathymetries (m) are illustrated in this figure for 180 days of simulation of the Ria de Aveiro lagoon inlet. Positive values represent erosion trends.

The bathymetric evolution obtained with the Bhattacharya et al. (2007) formulation (Figure 3a) is over-predicted when compared with the measured data. However, an erosion area is observed near the north jetty, just like the bathymetric data presented in Figure 2. Near the south jetty, a deposition region is observed, with an increase of the sand bank of about 1.5/2.0 m. This formulation over-predicts the results between the north and the south jetties, where a deposition area with a sand bank increase of 11 m is observed.

The numerical results obtained with the van Rijn and Karim-Kennedy (Figures 3b and c) formulations are more realistic, with maximum deposition values of 4 m and maximum erosion of 3 m. The simulations performed using these formulations reveal very similar patterns, with erosion areas in the zone between the north and south jetties. In both results the patterns of erosion near the north jetty and the deposition patterns near the south jetty are consistent with the observed bathymetric data.

Conclusions

The 2D morphodynamic modeling system MORSYS2D was used to simulate the bathymetric changes in the Ria de Aveiro lagoon inlet. The results obtained through numerical simulations are consistent with the bathymetric data, with erosion areas near the north jetty and deposition near the south jetty. The best results are those obtained through the van Rijn and Karim-Kennedy formulations, with maximum deposition values of 4 m and erosion of 3 m, for 180 days of simulation.

Acknowledgements

The first author has been supported by FCT grant through a PhD grant, FRH/ BD/ 29368/ 2006. This work has been supported by FCT in the frame of the research project POCI/ECM/59958/2004 – EMERA, Study of

the Morphodynamics of the Ria de Aveiro Lagoon Inlet. Nuno Vaz is supported by the FCT through a post-doc grant (SFRH/BPD/37325/2007).

The authors would like to thank Profs. A.M. Baptista and Joseph Zhang for the model ELCIRC, and the Aveiro Harbour Administration (A.P.A.) for providing the bathymetric data.

References

Bertin, X., Fortunato, A.B., Oliveira, A. (2008), Simulating morphodynamics with unstructured grids: description and validation of an operational model for coastal applications, *Ocean Modelling*. (Submitted.)

Bertin, X., Fortunato, A.B., Oliveira, A. (2007), *Sensitivity analysis of a morphodynamic modeling system applied to a Portuguese tidal inlet*. In: RCEM2007, Dohmen-Janssen, C.M., Hulscher, S.J.M.H. (Eds.), Vol. 1, 11–17, Taylor & Francis Ltd, London.

Bhattacharya , B., Price, R.K., Solomatine, D.P. (2007), A machine learning approach to modeling sediment transport, *ASCE Journal of Hydraulic Engineering,* 133(4), 440–450.

Booij, N.R., Holthuijsen, L.R., Ris, R.C. (1996), The SWAN wave model for shallow water, *ICCE'96*, Orlando, USA, 668–676.

Fortunato, A.B., Oliveira, A. (2004), A modeling system for long-term morphodynamics, *Journal of Hydraulic Research,* 42(4), 426–434.

Fortunato, A.B., Oliveira, A. (2007), Improving the stability of a morphodynamic modeling system, *Journal of Coastal Research,* SI 50, 486–490.

Karim, M.F., Kennedy, J.F. (1990), Menu of couple velocity and sediment discharge relation for rivers, *Journal of Hydraulic Engineering*, 116(8), 978–996.

Oliveira, A., Fortunato, A.B., Dias, J.M. (2007), *Numerical modeling of the Aveiro inlet dynamics*. In: Proc. of the 30th International Conference on Coastal Engineering, Smith, J.M. (Ed.) Vol. 4, pp3282–3294, World Scientific Publishing Co.

Plecha, S., Rodrigues, S., Silva, P., Dias, J.M., Oliveira, A., Fortunato, A.B. (2007), *Trends of bathymetric variations at a tidal inlet*. In: RCEM2007, Dohmen-Janssen, C.M., Hulscher, S.J.M.H. (Eds.), Vol. 1, 19–23, Taylor & Francis Ltd, London.

van Rijn, L.C. (1984), Sediment transport – Part 1: Bed load transport, *Journal of Hydraulic Engineering*, 110(10), 1431–1456.

van Rijn, L.C. (1984), Sediment transport – Part 2: Suspended load transport, *Journal of Hydraulic Engineering*, 110(11), 1613–1614.

van Rijn, L.C. (1984), Sediment transport – Part 3: Bed forms and alluvial roughness, *Journal of Hydraulic Engineering,* 110(12), 1733–1754.

Vaz, N. (2007), *Study of heat and salt transport processes in the Espinheiro Channel (Ria de Aveiro),* PhD Thesis, University of Aveiro, Portugal.

Zhang, Y., Baptista, A.M., Myers, E.P. (2004), A cross-scale model for 3D baroclinic circulation in estuary-plume-shelf systems: I. Formulation and skill assessment, *Continental Shelf Research*, 110(10), 1431–1456.

Salt flux mechanisms in short, stratified estuary

DAVID K. RALSTON[1], W. ROCKWELL GEYER[1], JAMES A. LERCZAK[2]

1. Woods Hole Oceanographic Institute, 266 Woods Hole Road,
Woods Hole MA 02543-1050, USA
email: dralston@whoi.edu, rgeyer@whoi.edu

2. College of Oceanic and Atmospheric Sciences, Oregon State University,
104 COAS Administration Building, Corvallis OR 97331-5503, USA
email: jlerczak@coas.oregonstate.edu

Keywords: salt flux, salt wedge estuary, tidal pumping, turbulent mixing

ABSTRACT

In the Merrimack River estuary on the Gulf of Maine, strong tidal and river forcing combine to make conditions highly unsteady at tidal timescales. The length of the salinity intrusion is similar to the tidal excursion, and there is significant bathymetric variability both along- and across-estuary. Each tidal cycle, a sharp salinity front advects into and out of the estuary; sills and constrictions act as hydraulic controls on the propagation of the salinity intrusion, and strong stratification inhibits vertical mixing. Exchange of salt and other scalars between the estuary and the coastal occurs through both tidal and subtidal processes. The strong along-estuary salinity gradient (~10 psu km^{-1}) drives up-estuary salt flux baroclinically. The subtidal salt flux has vertical structure like classical estuarine circulation in the deeper channels, but also has significant lateral structure due to the channel/shoal bathymetry and secondary circulation. Because of the heterogeneous bathymetry, tidal salt flux mechanisms are also critical. Partitioning of salt flux between subtidal and tidal mechanisms is not constant, but varies spatially along the estuary and temporally with river discharge and tidal forcing. Based on extensive field observations at several locations and times, we evaluate the salt flux mechanisms in the Merrimack. We also develop and calibrate a numerical model of the estuary, and apply similar salt flux analyses to the model for enhanced resolution of the system. We use the model results to describe the tidal salt flux mechanisms in greater detail, and find that along-estuary variability in bathymetry combined with intense vertical mixing at sills and constrictions creates a few localized regions where most of the mixing of oceanic and fluvial water occurs.

Introduction

Mechanisms for exchange of salt between estuaries and the coastal ocean depend on the combined tidal, fluvial and baroclinic processes in the estuary. To distinguish among the exchange processes, the salt flux can be decomposed into steady and tidally varying components. In many estuaries, the steady, or tidally averaged, exchange driven predominantly by baroclinic circulation dominates the salt flux. The baroclinic salt flux can be scaled as $\overline{u's'} \sim (g\beta)^2 H^5 (\partial S/\partial x)^3 U_T^{-3}$, where β is the saline expansivity, H is the depth, $\partial S/\partial x$ is the along-estuary salinity gradient, and U_t is the tidal velocity (Hansen and Rattray, 1965). The scaling shows that the baroclinic salt flux increases with H and $\partial S/\partial x$ and decreases with U_t. As tidal velocity increases, so does vertical mixing that inhibits gravitational exchange and reduces the steady salt flux. Instead, salt fluxes in estuaries with large tides tend to be dominated by correlations between salinity and velocity at tidal time scales. Examples of tidal salt flux mechanisms include tidal pumping due to asymmetry between jetting and draining flow at a constriction and lateral trapping due to frictional phasing between channel and shoals.

Characteristic velocity scales for the estuarine forcing factors are the tidal velocity (U_t), the mean velocity due to river discharge (U_0), and a baroclinic exchange velocity ($C_0 \sim g\beta S_0 H/4)^{1/2}$), where S_0 is the ocean salinity. Ratios of these velocities can help quantify where in parameter space an estuary falls: the freshwater Froude $F_m = U_0/C_0$, and the tidal Froude number $\Gamma = U_t/C_0$ (Hansen and Rattray, 1966; MacCready, 1999). For small F_m and Γ, baroclinic forcing dominates and the salt flux is largely due to steady exchange. A substantial amount of research has quantified exchange in estuaries of this type that are relatively deep and have moderate tides, including the Hudson River (Lerczak et al., 2006), San Francisco Bay (Monismith et al., 2002), the James River and Chesapeake Bay. Much less work has been done on estuaries that are strongly

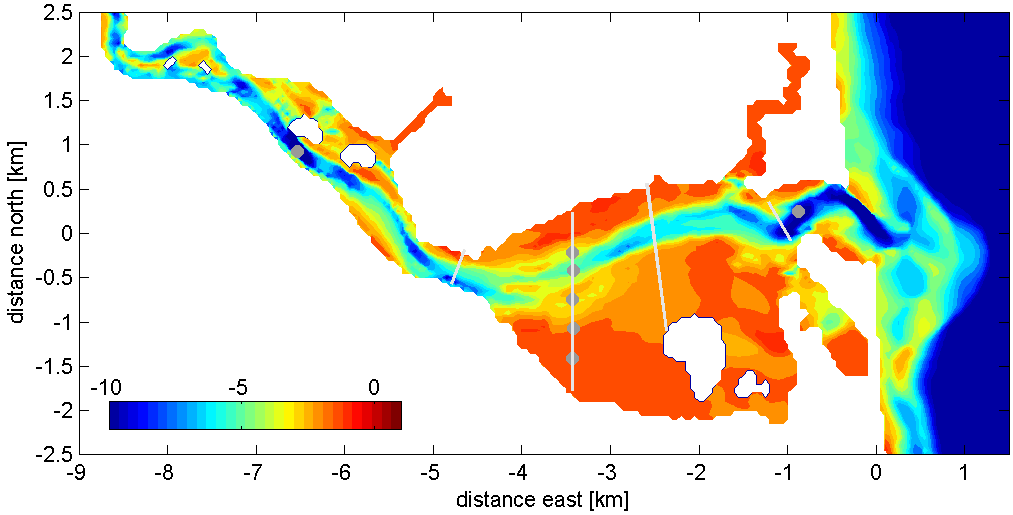

Figure 1. Merrimack River estuary bathymetry marked with locations of moorings (gray dots) and cross-section surveys (white lines) during 2005 observations.

forced by tides and river so that F_m and Γ are both large. Strong river discharge makes the salinity intrusion the same order of magnitude as the tidal excursion. Consequently, the estuaries are highly time-dependent, and along-estuary bathymetric features (sills, contractions) are important for generating tidal trapping and pumping. Examples include the Fraser River (Geyer and Farmer 1989), the Columbia River, and the Connecticut River. Note that the relative strength of the forcing factors can vary substantially in a given estuary over seasonal and spring-neap cycles. For example, during high river discharge and spring tides, the Hudson River can become like a salt wedge with features similar to more strongly forced estuaries.

Methods

To investigate salt flux in an estuary forced strongly by river and tides, we study the Merrimack River estuary (MA, USA) using both field observations and a numerical model (Figure 1). The Merrimack is a strongly stratified, time dependent salt wedge estuary that flows into the Gulf of Maine. The Merrimack has a tidal range of 3 to 4 m, river discharge up to ~1500 m^3s^{-1} during the spring freshet, and has relatively shallow, heterogeneous bathymetry with a deeper channel (~5 m) adjacent to shoals (2 m-to-intertidal) and a series of sills and constrictions.

We collected field observations in the spring of 2005. Seven moorings were deployed for 55 days with acoustic Doppler current profilers to measure water column velocities and conductivity-temperature sensors for near- bottom and near-surface salinity and temperature; three of the moorings also had pressure gauges (Figure 1). Several times during the deployment, hydrographic surveys mapped the along-estuary extent of the salinity intrusion and recorded cross-estuary distributions of salinity and velocity over full tidal cycles (~12.5 hr) at four locations along the estuary (Figure 1). Cross-section surveys of salinity and velocity were projected onto regular grids interpolated in time through the tidal cycle for salt flux analysis.

In addition to the observations, we have developed a numerical model of the Merrimack using the Finite Volume Coastal Ocean Model (FVCOM) (Chen et al., 2003). FVCOM uses an unstructured grid, an important attribute for resolving the complex bathymetry in the Merrimack and similar shallow tidal systems. The model has been calibrated against the observations and achieves high skill at tidal to seasonal time scales by reproducing the time series of water surface elevation, salinity and velocity at the moorings. In addition, the model capably simulates features noted in the along- and across-estuary surveys of salinity and velocity, including the extent of the salinity intrusion, the development and breakdown of stratification, complex lateral circulation, and location of salinity fronts. Observations of stratified turbulent mixing near a sill taken in the Merrimack in 2007 also lend support the k-ε turbulence closure scheme used in the model.

In both the field observations and the model results, the salinity and along-channel velocity cross-sections were decomposed into subtidal and tidal components to distinguish transport mechanisms (Lerczak et al., 2006). Initially, we transformed the tidal-cycle cross-sectional surveys into sigma coordinates to reduce the

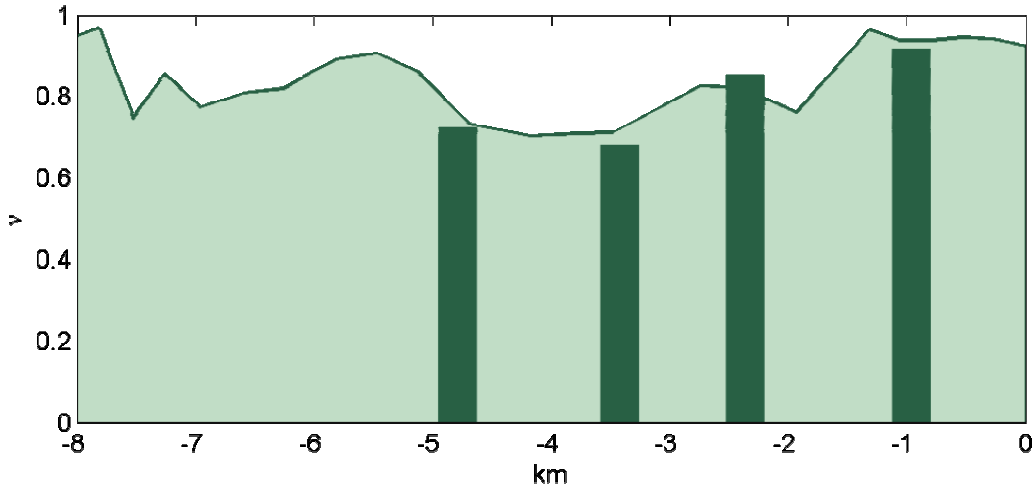

Figure 2. Along-estuary distribution of v, the ratio of tidal salt flux to steady salt flux. Dark bars are from field observations at the four cross-sections shown in Figure 1; in the background are model results at regular intervals along the estuary. Tidal processes dominate ($v > 0.5$), but with along-estuary variability tied to the bathymetry.

effect of Stokes drift on the decomposition. Salinity and along-channel velocity were then broken into three components:

1) tidally and cross-sectionally averaged,
2) tidally averaged and cross-sectionally varying, and
3) tidally and cross-sectionally varying.

The total salt flux is the balance of integrals of the products of these terms, with (1) river flow advecting the mean salinity out of the estuary, and dispersive salt flux up-estuary due to (2) steady shear dispersion and (3) tidal oscillatory shear dispersion. Net salt flux through the cross-section was calculated for each of the tidal cycle surveys.

Results

Salt flux in the Merrimack is dominated by tidal processes. The parameter v is the ratio of the tidal salt flux to total salt flux at a section, so tidal fluxes are greater than steady fluxes for $v > 0.5$. In both the observations and the model we find that v ranges between about 0.6 and 0.9, with along-estuary variability due to the heterogenous bathymetry (Figure 2). In the vicinity of sills and constrictions (e.g., near −6 or −1 km), along-estuary gradients in depth and cross-sectional area contribute to the salt flux (Dronkers and van de Kreeke, 1986). In sections with relatively uniform along-estuary bathymetry (e.g., near −3 km), steady salt flux is a greater factor.

Field observations of salt flux were focused on the section with the cross-estuary line of moorings (Figure 1). Flow at that section is laterally segregated between a flood-dominant channel to the north and an ebb-dominant channel to the south. The northern channel is relatively deep and straight, so baroclinic circulation makes a significant contribution to the total flux. However, lateral redistribution of salinity and momentum due to channel curvature and the cross-channel bathymetry make the lateral steady salt flux approximately equal to the baroclinic steady flux. As in the rest of the estuary, tidal fluxes are important. During floods, the flow is stratified and laterally uniform. During ebbs, significant mixing occurs at a sill and contraction immediately up-estuary of the cross-section. Shoals on the south side of the estuary trap mixed water while the deeper channels remain stratified through much of the ebb. The mixing at the sill during ebbs creates a tidal asymmetry at the cross-section and a net flux up-estuary.

Stratified turbulent mixing is critical for generating tidal asymmetries in the flux through a cross-section. In the Merrimack, turbulent mixing occurs predominantly during the ebb and is localized to bathymetric features where the flow is hydraulically controlled. Snapshots of depth integrated buoyancy flux show little mixing during the flood with the exception of a region near the mouth where flow is constrained by jetties (Figure 3). Upstream from the jetties, significant mixing begins during the ebb. Early in the ebb, mixing is dominated by interfacial shear across the pycnocline. The baroclinic pressure gradient opposes the ebbing

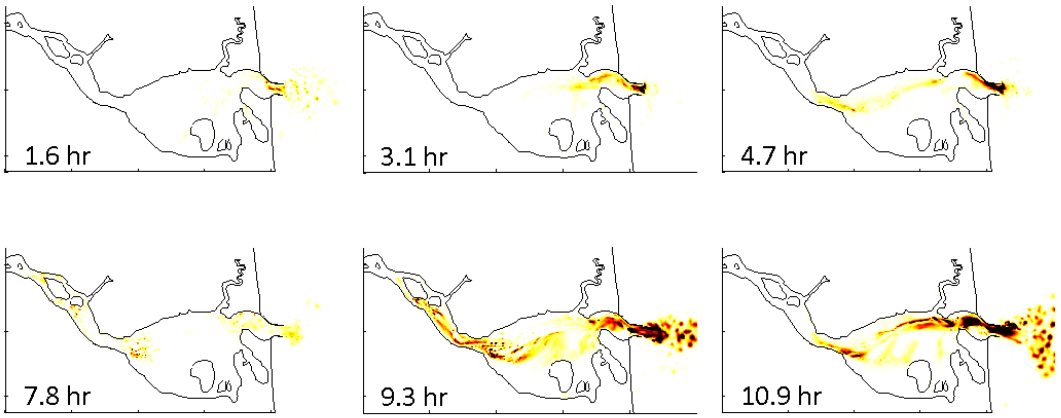

Figure 3. Depth integrated buoyancy flux through the tide. Times are relative to high water, with the top panels during flood and the bottom panels during ebb. Vertical mixing of salt is greatest during the ebb and is localized at sills and expansions. Mixing also occurs in the mouth where the channel is constrained by jetties and in the plume offshore (not shown).

barotropic gradient to yield near-zero velocities in the lower layer. Later in the ebb, both the baroclinic gradient and stratification weaken and bottom-generated turbulence mixes the toe of the salt wedge as it moves down-estuary. Because of the importance of hydraulic controls to the along-estuary dynamics, the overmixing limit (Stommel and Farmer, 1952) provides a reasonable estimate of the salinity of the water exiting the estuary over a wide range of discharge and tidal forcing conditions.

References

Chen, C., Liu, H., Beardsley, R.C. (2003), An unstructured grid, finite-volume, three-dimensional, primitive equations ocean model: Application to coastal ocean and estuaries, *Journal of Atmospheric and Oceanic Technology*, 20(1), 159–186.

Dronkers, J., van de Kreeke, J. (1986), Experimental determination of salt intrusion mechanisms in the Volkerak estuary, *Netherlands Journal of Sea Research*, 20(1), 1–19.

Geyer, W.R., Farmer, D.M. (1989), Tide-induced variation of the dynamics of a salt wedge estuary, *Journal of Physical Oceanography*, 19(8), 1060–1072.

Hansen, D.V., Rattray, M. (1965), Gravitational circulation in straits and estuaries, *Journal of Marine Research*, 23, 104–122.

Hansen, D.V., Rattray, M. (1966), New dimensions in estuary classification, *Limnology and Oceanography*, 11(3), 319–326.

Lerczak, J.A., Geyer, W.R., Chant, R.J. (2006), Mechanisms driving the time-dependent salt flux in a partially stratified estuary, *Journal of Physical Oceanography*, 36(12), 2296–2311.

MacCready, P. (1999), Estuarine adjustment to changes in river flow and tidal mixing, *Journal of Physical Oceanography*, 29(4), 708–726.

Monismith, S.G., Kimmerer, W., Burau, J.R., Stacey, M.T. (2002), Structure and flow-induced variability of the subtidal salinity field in northern San Francisco Bay, *Journal of Physical Oceanography*, 32(11), 3003–3019.

Stommel, H., Farmer, H. (1952), *On the nature of estuarine circulation*. Technical Report No. 52-88. Woods Hole Oceanographic Institution, Woods Hole, MA.

Estuarine shoreline processes: a dynamic low energy system

ANA VILA-CONCEJO[1], MICHAEL G. HUGHES[1], ANDREW D. SHORT[1], ROSHANKA RANASINGHE[2]

1. School of Geosciences, University of Sydney, Madsen Building, Sydney 2006, New South Wales, Australia
email: a.vilaconcejo@usyd.edu.au, michaelh@usyd.edu.au, a.short@usyd.edu.au

2. Department of Environment and Climate Change, P.O. Box 580, Queanbeyan 2620, New South Wales 2620, Australia
email: rosh.ranasinghe@dipnr.nsw.gov.au

Keywords: estuarine beach, GIS, longshore currents; Port Stephens, Australia

ABSTRACT

Estuarine shorelines are often classified as low energy coasts and thus are expected to undergo little variation. Port Stephens (SE Australia) is a ria-like microtidal estuary (Roy et al., 2001) located 230 km north from Sydney, on a wave dominated coast (Figure 1). It has an E-W orientation and connects to the ocean through a 1.24 km wide entrance that allows the dominant SE waves to propagate into the estuary. The outer port is tide dominated and has a large and shallow flood-tide delta which is affected by waves and provides some protection to the estuarine shorelines. The northern shoreline of outer Port Stephens is a continuous stretch of sand (over 4 km) that comprises a barrier (Yacaaba) undergoing accretion, a narrow beach (Jimmy's Beach) undergoing erosion (greater than 1 m yr^{-1}), and a spit (Winda Woppa) which has narrowed in width and extended its length more than 500 m in the last 50 years. Previous studies in the area indicate contradictory longshore transport with geomorphologic studies stating westwards transport while numerical models show eastwards transport. The present study establishes longshore current directions and intensities under different conditions, through field based process studies, and links short term process to the decadal evolution obtained with GIS analyses.

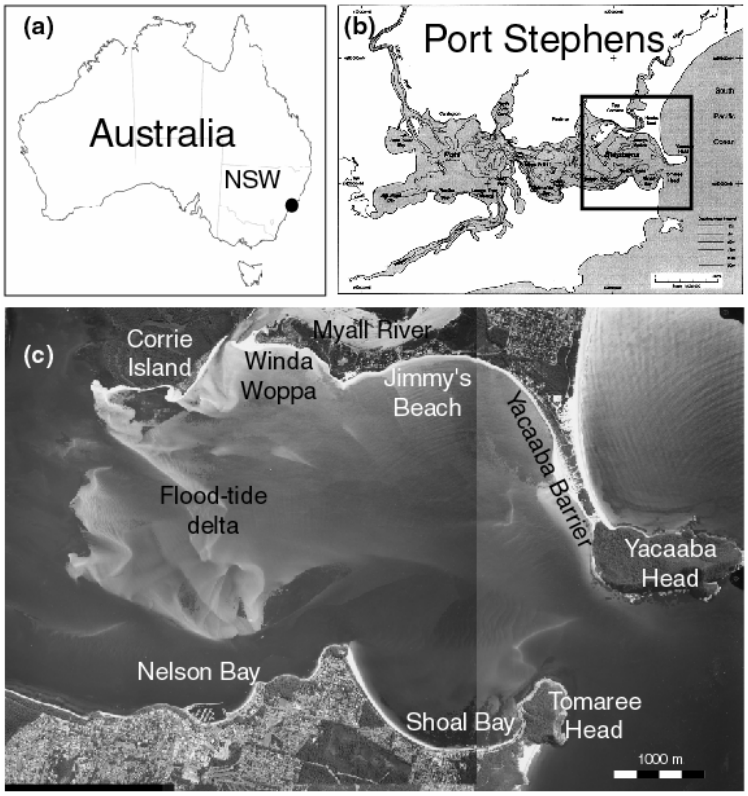

Figure 1. (a) Location of Port Stephens on east coast of Australia; (b) Map after DPWS (1999) showing two well differentiated basins and the study area; (c) Aerial photo of the study area (April 2006).

Methods

Over 50 aerial photographs taken since 1951 were rectified and analyzed using ArcGIS with the objective of establishing medium to long-term trends of shoreline evolution. The obtained results had an estimated error of ±7 m across-shore (Vila-Concejo et al., 2007). The areas of interest included Winda Woppa spit (westward extension and shoreline retreat), Jimmy's Beach (shoreline retreat) and Yacaaba Barrier (sandwave evolution).

Field based process studies on the northern shoreline started in March 2007 and include periodic topographic surveying using a total station and a RTK-GNSS (Real Time Kinematic Global Navigation Satellite System). Harley and Turner's (2008) data transformation technique was used to eliminate the curvature of the beach to facilitate a more accurate gridding process; the same author's methodology was used to transform the data back to the original co-ordinates. Hydrodynamic measurements using current meters (ADV on the beach and ADCP on the flood-tide delta) and pressure transducers were also undertaken between March 2007 and April 2008. ADCP measurements during an entire tidal cycle have been obtained in seven locations in the estuary and are still ongoing. Table 1 shows measurements taken between March 2007 and April 2008. All results were then coupled with computed hourly offshore wave power.

Table 1. Fieldwork undertaken in the study area between February and April 2008.

Date	Beach Topography	Beach Hydrodynamics	ADCP deployment
March 2007	Yes	Yes (single location)	No
May 2007	Yes	No	No
June 2007	Yes	Yes (single location)	No
July 2007	Yes	No	No
October 2007	Yes	No	No
November 2007	Yes	No	Yes
December 2007	Yes	No	Yes
February 2008	Yes	No	Yes
April 2008	Yes	Yes (simultaneous loc.)	Yes

Results

Spatial GIS analyses between 1951 and 2008 show that Winda Woppa has undergone ~800 m westward extension and between 50–100 m shoreline retreat (Figure 2). Simultaneously, Jimmy's Beach has retreated between 50 and 80 m and the area towards the sandwave has remained reasonably stable while the sandwave has undergone several cycles of formation/destruction (Figure 2).

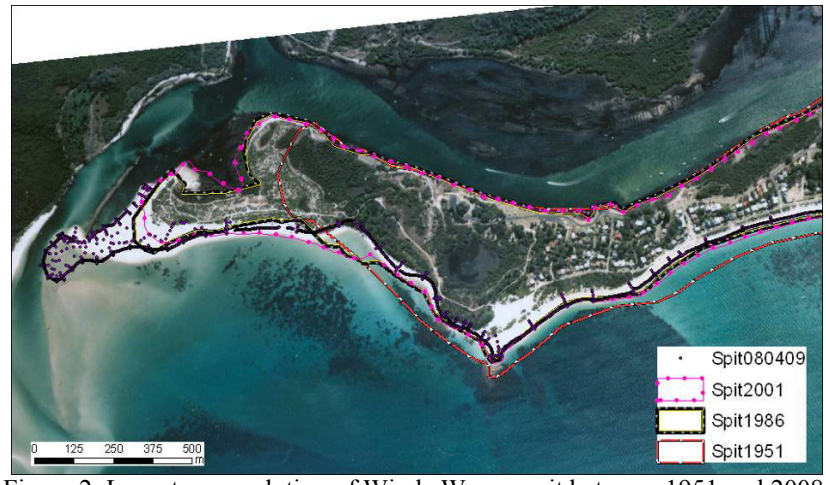

Figure 2. Long-term evolution of Winda Woppa spit between 1951 and 2008.

Medium-term morphologic analyses confirmed long-term trends with intense erosion in Jimmy's Beach (see Profile 1 in Figure 3). There were, however, emergency works that dumped 6000 m^3 in the erosion spot before June's survey and therefore topographic analyses indicate no change (see Profile 4 in Figure 3). The overall evolution of the study area revealed significant changes in the sandwave with the development of a transverse bar (Figure 3).

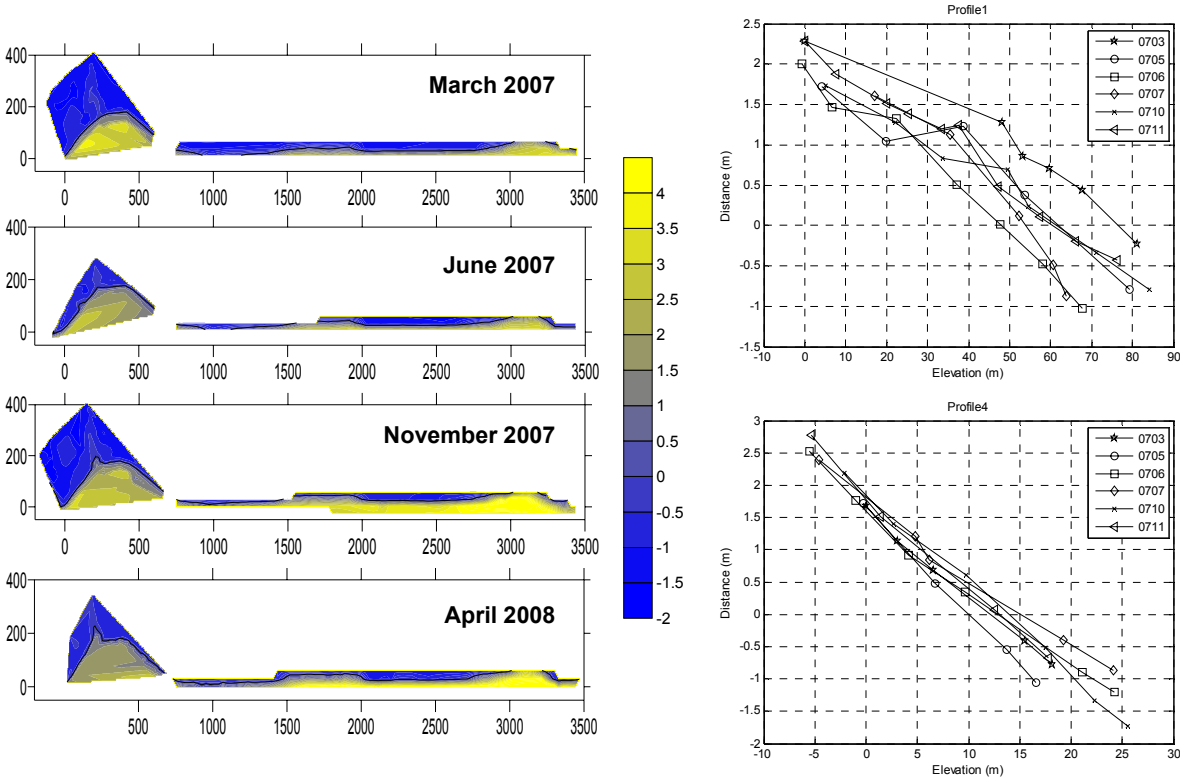

Figure 3. The left panel shows topographic maps of the transformed points using Harley and Turner's (2008) logspiral transformation (the solid black line corresponds to mean sea level). The origin of the logspiral is near the sandwave and thus it is located on the left hand side of the maps, the *x*-axis indicates distance (m) westwards from the sandwave and the *y*-axis corresponds to across-shore distance (m). The right panel shows the evolution of two cross-shore profiles between March and November 2007: Profile 1 is located westward from Jimmy's Beach erosion spot and Profile 4 corresponds to the erosion spot.

The study period was dominated by SE waves that propagate into the estuary (Figure 4) with most of the energy concentrated during the severe storm events of June-July 2007. Beach hydrodynamic measurements undertaken by Ainley (2007) under calm SE conditions in the surf zone showed consistent weak westward currents along the beach that seemed to be modulated by the tidal currents. Strong SE conditions in March and June 2007 near the erosion spot in Jimmy's Beach showed weak eastward currents along the beach (0.08 m s^{-1}) encompassing mean significant heights of 0.46 m. High-energy westerly conditions were recorded in June 2007 westward from the sandwave; results indicated sea development inside the estuary (mean H_s = 0.27 m, Ainley, 2007) that produced negligible currents. Simultaneous hydrodynamic measurements were undertaken in April 2008 and the data are still being processed but preliminary results show existence of null points along the beach and tidal modulation of the nearshore currents and incident waves. Depth averaged currents measured with ADCPs deployed nearby the study area show bi-directional currents off the sandwave with maximum ebbing currents of 0.6 m s^{-1} and maximum flooding currents <0.5 m s^{-1}.

Discussion and concluding remarks

According to Short (2006) there are no definitive studies on the morphodynamics of low energy tide-modified or tide-dominated beaches; they are however, expected to undergo little change given the dominant conditions under which exist. This paper presents however, a low-energy beach system that undergoes severe changes in both the long- and medium-term scales of study. The following zones were identified:

- The sandwave. It is a sandy protrusion that has undergone several cycles of formation/destruction between 1951 and 2008. Existing studies established westerly migration rates of 70 m yr^{-1} between 1993 and 2003 (Cholinski, 2004). This study shows dynamic changes and transverse bar formation (Figure 3). Occurrence of high-energy conditions in June/July 2007 did not seem to cause strong erosion.
- The area between the sandwave and the erosive spot on Jimmy's Beach appears stable and has not undergone significant changes during the study period, neither in the long- or the medium-term.
- The erosive spot on Jimmy's Beach receives high energy under SE storms and did not undergo strong erosion in June/July 2007 because emergency works placed 6000 m^3 in an area approximately 170 m

long. All 6000 m^3 were subsequently removed by the storms indicating an erosion of 35 m^3 m^{-1}. Historic values between 1951 and 2006 indicate shoreline retreat at a rate of 1 m yr^{-1}.

- Winda Woppa spit underwent erosion most of which was caused by the June/July 2007 storms (55 m^3 m^{-1}). In the long-term, this are has been undergoing significant retreat since 1951 and has experienced westward extension of 800 m.

It is expected that detailed hydrodynamic analyses of both the nearshore currents and the ADCP deployments will improve our understanding of the physical processes that drive such changes in estuarine beaches as well as the sediment transport paths and magnitudes including the relation between estuarine beaches and flood-tide deltas. The processes that control sandwave formation and evolution will also be investigated taking into account both sediment source, tidal currents and shoreline instability due to large incident wave angles (i.e., Ashton et al., 2001).

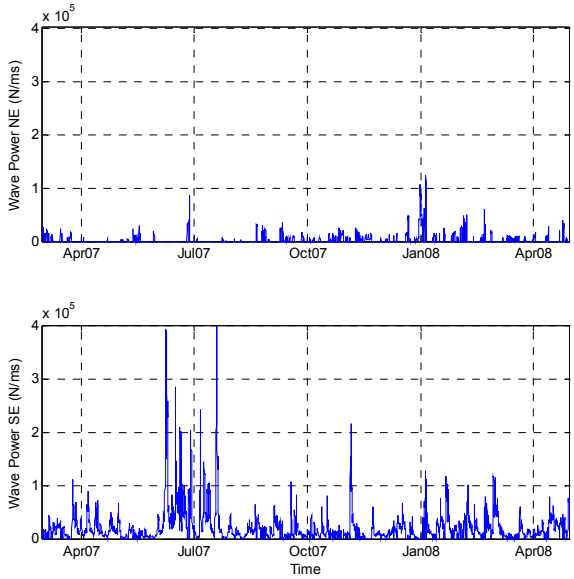

Figure 4. Directional wave power calculated for NE conditions and SE conditions.

Acknowledgements

This study is funded by the Australian Research Council (ARC) in collaboration with the NSW Department of Environment and Climate Change (DECC), DHI Water and Environment, Port Stephens Council, Great Lakes Council and Jimmy's Beach Restoration Society (LP 0668979). Wave data were kindly provided by Manly Hydraulics Laboratory (DECC). Many thanks to Dave Mitchell, Tim Austin, Lara Ainley, Genoveffa Pezzimenti, Hannah Power and all those who helped with fieldwork.

References

Ainley, L. (2007), *Sediment transport on Jimmy's Beach: implications for coastal erosion*. Honours Thesis, School of Geosciences, University of Sydney, 80pp.

Ashton, A.A., Murray, B., Arnoult, O. (2001), Formation of coastline features by large-scale instabilities induced by high-angle waves. *Nature*, 414, 296–300. 15 November 2001.

Cholinski, M. (2004), *Sandwave dynamics at Port Stephens, NSW. School of Geosciences*, University of Sydney, Australia. Honours Thesis. 150pp.

Harley, M.D., Turner, I.L. (2008), A simple data transformation technique for pre-processing survey data at embayed beaches, *Coastal Engineering*, 55(1), 63–68, doi:10.1016/j.coastaleng.2007.07.001.

Roy, P.S., Williams, R.J., Jones, A.R., Yassini, I., Gibbs, P.J., Coates, B., West, R.J., Scanes, P.R., Hudson, J.P., Nichol, S., 2001, Structure and function of south-east Australian estuaries, *Estuarine, Coastal and Shelf Science*, 53, 351–384.

Short, A.D. (2006), Australian beach systems – nature and distribution, *Journal of Coastal Research*, 22(1), 11–27, doi:10.2112/05A-0002.1.

Vila-Concejo, A., Short, A.D., Hughes, M.G., Ranasinghe, R. (2007), Shoreline implications of flood-tide delta morphodynamics. The case of Port Stephens (SE Australia), *Proceedings of Coastal Sediments*, ASCE, New Orleans, 1417–1430.

Dynamics of the Curimataú estuary coastal zone by numerical experiments

FERDANDO P. ANDUTTA[1], LUIZ B. DE MIRANDA[1], PETER V. RIDD[2], LANCE BODE[2]

1. Instituto Oceanográfico, Universidade de São Paulo, Praça do Oceanográfico 191, São Paulo SP 05508120, Brazil
email: andutta@io.usp.br, miranda@io.usp.br

2. School of Physics, Mathematics and Information Technology, James Cook University, Townsville 4811, Queensland, Australia
email: peter.ridd@jcu.edu.au, lance.bode@jcu.edu.au

Keywords: estuary, reefs, circulation, vortices

ABSTRACT

The inner shelf close to the Curimataú tropical estuary in the Rio Grande do Norte (RN) state, northeast Brazilian coast (latitude 06°18′S), is a shallow coastal region (6–15 m) located in the narrowest Brazilian shelf (~10 km). The numerical model Delft3D-Flow was applied to analyze the hydrodynamics on the inner shelf of the Curimataú estuary mouth, located behind small reef on its right side. The whole computational grid is curvilinear with around 6000 damp points, including the inner shelf and its main tributaries. The coastal open boundary condition arose from tidal forcing components (M_2, S_2, N_2, K_2, K_1 and O_1) obtained from tidal analysis of ~2.7 years of hourly heights, recorded in the Natal harbor located 60 km to the north of the estuarine mouth. At the estuary head the fresh water input estimated from the residual flow was distributed between the Curimataú river and its two main tributaries, the Cunhaú and Guaratuba rivers. The previous initial conditions of the simulation were uniform, then after a time period of month of simulation the output data were adjust to the new initial conditions to take into account the baroclinic circulation; due to the small temperature variation it was set a constant value (28°C) typical for this season.

This paper provides a vertical averaged structure of current close to the mouth estuary, that were used in order to analyze the influence of the reefs during a spring tide conditions and at the flood and ebb tides respectively. The reefs were included in the computational grid as thin dams, and their presence has been linked to the generation of small vortices between the reefs and the coast which may cause a deposition processes at its right flank.

Introduction

The Curimataú River estuary (Figure 1) in the Rio Grande do Norte (RN) state, northeast Brazilian coast (latitude 06°18′S), is a partially mixed tropical estuary. This estuarine region has been impacted due to human activities such as: shrimp cultivation, sugar cane plantation, poorly planned urban occupation and so on (Lageoma / IDEMA, 2003; IDEC/RN, 1991). The area of the hydrographic basin is around 3,589 km^2 and ~77% is in the neighbour Paraíba (PA) state.

The estuary is forced by semidiurnal and mesotide with tidal heigth above 2 m in spring conditions. As a result of the combination of the semidiurnal tides, baroclinic forcing and river discharge, the lower reach of the estuary alternates between being partially mixed (type 2b, $\nu = 0.64$) during the neap tide, and being partially mixed but weakly stratified (type 2a, $\nu = 0.99$) during the spring tide (Miranda et al., 2005; Miranda et al., 2006). Numerical simulation of the estuary had shown interesting features in the whole hydrodynamics due to the complex estuary geometry, especially the relative lateral and vertical circulation generated by the centrifugal acceleration and topographic features (Andutta, 2006).

The objective of this paper is to provide a theoretical simulation of the circulation pattern close to the estuary mouth and the reefs influence and its contribution to the sand deposition on its right flank.

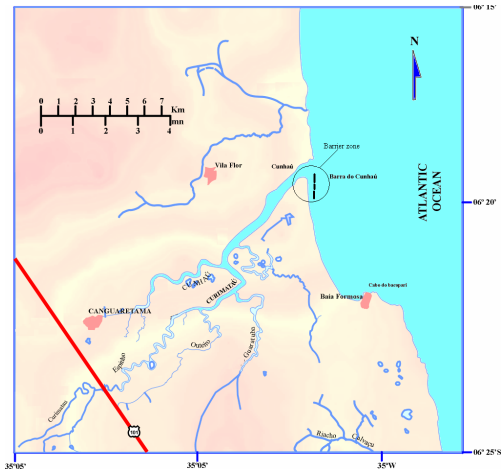

Figure 1. Geographic position of the Curimataú estuary, NE Brazil.

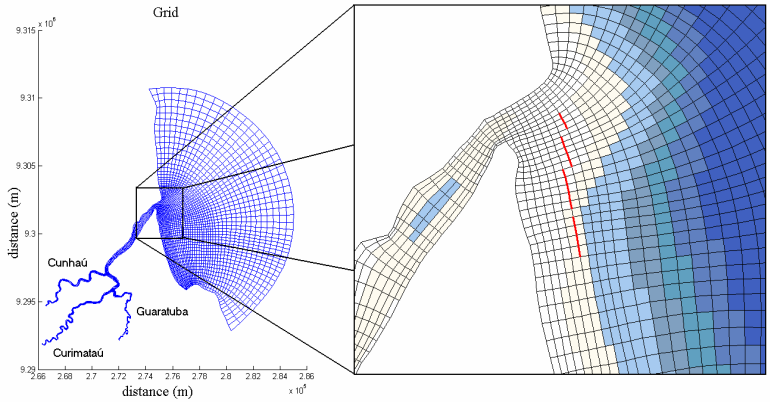

Figure 2. Numerical grid applied to the simulations. In red the reefs representation.

Model evaluation and results

No tide measurements were available in the estuary and the tidal height and phase of the main components used as barotropic forcing was obtained from tidal analysis of an hourly time series of 2.7 years of data from the Natal harbor, located 60 km northward of the estuary, using the methodology of Franco (2000). To confirm the confidence in using the analysis for tidal height and phase as open boundary conditions, the tide prediction for the observation period was compared with the in situ hourly water column height measurements and the quantitative agreement is indicated by the 'skill' mean parameter nearly equal to one (0.98).

Methodology

The numerical model Delft3D-Flow had been applied to the simulation of the Curimataú estuary. The external open boundary conditions arose from tidal height and phase of the 4 main semidiurnal (M_2, S_2, N_2 and K_2) and two diurnal components (K_1 and O_1) that were used as barotropic forcing which were obtained from tidal analysis of a time series of ~16,000 hourly data from the Natal harbor, located approximately 60 km northward of the estuary, using the methodology of (Franco, 2000). Both sides of the external open boundary grid were forced with the same height and phase because only minor differences from both sides have not significant influence. The bathymetry data used to develop the numerical grid (Figure 2) were collected by (Souza, 2004) for the estuarine sections of the grid. For the offshore regions, the bathymetric chart DHN n°.B-800 (1978) was used. For the region close to the estuary mouth where there are some reefs, data from SUDENE (1970) was used. The internal river discharges of the three main rivers Curimataú, Cunhaú and Guaratuba were based in residuals currents with measurements realized along the estuary using a CTD-currentometer Valeport, MKIII model.

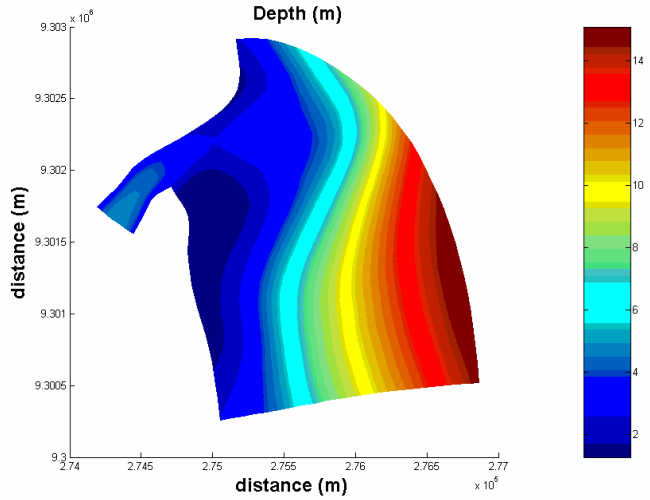

Figure 3. Bathymetry of the Curimataú tropical estuary entrance (color bar scale in meters).

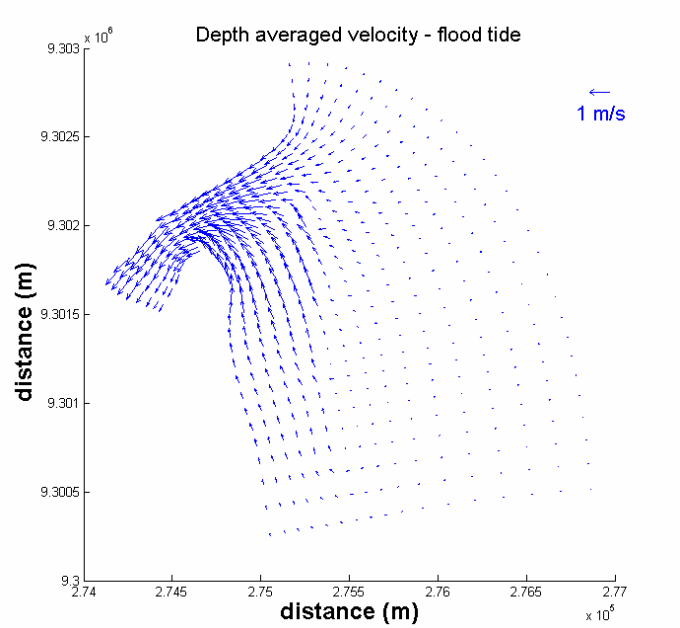

Figure 4. Vertical averaged velocity field in the Curimataú estuary mouth during the flood spring tide.

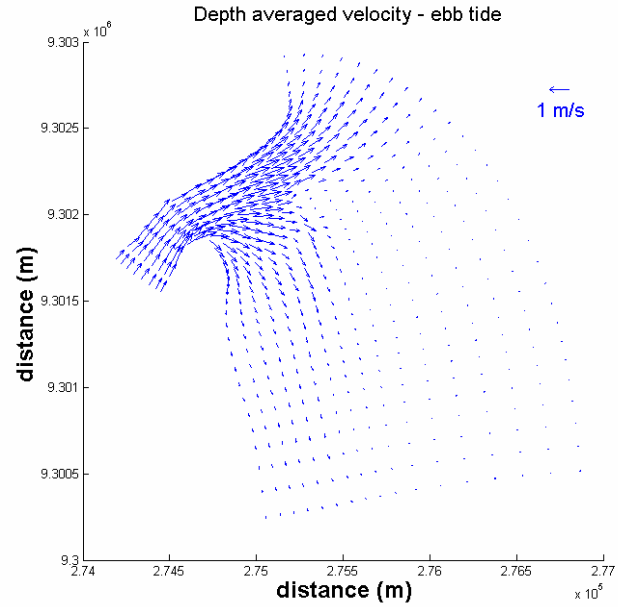

Figure 5. Vertical averaged velocity field in the Curimataú estuary mouth during the spring ebb tide.

A triangular interpolation of the bathymetry data was established and topographic characteristics at the entrance of the Curimataú estuary (Figure 3) indicates the sand bank on the right flank of the mouth, located between the reefs and the coast.

Results

The depth averaged velocity field during the spring tide flood shows the velocity increase as the circulation approach the estuarine mouth, reaching values up to 1 m s^{-1} (Figure 4). The region between the reefs and the coast has prompted also higher values of the velocity than offshore.

The vertical mean current field at the ebb spring tide (Figure 5) also presents a great intensification of the velocity field. The flow out estuary is seen to split into two main patterns; one curving to the right in the region between the reefs and the coast, and the other one flow going in the along shore direction.

As in the flood spring tide the maximum velocities were of the order of 1 m/s, an indication that the estuary circulation was mainly driven by the tide, which is in close agreement with the low estuarine Richardson number ($Ri_e \approx 0.1$) obtained by Miranda et al. (2005).

Conclusions

The numerical simulation of the Curimataú tropical estuary allowed the verification of vortices between the reefs and the coast, which have prompted the deposition of sediments on the south side of the estuarine mouth. In events of flood and ebb tides the geometry of the estuary brings out values of velocity close to 1 m s^{-1}, and during events of high and low tides the velocity falls down to values in a maximum of 0.10 m s^{-1}. The banks observed in the interpolated bathymetry show clearly that deposition is undergoing and depending how fast is the process of deposition, within some years the channel between the reefs and the coast may not exist due to the local deposition.

References

Andutta, F.P. (2006),. *Experimentos e modelagem numérica com aplicação ao estuário tropical do rio Curimataú, RN*. M.Sc. Dissertation, Oceanographic Institute of University of São Paulo, 122pp.

Franco, A.S. (2000), M*ARÉS: Programa para Previsão e Análise*. In: Manual, BSP, São Paulo, 36pp.

Hansen, D.V., Rattray, M. Jr. (1966), New Dimensions in Estuary Classification. *Limnology and Oceanography*, 11(3), 319-325.

IDEC/RN. (1991), *Instituto de Desenvolvimento Econômico e Meio Ambiente do RN. Manguezal: ecossistema ameaçado*. SEPLAN/IDEC, 30pp.

LAGEOMA / IDEMA. (2003), *Mapeamento, Caracterização e Determinação de Potencialidades de uso do Solo para o Estuário do Rio Curimataú – Canguaretama/ Baía Formosa (RN) em Escala 1:10.000*. Relatório Técnico Final, 43pp.

Miranda, L.B., Bérgamo, A.L., Castro, B.M. (2005), Interactions of river discharge and tidal modulation in a tropical estuary, NE, Brazil, *Ocean Dynamics*, 55, 430–440.

Miranda, L.B., Bérgamo, A.L., Silva, C.A.R. (2006), Dynamics of a Tropical Estuary: Curimataú River, NE Brazil, *Journal of Coastal Research*, SI 39, 697–701.

Souza, F.E.S. (2004), *Evolução Morfodinâmica da Região de Influência Estuarina do Rio Curimataú, com Ênfase nas Alterações do Ambiente Deposicional de Manguezal e a Integração de Geodados em SIG*. Ph.D. Thesis, Federal University of Rio Grande do Norte, 150pp.

Vertical structure of subtidal currents in a semiarid coastal lagoon

JUAN A. DWORAK[1], HERIBERTO VAZQUEZ-PERALTA[2], JOSE GOMEZ-VALDES[2], MANUEL PAZ[1]

1. Instituto Tecnológico de Guaymas, Apdo. P. 563, Guaymas, Sonora, Mexico
email: jdworak@cicese.mx, manuelpaz@gmail.com

2. Departamento de Oceanografía Física, CICESE, Ensenada, Mexico
email: hvazquez@cicese.mx, jgomez@cicese.mx

Keywords: coastal lagoon, EOF analysis, meteorological forcing

ABSTRACT

The study of the vertical structure of currents in a stratified fluid, at the entrance of estuaries and coastal lagoons, is useful for the description of the mechanisms that regulate the exchanges with the ocean. For semiarid coastal lagoons, this topic is scarcely reported. In this work, a 5-month time-series of observations were performed at the entrance of Bay of Guaymas; a semiarid system in the Gulf of California. Observations of currents, from a moored ADP, and winds at a terrain station were performed from 28 June to 19 November 2000. Currents were projected along the principal-axis (~94% of the variance). The along-principal-axis components of the time-series were filtered to remove tidal oscillations. The low-frequency signal was split into vertically-integrated and depth-dependent components. The anomaly of the depth-dependent current component was obtained by subtracting the temporal mean at each layer. The vertically-integrated velocity component was highly correlated (negative) with the wind principal-axis component, which suggests a balance between the wind-stress and the bottom-friction. The depth-dependent velocity contributed with ~56% of the variance. EOF analysis of the velocity-anomaly revealed the presence of two modes, with ~75% and ~17% of the variance, respectively. The spatial structure of the EOF modes resembles the first two internal modes of the baroclinc field. The temporal part of the modes was explored by cross-spectral methods. At periods of 7–8 days, wind stress seems to be the mechanisms responsible for the excitation of the modes, while for longer periods (21–24 days), precipitation-evaporation plays a more significant role.

Introduction

Measurements of flows in estuaries and coastal lagoons allow the understanding of the water exchanges with the adjacent ocean. Acoustic current profilers have improved the observations of the current's vertical structure (e.g., Teague et al., 1998; Tsimplis, 2000). The knowledge of the vertical structure of currents helps to elucidate the contributions of the forcing mechanisms that regulate them. Tides are the most important energy source in the Gulf of California's coastal lagoons; in consequence, detiding is necessary in order to decompose the flows into tidal- and subtidal-frequency bands.

Valle-Levinson et al. (2001) documented that in the Bay of Guaymas, in the Gulf of California, the circulation, for late-spring, corresponds to that of an inverse estuary, regulated mainly by horizontal density gradients produced by the excess of evaporation over precipitation. This work describes the vertical structure of the currents, with periods longer than two-day at the mouth of the bay, and the meteorological forcing mechanisms.

Methods

The Bay of Guaymas is situated in the semiarid regions of the eastern-side of the Gulf of California (Figure 1). The semi-major axis (~10 km) is along the coast, and its semi-minor axis (~6 km) is perpendicular to the coast. The bay's area is 33.6 km^2 with an average depth of 2.5 m, and it has a single inlet 1.2-km wide and an averaged 8 m depth.

Current profiles were obtained with a Sontek ADP of 1500 kHz, that was moored 0.7 m from the bottom, at the mouth of the bay. The observations lasted from 28 June to 19 November 2000. The parameters recorded were velocity and sea-surface level. The ADP cells were 0.5 m and a record was taken every 20 mins, with

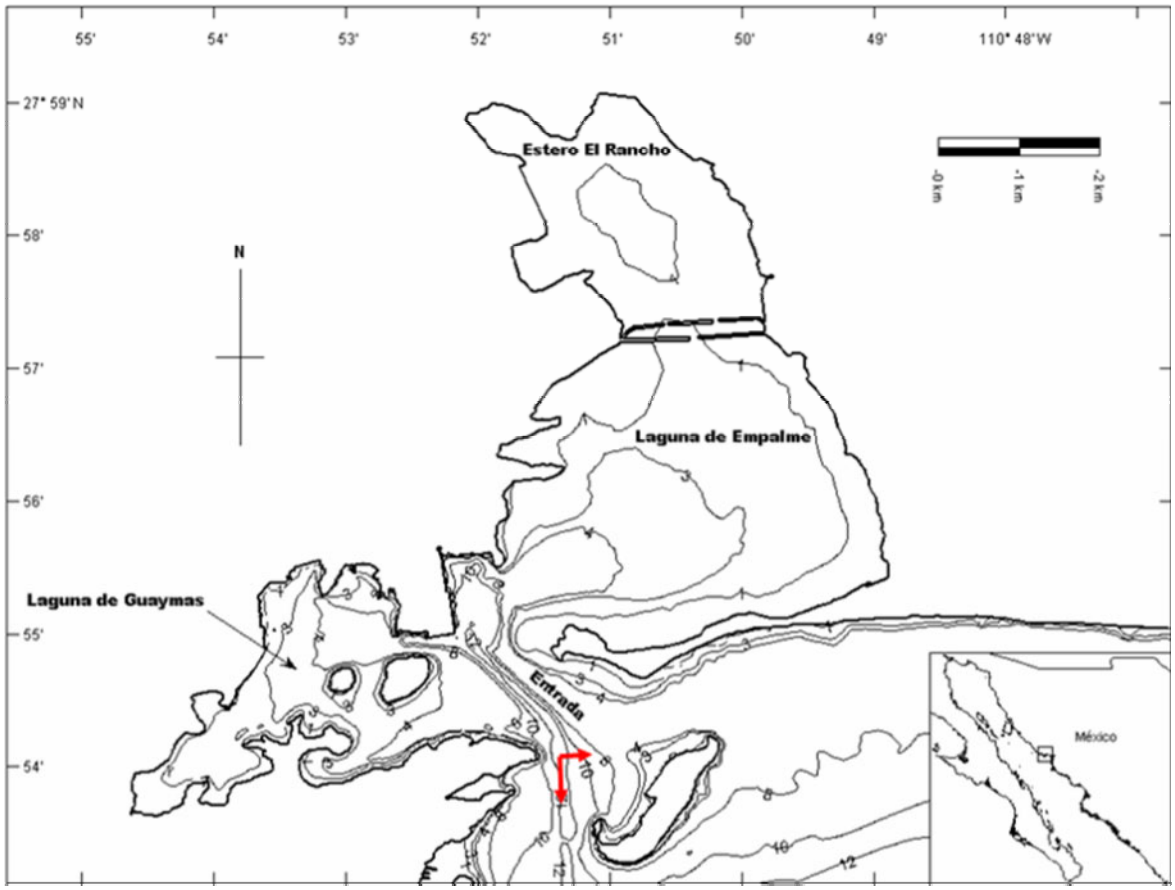

Figure 1. Geographical location of Bay of Guaymas in the Gulf of California. Bathimetry in m, referred to LLW. Arrows show were the ADP was moored, and the orientation of the principal axis.

an averaging of assembles for 3 min to remove waves. Hourly weather data was provided by Comision Nacional del Agua, a federal agency in charge of a weather station nearby. Both, current- and wind-velocity were projected along the principal axis, the maximum variance axis (Valle-Levinson et al., 2001; Dworak and Gomez-Valdes, 2005). For the currents, the explained variance along the principal axis was ~94%, aligned with the South; because of this, the current *v*-component is the only one left. Meanwhile, for the wind, the principal axis concentrated the ~70% of the variance with a direction of ~294°T. The low-frequency signals were separated using a 0.02 cph cutoff frequency. For currents, the low-frequency signal is separated into vertically averaged and depth-dependent one following Teague et al. (1998). The variability of the depth-dependent velocity is separated by Empirical Orthogonal Functions (EOF) (Emery and Thomson, 1998).

Results

The maximum of the low-frequency current velocity was ~11 cm s^{-1} at flow, while at ebb it was of ~ 13 cm s^{-1}. The wind stress was of the order of 10^{-2} m s^2, which agrees with that reported by Valle-Levinson et al. (2001). The low-frequency vertically-averaged current velocity it is shown with that of the wind stress (Figure 2). Most of the time, the wind stress is negatively correlated with the wind stress. The depth-dependent current velocity $v(z)$ had the ~56% of the variance of the total low-frequency current velocity. The EOF decomposition reveals that the first mode has ~75% and the second the ~17%. The EOF analysis reveals a spatial pattern corresponds to those of the dynamic normal modes.

The spectral analysis of the meteorological data (not shown) suggest that for periods of ~7–8 days, wind is the main mechanisms that excited the first two baroclinic modes. For longer periods (~21–24 days), the precipitation-evaporation. The barotropic mode seems to be the result of the balance between the wind-stress and the quadratic bottom friction.

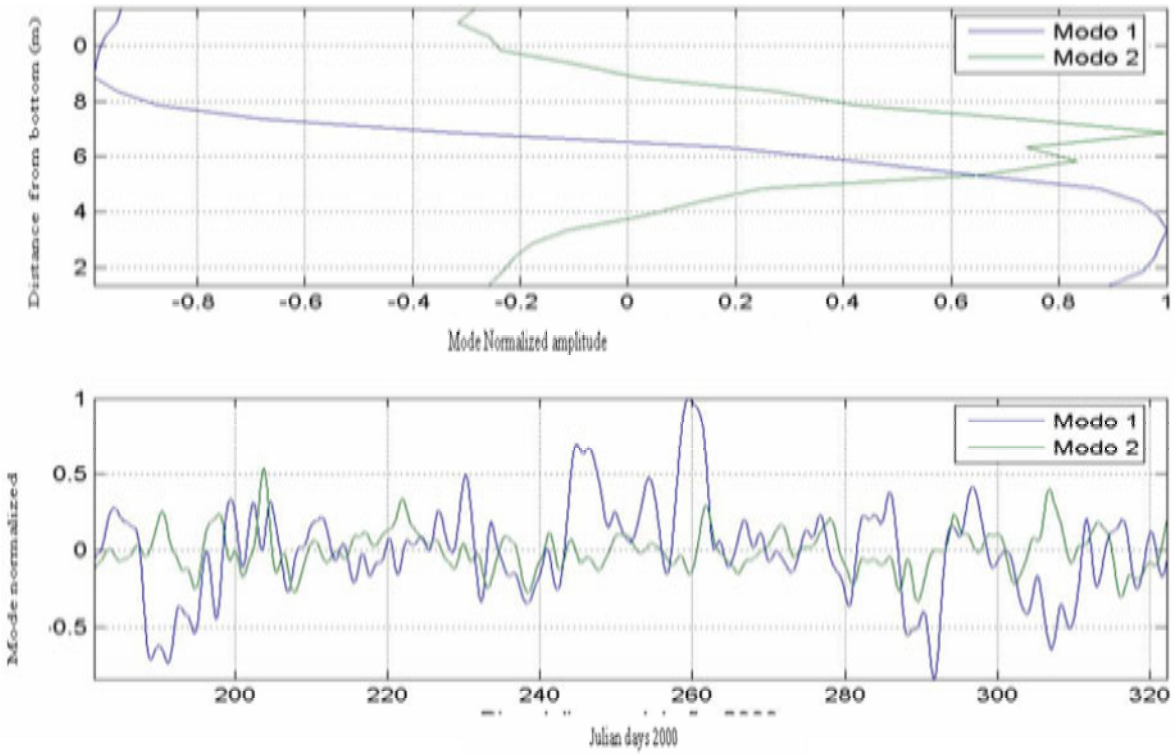

Figure 3. Upper panel. spatial part of the first two EOF modes. Lower panel, the temporal part of the modes.

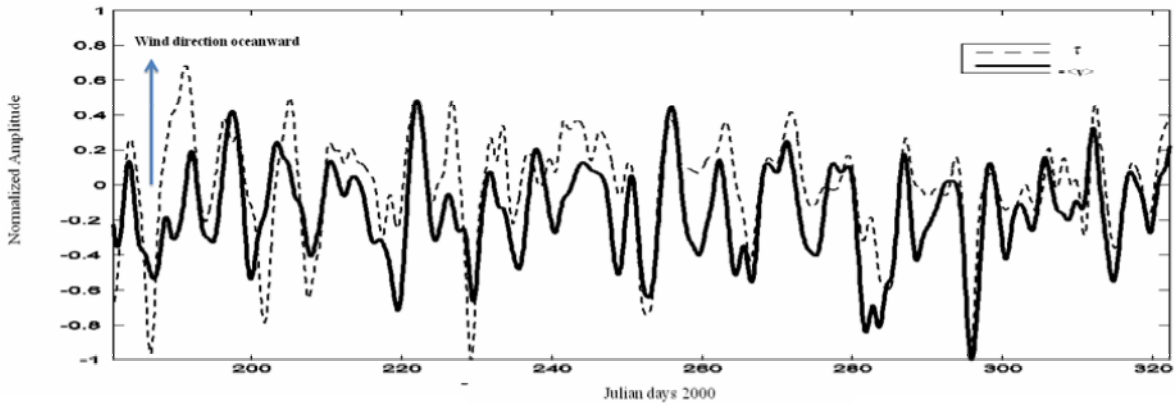

Figure 4. Normalized principal axis, low-frequency wind stress and negative vertically averaged current time series.

The spectral analysis (not shown) of the temporal modes and those of the meteorological variables suggest that for periods of ~7–8 day, wind is the mechanism that excites the two baroclinic modes. For longer periods (~21–24 day), the precipitation-evaporation plays a more important role. As for the barotropic mode, wind stress sets a pressure gradient which is in dynamic balance with the quadratic friction (Figure 4).

Discussion

Wind stress sets a pressure gradient that gives as a result a counter-flow, quadratic friction opposes the flow, so the wind stress and the quadratic bottom friction are collinear. This balance has a period of ~7–8 days.

The first EOF mode shows a pattern similar to the internal wave en a two-layer fluid (Gill, 1982). While the second EOF mode, it seems to be associated to the second internal mode, in which the horizontal velocity is the same in both layers with a maximum in the central part.

Conclusions

It has been found three oscillation modes in the low-frequency currents at the entrance of a semiarid coastal lagoon. The barotropic mode corresponds to the vertically-integrated current, and it is correlated to the wind stress. The two EOF modes seem to correspond to those of the baroclinic internal modes.

References

Dworak, J.A., Gomez-Valdés, J. (2005), Modulation of shallow water tides in at inlet-basin system with a mixed tidal regime, *Journal Geophysical Research*, 110, C01007, doi:10.1029/2003JC001865.

Emery, W.J., Thomson, R. (1998), *Data analysis methods in physical oceanography*. Pergamon Press. Tunbridge Wells. UK 634pp.

Gill, A.E. (1982), *Atmosphere-Ocean Dynamics*. Academic Press, New York. 662pp.

Teague, W.J., Perkins, H.T., Hallock, Z.R., Jacobs, G.A. (1998), Current and tide observations in the southern Yellow Sea, *Journal Geophysical Research*, 103, 783–793.

Tsimplis, M.N. (2000), Vertical structure of tidal currents over the Camarinal Sill at the Strait of Gibraltar, *Journal of Geophysical Research*, 105, 709–728.

Pawlowicz, R., Beardsley, B., Lentz, S. (2002), Classical tidal harmonic analysis including error estimates in MATLAB using T_TIDE, *Computers and Geosciences*, 28, 929–937.

Valle-Levinson, A., Delgado, J.A., Atkinson, L. (2001), Reversing water exchange patterns at the entrance to a Semiarid Coastal Lagoon, *Estuarine, Coastal and Shelf Science*, 53, 825–838.

What causes periodic stratification in Maputo Bay?

JOÃO D. LENCART E SILVA[1], JOHN H. SIMPSON[2]

1. Institute of Marine Research, Centre for Ecological Modelling, DCEA-FCT, Qta. Torre, 2829-516 Monte de Caparica, Portugal
email: j.lencart@gmail.com

2. School of Ocean Sciences, College of Natural Science, Bangor University, Menai Bridge, Anglesey LL59 5AB UK
email: j.h.simpson@bangor.ac.uk

Keywords: periodic stratification, freshwater, buoyancy, tidal straining, subtropical bay

ABSTRACT

Coastal systems, where freshwater is input in a monsoon-like regime, are characteristic features of semi-arid subtropical latitudes. There, sudden increase in rainfall induces large river runoff and creates the conditions for a change in circulation patterns. A system with a marked seasonal variability in freshwater supply and subjected to a wide range of tidal stirring constitutes a good observational testing ground for the theories of buoyancy-stirring interaction and the control of exchange characteristics of estuaries and Regions of Freshwater Influence, ROFIs (Simpson, 1997). Maputo Bay possesses these attributes by being a tidal energetic embayment subjected to large seasonal freshwater and tidal variations.

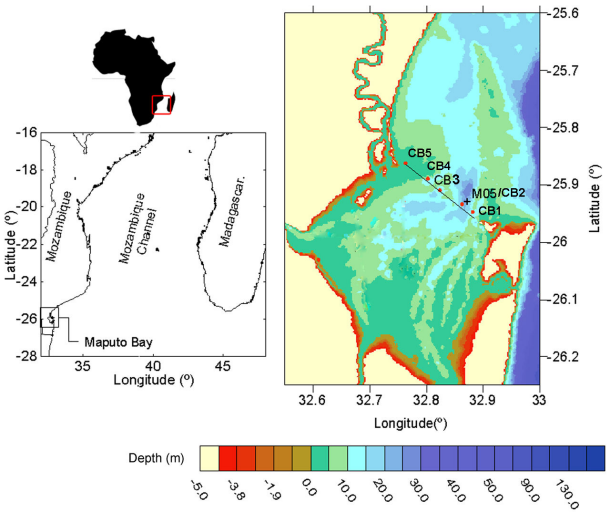

Figure 1. Study location, stations and bathymetry.

Maputo Bay is a tidally energetic embayment located in the south of Mozambique with its centre at 32°47′E, 26°03′S (Figure 1). Its bathymetry is shallow with an average of ~5 m reaching ~30 m at the ocean boundary. The bay opens to the shelf through an 18 km wide inlet, spanning from the Macaneta sand spit on the northwest side to Ilha dos Portugueses on the southeast side. The bay is forced by a semidiurnal tide with a marked spring to neap tide cycle, with velocity amplitudes from ~0.2 in neaps to ~1.2 m s^{-1} (Figure 2a) in springs. The main basin flowing is the Incomati River (Figure 2b). There is a marked seasonality, with most of the flow concentrated in the period

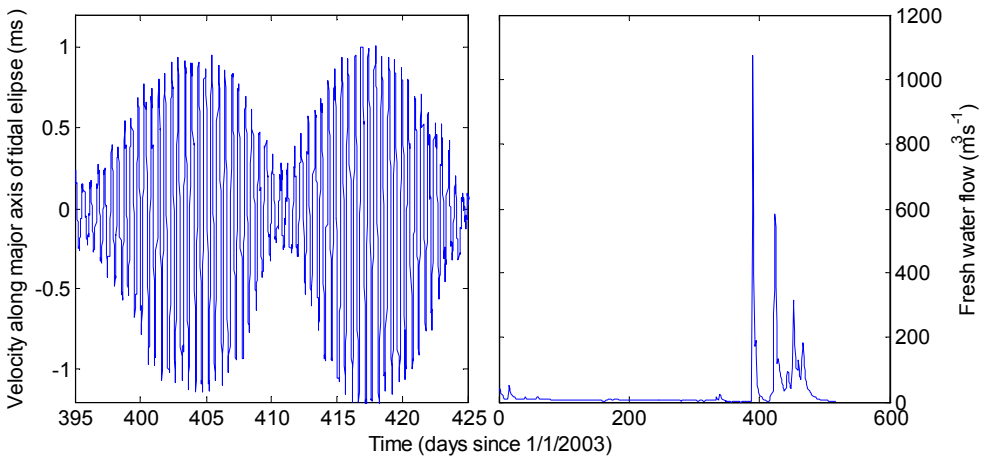

Figure 2. Forcing: a) tidal velocity along major axis of the tidal elipse at M05; b) Incomati river flow.

from January to April. The city of Maputo has a population of about one million people hosting a number of activities with considerable areas of conflict in terms of water uses and sustainability. Thorough characterization of the exchange between bay and shelf is needed to develop robust insight on the persistence within the bay of pollutants from domestic and industrial waste disposal.

A series of observational and modeling experiments showed that in the presence of significant freshwater input and under tidal action, Maputo Bay exhibits periodic stratification across the interface between the bay and the Mozambique Channel. The origin of this periodic change in structure is relevant to the characterization of the transport across the mouth, while a tidally advected stratified plume that exits and enters the bay in an elastic form does not interfere with the residual flow, the local creation of stratification through Strained Induced Periodic Stratification (SIPS, Simpson et al., 1990) will increase the flushing of the bay by enhancing estuarine circulation. The work presented here combines observations with a schematic model of the potential energy anomaly to gauge the relative importance of the several buoyancy and stirring terms.

Observations

The tidal survey analyzed here was taken on 22 March 2004 by sampling sequentially the five stations in the CB section from a 7 m power boat. The sampling cycle was carried out for approximately 11 hours, where a SBE 19plus CTD was hand lowered from the side of the boat. Velocity was measured at M05 where two Aanderaa RCM9 current meters were moored at 2.5 and 14 m from the bottom at a water depth of ~20 m. The spring tide survey begins near high water with some significant stratification, ~15 J m^{-3} encountered in the deep part of the transect (M05, Figure 1). When tidal velocity reaches its maximum, the structure has been eroded into a vertically-mixed water column as shown by the near zero values of Φ. Near low water slack, stratification develops throughout the section enduring longer in the deepest part of the transect (~10 J m^{-3}). During the following flood, stratification is again eroded throughout the section, reappearing only in the deepest part near high water.

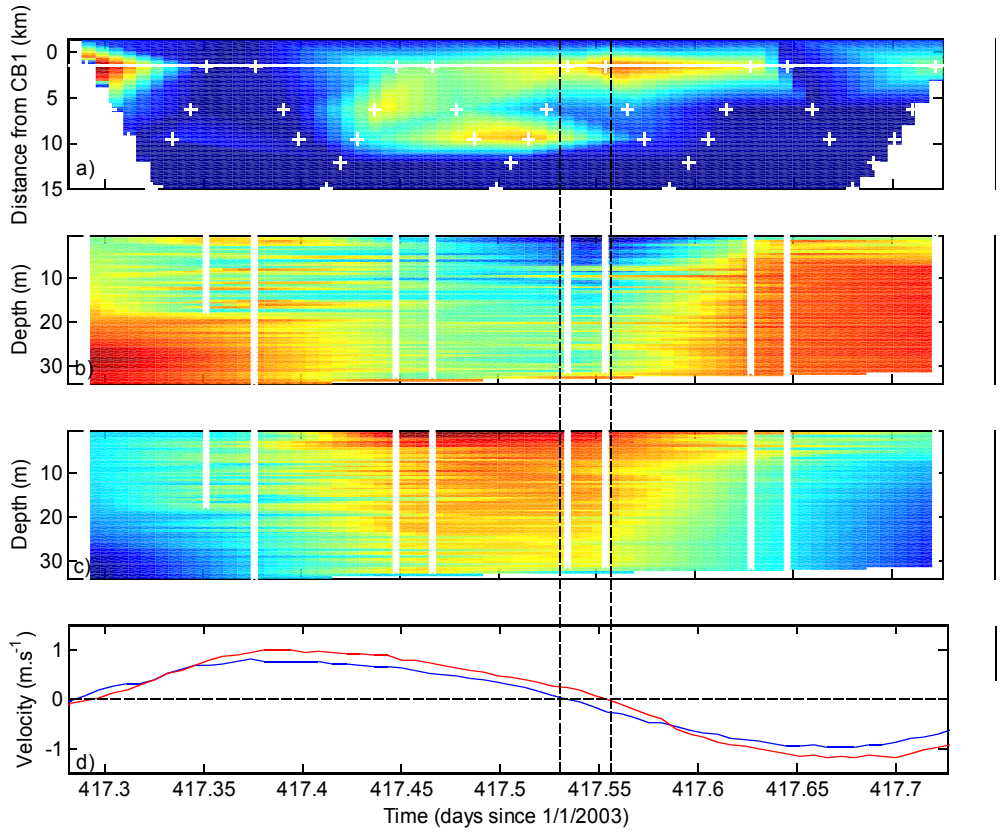

Figure 3. Water column properties at CB section semidiurnal tidal cycle during spring tide: a) potential energy anomaly variation; b) salinity profile at M05(CB2); c) temperature profile at M05(CB2); d) velocity at M05 marked in white across the top panel (red – bottom current meter, blue – top current meter). Vertical lines mark low water slack.

Three main features should be noted:

i) the transient stratification observed at the end of the ebb coincides with the maximum top to bottom displacement in the density up-gradient direction;
ii) the asymmetry about low-water in the density cycle where stratification was eroded faster during the flood;
iii) the sudden stratification at high-water due to the temperature vertical profile.

These suggest that the observed stratification mainly results from the tidal straining of the horizontal density field during the ebb and to advection of temperature stratified water from the shelf during high water. To test the local importance of straining, a model depicting the production and erosion of stratification is presented using potential energy anomaly as a measurement of the stability of vertical stratification.

The potential energy anomaly model

Potential energy anomaly (Φ) is defined as the amount of work required to bring about complete vertical mixing (Simpson et al., 1978) and can be written as:

$$\Phi = \frac{1}{h}\int_{-h}^{0}(\hat{\rho}-\rho)gz\,dz, \quad \text{with} \quad \hat{\rho} = \frac{1}{h}\int_{-h}^{0}\rho\,dz \tag{1}$$

where ρ is seawater density, h is depth and g acceleration due to gravity.

The positive contributions to Φ come from buoyancy input from heating, pycnocline intensification by velocity shear due to estuarine circulation and tidal straining of the density field. The negative contributions come from bottom tidal mixing, surface wind mixing and convective overturning from the action of the tidal velocity profile over the density field in the down-gradient direction (Simpson et. al., 1990). For the present model, the heating term was disregarded since full heat storage capacity of the bay was already attained at the time of the semidiurnal campaigns. These terms are expressed as:

$$\frac{\partial\Phi}{\partial t} = \left(\frac{\partial\Phi}{\partial t}\right)_{STR} + \left(\frac{\partial\Phi}{\partial t}\right)_{E} - \left(\frac{\partial\Phi}{\partial t}\right)_{Mixing}. \tag{2}$$

For the straining term, a velocity profile is obtained from the top current meter at M05 using the Bowden and Fairbairn (1953) parameterization and extracting from it the depth averaged velocity, $\hat{u}$:

$$u(\zeta) = \hat{u}(a + b\zeta^2) \tag{3}$$

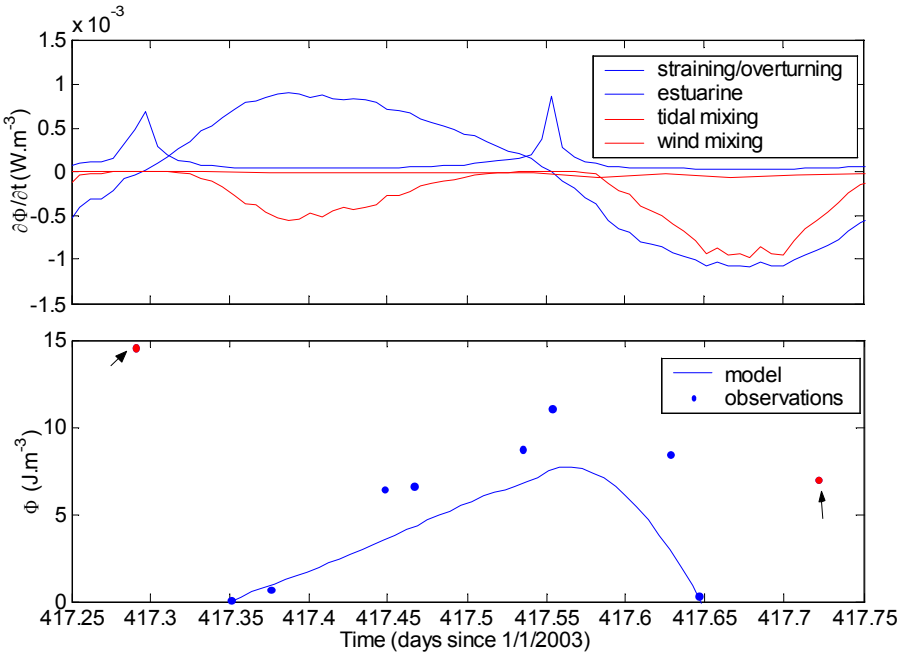

Figure 4. Φ-model results: top panel: comparison of each of the terms of (2); bottom panel: Φ model and observations compared; points marked in red correspond to shelf water characteristics.

Considering the horizontal density advection $\frac{\partial \rho}{\partial t} = -u\frac{\partial \rho}{\partial x}$ and assuming a depth independent $\frac{\partial \rho}{\partial x}$, taking the time derivative of (1) and substituting,

$$\frac{\partial \Phi}{\partial t} = \frac{g}{h}\frac{\partial \rho}{\partial x}\int_{-1}^{0}(u-\hat{u})z\ dz. \tag{4}$$

Substituting (3) in (4) and integrating:

$$\left(\frac{\partial \Phi}{\partial t}\right)_{STR} = 0.031 g h \hat{u}\frac{\partial \rho}{\partial x}. \tag{5}$$

For the estuarine circulation term, velocity can be represented using a steady state flow equation that balances the pressure gradient against frictional forces from Officer (1976), that substituting in (4) and integrating over depth, with h u $N_z = 3.3 \times 10^{-1}\ \hat{u}h$, following Bowden (1953), result in:

$$\left(\frac{\partial \Phi}{\partial t}\right)_{E} = \frac{1}{320}\frac{g^2 h^4}{N_z \rho}\left(\frac{\partial \rho}{\partial x}\right)^2. \tag{6}$$

The mixing terms according to Simpson and Bowers (1984) can be expressed as:

$$\left(\frac{\partial \Phi}{\partial t}\right)_{Mixing} = \varepsilon\kappa\rho\frac{|\hat{u}|^3}{h} + \delta\kappa_s\rho_s\frac{|W|^3}{h}, \tag{7}$$

where ε and δ are mixing efficiencies by tide and wind respectively, the drag coefficient on the sea-bed κ and at the surface κ_s. The value for $(1/\rho)\,\partial\rho/\mathrm{d}x = 1.4 \times 10^{-7}\ \mathrm{m}^{-1}$ was found by taking the density gradient along the major axis of the tidal ellipse, calculated using the depth averaged density difference between high water and low water casts divided by the tidal cycle excursion during the same period inferred from the top RCM9 at M05.

The terms in (2) were forward integrated from $\Phi = 0$ at $t = 417.35$ when the water column was totally mixed. In Figure 4 top, the separate contributions to the rate of change in Φ are plotted showing that the main contribution is given by tidal straining. In the bottom panel, the modeled Φ is plotted together with observations. The simulated results (blue line) describe reasonably well the behavior of the observed Φ (dots). Taking into consideration that far-field advection is not included in the model, these results show that:

- the observed Φ is explained both in magnitude and in phase by the local cycle of production and erosion of stratification;
- the local Φ cycle is mainly due to the straining term with some contribution of estuarine circulation to the production of stratification and tidal stirring to the erosion of stratification.

The stratification asymmetry about low-water is reproduced by the model. This can only be explained including tidal straining and overturning, which creates stratification against tidal stirring during the ebb and erodes stratification with tidal stirring during the flood, thus causing the asymmetry Φ production in (2). This resolves the eventual ambiguity between Φ locally produced and advected from the inner bay given that the latter would be symmetrical about low-water. The only symmetry about low-water is found in the high-water structures, the same that the model cannot explain locally (Figure 4, red dots). Additionally, the timing of these structures coincides with the maximum excursion into the bay. Hence, these can only be occurrences of stratified shelf water advected from the Delagoa Bight.

References

Bowden, K.F. (1953), Note on wind drift in a channel in the presence of tidal currents, *Proceedings of the Royal Society of London*,A219, 426–446.

Bowden, K.F., Fairbairn, L.A. (1952), A determination of the frictional forces in a tidal current, *Proceedings of the Royal Society of London*, A212, 371–392.

Officer, C.B. (1976), *Physical oceanography of estuaries (and associated coastal waters)*. New York, Wiley.

Simpson, J.H., Allen, C.M., Morris, N.C.G. (1978), Fronts on Continental-Shelf, *Journal of Geophysical Research*, 83(C9), 4607–4614.

Simpson, J.H., Bowers, D. (1981), Models of Stratification and Frontal Movement in Shelf Seas, *Deep-Sea Research*, 28(7A), 727–738.

Simpson, J.H., Brown, J., Matthews, J., Allen, G. (1990), Tidal straining, density currents, and stirring in the control of estuarine stratification, *Estuaries*, 13(2), 125–132.

Simpson, J.H. (1997), Physical processes in the ROFI regime, *Journal of Marine Systems*, 12, 1–4.

Simpson, J.H., Sharples, J. (1991), *Dynamically-active models in prediction of estuarine stratification*. In: Dynamics and Exchange in Estuaries and Coastal Zone, Prandle., D. (Ed.), Washington D.C., AGU. Vol. 40, pp101–113.

The role of advection on estuarine hydrodynamics

PENG CHENG, ARNOLDO VALLE-LEVINSON

1. Civil and Coastal Engineering, University of Florida, P.O. Box 116580, Gainesville FL 32611-6580, USA
email: arnoldo@ufl.edu, cheng@coastal.ufl.edu

Keywords: lateral circulation, advection, estuarine hydrodynamics

ABSTRACT

For several decades it has been assumed that the basic, lowest order, hydrodynamics of the along-estuary flow is determined by the balance between pressure gradient accelerations and stress divergence, or frictional effects (e.g., Pritchard, 1956). The flow resulting from this momentum balance consists of a vertically sheared exchange flow with near-surface outflow and inflow underneath. Bathymetric variations across the estuary can alter the vertically sheared exchange flow into a laterally sheared exchange flow that exhibits outflow throughout the water column over the shallow parts and inflow in the deep parts (e.g., Wong, 1994). The inclusion of Earth's rotation effects in the basic estuarine hydrodynamics explains different exchange patterns as a function of the Ekman number (Kasai et al., 2000), which is the ratio of frictional to Earth's rotational effects. At low Ekman numbers, under weak or no friction (nearly geostrophic dynamics), the estuarine exchange is vertically sheared. At high Ekman numbers, under frictionally dominated dynamics, the exchange is laterally sheared. The exchange patterns can also be laterally sheared at low Ekman numbers (i.e., under weak frictional influence) in wide systems, wider than the internal radius of deformation (Valle-Levinson, 2008).

The above exchange patterns result from linear hydrodynamics. However, it has been recognized that the nonlinear advective terms, related to lateral circulation in estuaries, may be as important as the pressure gradient and are crucial to the basic hydrodynamics in estuaries (Lerczak and Geyer, 2004). The lateral structure of the advective terms could be of similar shape as the pressure gradient and help reinforce the vertically sheared exchange flow. So a crucial question related to understanding the basic hydrodynamics of estuaries has arisen: which is more relevant to the hydrodynamics, advection or rotation? In order to begin to address this question, a series of 21 numerical experiments were carried out over simplified but laterally varying bathymetry.

Methods

In order to characterize the relative contribution of all terms to the along-estuary momentum balance, a total of 21 numerical experiments were carried out. The numerical experiments were executed with the Regional Ocean Modeling System (ROMS) over a rectangular channel with a triangular shaped bottom of maximum depth of 10 m at the axis of the channel (e.g., Figure 1). The initial conditions consisted of a depth-independent longitudinal density gradient of 1×10^{-4} kg m^{-4} and a prescribed river flow of 2 cm s^{-1} at the upstream boundary. The density gradient was allowed to self-adjust under the influence of gravity for 60 days. The influence of two parameters, the eddy viscosity and the width of the channel, on the exchange hydrodynamics was investigated. Up to eight different widths and three different eddy viscosity values were tested. The eddy viscosities prescribed on each simulation were constant in space and time. Each of three groups of experiments had eddy viscosity values of 10 (intermediate friction), 1 (low friction) and 100 (high friction) $\times 10^{-4}$ m^2 s^{-1}, respectively. Eight experiments, changing the width of the channel, were run for the first group of intermediate friction conditions; five experiments were executed for the low friction group; and eight more experiments were performed for the high friction group.

Results were analyzed in terms of the lateral structure of exchange flows and of the relative contribution of each dynamic term to the overall momentum balance in the along-estuary direction. The terms extracted from each numerical experiment were the total pressure gradient $\rho^{-1} p_x$, the vertical component of the stress divergence (or friction) $A_z u_{zz}$, Coriolis acceleration fv, lateral advection $vu_y + wu_z$, and axial advection uu_x.

Results

The first group of eight experiments with intermediate friction ($A_z = 10 \times 10^{-4}$ m^2 s^{-1}) showed that width was crucial in determining whether the exchange flow was vertically sheared or laterally sheared. As illustrated in a subsample of three out of the eight experiments, vertically sheared exchange flow developed in narrow channels and laterally sheared flows occurred in wide channels (Figure 1). Intermediate width channels exhibited a combination of vertically sheared and laterally sheared exchange flows. These patterns could be explained with the relative contribution of each dynamic term. For every width, the dominant terms were the pressure gradient and the frictional term but the lateral advective term is quite influential in narrow systems (Figure 2). The relative importance of lateral advection decreases while the influence of Coriolis accelerations increases as the width of the channel increases (Figure 2). The importance of axial advection is minimal, regardless of the width of the channel, because of the along-estuary uniformity in the channel.

The group of five experiments with low friction ($A_z = 1 \times 10^{-4}$ m^2 s^{-1}) showed slightly different lateral structure of exchange flows from the pattern obtained with intermediate friction (Figure 3). In these low friction cases, the exchange flow was vertically sheared for most cases explored. However, the wider the channel became, the more the exchange flow developed lateral shears (partially seen in Figure 3). The relative contribution of each term to the overall dynamics was consistent with the previous set of experiments. Lateral advection contributed to balance pressure gradient and friction for narrow channels (Figure 4). In wide channels, it was Coriolis accelerations that contributed to balance the pressure gradient and friction.

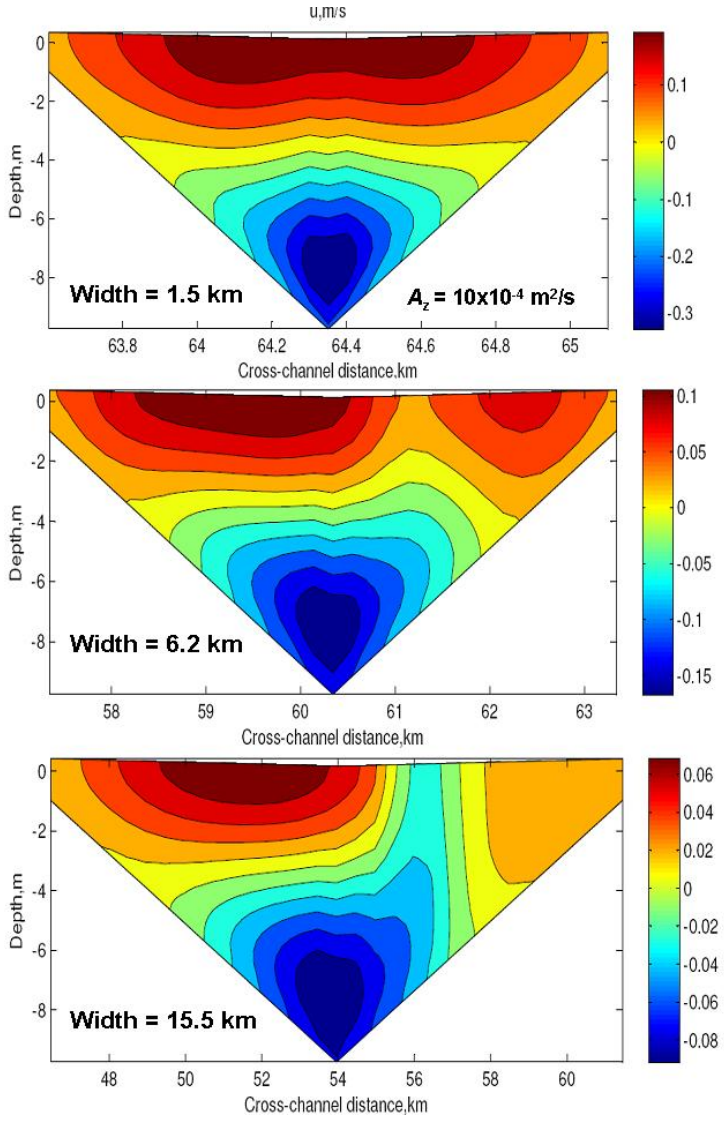

Figure 1. Cross-section of exchange flows (m s^{-1}) under moderate friction (looking into the estuary). Positive values (red and yellow) indicate outflow.

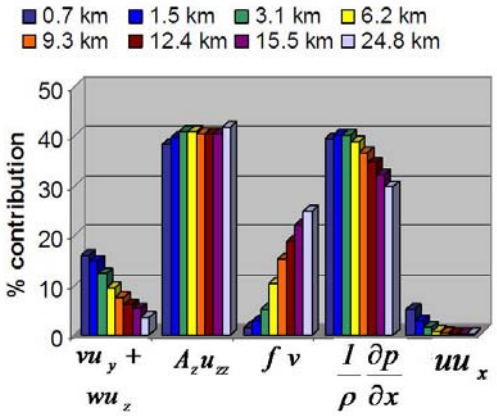

Figure 2. Relative contribution of each momentum term to the overall dynamics, at the estuarine cross-section illustrated in Figure 1, for different channel widths (shown in different colors).

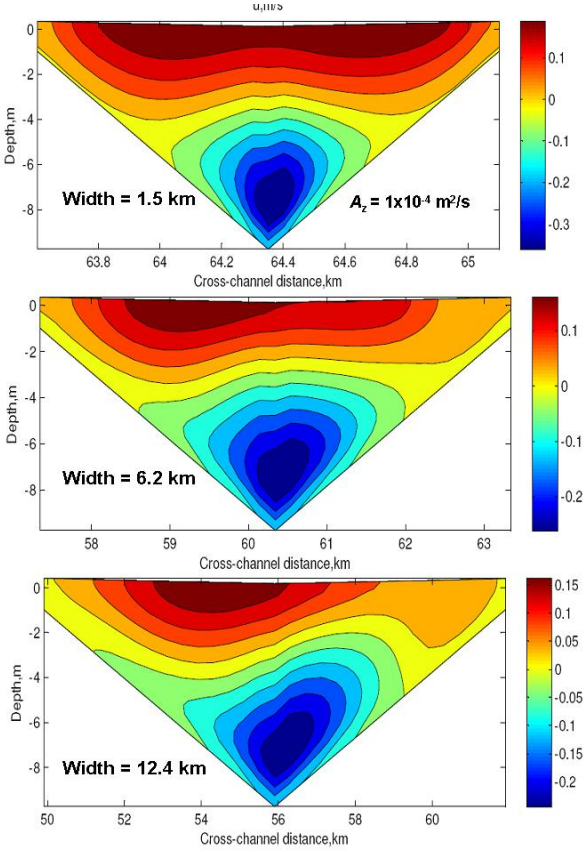

Figure 3. Same as Figure 1 but for experiments with low friction.

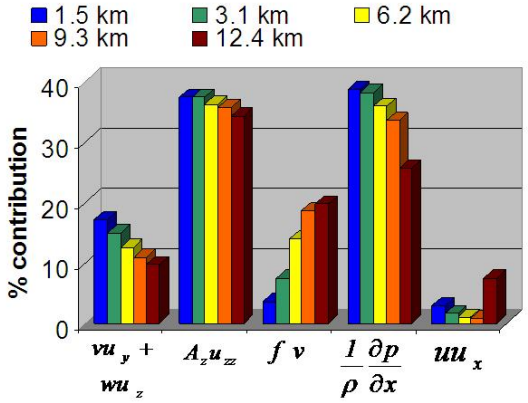

Figure 4. Same as Figure 2 but for weak friction.

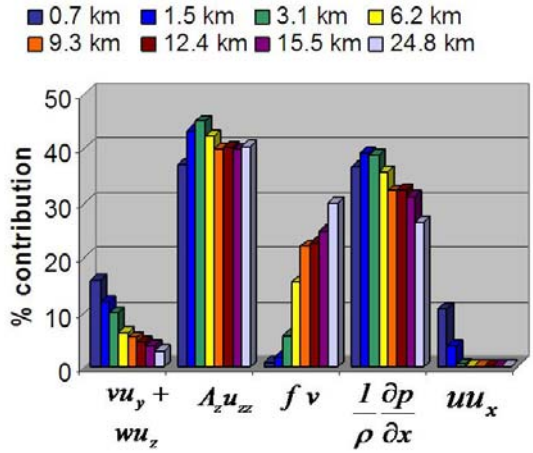

Figure 5. Same as Figure 2 but for strong friction.

The third set of eight experiments with increased friction (Az = 100 × 10^{-4} m^2 s^{-1}) showed exchange flows that were preferentially sheared in the horizontal rather than in the vertical direction (not shown). This pattern was consistent with previous findings (e.g., Wong, 1994; Valle-Levinson, 2008). Only the narrow channel exhibited vertically sheared exchange flows. This was likely produced by the lateral advection terms as suggested by Lerczak and Geyer (2004). However, as the channel width increased, the relative contribution from advection became negligible (Figure 5).

Further experiments with different channel depths explored the transition from advection-dominated to Coriolis-dominated scenarios. The relative contribution between Coriolis and advection can be characterized through the non-dimensional Rossby number. The experiments indicated that the transition occurred at a Rossby number of 0.5. Below this number the channel was wide and shallow, causing advective accelerations to be irrelevant to the dynamics. Above the critical Rossby number of 0.5 the channel was deep and narrow, and advection became dominant to the dynamics.

Conclusions

The results of these experiments indicate that the importance of lateral advection to the along-estuary dynamics depends on the width and depth of the estuary. Lateral advection contributes as much as pressure gradient or friction in narrow and deep estuaries. Lateral advection becomes irrelevant and Coriolis becomes important to the dynamics in shallow and wide estuaries. The transition from Coriolis being relevant to advection becoming important in the estuarine dynamics occurred around a Rossby number of 0.5.

References

Kasai, A., Hill, A.E., Fujiwara, T., Simpson, J.H. (2000), Effect of the Earth's rotation on the circulation in regions of freshwater influence, *Journal of Geophysical Research*, 105(C7), 16961–16969.

Lerczak, J.A., Geyer, W.R. (2004), Modeling the lateral circulation in straight, stratified estuaries, *Journal of Physical Oceanography*, 34, 1410-1428, 2004.

Pritchard, D.W. (1956), The dynamic structure of a coastal plain estuary, *Journal of Marine Research*, 15, 33–42.

Valle-Levinson, A. (2008), Density-driven exchange flow in terms of the Kelvin and Ekman numbers, *Journal of Geophysical Research*, 113, C04001, doi:10.1029/2007JC004144.

Wong, K.-C. (2004), On the nature of transverse variability in a coastal plain estuary, *Journal of Geophysical Research*, 99(C7), 14209–14222.

Barotropic optimization of a pre-operational circulation model

[1]BJARNE BÜCHMANN, CARSTEN HANSEN[1]

1. Royal Danish Administration for Navigation and Hydrography (RDANH),
P.O. Box 1919, 1023 Copenhagen, Denmark
email: bjb@frv.dk

Keywords: circulation model, bathymetry, bottom friction

ABSTRACT

A method is described to modify a model bathymetry in an iterative way to improve surge forecasting in the North Sea region. The method is applied to a pre-operational setup of the circulation model GETM (General Estuarine Transport Model, see http://getm.eu) thereby increasing the forecasting skill in Danish waters. Subsequently, the customized model setup has been implemented for operational use at RDANH for computation of oceanographic forecasts in the North Sea–Baltic Sea coupled system (see www.frv.dk/en/ifm) to increase safety at sea in Danish waters.

To correctly forecast currents, elevations and density in the inner Danish waters, it is imperative that the surges and tidal waves in the North Sea area are predicted with high accuracy. In the present study the modeled M_2 tide has been tuned to match observations by application of small successive modifications of the model bathymetry and bottom friction. Regional changes of bathymetry mean depth have been pre computed based on simple linear shallow water theory, and expected shifts of phase of the modeled tidal wave have been obtained. In parallel, bottom roughness has been modified to improve modeled wave amplitude. An increased wave amplitude in the German Bight gave surprisingly positive effects on the phase in the inshore Danish waters, where the modeled tide now was correctly delayed one hour. The effect gives insight into interference phenomena in the Skagerrak tidal pattern.

The Liverpool Bay Coastal Observatory

M. JOHN HOWARTH, ROGER PROCTOR, CHRIS BALFOUR, PHILIP J. KNIGHT,
MATTHEW PALMER, ROSE J. PLAYER

Proudman Oceanographic Laboratory, 6 Brownlow Street, Liverpool L3 5DA UK
email: mjh@pol.ac.uk, rp@pol.ac.uk, cabal@pol.ac.uk, pjk@pol.ac.uk,
rolm@pol.ac.uk, rose@pol.ac.uk

Keywords: Irish Sea, Coastal Observatory

ABSTRACT

A pre-operational Coastal Observatory has been operating since August 2002 in Liverpool Bay, Irish Sea. Its rationale is to develop the science underpinning the ecosystem based approach to marine management, including distinguishing between natural and man-made variability, with particular emphasis on eutrophication and predicting possible impacts of climate change. Liverpool Bay has strong tidal mixing, receives fresh water principally from the Dee, Mersey and Ribble estuaries, each with different catchment influences, and has enhanced levels of nutrients. Horizontal and vertical density gradients are variable both in space and time. The water column stratifies intermittently. The challenge is to understand and model accurately this variable region which is turbulent, turbid, receives enhanced nutrients and is productive.

The Observatory, with emphasis on physical and chemical / biological variables, has three components, for each of which the goal is at least some (near) real time operation – measurements; coupled 3-D hydrodynamic, wave and ecological numerical models; a data management and web-based data delivery system, see http://coastobs.pol.ac.uk (Howarth et al., 2006). In the next few years the Observatory will expand in spatial coverage and in capability, for instance through the deployment of gliders, forming a focus for Irish Sea studies.

Measurements

The integrated measurements are designed as a whole to test numerical models, provide a framework and basis for process studies and have as a major objective obtaining multi-year records, covering tidal, event (storm / calm / bloom), seasonal and inter-annual time scales. The four main strands, each on different complementary space or time scales are, Figure 1:

a) fixed point time series (both in situ and shore-based); very good temporal and very poor spatial resolution.
b) regular (nine times per year) spatial water column surveys on a 9-km grid; good vertical resolution for some variables, limited spatial coverage and resolution, and limited temporal resolution.
c) HF radar for surface currents and waves; very good temporal resolution, limited spatial resolution (4 km grid) and range (~75 km) (Howarth et al., 2007).
d) an instrumented ferry on the Birkenhead to Dublin route; along track 100-m resolution, crossing there and back most days (Balfour et al., 2007).

These measurements are supplemented by weekly composite (because of cloud cover) satellite images of sea surface temperature, suspended sediment and chlorophyll; excellent horizontal resolution for surface properties, poor temporal coverage.

The fixed point time series measurements include shore based tide gauges, a meteorological station on Hilbre Island at the mouth of the Dee, two in situ sites, one by the Mersey Bar, measuring waves and the vertical structure of current, temperature and salinity, along with a surface CEFAS SmartBuoy whose measurements include nutrients (Mills et al., 2005). Offshore surface data are transmitted in near real time to the laboratory via the Orbcomm low earth orbit satellite e-mail system. Some subsurface data are also telemetered to the surface via an acoustic modem for onward transmission. In addition river flows are gauged by the Environment Agency.

The cruises, to service the two in situ sites and conduct the water column surveys, on R.V. Prince Madog, a coastal research vessel, have attracted significant extra interest including making increased measurements of

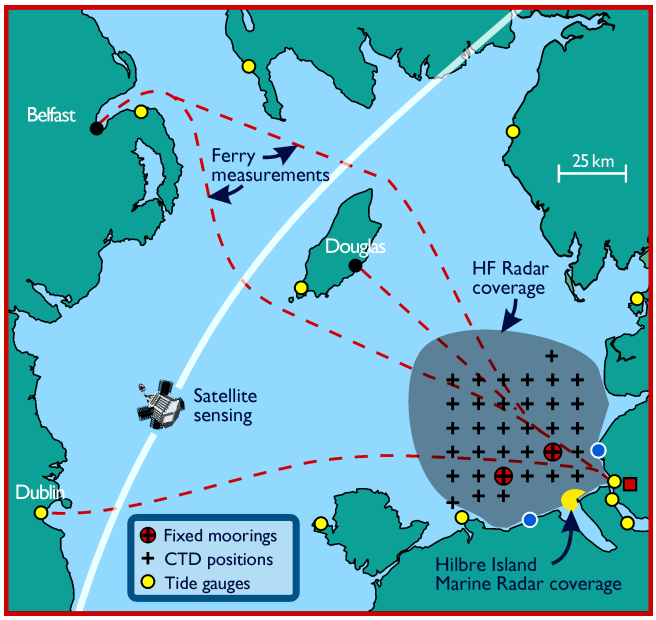

Figure 1. Scheme of measurements.

nutrients with now an on board analyzer on some cruises, grab sampling, swathe-bathymetry, microbial degradation measurements, and twice yearly benthic biological sampling at the two in situ sites. The suite of measurements is being enhanced with on board pCO_2 measurements, now routine showing at times Liverpool Bay is a net source of CO_2 and at other times a net sink. Dissolved oxygen is being measured on the ferry, as well as temperature, conductivity, fluorescence and turbidity, and at the surface and bed at the Mersey Bar site (seen as another avenue for estimating productivity).

Modeling

A suite of coupled 3-D hydrodynamic, wave and ecological models forced by forecast meteorology is being developed. The model domains are nested from a 12-km grid for the ocean / shelf domain, to 7 km for the northwest European continental shelf, to 1.8 km for the Irish Sea, finally to 180 m for Liverpool Bay. Seeking to make realistic real time forecasts for comparison with measurements is difficult since the forecast will only be as good as the forcing data, for instance meteorological inputs from numerical models should be on a spatial scale comparable with the oceanographic models'. Also river flow data need to be in real time (climatological mean data are not good enough, especially for local models). To obtain maximum benefit from the measurements, data are being assimilated into the models – a start has been made with satellite sea surface temperature, HF radar and ferry data.

The measurements and model results are displayed on the web site (http://coastobs.pol.ac.uk), from where they can also be downloaded. Access to the data is free – the largest groups of users are the general public, researchers and education. We are seeking to establish better links particularly with local authorities and central government but also with commercial users to improve applicability and usage. The data are banked with the British Oceanographic Data Centre.

Results

The Irish Sea is semi-enclosed so that despite at times strong, over 30 m s^{-1}, westerly winds blowing across the British Isles, waves in Liverpool Bay are locally generated with maximum significant wave heights of 5.4 m and peak periods of 12 s. However for 68% of the measurements the significant wave height is less than 1 m, 92% less than 2 m and 98% less than 3 m. The notable features of the currents in Liverpool Bay, which is relatively shallow (less than 50 m), are the tides (over 1 m s^{-1} at spring tides), persistent mean currents and the lack of strong residual, wind driven, currents (less than 0.3 m s^{-1}). The mean current pattern driven by the horizontal density gradient (Verspecht et al., 2008) is of south or southeastward, shoreward, flow near the bed and northward flow near the surface of a few cm s^{-1}.

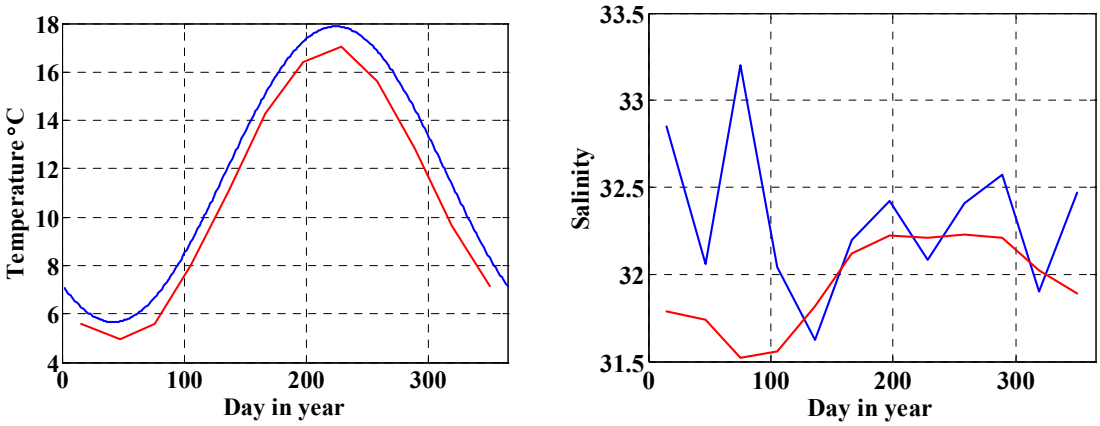

Figure 2. Surface temperature and salinity measurements from the Mersey Bar (blue) compared with monthly means from 1935–1969 (red).

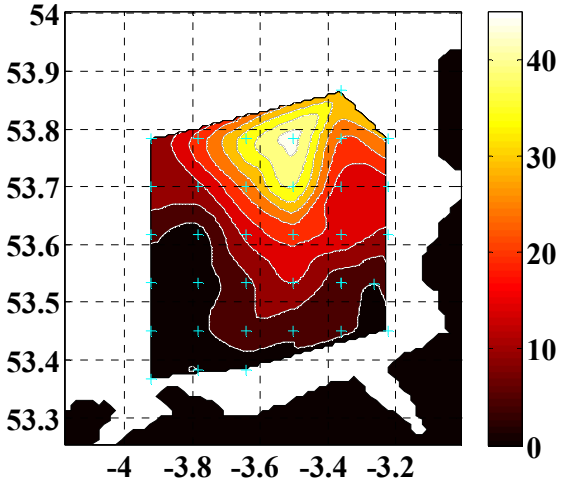

Figure 3. Per cent of the variance in the seasonal cycle for near bed salinity. Contours are at intervals of 5%.

In the five year period there have been over 50 cruises. The CTD stations show that temperature is dominated by the seasonal cycle, accounting for more than 95% of the variance at each site, Figure 2a. In contrast, for salinity the seasonal cycle accounts for less than 40% of the variance, variable spatially and at most sites less than 10%, Figure 3. For instance Figure 2b shows the annual signal from month by month averages in blue. There are inter-annual variations in salinity but a longer data set is needed to elucidate the driving forces, for instance river discharge or changes in circulation, and responses. Comparison with earlier measurements at the Mersey Bar show that the water has warmed by 1.1°C relative to 1935–61 (Hughes, 1966), in line with warming air temperatures but that salinities probably have not changed, Figure 2.

Liverpool Bay is an interesting region, on the edge of well mixed water to the west, near Anglesey; the latter a consequence of tidal mixing being sufficiently vigorous to mix heat and salinity inputs uniformly through the water column. Hence much of Liverpool Bay, apart from the shallowest areas, stratifies weakly in early summer by a few degrees centigrade in a complex interaction involving competition between buoyancy inputs (surface heat flux and freshwater from rivers and rainfall) and mixing by tides, (weaker than further west), winds and waves. The intermittent nature of the stratification is discussed by Howlett et al., (this volume). Being able to predict the variable water column structure and also the penetration of light with depth in these turbid waters is an essential prerequisite for biological modeling.

For example, suspended sediment in the water column tends to settle out as tidal mixing decreases towards neap tides, allowing light to penetrate deeper and thus triggering a bloom if sufficient nutrients are available, which happens intermittently throughout the summer from river discharge. The time taken for the bloom to reach maximum means counter-intuitively this can occur when the water column is most turbid, at the following spring tide.

Conclusions

The Liverpool Bay Coastal Observatory is unique, bringing together measurements on a wide range of space and time scales with a comprehensive modeling suite and a data management and web-based data delivery system. It has been in operation over 5 years. However such observing systems are resource hungry, in terms of equipment, cash and especially in people. Its design naturally involved compromises, for instance should the detailed geographic coverage be wider, including more of the Irish Sea, and / or should it extend closer to the shore, where biologically activity is greater? How many cruises should there be per year – nine visits, if achieved, will over-sample for a well defined seasonal cycle, such as temperature, but not for a variable with a more unpredictable or shorter time scale, such as salinity or phytoplankton? It is a perpetual struggle to ensure high data returns and data quality, with some variables easier to measure, for instance temperature, and others more difficult, sensors subject to fouling by sediment or to biofouling in the case of optics. There are also a range of outputs – scientific, management related, public awareness – which makes it more difficult to assess the Observatory's performance and effectiveness.

After five years the main scientific challenges remain both in understanding processes and in translating this understanding into predictive models whose accuracy has been quantified and which make best use of the measurements. The challenges relate to the physical environment (salinity, circulation in Liverpool Bay, the flow through the Irish Sea, flushing events); the role of sediments in the optical characteristics of the water column; the ecosystem and eutrophication. Only once these building blocks are in place will it be possible to predict possible impacts of climate change.

In the next few years the Observatory will expand collaboratively in spatial coverage to encompass the whole Irish Sea, both in acknowledgement of imminent UK and EU legislation but also because the Irish Sea embraces a wide variety of water column structure and of ecohydrodynamic regimes and is a better defined oceanographic entity. It is an excellent test bed for any continental shelf sea. The Observatory will also expand in capability, for instance through the deployment of a glider, by operating a second instrumented ferry on the Birkenhead to Belfast route and by maintaining a third in situ site.

References

Balfour, C.A., Howarth, M.J., Smithson, M.J., Jones, D.S., Pugh, J. (2007), *The use of ships of opportunity for Irish Sea based oceanographic measurements*. In: Oceans '07 IEEE Aberdeen, conference proceedings. Marine challenges: coastline to deep sea. Aberdeen, Scotland: IEEE Catalog No. 07EX1527C, 6pp.

Howarth, M.J., Proctor, R., Knight, P.J., Smithson, M.J., Mills, D.K. (2006), *The POL Liverpool Bay Coastal Observatory*. In: Proceedings of the World Maritime Technology Conference, 6–10 March 2006, London, 5pp.

Howarth, M.J., Player, R.J. Wolf, J., Siddons, L.A. (2007), *HF radar measurements in Liverpool Bay, Irish Sea*. In: Oceans '07 IEEE Aberdeen, conference proceedings. Marine challenges: coastline to deep sea. Aberdeen, Scotland: IEEE Catalog No. 07EX1527C. 6pp.

Hughes, P. (1966), The temperature and salinity of surface waters of the Irish Sea for the period 1947–61, *Geophysical Journal of the Royal Astronomical Society*, 10, 421–435.

Mills, D.K., Greenwood, N., Kröger, S., Devlin, M., Sivyer, D.B., Pearce, D., Cutchey, S., Malcolm, S.J. (2005), New approaches to improve the detection of eutrophication in UK coastal waters, *Environmental Research, Engineering and Management*, 2(32), 36–42.

Verspect, F., Rippeth, T.P, Souza, A.J., Burchard, H., Howarth, M.J., Simpson, J.H. (2008), Residual circulation and horizontal density gradients in the Liverpool Bay region of freshwater influence. (This volume.)

A 3-D numerical model of Liverpool Bay for the Coastal Observatory

ANDREW LANE

Proudman Oceanographic Laboratory, 6 Brownlow Street, Liverpool L3 5DA UK
email: ale@pol.ac.uk

Keywords: 3-D hydrodynamic model, bathymetry, tides; Liverpool Bay, UK

ABSTRACT

The Proudman Oceanographic Laboratory's Coastal Observatory, now running for more than five years, aims to understand how coastal seas respond to natural and man-made forcing. It is a 'pre-operational' monitoring system that integrates real-time measurements with coupled numerical models. These models provide daily forecasts of met-ocean conditions on a variety of scales, ranging from 12 km (Atlantic Margin) and 6 km (Medium Resolution Continental Shelf) to 1.8 km (Irish Sea).

The latest addition to this suite of models will be a 180-meter model of Liverpool Bay and the Dee, Mersey and Ribble estuaries, covering the Coastal Observatory's survey stations and mooring sites. This 3-D hydrodynamic model uses POLCOMS (Proudman Oceanographic Laboratory Coastal Ocean Modelling System) with meteorology and river flows as inputs, to predict temperature, salinity and sediment transport.

Here, we explore the model's performance, and how it can be used to support process studies. Our objective is to routinely compare real-time and survey data with model outputs, specifically vertical profiles and horizontal gradients. Results will inform planning of future surveys and coastal management, as well as improve model performance.

Model description

POLCOMS is a 3-D baroclinic B-grid model developed by Holt and James (2001), which incorporates refinements such as a 'Piece-wise Parabolic Method' (PPM) advection scheme, turbulence closure and, more recently, a 'Total Variation Diminishing' (TVD) wetting-drying scheme. This model is well suited to high-performance (large area and/or high resolution) applications executing on parallel computers. Figure 1 summarizes the suite of POLCOMS models that produces forecasts to supplement the near real-time measurements in the Coastal Observatory (Howarth et al., 2008; http://coastobs.pol.ac.uk/polcoms).

Models require bathymetry and other boundary conditions (e.g., tides on open boundaries, river inputs, etc.) in order to work; their specifications for the Liverpool Bay model are described below.

Bathymetry data sets

Bathymetry data are from LIDAR and echo sounding surveys for the Dee, Mersey and Ribble estuaries conducted by the UK Environment Agency and these are given with respect to Ordance Datum Newlyn (ODN). The estuaries bathymetry data are accurate to a few centimeters and originally at 2-m horizontal resolution on British National Grid coordinates; they are first mapped on to longitude/latitude. At Liverpool Gladstone Lock and Hilbre Island at the mouth of the Dee, local CD is 4.93 m below ODN, therefore an offset of −4.93 m was added to the Dee and Mersey estuary depths to convert them to CD. Similarly the offset for the Ribble is −4.90 m. Water depths for the remaining parts of Liverpool Bay, from Admiralty Charts, are below the local Chart Datum (CD), which corresponds approximately to the Lowest Astronomical Tide (LAT) level. Admiralty Chart depths are to the nearest 0.1 m nearshore, and to the nearest meter offshore on a WGS84 longitude/latitude coordinate system.

Differences between how depths are referenced should be resolved through the use of a Vertical Offshore Reference Frame (www.cege.ucl.ac.uk/research/geomatics/vorf). A simpler approach is to reduce all datasets (in local CD) together on to a 1/400° long × 1/600° lat (approximately 180-m) rectangular grid, using gridding software (e.g., Kriging method in 'Surfer'). However, this does not account for increasing mean level with distance upstream in estuaries.

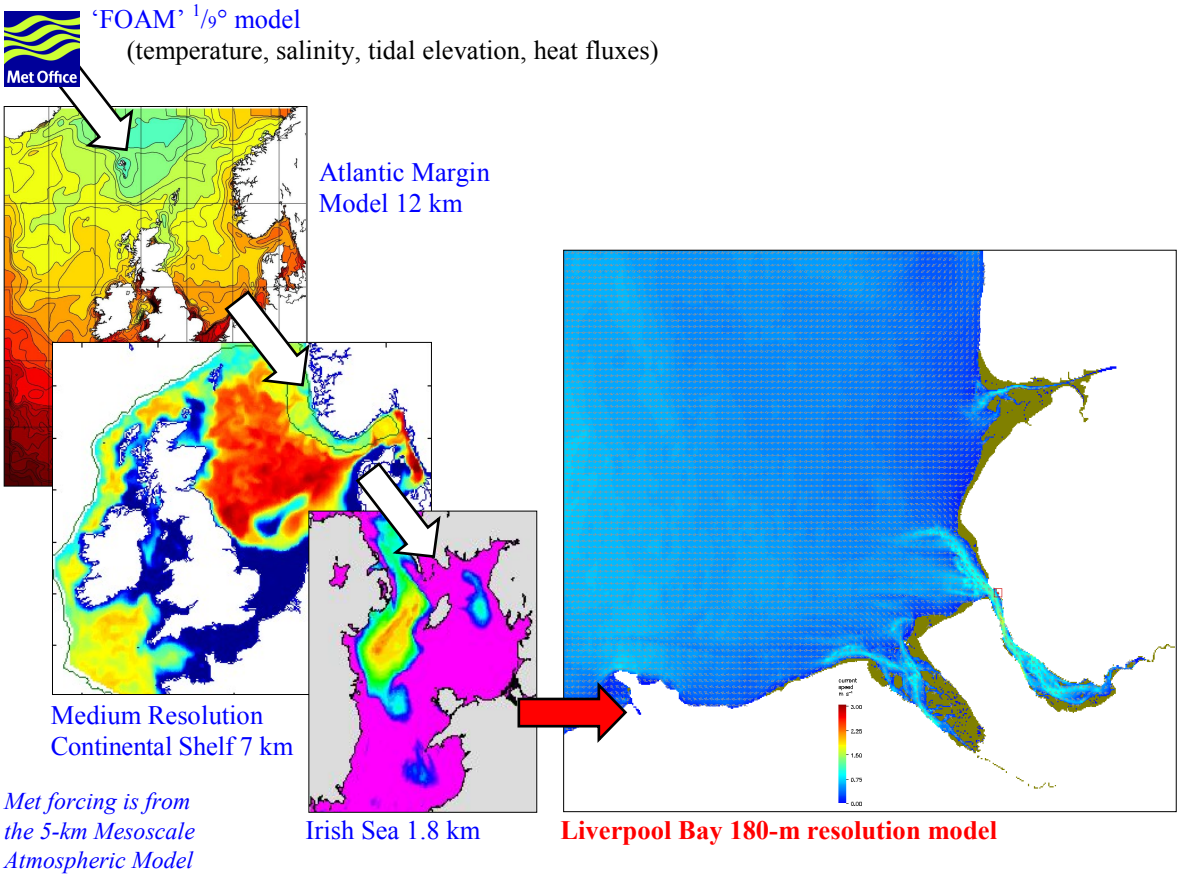

Figure 1. The suite of pre-operational models: Atlantic Margin, Medium Resolution Continental Shelf and Irish Sea. Information from the Met Office's FOAM model feeds into the Atlantic Margin model; results from one model are used as inputs in the next model. These POLCOMS models forecast sea temperature, salinity, tidal elevations and currents, waves, suspended sediments, light levels, nutrients and biology.

Model open boundary conditions

For tide-only model runs, amplitudes and phases of elevations and currents for each of 15 tidal constituents (diurnal: Q_1, O_1, P_1, S_1, K_1; semi-diurnal: $2N_2$, Mu_2, N_2, Nu_2, M_2, L_2, T_2, S_2, K_2; quarter-diurnal: M_4) were obtained from the Irish Sea 1.8 km model. Alternatively, timeseries of elevations and currents can be used. These are interpolated onto the open boundary locations, to drive the Liverpool Bay model. POLCOMS uses flux and radiation boundary conditions (Holt and James, 2001).

Model bathymetry

Models require bathymetry with respect to Mean Tide Level (MTL). Jones (1994, pp43–45) outlines a method for determining differences between MTL and LAT, linked to the amplitude of the M_2 tidal elevations. An amplitude factor is calculated,

$$A_{FACT} = \frac{\text{MTL} - \text{LAT}}{\text{MTL} - \tfrac{1}{2}(\text{MLWS} - \text{MLWN})} \qquad (1)$$

where MLWS and MLWN are Mean Low Water Springs and Mean Low Water Neaps, respectively. Values for these can be found in Admiralty Tide Tables (ATT). Table 3.1 in Jones (1994) lists values for European shelf seas, in which the mean value of A_{FACT} is 1.71. This is the factor by which the M_2 elevation amplitude is multiplied to obtain the LAT to MTL offset.

The initial bathymetry has 5.15 m added to it to give the appropriate MTL at Liverpool. At this stage the water depths become deeper than their 'correct' values towards the western side of the model area; on the north-western part they are approximately 0.8 m too deep. The Liverpool Bay model was run to obtain timeseries of elevations from which the M_2 elevation amplitude at each model grid-point $\hat{\zeta}_{M_2}(x, y)$, and then

Table 1. Amplitudes and phases of four tidal constituents from the Liverpool Bay model, and corresponding values from the UK Tide Gauge Network and Admiralty Tide Tables (2000, Vol. 1, Part III).

Location	**Mean tide level**	**M_2**		**S_2**		**K_1**		**O_1**	
Liverpool Bay model	**(above CD)**	**ampl.**	**phase**	**ampl.**	**phase**	**ampl.**	**phase**	**ampl.**	**phase**
Liverpool Gladstone	5.15 m	3.11 m	324°	1.08 m	015°	0.12 m	185°	0.10 m	033°
Hilbre Island	5.09 m	3.04 m	317°	1.06 m	008°	0.12 m	182°	0.10 m	029°
Llandudno	*4.59* m	2.78 m	310°	0.99 m	358°	0.12 m	174°	0.10 m	022°
UK Tide Gauge Network									
Liverpool Gl, 1992–2000	5.20 m	3.03 m	321°	0.97 m	005°	0.12 m	191°	0.11 m	041°
Hilbre Island, 1964	5.14 m	2.92 m	318°	0.95 m	000°	0.11 m	189°	0.11 m	039°
Llandudno, 1994–2000	4.07 m	2.68 m	310°	0.86 m	351°	0.12 m	185°	0.11 m	036°
Admiralty Tide Tables									
Liverpool Gladstone	5.15 m	3.08 m	322°	1.00 m	007°	0.12 m	190°	0.11 m	042°
Hilbre Island	5.15 m	2.94 m	318°	0.96 m	001°	0.14 m	186°	0.12 m	041°
Llandudno	4.10 m	2.61 m	312°	0.82 m	355°	0.14 m	186°	0.12 m	036°

the correction from CD to MTL is calculated as $A_{FACT} \times \zeta_{M_2}$, using $A_{FACT} = 1.71$. The model was run again with the adjusted bathymetry and with the same open boundary conditions. After the second iteration, differences are less than 0.05 m.

Comparisons with observations

Elevations

Table 1 lists some results from the Liverpool Bay model (run for a spring-neap cycle) of four main constituents at three locations. Also listed are corresponding values from the UK National Tide Gauge Network (part of the National Tidal and Sea Level Facility, www.pol.ac.uk/ntslf) and Admiralty Tide Tables. While the model phases of M_2 and S_2 are similar, the amplitudes are generally a few centimeters larger than those observed. For K_1 and O_1, amplitudes are similar, and model phases lead slightly. Results will likely improve for longer model runs.

Sea surface currents

Two HF radar stations (at Formby Point and Llanddulas) each record radial components of sea surface currents for the Coastal Observatory (see http://cobs.pol.ac.uk/wera/). The M_2 tidal constituents from a harmonic analysis of surface currents (combined vectors) recorded in 2007 are shown in Figure 2 (red). These overlay surface currents from the Liverpool Bay model (shown in blue).

Offshore currents are mostly east-west and nearly rectilinear, becoming elliptical nearer the deeper northern part of the model area. Model currents are almost orientated in line with the HF radar currents, except for nearshore. However, the model major axis amplitudes are smaller than radar amplitudes by a few percent, and there are also subtle differences in the eccentricities.

Future work

POLCOMS' advection-diffusion sediment transport routines will be adapted for use in Liverpool Bay, and this will complement a Lagrangian particle-tracking module. The Coastal Observatory has recently obtained near real-time river flow data which will be incorporated, with meteorological information, to model density effects on the circulation.

The overall objective is for the Liverpool Bay model to have similar capabilities of the existing pre-operational model suite. Its finer resolution will facilitate studies of processes that can't be determined by the larger scale models.

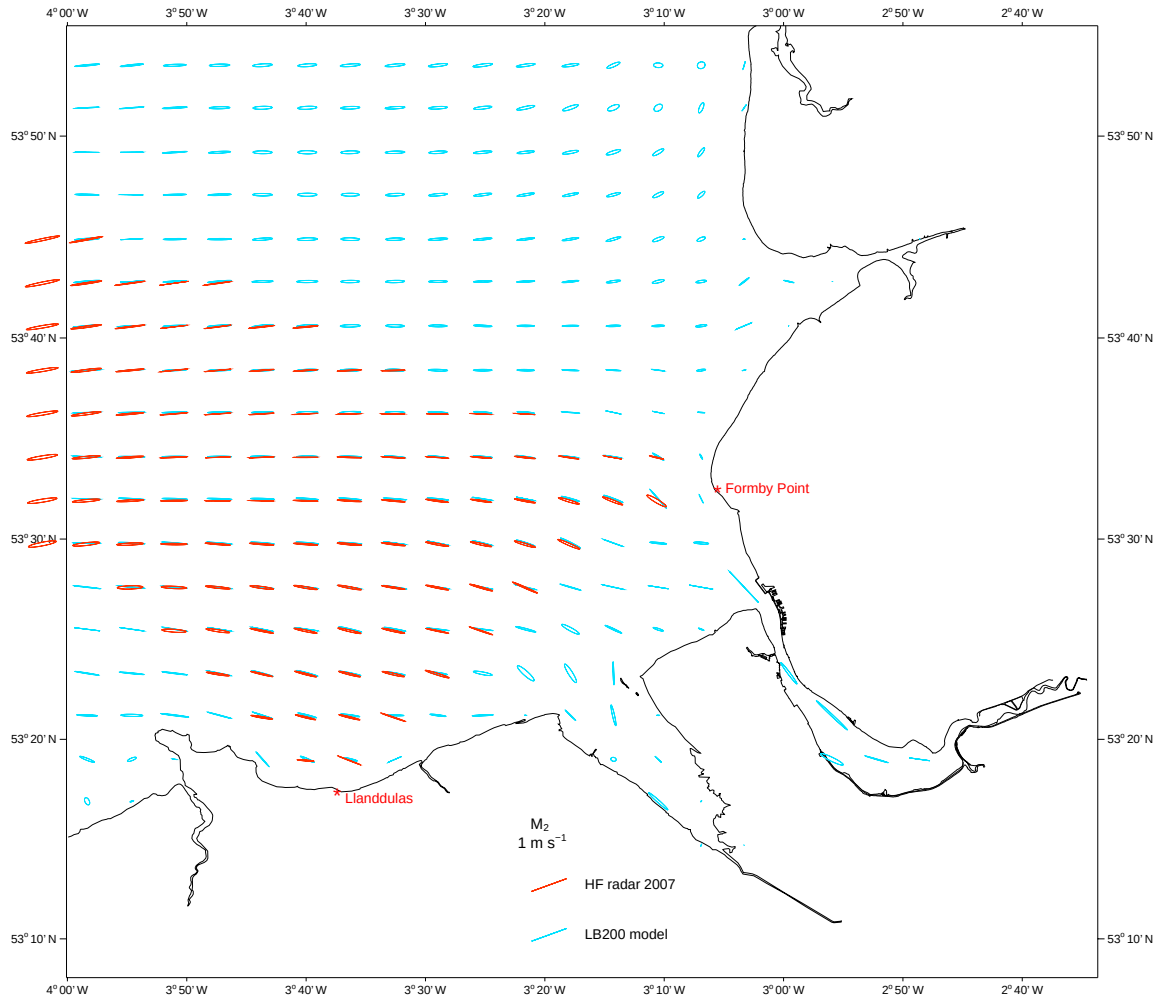

Figure 2. Comparison of M_2 surface current ellipses: HF radar during 2007 (red), and 180-m Liverpool Bay model (approximately one out of every 25 points is shown, in blue).

References

Admiralty Tide Tables (Published annually, in four volumes), *Vol. 1: United Kingdom and Ireland*. United Kingdom Hydrographic Office, Taunton.

Coastal Observatory Irish Sea: *POLCOMS Models* (http://cobs.pol.ac.uk/polcoms), and *The POL High Frequency (HF) Radar web site* (http://cobs.pol.ac.uk/wera/).

Department of Civil, Environmental and Geomatic Engineering, University College London, *Vertical Offshore Reference Frames project* (www.cege.ucl.ac.uk/research/geomatics/vorf).

Holt, J.T., James, I.D. (2001), An *s* coordinate density evolving model of the northwest European continental shelf: 1, Model description and density structure, *Journal of Geophysical Research*, 106(C7), 14015–14034.

Howarth, M.J., Proctor, R., Balfour, C., Knight, P.J., Palmer, M., Player, R.J. (2008), The Liverpool Bay Coastal Observatory. (This Volume.)

Jones, J.E. (1994), Numerical modelling of tides, surges, residual circulation and salinity in shelf seas. Ph.D. Thesis, University of Liverpool. 300pp.

Stratification patterns induced by fortnight and semi-diurnal changes in an estuarine tidal channel: a modeling study

NUNO VAZ[1, 2], JOÃO MIGUEL DIAS[2], PAULO CHAMBEL LEITÃO[3]

1. Instituto Superior Técnico, Universidade Técnica de Lisboa,
Av. Rovisco Pais, 1049-001 Lisboa, Portugal
email: nuno.vaz@ist.utl.pt

2. Departamento de Física, Universidade de Aveiro, Campus de Santiago,
3810-193 Aveiro, Portugal
email: joao.dias@ua.pt, nuno.vaz@ua.pt

3. Hidromod, Av. Manuel da Maia, 36, 3ºesq., 1000-201 Lisboa, Portugal
email: paulo.chambel@hidromod.com

Keywords: stratification, estuarine circulation, baroclinic model, tidal channel

ABSTRACT

A three-dimensional model is used to study ebb-flood and spring-neap variations of stratification induced by tidal flows in the Espinheiro Channel (Ria de Aveiro, Portugal). The model accurately reproduces sea surface height in the channel. At the lower portion of the channel, the depth-averaged current oscillates at the M_2 frequency presenting ebb values about 30% (10%) higher than the flood one at neap (spring) tide. At peak flood, the velocity profiles present a subsurface maximum (at neap tide) and a nearly linear variation during spring tide. At peak ebb, the velocity profiles vary almost linearly in depth. The salinity profiles reveal stronger stratification on flood during the neap tide. This stratification is almost destructed during the spring tide when the tidal currents are higher. The modulation of tidal currents over the spring-neap cycle, induced by the interaction between the major semi-diurnal tidal constituents, induces fortnight fluctuations in stratification and turbulent mixing in the low portion of the channel (near the channel's mouth).

Introduction

Recent observations in estuarine regions have revealed an asymmetry in stratification and turbulent mixing over a tidal cycle. At the Columbia River estuary, Jay and Smith (1990) found a flood-ebb asymmetry with enhanced shear and stratification during ebb and stronger mixing and weaker stratification during flood tides. Stacey and Ralston (2005) suggested that the asymmetry is induced by a strain-induced buoyancy flux that stabilizes on ebb and destabilizes on flood tides. At Chesapeake Bay, Li and Zhong (2007) used a three-dimensional numerical model to investigate this issue and found that the asymmetric tidal mixing causes significant variation in salinity distributions over the flood-ebb cycle. In contrast to these investigations at those estuaries, no observations of tidal variability have been made in the Espinheiro Channel. In this work, the effect of tidal variability on stratification is investigated in one station (station A, lower portion of the channel), near the channel's mouth.

The Espinheiro channel is approximately 11 km long, has an average width of about 200 m and a mean depth along its longitudinal axis of about 10 m (Figure 1). The tides are mixed semi-diurnal, with M_2 being the most important constituent, representing more than 90% of the tidal energy (Dias et al., 1999). The channel's dynamics is mainly controlled by the interaction of tides and incoming river flow (Vaz et al., 2007). In the lower portion of the channel (near the mouth) during neap tides, tidal currents present values between 0.6 (flood) and ~1.0 m s^{-1} (ebb). At spring tides, these values are higher ranging from 1.6 (ebb) to 1.5 m s^{-1} (flood). The Espinheiro channel presents characteristics of an ebb-dominated channel (Vaz et al., 2007).

A 3-D baroclinic numerical model (Mohid, Martins et al., 2001) was used to perform hindcast simulations of the Espinheiro Channel covering short periods of time in order to assess the channel's vertical structure under different tidal and river inflow conditions. However, no effort was made until now, to understand how intra-tidal and spring-neap variations of tidal flow affect stratification. The results obtained with this study points to the inevitability of future application of pre-operational methods to successfully monitor this channel.

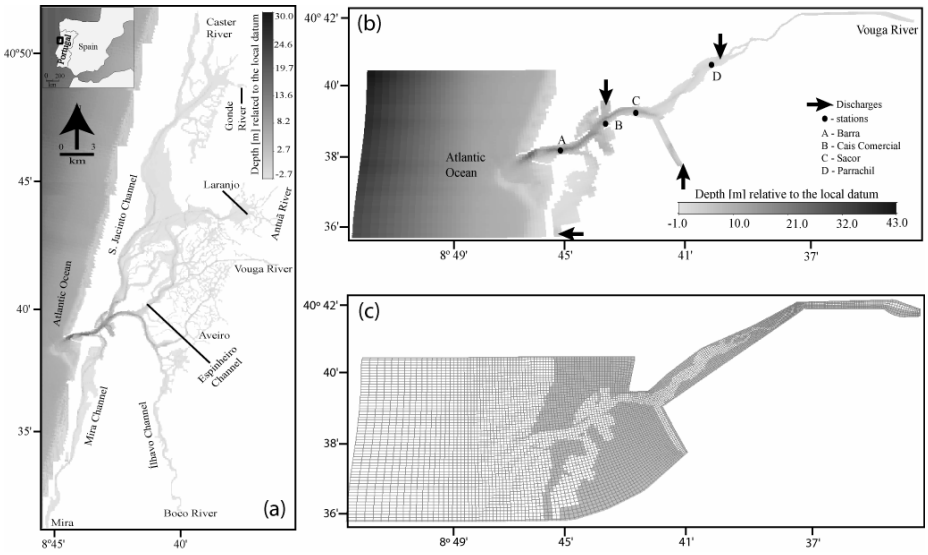

Figure 1. (a) Bathymetry of the Ria de Aveiro lagoon and adjacent coastal area. Major tributaries are marked. (b) Bathymetry of the Espinheiro Channel with the discharge points (marked with arrows) and its major freshwater tributary. The location of the stations used in the hydrodynamic calibration procedure is marked. Depths are in meters (over the local datum). (c) Horizontal curvilinear coordinate system

The numerical model

Mohid (Martins et al., 2001) has been configured to be applied in this channel. An orthogonal curvilinear coordinate system is designed to follow the general orientation of the Espinheiro Channel. The grid spacing is less than 100 m in the longitudinal and about 50 m in the cross-channel direction. The model uses ten vertical sigma layers. Ria de Aveiro is a branched coastal lagoon in which the tidal prism divides spreading toward the main channels. Thus, the tidal prism decreases upstream affecting the channel's dynamic. In order to simulate the inflow/outflow at the arrow marked boundaries the model uses flow values computed using a two-dimensional application of the model for the entire area of the lagoon (Figure 1a).

At the bottom, the friction shear stress is imposed assuming a velocity logarithmic profile. The vertical eddy viscosity and diffusivity are computed by the model using the General Ocean Turbulence Model (GOTM) (coupled to Mohid) (Burchard et al., 1999). Coefficients of horizontal eddy viscosity and diffusivity are set to 2 $m^2 s^{-1}$. Initial conditions for the hydrodynamic model are null free surface gradient and null velocity in all grid points. Initial conditions for the transport model are constant values of salinity and water temperature (typical values of oceanic waters).

The model is forced with tidal heights at the ocean open boundary, freshwater inflows at river mouths, water inflow, salinity and temperature time series at the locations marked with arrows (Figure1b) and heat exchange across the surface. In order to calculate the water, salinity and temperature fluxes in each arrow mark location (Figure 1b), the hydrodynamic and transport models were run in a 2-D (depth integrated) mode for the entire area of the lagoon (Vaz et al., 2005), calculating time-varying discharge, salinity and water temperature time series.

The simulation period was June 2004 under medium-to-low river discharge, with maximum and minimum freshwater discharges of the order of 20 $m^3 s^{-1}$ and 2 $m^3 s^{-1}$, respectively.

Results and discussion

In order to study the effects of tidal flow on stratification it is important that the model accurately predicts tidal heights and tidal currents in the channel. In a previous study, Vaz et al., (2007) show that the model accurately predicts tidal heights in the channel. The skill coefficient between data and model outputs is of the order of 0.9 in the four stations marked at Figure 1b.

Then, it was analyzed the flood-ebb asymmetry during a neap and a spring tide. It was selected a station in the lower portion of the channel (Station A, see Figure 1b for its location) and were chosen two instants

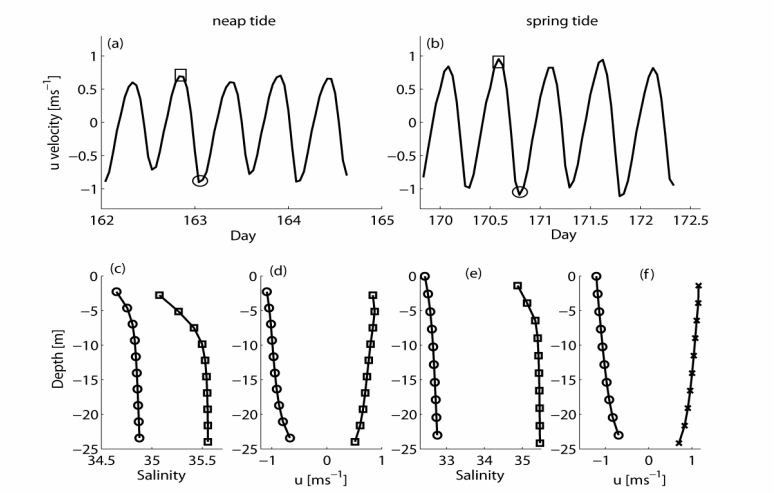

Figure 2. (a, b) Time series of along-channel depth-averaged velocity (*u* component) at station A at neap and spring tide; (c, d) Vertical profiles of salinity at the peak flood (squares) and peak ebb (circles) at neap tide and (e, f) spring tide.

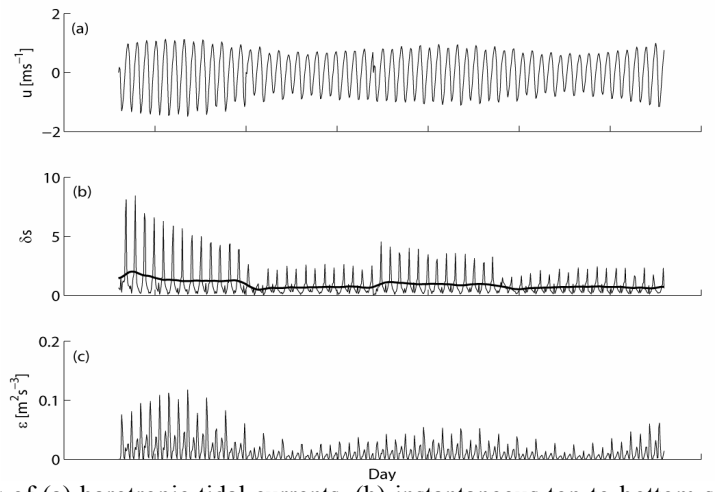

Figure 3. Time series of (a) barotropic tidal currents, (b) instantaneous top-to-bottom salinity difference, (c) depth-average energy dissipation at the lower portion of the channel (station A). The thick line in (b) represents the filtered salinity difference.

during the tidal cycle: one representing the peak flood and the other representing the peak ebb. As shown in Figures 2a and 2b, the depth-averaged current oscillates at the M_2 frequency. The barotropic current presents ebb values about 30% (10%) higher than the flood one at neap (spring) tide. In Figures 2c-f, it were compared the vertical profiles of salinity and current velocity between the peak flood and ebb tides.

Both at neap and spring tide, the salinity profiles (Figures 2c and 2e) show higher stratification on peak flood than on peak ebb. This feature may be induced by the higher tidal velocities on ebb tide that increases turbulent mixing which causes a decrease on stratification. At neap tide, the peak flood velocity profile shows a subsurface maximum (~5 m depth) and a quasi-linear distribution on ebb tide (Figure 2d). On the flood, this slight drop of the water velocity may be caused by the non-tidal pressure gradient that reinforces the tidal pressure gradient at the deepest layers but opposes it near the surface. On ebb, the non-tidal pressure gradient reinforces the tidal pressure gradient near the surface but opposes it at the bottom layers, resulting in a nearly linear depth distribution of the depth-average velocity. At spring tide, the depth variation of the barotropic current is nearly linear at peak flood and peak ebb.

The spring-neap variability was analyzed at station A. The tidal currents show semi-diurnal and fortnight cycles (Figure 3a). The tidal current varies from 1.6 m s^{-1} at the strongest spring to nearly 0.6 at the weakest neap (on ebb). The vertical stratification (Figure 3b), reveals a maximum of about 8 and a minimum of nearly 2. The relationship between the tidal currents and vertical stratification appears to be more linear than that found by Li and Zhong (2007) at the Chesapeake lower bay. Maximum stratification is reached on the

first spring tide. This was found closely related to the freshwater inflow occurred at the beginning of June (about 18 $m^3 s^{-1}$). In fact, due to the small size of the channel, the freshwater inflow also plays a key role in the modulation of stratification even at the lower portion of the channel.

The competition between tidal currents and freshwater inflow creates stratification-destratification in the water column on flood and ebb tide, respectively.

Small changes in the tidal velocity may induce large variation in turbulent kinetic energy (TKE) which is proportional to the cube of tidal current velocity. As shown in Figure 3c, the depth-averaged energy dissipation rate show strong fluctuation over the spring-neap cycle. The peak dissipation rate is reached on the first spring when stratification is destructed by the effect of the large tidal currents on ebb tide which increases vertical mixing. The peak dissipation rate on spring is at least 6 times higher than that on the weak neaps.

Conclusions

The results presented here show that there is a marked difference in stratification during the ebb-flood cycle. It is noted that the water column is more stratified on peak flood than on peak ebb. This could be due to the competing effect between tidal propagation and freshwater discharge into the channel.

At the lower portion of the channel, the depth-averaged current oscillates at the M_2 frequency presenting ebb values about 30% (10%) higher than the flood one at neap (spring) tide

The relationship between the tidal currents and vertical stratification appears to be more linear than those found by Li and Zhong (2007) at the Chesapeake lower bay.

It was used a baroclinic model to examine how flood-ebb and spring-neap flows affect stratification in Espinheiro Channel. In spite of the previous validation of the model (Vaz et al., 2007), there are no available data in order to resolve spring-neap tidal cycles in this channel. Therefore, the results presented here could (and should) motivate future observational program on this issue and also future applications of the model in order to monitor this channel.

Acknowledgments

This work was made under the scope of AMDRAPHYD (POCTI/AMB/57928/2007). Nuno Vaz is supported by the Portuguese FCT through a post-doc grant (SFRH/BPD/37325/2007).

References

Burchard, H., Bolding, K., Villarreal, M.R. (1999), *GOTM, a general ocean turbulence model: Scientific documentation*, Technical Report, European Commission, Ispra, Italy.

Dias, J.M., Lopes, J.F., Dekeyser, I. (1999), Hydrological characterization of Ria de Aveiro, in early summer, *Oceanologica Acta*, 22 (5), 473–485.

Jay, D.A., Smith, J.D. (1990), Residual circulation in shallow estuaries. II. Weakly stratified and partially mixed, narrow estuaries, *Journal of Geophysical Research*, 95, 733–748.

Li, M., Zhong, L. (2007), Flood-ebb and spring-neap variations of mixing, stratification and circulation in Chesapeake Bay, *Continental Shelf Research*, doi:10.1016/j.csr.2007.06.012. (In press.)

Martins, F., Leitão, P., Silva, A., Neves, R., (2001), 3-D modelling in the Sado estuary using a new generic vertical discretization approach, *Oceanologica Acta*, 24(1), S51–S62, suppl. S.

Stacey, M.T., Ralston, D.K. (2005), The scaling and structure of the estuarine bottom boundary layer, *Journal of Physical Oceanography*, 35, 55–71.

Vaz, N., Dias, J.N., Leitão, P., Martins, I. (2005), Horizontal patterns of water temperature and salinity in an estuarine tidal channel: Ria de Aveiro, *Ocean Dynamics*, 55, 416–429, doi:10.1007/s10236-005-0015-4.

Vaz, N., Dias, J.M., Leitão, P.C. (2007), Three-dimensional modelling of a tidal channel: The Espinheiro Channel (Portugal), *Continental Shelf Research*, doi:10.1016/j.csr.2007.12.005. (In press.)